Spiral galaxy HI models, rotation curves and kinematic classifications

Theresa B. V. Wiegert

A thesis submitted to the Faculty of Graduate Studies of

The University of Manitoba

in partial fulfillment of the requirements of the degree of

Doctor of Philosophy

Department of Physics & Astronomy

University of Manitoba

Winnipeg, Canada 2010

Abstract

Although galaxy interactions cause dramatic changes, galaxies also continue to form stars and evolve when they are isolated. The dark matter (DM) halo may influence this evolution since it generates the rotational behaviour of galactic disks which could affect local conditions in the gas. Therefore we study neutral hydrogen kinematics of non-interacting, nearby spiral galaxies, characterising their rotation curves (RC) which probe the DM halo; delineating kinematic classes of galaxies; and investigating relations between these classes and galaxy properties such as disk size and star formation rate (SFR).

To generate the RCs, we use GalAPAGOS (by J. Fiege). My role was to test and help drive the development of this software, which employs a powerful genetic algorithm, constraining 23 parameters while using the full 3D data cube as input. The RC is here simply described by a tanh-based function which adequately traces the global RC behaviour. Extensive testing on artificial galaxies show that the kinematic properties of galaxies with inclination $> 40\,^{\circ}$, including edge-on galaxies, are found reliably.

Using a hierarchical clustering algorithm on parametrised RCs from 79 galaxies culled from literature generates a preliminary scheme consisting of five classes. These are based on three parameters: maximum rotational velocity, turnover radius and outer slope of the RC.

To assess the relationship between DM content and the kinematic classes, we generate mass models for 10 galaxies from the THINGS and WHISP surveys, and J. Irwin's sample. In most cases mass models using GalAPAGOS RCs were similar to those using traditional "tilted-ring" method RCs.

The kinematic classes are mainly distinguished by their rotational velocity. We confirm correlations between increasing velocity and B-magnitude, optical disk size, and find

earlier type galaxies among the strong rotators. SFR also increases with maximum rotational velocity. Given our limited subsample, we cannot discern a trend of velocity with DM halo properties such as M_{halo}/M_{baryon}.

Using this strategy on upcoming large databases should reveal relationships between the DM halo and our kinematic classification scheme. If NGC 2841, NGC 3521 and NGC 5055 are understood to have declining RC after further investigation, this cannot be explained by the usual morphology scenarios.

Acknowledgements

First and foremost I would like to thank my supervisor, Dr. Jayanne English, for her ideas, help, patience, and consequently all that she has taught me during these years.

I am also very grateful to Dr. Jason Fiege, the creator of GalAPAGOS, who has acted as an unofficial co-supervisor.

Dr. Samar Safi-Harb provided access to her powerful computer cluster, without which it would have been nearly impossible to finish the multitude of GalAPAGOS runs.

Huge thanks to Dr. Rob Swaters who taught me mass modelling, and for answering questions and giving valuable advice. Thanks to Dr. Judith Irwin for providing data for this thesis, being excellent support during JCMT observations, and for words of encouragement. Thanks to Dr. Brian Yanny for helping with the SDSS photometry and to Dr. Chris Fluke for helping with s2plot scripts.

Thanks to all members of our small but cosy astronomy society at the University of Manitoba that I have not mentioned yet: Jennifer, Heather, Harsha, Adam, Ian... And a special thanks to Maiko for awesome computer support. Huge thanks to Susan Beshta for all her hard work making it all happen!

Elizabeth – thank you for reading a number of my chapters. Sofia, Eva, Alyssa, and all the wonderful friends I have not mentioned - you know who you are, and I hope you realise how much I appreciate your help throughout these years.

Ett stort tack to my wonderful family who have been so near despite the great distance, and always given me support: Monica (who read the entire thesis in search of typos), Lars, Benjamin, Daniel, och Joachim. My experience in Winnipeg provided me with the greatest 'gift' of all: my husband David, thanks for always being there for me.

I would like to acknowledge the Department of Physics & Astronomy and the Faculty of Science at the University of Manitoba for financial support.

Thanks to the WHISP team for providing data from the WHISP survey, van der Hulst, J. M., van Albada, T. S., & Sancisi, R. 2001, ASPC series, Vol. 240.

This work made use of THINGS, 'The HI Nearby Galaxies Survey', Walter et al. 2008, AJ, 136, 2563

This research has made use of the NASA/IPAC Extragalactic Database (NED) which is operated by the Jet Propulsion Laboratory, California Institute of Technology, under contract with the National Aeronautics and Space Administration.

We acknowledge the usage of the HyperLeda database (http://leda.univ-lyon1.fr).

This research has made use of the Sloan Digital Sky Survey. Funding for the SDSS and SDSS-II has been provided by the Alfred P. Sloan Foundation, the Participating Institutions, the National Science Foundation, the U.S. Department of Energy, the National Aeronautics and Space Administration, the Japanese Monbukagakusho, the Max Planck Society, and the Higher Education Funding Council for England. The SDSS is managed by the Astrophysical Research Consortium for the Participating Institutions. The SDSS Web Site is http://www.sdss.org/.

This research made use of Montage, funded by the National Aeronautics and Space Administration's Earth Science Technology Office, Computational Technnologies Project, under Cooperative Agreement Number NCC5-626 between NASA and the California Institute of Technology. The code is maintained by the NASA/IPAC Infrared Science Archive.

Three-dimensional visualisation was conducted with the S2PLOT programming library (D.G.Barnes, C.J.Fluke, P.D.Bourke & O.T.Parry, 2006, Publications of the Astronomical Society of Australia, 23(2), 82-93).

For Pi

Contents

List of Figures

List of Tables

Chapter 1

Introduction

"This very starry heaven, stupendous as it is, forms, perhaps, but a single sphere, of which our solar vortex constitutes only a part; for the universe is finited in the infinite. Possibly there may be other spheres without number similar to those we behold; so many indeed and so mighty, perhaps, that our own may be respectively only a point; for all the heavens, however many, however vast, yet being but finite, and consequently having their bounds, do not amount even to a point in comparison with the infinite."

– Emanuel Swedenborg, 1734

Even though observational evidence of the existence of galaxies did not take place until the beginning of the 20th century, the concept was born already in the early and mid-18th century, by Swedish philosopher Emanuel Swedenborg and Thomas Wright of Durham in England, who apparently conceived the ideas independently of each other (Swedenborg, 1734; Wright, 1750). Building upon the ideas of Wright, German philosopher Immanuel Kant referred to galaxies as "island universes" (Kant, 1755). He brought forth many astonishingly correct theories, given the small amounts of observational aid at the time, about the nature of the Milky Way and the possibility of other such similarly structured collections of stars at great distances.

However, there was no way of distinguishing the difference between star clusters belonging to our own Milky Way Galaxy from anything located much further away, since no telescopes had sufficient capabilities. The first indications of validation of the "island universe" concept came through spectroscopy. Measurements of both systemic velocities and rotational velocities indicated that the spiral-shaped nebulae were moving too fast to be gravitationally bound by the Milky Way. These measurements took place in the early 20th century by Slipher (1913) and Wolf (1914), who detected inclined absorption lines for the "nebulae" they observed. With this first observational evidence for galaxies beyond the Milky Way, a new paradigm of the Universe was born.

The common features of galaxies are that they are vast, gravitationally bound collections of gas, dust, stars and dark matter. Beyond these common characteristics, they exhibit a plethora of individual traits – they can be found in many different shapes, colours and with different characteristics, with constituents differing in age and elemental abundance. There are red elliptical galaxies with old stars, beautiful blue spiral galaxies with areas of massive star formation, and enigmatic irregular galaxies which can be rather chaotic in their structure. Some galaxies are small (dwarfs), some are massive and some are extremely bright. Despite the range of differences (of which only a few were mentioned here), galaxies can be divided into classes based on similarities in their characteristics. Hubble (1936) devised a widely used morphological classification scheme, later revised and expanded by e.g. de Vaucouleurs (1959). The basic scheme is referred to as a tuning fork diagram, where elliptical galaxies of type E0 to E7 follow the "handle" of the tuning fork, and disk galaxies – in particular spiral galaxies – with normal bulges on one side of the fork and with barred bulges on the other. Figure 1.1 shows an example of the tuning fork with galaxies observed with the Sloan Digital Sky Survey (SDSS). See Hubble's original sketch of the tuning fork in Hubble (1958). In the de Vaucouleurs extension, the nomenclature for the presence of a bar was expanded upon (A = no bar, AB

= intermediate/small bar, B=bar) and other characteristics were included, such as the presence of a ring ((r)=ring, (s)=no ring, (rs)=intermediate stage between (r) and (s)).

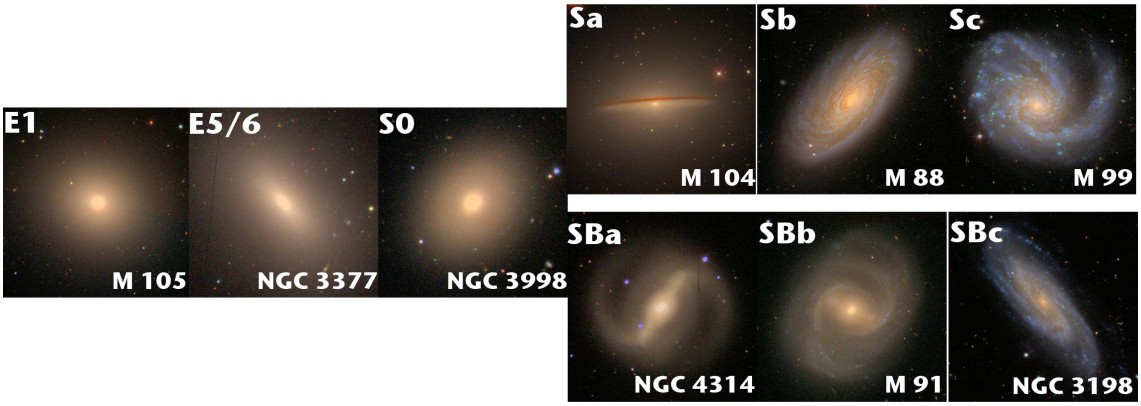

Figure 1.1: The Hubble tuning fork displaying the different galaxy morphologies. These images are from the Sloan Digital Sky Survey (SDSS, http://www.sdss.org), a survey from which near infrared (NIR) data is used in this thesis. Due to these images being part NIR, (constructed from SDSS i, g and i-bands) no strong dust lanes are shown, making some of the Hubble morphology lost in the pictures. Additionally, the images are not optimised to show features since the image manipulation process is not uniform.

The Hubble type nomenclature is still in use, not only for the individual galaxy types, but also according to what was then hypothesized to be an evolutionary direction along the tuning fork. Thus, E, S0, and Sa galaxies with a large bulge in relation to its disk and tightly wound arms, are referred to as *early type* galaxies, while the spiral galaxies further out on the fork with smaller bulges and arms less tightly wound around the bulge (Sc, Sd) are referred to as *late-type* galaxies (note that this is opposite to what the age of the stellar populations in the different types imply and the names should not be interpreted as actual evolutionary steps).

In this thesis, the focus is laid on disk galaxies of types Sa through Sd, regardless of whether they have clearly defined spiral arms or not. Hereafter the usage of the term "galaxies" will refer to disk galaxies, unless otherwise stated.

This thesis is, however, not about how the galaxies look (morphology). The thesis is

about how they *move* (kinematics), and the endeavour of the thesis is to explore their different choreographies, and what common personal characteristics influence their 'dance'.

1.1 Galaxy structure and neutral hydrogen content

The stars in a spiral galaxy form a disk structure with a central spheroid which includes a bulge and a nucleus. Roughly half of the galaxies also have a bar of stars stretched across the nucleus. A spiral pattern is often superimposed on the disk, with the arms of the spiral delineated by molecular gas, dust and young stars. The galaxy is surrounded by stars and clusters of stars called globular clusters. This distribution extends from the disk outwards, in a spherical shape, forming the stellar halo of the galaxy.

The most abundant element in the universe, atomic neutral hydrogen (HI), is one of the major constituents of a galaxy. The gas forms a thin layer in the galaxy mid-plane but often extends far beyond the radius of the stellar disk, making HI observations ideal for observing behaviour beyond the optical radius such as rotational kinematics.

HI emission, caused by a spin flip transition of the electron, has a very small probability with a lifetime of 1.1×10^7 years for the excited state (e.g. Binney & Merrifield, 1998, Chapter 8). Although HI emission is thus very unlikely to be observed in a laboratory, the large HI prevalence in galaxies makes its 21 cm (1.420 GHz) emission line a traditional observing wavelength for radio telescopes.

HI can be used to study galaxy formation and evolution. An example of this comes from detailed HI studies of the Milky Way Galaxy: due to the Galaxy's tangible proximity to our interior location, details can be studied which are difficult to discern in other galaxies, revealing an abundance of interesting features. One such class of features is High Velocity Clouds (HVC), gas clouds moving at velocities anomalous compared to the orbit of the disk. Gas features with anomalous velocities, which we may be able to identify

as the counterparts of the HVCs, are being found in other galaxies where we have good enough resolution to see details in the velocity fields (e.g. King & Irwin, 1997).

These anomalies can illuminate how galaxies form and evolve as well as constrain cosmological models. For example, the HVCs proximity to a particular galaxy may indicate whether they are debris (tidal or blowout from the disk) or if they are residual clouds created shortly after the Big Bang. Additionally, gas features observed to extend perpendicularly away from the disk of a galaxy may be the result of star formation. If so, these extensions would be distributed near the centres of galaxies rather than their outer regions where star formation is known to be low.

However, rather than studying features that are anomalous compared to the disk, this research uses HI data to focus on the HI disk layer itself. The HI disk harbours much information on the galaxy, and indeed, it was studies on the HI disk that led to the fruitful discovery of dark matter, first observationally confirmed in NGC 300 by Freeman (1970).

This work uses the HI disk layer to assess the disk kinematics, help determine the amount of dark matter and develop a galaxy classification scheme based on kinematics.

Although I observed carbon monoxide (CO) emission using the sub-millimetre telescope JCMT during the course of my thesis work (see Chapter 2), the work presented in this thesis utilizes privately provided and publically available HI data of 16 galaxies. The CO data, useful for determining kinematics in the centre of galaxies, were not used in the final analysis due to a combination of no results (minimal CO emission in NGC 925) and timing constraints (access to both CO and HI data for a number of galaxies was not possible until a later stage of the thesis work).

The HI data were observed with the VLA (J. Irwin, the publically available THINGS survey (de Blok et al., 2008)) and Westerbork (provided from the WHISP survey by R. Swaters (van der Hulst et al., 2001)) as well as the single dish telescope Parkes (the HIPASS survey, Koribalski et al., 2004). Details about the data are presented in Chapter 2.

1.2 Rotation curves and dark matter

HI observations acquired with radio interferometers combine imaging and spectroscopy and hence include information on the radial velocity[1] of the emission, via the Doppler shift. That is, the rotation of a galaxy (of sufficient inclination to exhibit radial velocities) is measured and can be displayed in a rotation curve as a function of radius (see Figure 1.2).

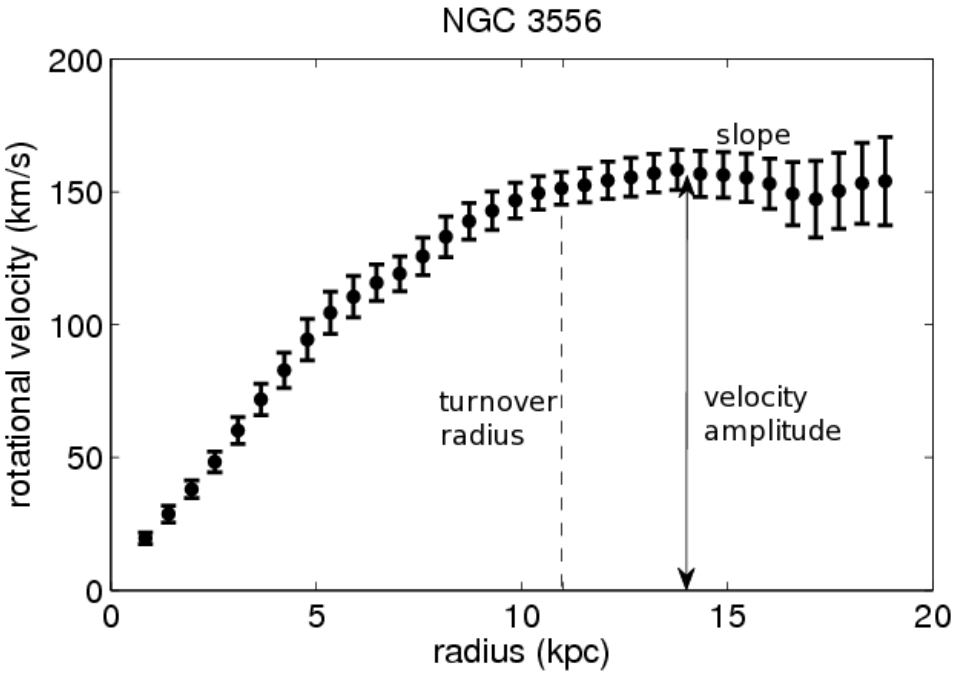

Figure 1.2: Rotational behaviour of nearly edge-on spiral galaxy NGC 3556 measured from VLA data provided by J.Irwin (see Chapter 3 for information of the measurements). The velocities of the approaching and the receding sides of the galaxy have been averaged together in this rotation curve. The rotation curve is ultimately determined by its velocity amplitude (maximum velocity of the curve), its turnover radius (the radius where the curve changes from rising to a flat shape) and the slope of the curve at radii beyond the turnover radius. This particular galaxy has an unusually large turnover radius. The error bars are the uncertainties as determined by the velocity dispersion of the data at that particular radius.

Rotation curves of spiral galaxies are the major tool for determining the distribution

[1]Radial velocity is the velocity measured in the direction of a line of sight, i.e. the velocity component towards or away from the observer.

of mass in the galaxies. They provide fundamental information for studying and understanding the kinematics of galaxies, as well as their formation and evolution. Evolutionary history and the roles interactions might have played are inferred by rotation curves, and the amount of dark matter is directly implied by the prevalent deviation from a historically expected Keplerian decline that our solar system exhibits (i.e. the velocity squared is proportional to the inverse of the distance). As mentioned in the beginning of this chapter, Slipher and Wolf were the first to notice galaxy rotation in what was recognised as galaxies, at great distances from our Milky Way. Not too long after, questions were raised about the mass distribution of galaxies, since the high velocities measured at large radii seemed to indicate that the distribution of mass appeared to have little relation to that of the light. Indeed, the rotation curve stayed flat at large radii, rather than declining. Such a flatness is a clear indication of the presence of additional matter which evidently does not emit any observable radiation.

A simple demonstration of this is shown in the equilibrium of force in an orbit, where the centripetal force is equal to the gravitational force, i.e. :

$$\frac{mv(r)^2}{r} = \frac{GmM(r)}{r^2} \tag{1.1}$$

where M(r), referred to as the dynamical mass, is the rotational velocity at this radius and G is the gravitational constant. As the radius increases and the velocity stays constant (denoted as a "flat" rotation curve), the amount of mass must increase (assuming a spherical mass distribution).

These discrepancies between the luminous and dynamical mass were indicated by Zwicky (1933), and later observationally confirmed in the 1970's by both single dish observations (Freeman, 1970) and observations using synthesis radio telescopes by e.g. Rogstad & Shostak (1972). At the same time, Ostriker & Peebles (1973) proposed the

existence of what is referred to as a dark matter (DM) halo of a galaxy to explain the discrepancy.

The first large study of mass distributions from HI rotation curves was done by Bosma (1978, 1981a,b). While e.g. Rubin et al. (1978) showed that optical rotation curves flattened at moderate radii (largely due to the combination of the bulge and disk contributions), Bosma observed that the rotation curves of most spiral galaxies also remain flat for HI far beyond the optical radius. It was thus concluded that there are substantial amounts of unseen matter in galaxies (e.g. Bosma, 1981b; Carignan & Freeman, 1985; van Albada & Sancisi, 1986; Begeman, 1987).

Not only rotation curves predict the existance of DM - for example gravitational lensing is another strong indicator of large amounts of unseen matter, where the gravity of a galaxy or cluster of galaxies (the lensing object) bends the light of an object at a far away distance hidden behind the lensing object, to an extent determined by the mass of the lensing object. This mass is far greater than its emission reveals. Another example of evidence of DM is provided by the kinematics of galaxy clusters. Similar to galaxy kinematics, the movement of member galaxies gives a larger virial mass in the cluster than can be accounted for by the luminous mass. Even though the X-ray emission from hot gas in such galaxy clusters is measured to be larger than the stellar mass in galaxies, it does not compensate for the missing mass.

X-ray emission, both in clusters and in elliptical galaxies, also indicate the presence of DM through the balance between pressure and gravitational pull. That is, the pressure extended by the hot gas and the gravitational pull from the matter in the system need to be in balance in order for the gas not to be dispersed. Again, the mass required to balance the pressure determined from the X-ray emission is far greater than the luminous matter can account for.

An interesting example that combines gravitational lensing and X-ray emission in a

cluster as evidence for DM, is the Bullet cluster (Clowe et al., 2006). Thus, the existence of DM does not rely (observationally) on rotation curves alone.

Other explanations, such as Modified Newtonian Dynamics (MOND Milgrom, 1983) have been proposed to explain the "missing mass". This theory proposes a modification to Newtonian gravitation at low accelerations. In this work, we did not see MOND as a useful alternative to the halo model, since it so far does not explain the additional evidences for DM listed above. Also Buote et al. (2002) found evidence that favours DM to MOND to explain the hot gas of elliptical galaxy NGC 720. The hot gas (as shown by its X-ray emission) has an orientation that is different from the orientation of the optical counterpart of the galaxy, with a flattening shape, that cannot be explained by MOND. Additionally, there are problems in the theory regarding the acceleration parameter a_0, the one parameter that defines the theory and which is supposed to have a universal value in order for MOND to be accurate. However, many different values are found for this parameter in mass models for different galaxies (see for example Blais-Ouellette et al., 2001). Indeed, in an experiment, MOND was applied in some of the mass models in this thesis, and a similar inconsistency in the a_0 parameter was found.

Since DM is not detectable directly, many riddles remain pertaining to its spatial distribution in galaxies as well as its nature. Much of it is currently expected to be non-baryonic particles, i.e. not consisting of atoms, that do not interact much with other particles. For instance neutrinos, which have been observed to have mass, were once postulated to account for DM. However, the amounts in the Milky Way Galaxy are not sufficient to account for the Milky Way rotation curve (Alcock et al., 2000). Therefore physicists are hunting for exotic weakly interacting massive particles (WIMPs) using underground facilities such as the Sudbury Neutrino Observatory (e.g. the PICASSO project).

1.2.1 Measuring the rotation curve

The traditional strategy for deriving rotation curves is to use the so called "tilted ring" approach, where the velocity is measured in elliptical rings along the radius of the 2-dimensional velocity field. Using the full 3D cube is however preferrable, to avoid problems that can occur with e.g. highly inclined galaxies. Recently, a few software packages have implemented this, such as Cubit (Irwin & Seaquist, 1991) and TiRiFiC (Józsa et al., 2007).

This is also the approach in this thesis, where we test a new software suite developed by J. Fiege and summer research students. This software, GaLAPAGOS, models the HI component of galaxies, and delivers parametric rotation curves. We use the software on 11 galaxies and compare their rotation curves to those generated using the traditional tilted ring method (§ 5.2). The background for this is described in detail in § 4.1. My role in the development of the software has been as a user, tester and analyser of results. The goal is to use these rotation curves to a) determine the DM content for these 11 galaxies (see below) and b) devise a classification scheme, by using the kinematic parameters that characterise the rotation curve (see § 1.4)

1.3 Mass models

While the actual nature of DM is still unknown (and beyond the scope of this thesis), its amount and its possible distribution in a galaxy can be assessed through mass modelling. Sometimes referred to as mass decomposition, a mass model is the mass distribution required to produce the observed velocity behaviour. It uses the velocity contributions (squared) from all galaxy constituents, following Equation 1.2:

$$v_{tot}^2 = v_{bulge}^2 + v_{disk}^2 + v_{gas}^2 + v_{halo}^2 \tag{1.2}$$

Each velocity component is a function of radius in this equation. v_{tot} is due to the dynamical mass and is the velocity observed using the Doppler shift of the HI gas. In other words, it is the velocity traced out by the rotation curve (see Figure 1.2). To measure this rotation curve, both the traditional tilted ring rotation curves and parametric rotation curves from galaxy models are investigated in this thesis.

To determine the velocity contribution, we begin with an estimate of the distribution of luminous matter by measuring the light distribution of a constituent as a function of radius (photometry). This measured emission, as a function of radius, is converted into mass using a mass-to-light-ratio (M/L, defined below), thus generating a model of how the mass varies with radius for each of the major galaxy constituents; bulge, disk, and gas layer. Then individual rotation curves can be made for each of these components, since the velocity squared is proportional to the mass inside the radius (Equation 1.1). The remaining velocity contribution required to match the rotational velocity, is due to DM, and is referred to as the halo component. Valuable guidance was provided by R. Swaters for the mass modelling process part of the thesis.

1.3.1 Mass-to-luminosity ratio

The conversion (from measured luminosity into mass) is straightforward for the gas contribution: assuming the chemical composition is similar in other galaxies to the solar vicinity, the HI emission is scaled by $\sim$1.4 to account for helium (e.g. Irwin, 2007, p. 78).

The conversion for the stellar component is, however, problematic, and is one of the greatest uncertainties in the mass modelling process. The mass-to-light-ratio (M/L)[2] is a measure of how much mass the measured luminosity is responsible for. There is a strong dependence on the waveband that is used to measure the luminosity, i.e. there will be

[2]Note that we distinguish between stellar M/L which only takes the stellar component into account, and total M/L which is the M/L of the galaxy as a whole, including the DM halo

different stellar M/L values at different wavelengths, depending on the object's spectral energy distribution. Ideally, for stars, the bolometric M/L would give the most accurate picture, but it can only be obtained by measuring the luminosity over the entire EM spectrum, which is usually not feasible. Instead a spectral energy distribution for the galaxy has to be assumed, which may be unreliable (Binney & Merrifield, 1998, p. 60). Thus the uncertainty of the stellar M/L will allow for a fair room of variation for the stellar disk and bulge contribution to the rotation curve.

While mass modelling alone cannot be used to derive an exact value for the M/L ratio, it is possible to obtain limits on the M/L range by looking at the extreme 'maximum disk' and 'minimum disk' mass models (van Albada & Sancisi, 1986). The maximum disk model assumes a maximum contribution of the stellar matter to let it explain as much as possible of the kinematic rotation curve. A more recent treatment of the maximum stellar matter contribution is the 'sub-maximal disk' mass model by Courteau & Rix (1999). In the minimum disk model the stellar matter is reduced to a minimum, and most of the kinematic rotation curve is explained by the dark matter halo contribution.

In order to constrain a mass model better, the M/L value of the stellar contribution needs to be constrained. This can done using stellar population synthesis models, based on a certain initial mass function (IMF) (see e.g. Bell & de Jong, 2001). In this thesis, we have based our assumptions of stellar M/L on results from population synthesis models as a function of morphological type, instead of looking at each galaxy individually. See further discussion in Chapter 5.

We use data observed in the near-IR band to minimize the effect on the M/L of age and colour of the stars: the old low-luminosity stars (red population) provide most of the mass, while most of the luminosity comes from shortlived very bright, bluish stars. With near–IR observations, the bulk of the stellar mass is measured and this lowers the uncertainties in M/L (Bell & de Jong, 2001).

1.3.2 Dark matter halo in mass models

Even using the maximum disk assumption in a mass model, observers have noted that contributions to the rotational velocity from each galaxy constituent will not add up to the observed $v_{tot}(r)$ of the HI rotation curve (van Albada & Sancisi, 1986). The required mass to make up the difference is thus what the DM would contribute. For example, see Figure 1.3 of the mass model for NGC 3198 in which DM, assumed to be distributed in an isothermal sphere, generates a total velocity v_t which traces the observed HI data points.

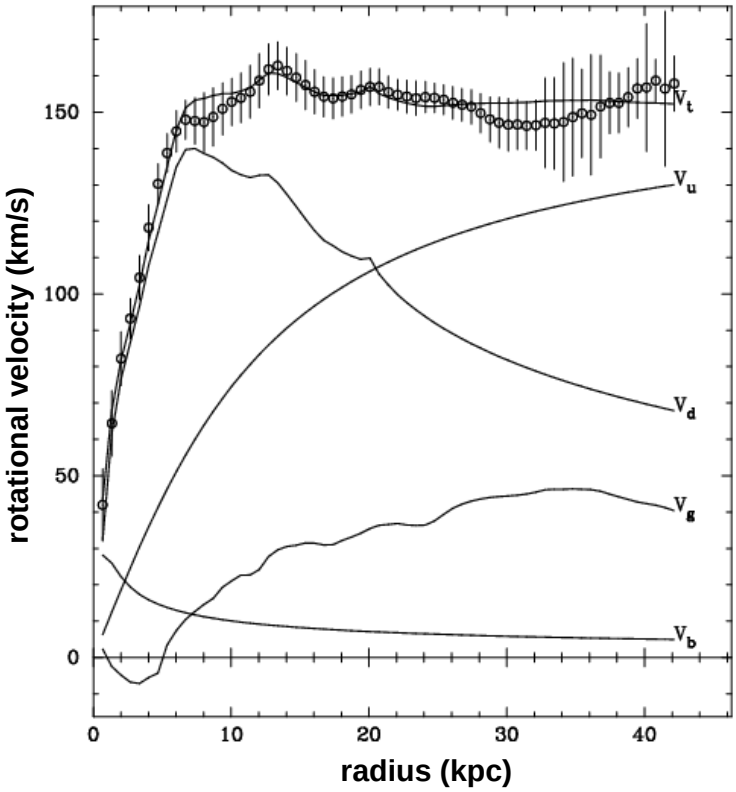

Figure 1.3: A maximum disk mass model of NGC 3198, with a tilted ring rotation curve (data points with error bars) measured from HI data from the THINGS survey. v_b is the bulge contribution to the rotation curve, v_g is the gas contribution (HI and He), v_d is the stellar disk contribution, v_u is the user defined halo model (here an isothermal sphere) and v_t is the total velocity.

Note that historically, there was suspicion that DM was not necessary to explain optical

flat rotation curves, since the optical components (disk and bulge) would be able to create flat curves on their own (Kalnajs, 1983). This was shown to be true within a radius of three disk scale lengths (the disk generally follows an exponential surface brightness law, $I = I_0 e^{-r/R_d}$, where R_d is the disk scale length), using large M/L values for the bulge and the disk (M/L$\sim$10). He thereby showed that optical observations are not enough to prove the existance of DM halos. It was confirmed in HI observations that maximum disk models easily can account for the flat rotation curve shape in the inner regions, but they also showed that they fail after a radius of four disk scale lenghts (Carignan & Freeman, 1985; van Albada et al., 1985), and the DM indeed has to be invoked to explain the continued flatness.

Another riddle was then born: Why is the transition from the disk dominated region to the halo dominated region so smooth? van Albada & Sancisi (1986) called this the 'disk-halo conspiracy', where the two components 'conspire' to keep the velocity on the same constant level. It is currently seen as less of a conspiracy, since rotation curves are not all exactly smooth - there are bumps and wiggles along the curve. Some authors (e.g. Barnes, 1987; Blumenthal et al., 1986; Athanassoula & Bosma, 1988) propose that part of the conundrum can (in the words of Barnes) "...be explained by the dynamical response of a pre-existing halo as a disk slowly grows inside it".

Carignan & Freeman (1985) used an isothermal sphere as a halo model, which is still frequently in use since it is one of the models that fits observations well. The isothermal sphere is a simple description of the spatial distribution of matter, defined by a central density which falls off with r^{-2} and a core radius, where the density has fallen off to half of the central density (see Chapter 3). Many other halo models exist, for instance the Navarro, Frenk and White (NFW) halo model, predicted from N-body simulations (Navarro et al., 1996). This halo harbours a controversial central cusp which in many cases does not fit well with observations.

Here, we concentrate on using the isothermal sphere model in the mass models. The results, presented in Chapter 5, are then used to investigate whether the amount of DM derived for 11 galaxies correlates with the kinematic classifications found in this thesis (see next section). This particular part of the investigation is of highly exploratory nature due to the low number of galaxies.

1.4 Galaxy classification

As mentioned earlier, the most famous classification system for galaxies was devised by Hubble (1936) and is based solely on the morphology of galaxies. He divided up galaxies into elliptical, lenticular, spiral and barred spiral galaxies, and irregular galaxies. The spiral galaxy division was based on tightness of spiral arms and size of bulge. The Hubble sequence was later expanded by de Vaucouleurs (1959) and Sandage (1975) to include more details on bars, spiral arms, and existence of ring structures.

Attempts to connect kinematic behaviour of galaxies to this morphological classification, as well as to luminosity, was made by Rubin et al. (e.g. 1978, 1985). It was found that the shape of the rotation curve is overall more a function of luminosity rather than of morphology. This would imply that optical morphology is not a strong indicator of the underlying gravitational potential (Sofue & Rubin, 2001). Also Bosma (1981b) explored whether there was a connection between rotation curves and morphological type using HI data to reach larger radii, but found no simple relation between the type and the mass distribution.

Tully & Fisher (1977) published the Tully-Fisher relation, which describes the empirical relationship between the galaxy luminosity and its velocity width (i.e. the amplitude of its rotation curve). Rubin's investigations show further connections with the shape of the rotation curve, where low-luminosity galaxies rarely have flat rotation curves and high-

luminosity galaxies have a shorter turnover radius compared to low-luminosity galaxies. Figure 1.4 shows a schematic of prevalent rotation curve behaviours published in literature, constructed using the rotation curves collected and analysed in Chapter 6.

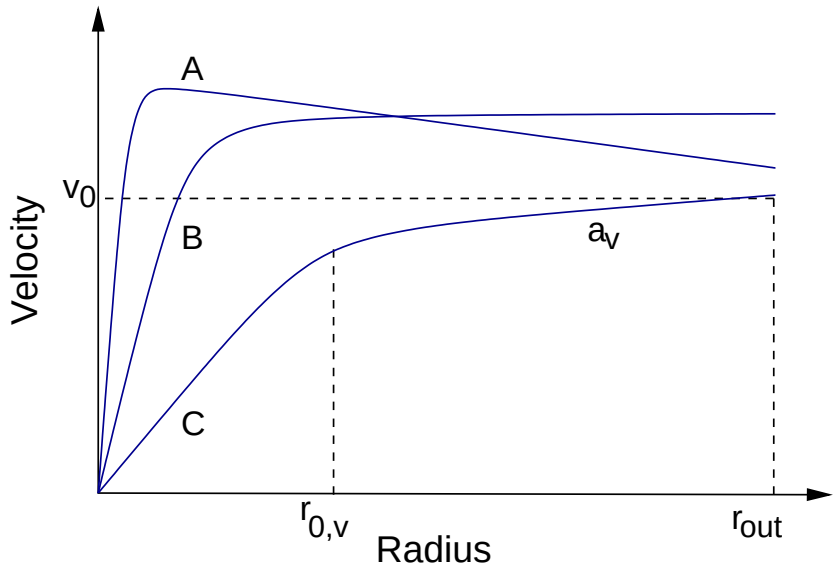

Figure 1.4: A schematic figure of common rotation curve shapes: (A) a rotation curve exhibiting steep rise/short turnover radius followed by a slight decline, (B) a flat rotation curve and (C) a shallow rise/long turnover radius followed by a rise. On curve (C), the rotation curve parameters used in this thesis are labelled with the nomenclature used hereafter: $r_{0,v}$ = turnover radius, a_v = outer slope, v_0=velocity amplitude (i.e. maximum rotational velocity), r_{out} = outer radius of the HI disk.

Other attempts at connecting galaxy characteristics with rotational behaviour have mainly emphasised the optical region of galaxies. For instance Persic et al. (1996) developed a universal rotation curve for this inner region. Vogt et al. (2004) also used optical rotation curves for a large number (329) of galaxies, to study the effect of cluster environment on spiral galaxies, and divided the rotation curves into groups based on their shape.

The most relevant paper to this thesis is that by Chattopadhyay & Chattopadhyay (2006), who recently investigated which galaxy characteristics affect the rotation curve

shape using principal component analysis on HI rotation curves. This thesis investigates their findings and others. That is, we search for additional correlations between galaxy characteristics and the kinematic behaviour of a galaxy (Chapter 6).

Many galaxies have rotation curves for which the shapes are affected by distortion such as tidal interaction. Indeed, such galaxy–galaxy interactions might be the reason for declining rotation curves (Whitmore et al., 1988). Thus, this study targets only isolated or non-interacting galaxies, in order to look for intrinsic characteristics of the rotation curve and develop the classification. This diminishes the number of available galaxies considerably, but enables a study of, for example, the prevalence of declining rotation curves and, if these exist, an assessment of factors other than interactions that can contribute to that rotation curve shape.

The kinematic classification is carried out by using a statistical method called "hierarchical clustering" which is able to find similarities between items in a multidimensional parameter space and assign them into groups (classes). We use this on the parameters that we have chosen to adopt to characterise the rotation curve shape; the velocity amplitude, the turnover radius (scaled by the outer radius) and the outer slope beyond the turnover radius (see Chapter 6). Subsequently these preliminary classes are examined to see if particular values for galaxy characteristics, such as luminosity, Hubble type, size of the dark matter halo etc, appear predominant in specific classes. This is a preliminary investigation, generating a strategy which has the potential to improve our understanding of how these galaxies were formed and evolved.

1.5 Goals

Rotation curve analysis, mass modeling and application of hierarchical clustering to a database, are the methodologies used to accomplish the following three goals of this

thesis:

- First, in a collaborative effort at the University of Manitoba, a new method for modelling HI disks of spiral galaxies called GalAPAGOS[3] has been developed by J. Fiege. The testing and usage of this method is a major part of this thesis, including evaluating the quality of the results by comparing the rotation curves with those derived using conventional methods. Additionally, the rotation curves are used in mass models to assess halo characteristics.

- Second, a classification scheme based on rotation curves (i.e. only on kinematics and not on morphology) is developed, and correlations between the classes and a variety of galaxy characteristics are investigated. This endeavor complements and goes beyond the investigation by Chattopadhyay & Chattopadhyay (2006), by using a different method involving a clustering algorithm, and including visualization to assess the correlations between parameters and classes. Additionally, only isolated/non-interacting galaxies are included in our evaluation, in order to isolate intrinsic galaxy properties and behaviour.

- Third, delinating properties for galaxies within classes of the kinematic classification scheme, including the amount of dark matter in a number of galaxies. The DM content is determined by creating mass models using HI rotation curves in combination with near infrared data to assess the stellar contribution.

[3]In future publications, the name of this software will be changed from GalAPAGOS to another name, since the name is already in use for another application in published papers.

1.6 Results

Here we briefly foreshadow our results and summary. GalAPAGOS was extensively tested on artifical galaxies and RC models were created for galaxies from 14 HI data cubes. For 10 of these, mass models were constructed to measure properties of the DM content. A kinematic classification scheme was devised based on a parametric form of the rotation curves for 79 galaxies. Its five classes, A, AS, AT, S and T, are predominantly distinguished by maximum rotational velocity and further differentiated using the turnover radius and slope in the outer region of the RC.

We confirm the following correlations between these classes and galaxy properties: the brightness (B magnitude) and optical disk size increase as the velocity increases; there are more earlier type galaxies in the class with the highest rotational velocity. We also find that the star formation rate increases with maximum rotational velocity. Due to the small sample of galaxies for which we measured DM halo characteristics, no trend between velocity and properties such as the ratio of halo mass over baryonic mass can be detected. Three candidates for declining rotation curves are found: NGC 2841, NGC 3521 and NGC 5055. These do not conform to properties usually connected to this rotation curve behaviour (such as grand design spiral arms, short disk scale length, interactions), and thus require further investigation.

1.7 Thesis outline

Chapter 2 presents the datasets that have been used and the criteria for choice of data and galaxies. Chapter 3 describes the methodology for measuring rotation curves, the HI density distribution and the stellar luminosity profile in order to create mass models as well as the mass modelling procedure. In chapter 4, the new galaxy HI modelling software GalAPAGOS is presented, tested and evaluated on artificial galaxies. Chapter 5 presents

the rotation curves from observations using the two different methods, and evaluates the results. The mass models are also presented in this chapter. Chapter 6 describes the derivation of a kinematic classification scheme based on rotation curve parameters, and investigates correlations between the kinematic classes and galaxy characteristics. Chapter 7 summarizes and discusses the findings, presents the conclusions of the thesis and gives an outlook on future work.

Chapter 2

Data: observations and processing

2.1 Introduction

The explorations of this thesis use mainly neutral hydrogen (HI) data, complemented by near infrared data. Additionally, we looked into the use of data of molecular emission from carbon monoxide (CO), to complement the HI data in the central regions of galaxies. This chapter describes the data that are presented in the thesis and the surveys from which they originate. Although I have experience reducing HI data, most data presented here were reduced by the respective survey teams, with the exception of the CO (3-2) data for NGC 925, which I reduced.

Note that we discuss additional data obtained from the literature for the classification scheme in Chapter 6 for reasons of continuity.

The spectral line emission we measure from neutral hydrogen is caused by a change in energy state in two hyperfine levels of the 1s groundstate: when the spin of the electron is parallel to that of the proton, the energy of the electron is higher than when their spins are anti-parallel. The transition between these two levels causes a photon to be emitted.

The spectral line occurs at 21 cm wavelength (1.420GHz frequency) in the radio regime

of the electromagnetic spectrum. The emission is weak; the transition is forbidden, with a very low probability of spontaneous occurence and a lifetime of the excited level of 1.1×10^7 years (Binney & Merrifield, 1998). However, the amounts of HI in the interstellar medium of galaxies is so large, that it can still easily be observed. In fact, the observations were predicted before they took place - by van de Hulst in 1945, and first observed by Ewen & Purcell (1951)

HI is optically thin[1] , and it is straightforward to calculate its column density (number of atoms/unit of area) only knowing its observed brightness temperature. The brightness temperature T_B is the temperature of a body emitting at an intensity I_ν, defined by

$$I_\nu = \frac{2k}{\lambda^2} T_B \tag{2.1}$$

with Planck's constant k and wavelength of emission λ (note that this is an approximation only valid at radio frequencies, see Chapter 8.1.4 of Binney & Merrifield (1998)). The intensity is measured in energy flux per unit solid angle and unit frequency ν, in radio data usually Jy/beam/channel.

The column density, N_{HI} in units of number of atoms per cm^2, follows Equation 2.2 (Binney & Merrifield, 1998, Eq. 8.22):

$$N_{HI} = 1.823 \times 10^{18} \int T_B \, d\nu \tag{2.2}$$

Once the column density is known, only knowledge of the distance is required to acquire the total HI mass. This is done by integrating the column density over the area

[1]Optical depth is a measure of transparency, i.e. how much a medium (here the HI gas) absorbs or scatters light. When few photons are absorbed, the medium is referred to as "optically thin" along a line of sight, or, $\tau \ll 1$ in the optical depth equation $I/I_0 = e^{-\tau}$, where τ is optical thickness and I/I_0 is the fraction of observed light over emitted light

to get the number of atoms.

$$M_{HI} = 2.36 \times 10^5 \cdot D^2 \cdot \int S\, dv \tag{2.3}$$

(Binney & Merrifield, 1998, Eq. 8.24) where the mass is given in units of $M_\odot$, D is the distance in Mpc, S is the flux density ($S = \int T_B\, d\Omega$, where $d\Omega$ is an element of solid angle on the sky, and an area element $dA = D^2 d\Omega$), and the integral over S is the total integrated flux (in Jy km/s).

2.2 HI Data

2.2.1 Background on neutral hydrogen observations

Angular resolution is directly proportional to the wavelength of the emission observed and the diameter, D, of the telescope used, following equation 2.4 (see e.g. Irwin, 2007, pages 38-40).

$$Resolution \approx \frac{\lambda}{D} \tag{2.4}$$

Thus radio telescopes need to be very large to achieve a sufficient resolution to detect small-scale variation in a galaxy for wavelengths of 21 cm. The aperture synthesis technique helps overcome the physical limit for a single radio antenna. With this technique, multiple telescopes are linked together forming a large interferometer, and the resolving power is determined by the distance between the antennas. The distance between each antenna pair is called a baseline and the placement of a set of (more than two) antennas is called an array configuration. Basically, the antennas "form" a single antenna, with a diameter equalling the largest baseline distance b (times the cosine of the angle to the object

observed).

The "synthesis" array uses the rotation of the Earth to simulate the disk of the large telescope. The longer the time of observation, the more coverage in the *u-v-plane* is accomplished, i.e. the area traced out by the location of the telescopes in the array is being filled out as well. The array can be reconfigured by positioning the antennas in different configurations, to fill in the area in the u-v plane. The signal measured in the u-v plane (the visibilities) is the fourier transform of the source brightness distribution in the x-y plane (image plane, i.e. the distribution of the emission).

Signals from different antennas in the array are cross correlated and calibrated to radio sources with well-known fluxes (such as stars). These calibration sources have to be observed in intervals throughout the observation time, since observing conditions change over time. Inverse Fourier transforming the u-v plane data finally provides the intensity of the object as a function of position on the sky (the *x-y-plane*). An important step in the reduction process is the usage of the CLEAN process, in which corrections remove the effects of antenna sidelobes. See Taylor et al. (1999) for more detailed information on this topic.

Observations are carried out by acquiring spectra, by the single antennas in the array observing simultaneously, within a field of view delineated by the "primary" beam (the beam pattern, which is the Fourier transform of the aperture). The cross-correlations and calibrations make it possible to synthesize one large dish and create the "synthesized" beam, which is in essence the resolution of the data.

The higher resolution provided by synthesis arrays is however won at the cost of sensitivity, since measuring over the entire area of the simulated telescope is a luxury in time not easily afforded. A compromise between sensitivity and resolution often has to be made, by choosing an array configuration for which an optimum between coverage and resolution is achieved depending on the objectives of the observations. Interferometers

can thus be used as a resolution filter, where large distances between the antennas will provide information on the small scale features of the object and small distances (or a single dish) will provide information on large spatial scales.

Another way of affecting the sensitivity vs resolution lies in the reduction process. The weighting applied when performing the transform from the u-v plane observed visibilities to the x-y plane surface brightness distribution can be chosen to be *natural, uniform* or *robust* (Briggs et al., 1999). Natural weighting gives the optimum sensitivity to a point source, thus minimizing the noise level. The beam size will however be larger - i.e. better signal-to-noise (S/N) at the cost of resolution. With the uniform weighting, effects of the sidelobes are minimized, the beam size is smaller (i.e. higher resolution), but the noise level will be elevated causing a lower S/N than for natural weighting. Robust weighting is an optimised compromise between natural and uniform weighting.

For the purposes of this thesis, high sensitivity is the first priority, and the data used are all naturally weighted.

HI data used in this thesis come from the radio observatories Westerbork Synthesis Radio Telescope (WSRT) in Netherlands and the NRAO Very Large Array (VLA) in New Mexico. Single dish data from the Australian Parkes telescope are also explored.

The data cube

After appropriate cross correlations between antennas and calibrations have been performed on the data, followed by inverse fast Fourier transformation and cleaning (as briefly described in § 2.2.1), they are displayed in a 3D cube. This data cube contains intensity as a function of both spatial coordinates (Right Ascension (RA) and Declination (Dec)) and frequency as a third dimension, usually converted to radial velocity. For extra–galactic observations, the radial velocity used has the sun as the point of reference, and is thus called heliocentric velocity. Mathematically, the name 'cube' is a bit of a

misnomer, since the frequency/velocity axis is different from the spatial axis both in units and resolution. Figure 2.1 is a schematic figure of a cube, showing the HI emission from a galaxy.

The data cube is usually shared in the Flexible Image Transport System (FITS) format, which also includes information about the observations in a *header* and the reductions performed in a *history* file. Throughout the subsequent reductions, the file might take on other format incarnations, suitable to the software with which it is reduced (e.g. GIPSY format and MIRIAD format).

Finding emission and distinguishing it from noise in the background is usually not straightforward. One needs to take into account the resolution of the data, which is entirely characterized by the synthesized beam size (which in its turn is dependent on the baselines, how the baselines are weighted and wavelength of emission). Both visual inspection and statistics are used to distinguish what is signal from what is noise. Visual inspection helps to discern astronomical objects from residuals of the sidelobes of the beam. It is important to not confuse the data resolution (beam size) with pixel resolution of the data. Indeed, a beam (which is circular or elliptical) is characterised by at least three pixels across.

The data sets in this thesis are inhomogenous with different synthesized beam sizes and sensitivity (see Tables 2.2, 2.3, 2.4, and 2.5).

The data cube can be collapsed (along the velocity axis) to form 2D spatial maps using the moment analysis technique described in Rupen (1999). One can produce an integrated intensity map (0th moment), a velocity field map (1st moment) and a velocity dispersion map (2nd moment). These maps are used for analysis in the rotation curve derivation process and mass model process described in Chapter 3.

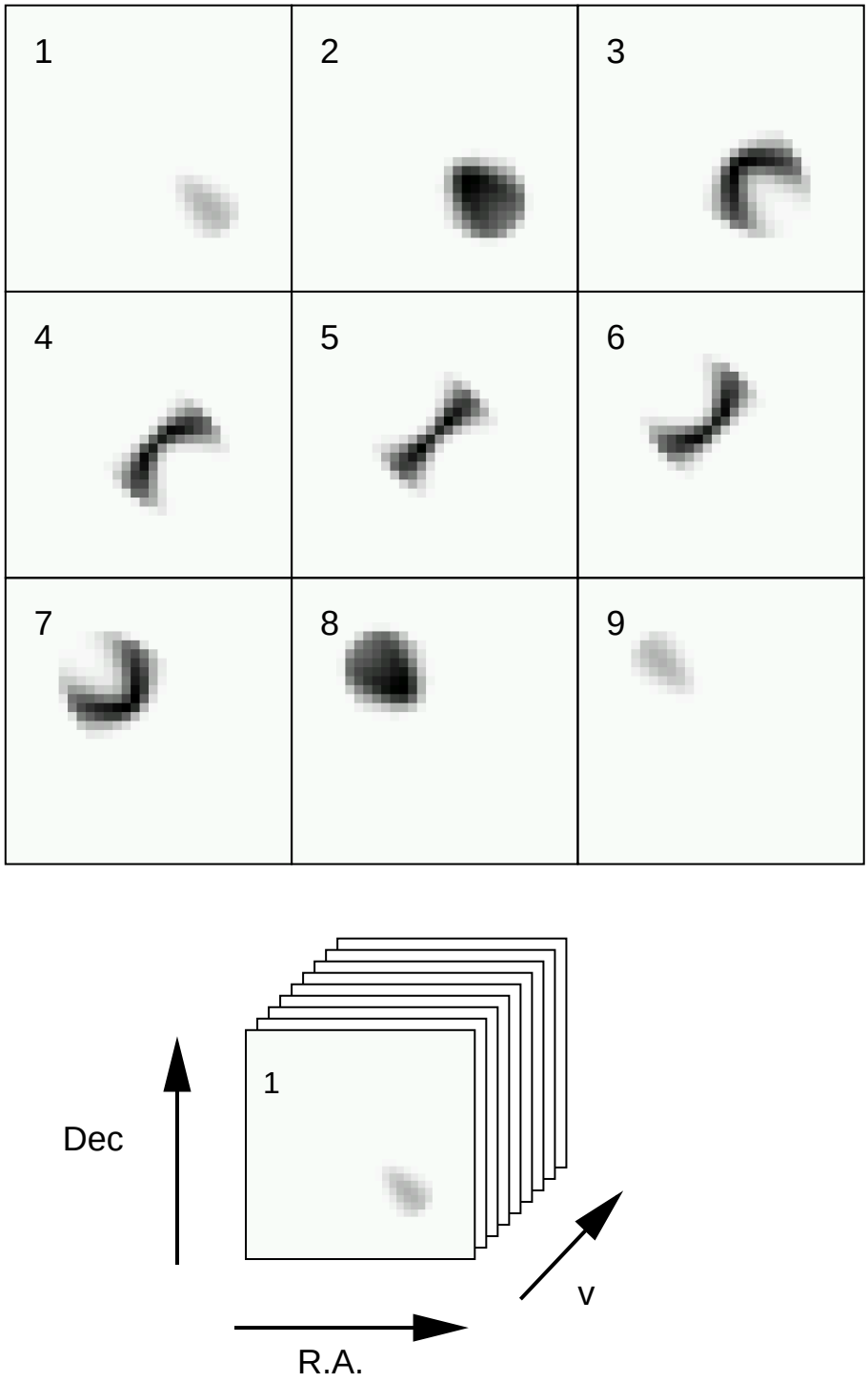

Figure 2.1: A schematic figure of a data cube, where the HI spectra are intensity vs frequency (velocity). Unstacking the cube generates channel maps (above), which show the individual velocity channels in the cube. An intermediately inclined galaxy will exhibit a "seagull" pattern (or a 'V' opening and closing) when looking through the channels.

2.2.2 Selection criteria

Since all parts of this project deal with comparisons of intrinsic properties of the disks of galaxies, it was important to use HI data of isolated, apparently non-interacting galaxies of morphological types Sa to Sd.

If no interaction (with another galaxy or in a cluster environment) has taken place since at least half of its mass was assembled, a galaxy is considered isolated (Hernández-Toledo et al., 2008). It is however hard to evaluate whether an apparently non-interacting galaxy has been interacting at some point of its history. Deviations from axisymmetry might be an indication as well as other anomalous behaviours (gas outflows), noticed in particular by scrutinizing the HI data cube of the galaxy. Note that some anomalies could also be due to internal processes in the galaxy.

The galaxies for this study also need to be sufficiently nearby to allow for anomalous details to be resolved. For example, a distance of less than 10 Mpc yields a beam resolution finer than 0.5-2.5 kpc per beam for our synthesis array data (for beam sizes ranging 10″-50″/beam) (as a comparison, anomalous gas details found by King & Irwin (1997) in NGC 3556 are of kpc scales). Initially, we searched for galaxies closer than 10 Mpc, but a few other galaxies at larger distances were included at a later stage to increase the sample size.

A large portion of edge-on or nearly edge-on galaxies is desirable, in an effort to clearly characterize the rotational velocity behaviour. Although it can be problematic to derive rotation curves for high inclinations (due to the line of sight passing through several velocities), the modelling software we use is able to handle this by modelling in 3D. Through tests of our HI modelling software we find a lower limit at 40 ° inclination (see Chapter 4).

Additionally, to be able to perform mass models, we need to perform the global pho-

tometry on the stellar component. Near infrared (NIR) data observed in the SDSS i-band (centered at 7481 Å) was used for this (see § 2.3.1). While Spitzer 3.6 mm would have been preferrable, due to its higher sensitivity, many of the WHISP galaxies in our sample were not available in the Spitzer sample. For consistency, we selected to use SDSS for as many galaxies as possible. With these selection criteria (isolation, distance, inclination, availability of ancillary data), there is a paucity of galaxies with available HI data. Many galaxies in the surveys appear to be interacting, and hence only 16 galaxies in the public surveys and privately provided data are appropriate for these studies. Of these, 11 are suitable for mass modelling (due to availability of NIR data). These data cubes are provided from the survey WHISP, (van der Hulst et al., 2001), personally provided by J. Irwin (NGC 2613, NGC 2903 and NGC 3556, see references in § 2.2.6) and 11 of them are publically available from the THINGS survey[2], (Walter et al., 2008). Note that 10 of these are used in the final analysis in Chapter 6. Additionally, rotation curve parameters for 79 galaxies taken from the literature are used in Chapter 6. Table 2.1 lists the HI data that are presented in this thesis.

2.2.3 THINGS data

The HI Nearby Galaxy Survey (THINGS) was observed during 2003-2005 with the Very Large Array (VLA) in New Mexico, and the results of the 500 hours of total observation time generated highly resolved data cubes for 34 nearby galaxies (Walter et al., 2008). The galaxies are chosen to cover a wide range of morphological types, star formation rates, luminosities, metallicities and total mass. Similar to the objective of the WHISP survey (§ 2.2.4), the goal was to observe a significant sample of nearby galaxies to have a systematic sample, with a homogenous sensitivity and an unprecedented resolution (both

[2]http://www.mpia.de/THINGS/

Galaxy (1)	**Data** (2)	**D (Mpc)** (3)	**ref** (4)	**i** (5)	**Morphology** (6)
NGC 925	W,T,N	9.12	(cep, 1)	60.3	SAB(s)d/Scd
NGC 2403	T,S	3.18	(cep, 2)	62.1	SAB(s)cd/SABc
NGC 2613	ID	25.9	(10)	90*	SA(s)b/Sb
NGC 2841	T,S	14.1±1.5	(cep, 11)	73.1	SA(r)b/Sb
NGC 2903	W,T,ID,S	8.9	(3)	62.1	SB(s)d/SABb
NGC 3198	T,S	13.8+/-0.51	(cep, 1)	71.7	SB(rs)c/Sc
NGC 3351	T,S	9.33	(cep, 1)	41.1	SB(r)b/Sb
NGC 3521	T,S	8.5	(4)	70.7	SAB(rs)bc/SABb
NGC 3556	ID,S	11.6	(5)	75.6	SB(s)cd/SBc
NGC 3621	T,H	6.55	(cep, 1)	65.6*	SBcd/SBcd
NGC 4096	W,S	10.2	(6)	75.5	SAB(rs)c/SABc
NGC 4258	W,S	7.83	(cep,1)	68.9	SAB(s)bc/SABb
NGC 5055	T,S	7.2	(7)	64.6/56.8	SA(rs)bc/Sbc
NGC 7331	T,S	14.52	(cep, 1)	76	SA(s)b/Sbc
NGC 7640	W	8.4	(8)	79.7	SB(s)c/Sc
NGC 7793	T,H	3.9±0.4	(9)	53*	SA(s)d/Scd

Table 2.1: The galaxy datasets used in this thesis. Column 1: The galaxy name shown in italics denotes that the galaxy has been mass modelled in this thesis. Column 2: W=WHISP, T=THINGS, H=HIPASS, ID=individual donations, S=SDSS, N=NGLS. Column 4 lists the references for the distances in Column 3: (1) Freedman et al. (2001), (2) Madore & Freedman (1991), (3) Karachentsev et al. (2004), (4) Zeilinger et al. (2001), (5) King & Irwin (1997), (6) García-Ruiz et al. (2002), (7) Pierce (1994), (8) García-Barreto et al. (2003), (9) Karachentsev (2005), (10) Irwin & Chaves (2003), (11) Macri et al. (2001), cep denotes that the distance was measured using Cepheids. The inclinations listed in Column 5 are measured in this thesis using GIPSY's ROTCUR task, unless followed by an asterisk, in which case they were taken from HyperLEDA. Note that inclinations are also tabulated in Chapter 5. In the case of NGC 5055, two inclinations are shown, due to the galaxy's change in inclination (and position angle) at a radius of 420″. The morphology in Column 6 is taken from NED and HyperLEDA, in that order. Both use the de Vaucouleurs system, but the NED morphology also includes information on presence of ring structure ((r) = ring, (s) = no ring, (rs) = somewhere in between).

in velocity and spatially). The survey has been used for a number of research projects (see Walter et al., 2008, for a sample).

The galaxies were observed using three different array configurations of the VLA (B,C and D, see Walter et al., 2008, for more information on the configurations). The longest baseline (B) provided the high resolution, but is not sensitive to large scale structure. The extended emission had to be measured using the shorter baseline C and D arrays (even higher resolution would have been possibly using the A configuration, but that would require unfeasibly large integration times). The calibrations, flagging of bad data and further reductions are described in detail in Walter et al. (2008).

Ten naturally weighted cubes from THINGS were used in this thesis since this weighting gives higher sensitivity to faint emission. The average spatial resolution for these data with this weighting is closer to $10''$. The pixel size for almost all galaxies is $1\farcs5$/pixel ($1''$/pixel for NGC 2403) and the cube size is 1024×1024 pixels^2. Coordinates, beam size and velocity resolution for each galaxy are listed in Table 2.2

2.2.4 WHISP

A survey called "Westerbork HI observations of Irregular and SPiral galaxies" (WHISP) was observed with the Westerbork Radio Synthesis Telescope (WRST) between 1992 and 2002, and include approximately 400 galaxies. The objective of the WHISP project is to systematically observe galaxies in order to map the density distribution and the velocity fields as a function of morphopology, luminosity and environment (see van der Hulst et al., 2001). The observations and reductions are described in Noordermeer et al. (e.g. 2005). The angular resolution is dependent on the coverage in the u-v plane (observational coverage) as well as declination. The data cubes for five of these galaxies were provided to us in a collaboration with R. Swaters (University of Maryland), and the results of four of these are presented in this thesis (see Table 2.1) (NGC 7640 was excluded due to lack

Galaxy	**R.A.**	**Dec**	**noise**	**beam size**	**BPA**	**Δv**
			$[mJy/bm]$	$[''] $	$[^\circ]$	$[km/s]$
(1)	(2)	(3)	(4)	(5)	(6)	(7)
NGC 925	$02h27m16.88s$	$+33d34m45.0s$	0.57	$5\farcs94 \times 5\farcs71$	30.58°	2.59
NGC 2403	$07h36m51.40s$	$+65d36m09.2s$	0.38	$8\farcs75 \times 7\farcs65$	25.16°	5.16
NGC 2841	$09h22m02.63s$	$+50d58m35.5s$	0.35	$11\farcs1 \times 9\farcs37$	-12.27°	5.19
NGC 2903	$09h32m10.11s$	$+21d30m03.0s$	0.41	$15\farcs3 \times 13\farcs32$	-51.34°	5.18
NGC 3198	$10h19m54.92s$	$+45d32m59.0s$	0.33	$11\farcs43 \times 9\farcs26$	-80.43°	5.19
NGC 3351	$10h43m57.70s$	$+11d42m13.7s$	0.35	$9\farcs94 \times 7\farcs15$	24.09°	5.18
NGC 3521	$11h05m48.58s$	$-00d02m09.1s$	0.40	$14\farcs1 \times 11\farcs15$	-61.66°	5.19
NGC 3621	$11h18m16.51s$	$-32d48m50.6s$	0.69	$15\farcs9 \times 10\farcs2$	3.61°	5.18
NGC 5055	$13h15m49.33s$	$+42d01m45.4s$	0.36	$10\farcs1 \times 8\farcs66$	-40.01°	5.18
NGC 7331	$22h37m04.10s$	$+34d24m56.3s$	0.44	$6\farcs13 \times 5\farcs61$	34.26°	5.17
NGC 7793	$23h57m49.83s$	$-32d35m27.7s$	0.92	$15\farcs6 \times 10\farcs9$	10.66°	2.58

Table 2.2: Galaxies from the THINGS survey used in this thesis. Columns (2) and (3) are the coordinates in right ascension and declination, given in J2000 format (NED). Column (4) is the rms noise of the data cube measured in empty channels (also in Walter et al. (2008)), column (5) is the size of the synthesized beam, i.e. the resolution. Column (6) is the position angle of the beam (measured north to east) and Δv in Column (7) is the velocity resolution per channel of the data cube.

of NIR data). The coordinates, beam size and velocity resolution per channel for each galaxy are listed in Table 2.3. The data cubes have a pixel resolution of 5″/pixel.

Galaxy	**R. A.**	**Dec**	**rms noise**	**beam size**	**Δv**
			$[mJy/beam]$	$[''] $	$[km/s]$
(1)	(2)	(3)	(4)	(5)	(6)
NGC 925	$02h27m16.88s$	$+33d34m45.0s$	1.6	$16\farcs73 \times 8\farcs56$	4.14
NGC 2903	$09h32m10.11s$	$+21d30m03.0s$	1.8	$23\farcs38 \times 8\farcs53$	4.14
NGC 4096	$12h06m01.13s$	$+47d28m42.4s$	1.7	$17\farcs15 \times 12\farcs48$	16.55
NGC 4258	$12h18m57.505s$	$+47d18m14.3s$	0.9	$13\farcs35 \times 10\farcs31$	16.54

Table 2.3: Galaxies from the WHISP survey used in this thesis. Columns (2) and (3) are the coordinates in right ascension and declination, given in J2000 format (NED). Column (4) is the rms noise of the data cube, column (5) is the beam size and column (6) is the velocity resolution per channel.

2.2.5 HIPASS

The Australian Parkes telescope is a large single dish antenna (64 m diameter) which was used for the HI Parkes All-Sky Survey (HIPASS), observed during 1997-2000. This was a blind survey in that the southern sky was observed at 21 cm wavelength in order to find all bright HI sources. The goal was to measure their redshifts and catalogue previously non-observed optically weak galaxies. The observations were carried out by scanning the telescope across the sky in 8 ° (in declination) strips. The HIPASS Bright Galaxy Catalogue (HIPASS BGC) consisting of 1000 bright galaxies was compiled from the survey. The beam resolution (the full width half maximum, FWHM) for these data is 15′.5, with a velocity resolution of 13.2 km/s. Due to the low resolution, most galaxies are detected as point sources in the survey, and only large or sufficiently nearby galaxies are extended. There are 24 galaxies with extended emission in the HIPASS BGC, of which most are nearby and thus well studied.

For this thesis, only data from the sample of galaxies with extended emission was explored. Any galaxy listed as dwarf, having a low inclination (below 40 °) or interacting was excluded. Of the remaining 14 galaxies, two galaxies are presented in this thesis and listed in Table 2.4, although most of them were used in our initial exploration of modelling data cubes using the HI modelling software GalAPAGOS, described in Chapter 4. These two galaxies are the only ones that are also available in the high resolution THINGS survey, which enabled quality comparison of the analysis for the different data sets. See Chapter 5 for the exploration of these data and the results thereof.

2.2.6 Other HI data

Three additional datasets have been provided to us by J. Irwin (Queen's University). These are observed with the VLA, and the specifics are listed in Table 2.5. The NGC 2613

Galaxy	R.A.	Decl	noise	beam size	Δv
			$[mJy/beam]$	$[']$	$[km/s]$
NGC 3621	11h 18m 16.5s	+32d 48m 50.6s	14	$15\farcm5 \times 15\farcm5$	13.12
NGC 7793	23h 57m 49.8s	-32d 35m 27.7s	14	$15\farcm5 \times 15\farcm5$	13.17

Table 2.4: Two extended galaxies from the HIPASS BGC. The coordinates are given in J2000 format (NED) with right ascension in column 3 and declination in column 4. The noise is the rms noise of the cube and Δv is the velocity resolution per channel.

data cube are from combined C+D array configuration VLA observations and details are available in Irwin & Chaves (2003). NGC 2903 was observed with the VLA D array configuration and the archival data are reduced by J. Irwin (see Irwin et al., 2009) but the first images are presented here. NGC 3556 was observed with the C array configuration and details on the reductions of NGC 3556 are available in King & Irwin (1997). All three cubes are naturally weighted to achieve high sensitivity.

Galaxy	R.A.	Declination	noise	beam size	Δv
			$[mJy/beam]$	$['']$	$[km/s]$
NGC 2613	$08h33m22.84s$	$-22d58m25.2s$	0.45	$47\farcs1 \times 32\farcs1$	20.8
NGC 2903	$09h32m10.11s$	$+21d30m03.0s$	0.82	$58\farcs1 \times 50\farcs7$	5.17
NGC 3556	$11h11m30.97s$	$+55d40m26.8s$	0.2	$21\farcs7 \times 17\farcs2$	20.7

Table 2.5: HI cubes of individual galaxies provided by J. Irwin. The coordinates are given in J2000 format (NED). The noise is the rms noise of the data cube listed in respective paper; NGC 2613: Irwin & Chaves (2003), NGC 3556: King & Irwin (1997). Δv is the velocity resolution per channel.

2.3 Ancillary data

2.3.1 Near infrared i-band SDSS data

The Sloan Digital Sky Survey (SDSS) is an imaging and spectroscopic survey observed with a 2.5 m telescope and a mosaic camera at Apache Point Observatory, New Mexico.

The camera images the sky by scanning along certain paths over the sky (Gunn et al., 1998). The goal is to provide a digital map of one quarter of the entire sky. The observations are carried out in five optical/NIR wavelength bands simultaneously; SDSS filters u, g, r, i and z. These are centered on the wavelengths 355.1 nm , 468.6 nm, 616.5 nm, 748.1 nm and 893.1 nm respectively. Since the bulk of the stellar mass in a galaxy comes from the older, red population of low-luminosity stars, NIR data, in this case the i-band, is most suitable for modelling the stellar component. The limiting magnitude for the i-band is 22.3. Details on the filters (width, etc) can be found in Gunn et al. (1998) and other technical details in York et al. (2000)

The resolution is $0.4''$/pixel and the exposure time per pixel is 53.9 s. The photometric data can be converted to flux and magnitudes in a magnitude system sufficiently close to the AB system (the error is less than 0.01 magnitudes for the i-filter). The data used in this thesis are from Data Release 7 (DR7) of the SDSS. The data products that are publically available[3] are already processed by the data processing pipeline by the SDSS team, in collaboration with Fermilab and Princeton University, who built the pipeline. I subsequently mosaicked images together to span the diameter of the galaxies (using the online software Montage), and I also converted the data intensities to flux and luminosity. The methods and equations for these steps are described in Chapter 3. This work was carried out for 11 of the galaxies we have HI data for, listed in Table 2.6. This table also lists the sensitivity measured as the sky level (with a softbias of 1000 DN, where DN is the Data Number, roughly the number of photons per pixel) and the reddening effect as we look through our own Milky Way Galaxy, E(B-V) (see Binney & Merrifield, 1998, p. 133) which is used to correct photometric measurements to values intrinsic to the target galaxy. The sky level has an average of 200 DN which corresponds to a limiting magnitude of 22.03 using a 2σ (twice the rms noise) cutoff. See Chapter 3 for how these values are used

[3]http://www.sdss.org/dr7/

in the photometric analysis.

Galaxy (1)	**Sky** [DN] (2)	**E(B-V)** (3)	**# of fields** (4)	**mosaic size** [′] (5)
NGC 2403	1246.6	0.040	9	18×18
NGC 2841	1174.1	0.016	6	12×12
NGC 2903	1265.1	0.031	5	12×12
NGC 3198	1186.9	0.012	3	9×9
NGC 3351	1222.4	0.028	5	9×9
NGC 3521	1218.5	0.058	9	15×15
NGC 3556	1286.5	0.017	6	12×12
NGC 4096	1198.4	0.018	4	9×9
NGC 4258	1205.6	0.016	16	27×27
NGC 5055	1224.7	0.018	8	18×18
NGC 7331	1283.4	0.091	5	12×12

Table 2.6: Galaxies with i-band data from SDSS. The sky level in Column (2) is the noise from the sky measured by the CCDs and a 1000 DN softbias has been added. Thus the sky contributes on average 200 DN/pixel. E(B-V) in Column (3) is a measure of the reddening effect from the Milky Way. Column (4) lists the number of fields used in the mosaic and Column (5) is the angular size of the mosaic in arcminutes.

2.3.2 NGLS 12CO(J=3-2)

Carbon monoxide (CO) is a molecule with a dipole. The spectral line emission of the 12CO(J=3-2) molecule is due to a rotational transition, with the rest frequency of 345.8 GHz. The James Clerk Maxwell Telescope (JCMT) Nearby Galaxies Legacy Survey (NGLS) is an extensive survey that is measuring the CO (J=3-2) content in a large number of galaxies, using the submillimetre telescope JCMT on Mauna Kea and the HARP-B receiver. The observations started in 2008. The survey includes galaxies sampled from the Virgo cluster, the infrared survey SINGS (Spitzer Infrared Nearby Galaxies Survey) and a number of field galaxies. The JCMT telecope consists of a single dish antenna for submm wavelengths, with a diameter of 15 m (currently the largest of its kind). The HARP-B consists of 16 receptors (receiving 'pixels') in a 4-by-4 matrix, separated by 30″,

which scans over targets in a raster pattern. CO(J=3-2) is an excellent tracer of star formation rates, and one of many goals with the NGLS is to measure the amount of warm dense molecular gas associated with star formation (see Wilson et al., 2009; Warren et al., 2010; Bendo et al., 2010).

We observed during two of the NGLS observing sessions; January and November 2008. In the first of these observing sessions, data were measured for the edge-on galaxy NGC 4613, and a paper on the CO(3-2) distribution and molecular outflows of this galaxy was accepted in 2010 (NGLS IV, Irwin et al., in prep). The reason for this collaboration was to attempt to use the CO(3-2) data to construct rotation curves in the centres of galaxies, where HI is often weak or even non-existing, and compare these rotation curves to those of the HI data. Initially, only one of the NGLS targets was present in our sample (before the THINGS data were released to the public), which is thus the one galaxy we reduced: NGC 925.

NGC 925 was observed during four nights in November 2007 and January 2008. A preliminary reduction following a pipeline developed by R. Tilanus and adapted by B. Warren was made, and the results showed very little CO(3-2) in this galaxy. We then carefully flagged the individual raw data files again to remove bad receptors and improve on the removal of data with bad baselines. We removed noisy end channels (due to bad coverage in the outskirts of the field), before binning the data to 20 km/s in velocity resolution. The baseline was removed before transferring the data into a cube for further inspection to find possible remnant bad baselines. This was done on each observation in an iterative manner. We then combined individual scans (observations), increasing the coverage and bringing down the noise, until a final cube could be produced. This was done using a 'sincsinc' kernel as a weighting function for the pixels. The beam size is 14.5″, with a pixel resolution of 7.3″, and the velocity resolution per channel is 20 km/s.

The reduction software used is part of the Joint Astronomy Centre's version of the

Starlink software, and the packages *KAPPA* (editing), *SMURF* (making cubes) and *CONVERT* (exporting to FITS format). *GAIA* was used for visualizing the data to enable inspection.

However, NGC 925 turned out to be harbouring very small amounts of CO(3-2) in the centre of the galaxy, and the data was not sufficient for this study.

Chapter 3

Methods: mass models

3.1 Introduction

As was mentioned in Chapter 1, the total rotation of a galaxy can be divided up into the contributions from each galaxy component, according to equation 3.1

$$v_{rot}^2 = v_{gas}^2 + v_d^2 + v_b^2 + v_{DM}^2 \tag{3.1}$$

where v_{rot} is the total kinematic rotation curve measured out to as large a radius as observational techniques will allow, v_d is the stellar contribution from the disk, v_{gas} is the contribution from gas (neutral hydrogen and primordial helium), and v_{DM} is the contribution from non-emitting matter in the galaxy, i.e. the dark matter halo. The contribution from the bulge can also be taken into consideration, by including v_b.

In reality, the situation is somewhat less simple. Since the v_{gas} we calculate is the contribution from HI only, it needs to be scaled by approximately 1.4 to take into account other gases in the galaxy, i.e. helium and molecular gas (e.g. Irwin, 2007, p. 78). The stellar contribution from the disk (v_d) and the bulge (v_b, when applicable) are derived from

the stellar luminosity in a radiation passband that represents the total stellar population. Determining the correlation between luminosity emitted by stars and the amounts of mass responsible for the emission, known as mass-to-luminosity ratio (M/L), is far from straightforward, and has to be predicted by population synthesis models (Worthey, 1994).

Thus stellar M/L is usually left as a free parameter in the mass modelling procedure, except for the two extreme cases of highest and lowest possible M/L, known as maximum and minimum disk models (van Albada & Sancisi, 1986). The sub-maximal disk (Courteau & Rix, 1999) is an adaptation of the maximum disk model which uses the Tully-Fisher relation (an empirical relation between luminosity and velocity), to scale down the contribution from the stellar disk. While the maximum disk often is defined as scaling the disk contribution to 85% at 2.2 disk scale lengths (Sackett, 1997), the submaximal disk is scaled to 60% at that same radius. Although using the sub-maximal disk can further constrain the maximum stellar M/L, we chose to explore the full range of the maximum and minimum disks in this study.

In mass models, the M/L is assumed to be constant over the entire stellar radius of the galaxy. Even though the M/L in reality might vary with radius (see e.g. Sofue, 1999), a division between bulge and disk will usually provide a sufficient approximation to the M/L and give a reasonable mass model. Eleven mass models were constructed in this thesis, the number limited by current (2010) availability of near-infrared data (SDSS i) for the stellar contribution calculations.

The kinematic rotation curve v_{rot}

Deriving a rotation curve is not always straighforward. The following list shows the diversity of features in a galaxy, which can make the derivation of rotation curves challenging:

- Warps in the outer disk (Bosma, 1981a,b). Perhaps these are created when galaxies interact with each other. This can misalign the morphological and kinematic axes.

The disk can appear as if it is constructed of rings tilted at different angles at different radii.

- Deviations from axisymmetry in the inner regions (Bosma, 1981b). Called oval distortions, these are features such as barred nuclei.

- Gas with velocities that differ from the rotation of the disk (van der Hulst & Sancisi, 1988; Kamphuis & Sancisi, 1993). These anomalies may eventually be identified as objects like the high velocity clouds (HVC) in our Milky Way.

- Anti-correlations between the spatial distribution of optical gas and HI gas (e.g. Saglia & Sancisi, 1988), which could make it difficult to find the kinematic centre.

There are various techniques to choose from to retrieve the rotation curve traces of a galaxy. Some approaches are described in, for example, Sofue & Rubin (2001); Schommer et al. (1993); Stil (1999); Swaters (1999).

One option that was used in the early investigations is to look at $H\alpha$ emission (at optical wavelength), using longslit spectroscopy of the ionized gas to retrieve the velocity information needed (see e.g. Rubin et al., 1978; Vogt et al., 2004). The carbon monoxide molecule (CO) is especially useful for measuring the velocities in the inner disk and central regions of the galaxy, since its rotational transition line is emitted in the millimeter (or submm) wavelength regime. At these wavelengths, extinction due to dust will not be a problem (e.g. Sofue & Rubin, 2001).

How the rotation curve behaves further out in the galaxy, was an historic question addressing the issue of the apparently flat rotation curves: Would the flat optical rotation curves still be flat when measured outside the optical disk?[1] The best option is to use neutral hydrogen gas, HI observations. The HI content in a galaxy generally reaches out

[1] yes.

well beyond the radius of the optical (stellar) matter, thus giving a better insight of the galaxy DM halo, which makes up about (or more than!) 90% of a spiral galaxy's content. There is a wide variety among galaxies in how far the HI extends beyond the optical disk, ranging from the edge of the optical disk to extremes of 10 times the optical disk (irregular dwarf galaxy DD0 154, Hoffman et al., 1993), but there is no clear connection between the type of galaxy that harbours a large DM halo vs a small one. Nevertheless, HI data provide an excellent tool for deriving a rotation curve, except in the inner regions where there is depletion of HI near the centre. In these cases, other data (e.g. CO) may have to be used to fill in the gap.

Hereafter, the name 'rotation curve' will refer to one based on HI data, unless otherwise noted.

Deriving a rotation curve is an art that can be approached in several ways. A rotation curve is generally constructed from the information provided in its velocity field. The velocity field is basically a two dimensional 'flattened' image of the galaxy, where each spatial position has been assigned a typical velocity. This velocity is ideally the velocity associated with the peak emission in the velocity profile at this location. Finding the peak emission might, however, not be completely straightforward. Less ideal conditions give rise to several effects which will affect the derivation of the velocity field. Examples of this are (de Blok et al., 2008) beam smearing (which will always lower the velocity), non-circular motions of gas in the galaxy and warps. Additionally, the galaxy inclination, if too low, makes it hard to measure radial velocities, and if too high, makes it hard to pinpoint the peak radial velocity when the line-of-sight might intersect the disk more than once. The tilted ring method (TR, Begeman, 1989) is a popular method that uses the information provided in the velocity field, and calculates the rotation curve through a series of concentric rings around the centre. It is flexible and can handle warped disks. That same ability also means that each data point (corresponding to a ring) that makes

up the total rotation curve does not vary smoothly as a function of radius, since each ring is completely independent from the next one.

An analytical description of the rotation curve is introduced in Chapter 4 in the galaxy modelling software GalAPAGOS, which uses the full 3D cube in the rotation curve derivation. It is based on a *tanh* function and four parameters, which are found through a χ^2 fitting procedure. In this thesis we compare the tilted-ring method on 2D velocity fields to the analytical fitting used in GalAPAGOS.

This chapter describes measuring rotation curves using Gaussian fitted velocity fields and tilted rings. We also describe how we determine the contributing components to the observed HI rotation curve from the gas mass and the optical matter of the galaxy, and outline how to combine these contributions in the procedure of mass modelling to find DM characteristics. Analytically modelled rotation curves are described in Chapter 4, and correlations between the kinematic parameters of rotation curves and other galaxy properties are investigated in detail in Chapter 5.

3.2 The HI rotation curve using velocity fields and tilted ring method

3.2.1 Motivation for using the Gaussian fitting method

Different methods of acquiring the 2D velocity field include the sigma clipping method, centroid-velocity and peak intensity methods, intensity weighted mean velocity method (IWM, Warner et al., 1973) and Gaussian fitting of velocity profiles (see e.g. Sofue & Rubin, 2001, for a review on several of the methods). The two latter methods are particularly popular in the literature and were discussed in e.g. Carignan et al. (1990a). They find that the Gaussian fitting method is suitable for lower S/N data, and especially in the centre of

the galaxy, where the IWM method often underestimates the velocities. Gaussian fitting also deals with beam smearing better and also with low S/N areas at the edge of the galaxy than the IWM method (Swaters, 1999). Therefore, we derive velocity fields by fitting a Gaussian to the data, as described in more detail in next section.

3.2.2 Deriving the velocity field

The GIPSY[2] task XGAUFIT was used to fit the line profile of the HI data with a Gaussian (i.e. the velocity profile of the spectral line in each voxel). We used a Gauss-Hermite h_3 polynomial on primary beam corrected data cubes. The extra h_3 term in this polynomial allows for potential skewness in the line profiles (van der Marel & Franx, 1993), which will increase the likelihood of getting as close to the correct peak velocity as possible, especially in central regions of the galaxy (Noordermeer et al., 2005).

All emission below 1.5σ were filtered out in the fitting of the data. Also, only velocities within the range of the galaxy emission (plus a suitable buffer zone) were included. A dispersion limit in velocity was also set, which should be approximately the channel width. However, it was generally found that a little larger than half the channel width would deliver the best results, i.e. find a balance between emission and noise without discarding too much real emission and not including too much noise at the edge of the galaxy. The output files from XGAUFIT include not only the velocity field, but also other maps of interest, such as integrated intensity and velocity dispersion maps. However, we used the zeroth moment map (integrated intensity) constructed directly from the non–fitted data (as described in § 3.3) and only used the velocity field resulting from the Gaussian fitting to the data cube.

The task BLOT was subsequently used in order to remove spatial regions of noise from

[2]See http://www.astro.rug.nl/∼gipsy for detailed information on GIPSY and the tasks mentioned in this chapter.

regions of emission. Great care was taken to compare the original cube and its integrated intensity map with the velocity field, in order to accurately discern between regions of emission and noise. In the case of data with lots of faint emission, a smoothed version of the cube was used to create the velocity field. In such cases, it might be easy to mistake noise for real emission, and the velocity field had to be compared with a non–smoothed intensity map and cube, so as to not interpret noise in the outskirts of the galaxy as real emission. Figure 3.1 shows the Gaussian fit velocity field and the zeroeth moment map (integrated intensity, measured from the data) of NGC 3556.

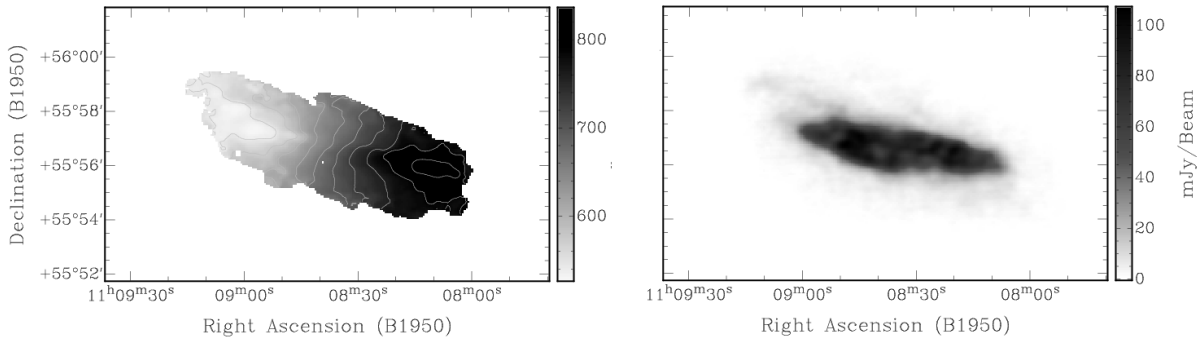

Figure 3.1: The left panel shows the velocity field of NGC 3556 derived using the Gaussian fitting method. The right panel shows a zeroth moment map of NGC 3556 showing the HI density distribution.

In preparation for the rotation curve derivation, some header changes and scaling were necessary. The task SCALE was used to scale the velocity to km/s. However, the unit in the header needed to be set to m/s. This seemingly convoluted manoever allowed uncertainties to be calculated.

3.2.3 Rotation curve derivation

The Gaussian fitted velocity field can now be used to derive the rotation curve. We use the GIPSY task ROTCUR (written by K. Begeman) for this endeavor, which fits parameters

to the velocity field using the tilted ring method (Rogstad et al., 1974; Begeman, 1989). With this method, the geometry is allowed to vary with radius during the fitting procedure, giving flexibility. This method, outlined below, is performed in several steps, where at each step the values of parameters are found and fixed. Figure 3.2 shows plots of each parameter after the first step of a ROTCUR run, in which all parameters are unfixed.

1) Only fix expansion velocity (v_{exp}) at 0 km/s, and keep fixed throughout the runs, while leaving all other parameters free. Note that we do not take v_{exp} into account in the rotation curve derivaton, since we assume that there is no flow of HI gas inwards toward the galactic centre, nor outwards.

2) Simultaneously find and fit the centre spatial position and the systemic velocity. The centre coordinates are thereafter compared with literature and with the HI intensity map of the data as a sanity check. The coordinates for the centre need to be entered as pixel values, which can be found by converting from any coordinate system using the task COORDS. If it is hard to fit the centre (due to for example depletion of HI in the centre) the latter method of estimating coordinates off the intensity map or using literature values may be used. In this case, teh centre position is fixed before the systemic velocity is found.

3) Fix v_{sys} and centre and find the inclination i and the position angle PA (counted from north to the receding side) simultaneously. Tests were subsequently made with i and PA taking turns with one parameter fixed and one free, to check for significant changes in either parameter fit. In such cases, previously fitted parameters were re-examined iteratively.

   In some cases, warping of the disk requires fitting to different values at different radii for inclination or position angle.

4) Fix all fitted parameters, and finally fit the rotation velocity (v_{rot}).

During the fitting process, the free angle (the angle around the minor axis around which radial velocities are not included) can also be tested and a weighting function (uniform, cosine or cosine squared) applied to all the points in a ring). We use a cosine weighting for the final iteration of the fitting process, although the difference between weightings is generally negligible for these data. We note that, for highly inclined systems, a cosine squared weighting is preferrable (not used here).

Note that if a parameter seems to vary strongly (e.g. v_{sys}, which can vary a lot due to galaxy asymmetry), its influence on the final rotation curve can be checked by letting it vary again after having fit all the other parameters. Generally, asymmetry will not affect the rotation curve considerably – the difference will mainly be present in the receding versus approaching sides of the rotation curve, which can be fit separately for comparison. There are also examples of galaxies which have an outer region with a different position angle (PA) (and/or inclination) than the inner region (e.g. NGC 2841, NGC 5055). For such cases, we calculate an average PA for the two different regions separately before the final fitting of v_{rot}.

The formal errors given by ROTCUR represent the uncertainty in the fit (i.e. the formal least square fit errors), rather than the uncertainty in the rotational velocity. These errors thus quite underestimate the uncertainty in the rotational velocities. A more accurate uncertainty could be constructed, for example, from the difference between the approaching and receding side of the rotation curve. The velocity dispersion σ in each annulus is also given by ROTCUR, which we adopt in this thesis as the uncertainty measurement. We use this since the galaxies in the sample are fairly symmetric, and we found that the σ values do not differ much from calculated uncertainties using the difference between approaching and receding sides. Note that in the plots (e.g. Figure 3.3), the errorbars are represented by the velocity dispersion.

Figure 3.3 displays the approaching, receding and total rotation curves of NGC 3556, in which it can be noticed the difference in the curves at radii beyond 300″. This is due to the extended emission along the major axis in the north east direction of the galaxy, which has an anomalous higher velocity than the HI in the disk (see also the velocity field in the left panel of Figure 3.1).

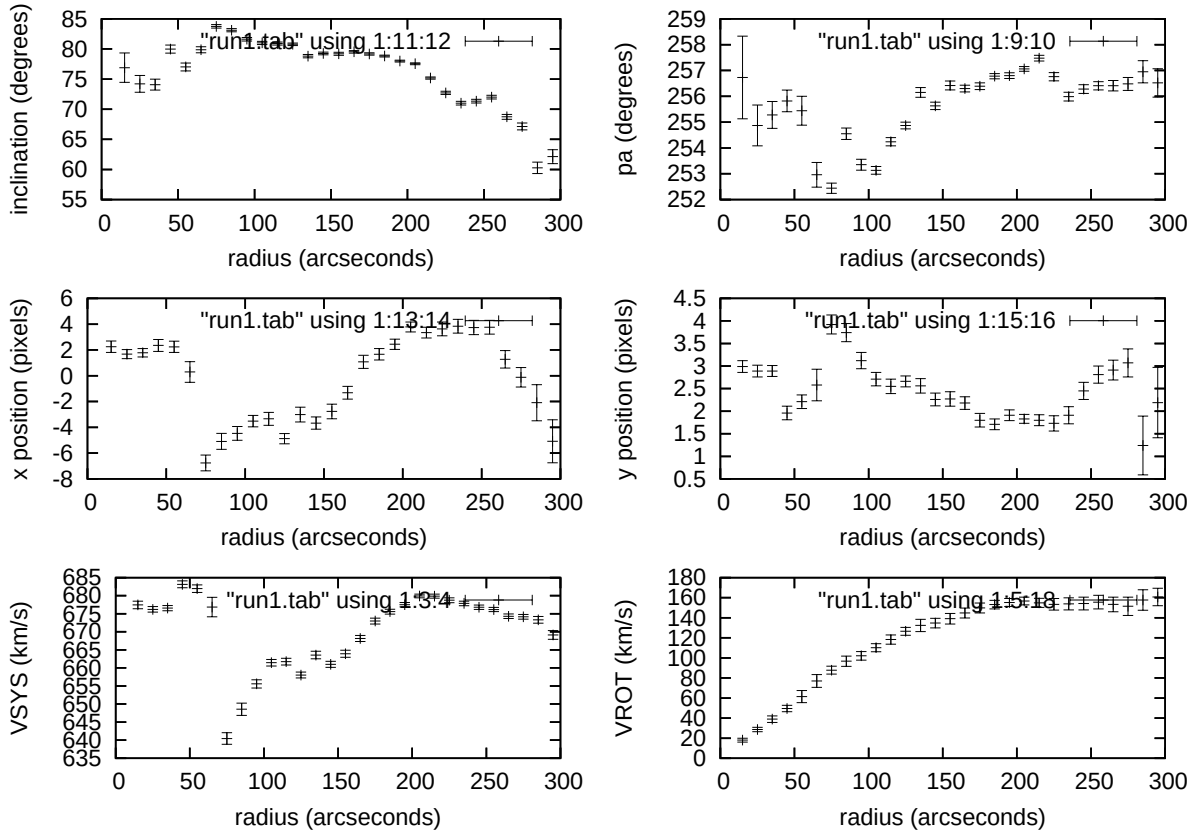

Figure 3.2: A ROTCUR run with all parameters unfixed. The first step is to fix the centre position parameters, after which the other parameters can be fitted, one by one.

3.3 Gas contribution

In order to assess how much the amount of HI gas contributes to the dynamical (total) rotation curve, the mass of the gas needs to be calculated. This is done by measuring the

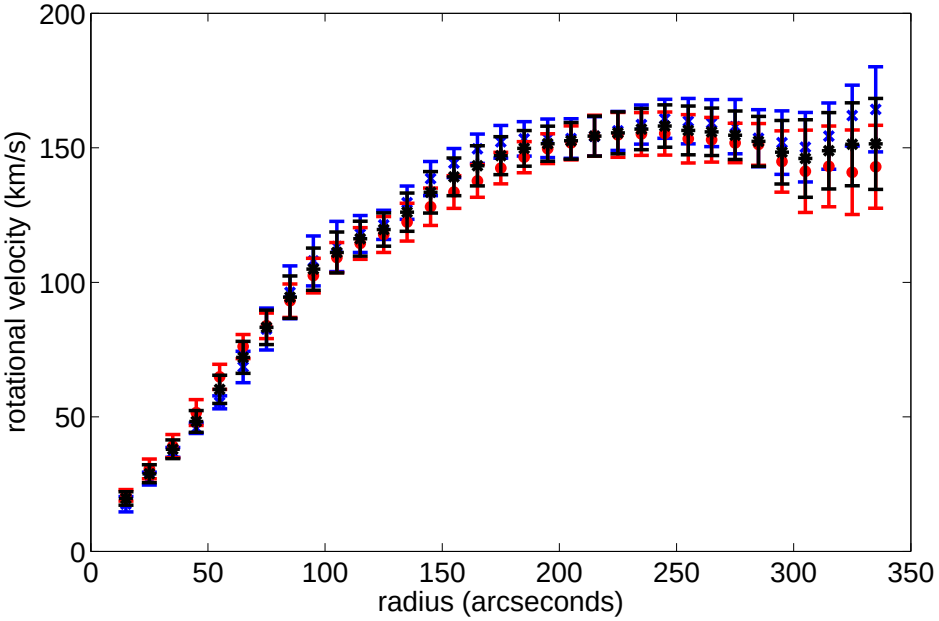

Figure 3.3: The rotation curve of NGC 3556 after all free parameters have been optimised. The total rotation curve (black asterisks) is compared to the rotation curves derived for receding (red dots) and approaching (blue crosses) side. Note that the errorbars are represented by the velocity dispersion which we use as an uncertainty rather than the formal errors given by ROTCUR. The curves match well (with symbols overlapping) out to 300″, where the symbols become discernable.

distribution of the gas emission in concentric rings, assuming that the gas takes the shape of an infinitely thin disk, and then converting the emission from flux density in units of Jy/beam to HI gas surface density in units of solar masses per parsec squared.

- The HI cube measured was primary beam corrected using the MIRIAD task LINMOS or the GIPSY task PBCORR. The data were then converted to the GIPSY format (using the task RFITS).

- In order to remove the noise, we first made a mask cube, and used it to select voxels in the data cube which contained emission. The following steps describe the procedure:

    1. The data were smoothed to twice the beam size (using the task SMOOTH). If the data included a considerable amount of faint gas in the outer parts, a larger beam was used for the smoothing. This ensured that emission would not be diluted in the subsequent steps.

    2. Hanning smoothing of the velocity axis was also applied on some of the datacubes[3], (using the task VELSMO), with a weight of 0.5 (for neighbouring channels).

    3. All values below a level of 2.5 times the rms noise in the smoothed cube were then "blanked", by replacing the values with a 'blank' value using the task COMBIN).

    4. After this, the (somewhat painstaking) manoever of 'blotching' the data (using the task BLOT), channel by channel, was performed. That is, a visual inspection was performed to distinguish between spatial regions of signal and noise

[3]Although this step was not performed on all the THINGS data, a test on one of the THINGS cubes showed that the Hanning smoothing did not have any discernable effect on the end results, likely due to the high quality of the data.

in each channel, and only the regions with signal would be kept. The result, a smoothed and blotched cube, would serve as a mask.

- The noise from the non-smoothed primary beam corrected data was then removed, by creating a new cube with values only in the spatial regions of the mask containing emission (using the task CONDIT). This is now referred to as the masked cube.

- Moment maps were subsequently created from this masked cube (using the task MOMENTS). The moment map of the zeroth order is a map of the gas intensity of the galaxy, integrated along the velocity axis. The finished masked intensity map (moment-0 map) is displayed in the right side panel of Figure 3.1.

- Using the moment-0 map as input data to the task ELLINT, the mean emission is calculated in concentric rings. Other inputs such as position angle, inclination and centre position of the galaxy are taken from a previous ROTCUR run. A tabulated output contains a variety of statistics including mean emission measured in Jy/beam.

- The mean values were converted from intensities in units of Jy/beam into mass in units of $M_{\odot}/\mathrm{pc}^2$. The HI mass is given by Equation 2.3, restated here as Equation 3.2 (see e.g. Eq. 8.22 Binney & Merrifield, 1998):

$$M_{HI} = 2.36 \times 10^5 \, D^2 \int S \, dv \tag{3.2}$$

The flux density (the integral component) of Equation 3.2 is integrated over velocity and beam size, such that $\int S \, dv = T_B \int dv \int_{\Omega} d\Omega = T_B \times \Delta v \times \Omega$. (where T_B is the mean emission measured in Jy/beam/channel, Δv is the channel width (km/s) and Ω is the beam element). By converting the emission to be expressed in units measured over an area element spanning a pc^2 and using the above, the following

relation is derived:

$$m_{HI} = 8.892 \cdot \frac{MEAN \cdot \Delta v \cos i}{b_{maj} \times b_{min}} \tag{3.3}$$

(from R. Swaters, priv. comm.) Here, m_{HI} is in units of $M_{\odot}/\mathrm{pc}^2$, MEAN is given in mJy/beam, Δv is the channel width in km/s, i is the inclination in degrees[4] and b_{maj} and b_{min} give the beam FWHM size along major and minor axis, in units of seconds of arc.

- The task ROTMOD is then used to convert input radii ($''$) and corresponding masses ($M_{\odot}/\mathrm{pc}^2$) to radii (kpc) and corresponding velocities (km/s), using the method outlined in Casertano (1983). We use distances listed in Table 2.1 for conversions to spatial lengths.

3.4 Contribution of stellar matter using luminosity profiles

The stellar contribution to the galaxy rotation was measured via the use of near-infrared data from the SDSS survey, data release DR7 (see Chapter 2). It is important to choose a wavelength band that well represents the full stellar population. While it would be unfeasible (or at least beyond the scope of this thesis) to use the entire spectrum and acquire bolometric magnitudes, the best limited bandwidth choice is to use red or IR. This part of the wavelength spectrum is preferred, as it will include the peak of the blackbody spectrum of older (redder) dwarf stellar population which make up $\sim 90\%$ of the stellar population in spiral galaxies (Rubin, 1983). Additionally, this part of the spectrum is relatively free from effects of dust absorption and less sensitive to recent star

[4]Caution should be taken with software packages such as IRAF and MATLAB, for which angles need to be converted to radians.

formation, which is another reason that makes emission in the near IR regime a more precise tracer of the mean distribution (as a function of radius) of the dominant stellar population.

The stellar M/L ratio acquired in the mass modelling procedure will thus be band-specific, and slightly different M/L will be acquired depending on choice of band.

3.4.1 Deriving the luminosity profile

Mosaicing

Each observed field of view in the SDSS data covers a $9\farcm8 \times 13\farcm5$ piece of the sky. Only in some cases were the galaxies in our sample placed in the centre of this field of view. More often than not, the galaxy is near a corner, and two or more fields are required for the full galaxy. The image mosaic software *Montage* service provided by the NASA/IPAC Infrared Science Archive, IRSA, was used to mosaic the necessary data, by converting the data to a common background and flux level. The number of fields used in each mosaic as well as the angular size of the mosaic are listed in Table 2.6.

Removal of foreground stars

For some data, contaminating foreground Milky Way stars might be a problem. If not removed, the stars will show up as intensity spikes on the luminosity profile. For galaxies for which this might be an issue, the foreground stars were removed using the IRAF task IMEDIT. In this process, the area of the star was displayed as a surface plot, allowing us to visually determine the radius at which the wings of the stars merged with the background. A radius was chosen to exactly cover the star, and the area was filled with an average value measured in an annulus around the star. The annulus would typically be a couple of pixels wide, outside a buffer zone of 2 pixels. In case of stars with spikes, the spikes

were first removed using a square aperture.

Surface profile

The next step is to find the surface brightness profile of the galaxy. This is done in the same manner as for the HI data, using GIPSY's task ELLINT, where the mean intensity is measured in ellipses around the centre of the galaxy, to find the radial distribution of intensity.

Converting to luminosity via flux and magnitude

The intensity levels in a pixel is in units of counts over the integration time, called Data Numbers (DN). This value is dependent on the characteristics of the CCD, as well as the amount of atmosphere between the observer and target (airmass) and intensity of the sky at the time of observation. These conditions change continually, and while datasets taken in sequence will differ minimally, data observed days apart will experience large differences. Instrumental reductions had already been taken care of for the SDSS data.

The conversion from intensity measured in DN to luminosities ($L_{\odot}/pc^2$) is done by first converting to flux (energy measured per time and area, usually $ergs/cm^2$) and then to magnitudes.

The mosaic service script (Montage) automatically uses information provided by the SDSS project[5] to convert all the target frames to a common background level. What is left for the user to do, is a simple conversion from flux to magnitudes using Equation 3.4:

$$M = \mathrm{MAGZP} - 2.5 \log (I - sky) \tag{3.4}$$

Here I is the intensity in DNs measured from the mosaic, and MAGZP is the magnitude

[5]see for example http://www.sdss.org/dr7/algorithms/fluxcal.html for information on photometry conversions

zeropoint, given in the header of the mosaicked data. Sky is the background sky level estimated from the luminosity profile in the plot region extending beyond the luminosity profile of the galaxy. The value was confirmed by using the statistics task in kvis on boxes in the sky region of the data.

The true magnitude is affected by internal extinction by dust and is due to the inclination of the target galaxy, as well as foreground Galactic (Milky Way) extinction. Therefore a corrected magnitude has to be calculated, following Equation 3.5:

$$M_{cor} = M - 1.0857 \cdot \ln \cos i - GE_i \tag{3.5}$$

The Galactic extinction GE is band-specific, i.e. we need to use the extinction corresponding to the SDSS i–filter. The NASA/IPAC Extragalactic Database (NED) lists the extinction $E(B-V)$ for the object in question, and Schlegel et al. (1998, Appendix B) provides the necessary information (R_i) for the i-band adaptation, following Equation 3.6:

$$GE_i = E(B-V) \cdot R_i \tag{3.6}$$

Finally, the galaxy intensity per unit area can be expressed in solar luminosities $L_\odot/pc^2$, following equation 3.7:

$$\frac{L}{L_\odot} = e^{0.921034(X_i - M_{cor})} \tag{3.7}$$

X_i is the apparent magnitude of the sun in the i-band as it would be observed at a distance of 206265 pc. As per convention we use a distance of 206265 pc which for an angular measure of $1''$ gives a linear size of 1pc in $S = a \times D$ (S=linear size, a=angular size, D=distance). Thus our units are $L_\odot/\mathrm{pc}^2$.

For the i-band filter, this value is 26.052, derived from the absolute magnitude of the

sun in the SDSS i-band, made available by C. Willmer[6] (Absolute $M_{\odot} = 4.48$ in the i-band) using the standard magnitude-distance relation in Equation 3.8, where the distance D is measured in pc:

$$m - M = 5 \log D - 5 \tag{3.8}$$

Disk-Bulge decomposition

Separation of the disk and bulge components were then performed, by fitting a bulge and a disk model to the radial surface brightness distribution. There are many different approaches to perform a disk-bulge decomposition (see e.g. Barnes et al., 2004; Palunas & Williams, 2000). Normally the bulge is modelled by a de Vaucouleurs $R^{1/4}$ law (de Vaucouleurs, 1948), and the disk is generally well-fit by an exponential model (Freeman, 1970).

However, Chemin et al. (2009) found that the traditional de Vaucouleurs law generally will overestimate the emission from the centre of the galaxy. Instead they chose a generalized Sérsic $R^{1/n}$ model for the bulge contribution to create a more robust disk-bulge decomposition, for which the de Vaucouleurs bulge is the case where $n = 4$.

In our decomposition, we also use the Sérsic bulge (Equation 3.9, 3.10) and an exponential disk model (Equation 3.11). For the bulge this is:

$$I(R) = I_e \ \exp[-b_n((R/R_e)^{1/n} - 1)] \tag{3.9}$$

$$b_n = 1.9992n - 0.3271 \tag{3.10}$$

I_e is the intensity at the effective radius R_e, which is defined as the radius that contains half of the galaxy's luminosity and $n\,(0.5 < n < 10)$ is a dimensionless parameter

[6]http://mips.as.arizona.edu/∼cnaw/sun.html

characterizing the curvature of the profile (Capaccioli, 1989).

For the disk:

$$I(R) = I_0 \ \exp(-R/R_d), \tag{3.11}$$

where I_0 is the intensity at $R = 0$ and R_d the scale-length of the disk.

A script was provided by J. Fiege and the fitting was performed using the genetic optimizer Ferret, which is the same optimizer that was used to model HI disks of galaxies, described in Chapter 4. The five parameters from the two models (I_e, R_e, n, I_0 and R_d) were fit simultaneously.

Figure 3.4 shows the disk-bulge decomposition for NGC 2841. The results for this galaxy and the other galaxies in the sample are further discussed in Chapter 5, with values listed in Table 5.10.

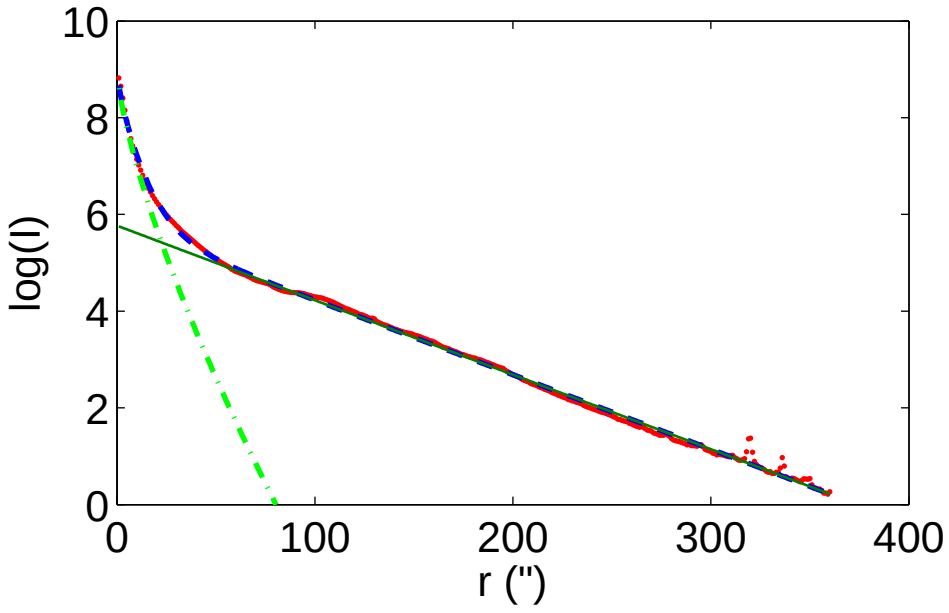

Figure 3.4: Disk-bulge composition of the luminosity profile (red) of NGC 2841 using a Sérsic model for the bulge (dashed green line) and an exponential disk model (black line) for the disk. The sum of the fitted bulge and disk is shown by the dashed blue line.

3.4.2 Stellar matter rotation curves

Again, GIPSY's task ROTMOD was used to find the rotational behaviour of the stellar matter, using the radial luminosity in units of $L_{\odot}/pc^2$ as input and delivering the rotational velocity as a function of radius. In order to derive the rotation curve from the stellar mass of the disk, disk scale height will be needed. We adopt the scale height to be a 5th of the disk scale length. This ratio was confirmed by Kregel et al. (2002), who used 34 edge-on galaxies to find accurate values of the scale height, and found a relation of scale length over scale height to be 4.8 ± 1.3.

We assume the disk stellar matter to be a vertical $sech^2$ distribution (van der Kruit & Searle, 1981), and use ROTMOD (Casertano, 1983) to calculate the rotation curve. In the ROTMOD process, a M/L of unity is assumed by ROTMOD (see Casertano, 1983), which infers that the entered luminosities (in $L_{\odot}$) are equal to the same amount of mass measured in $M_{\odot}$. The M/L for the stellar disk is later fit (or set from precalculated values) during the mass modelling process.

When calculating the contribution from the bulge, the ROTMOD setting is changed from disk to a spherical bulge. As is the case for the disk, the M/L is assumed to be unity and is not set/fit until the mass modelling process.

3.5 Mass models

Rotation curves have thus been derived for all the above mentioned observations; the dynamical (total) rotation curve, and the contributions from the gas mass, the bulge mass and the disk mass. This leaves only the DM contribution to be fit in the mass model in Equation 3.1. The GIPSY task ROTMAS was used for this fitting. Each contributing constituent is allowed to be scaled by the user, using either a fixed or free scaling parameter. As mentioned earlier, the gas contribution was set to a fixed scaling value of 1.4, to account

for He and other heavier elements. The scaling parameters for the stellar contributions (disk and bulge) are equal to their M/L. Two different mass models were made: the first with these scaling parameters free (a "best fit" mass model), in essence using the mass model to find not only the DM halo parameters, but also the M/L of the disk and the bulge, and the second with M/L set to a pre-determined M/L value based on an Initial Mass Function (IMF) and the morphology of the galaxy (see more of this in Chapter 5).

As for the DM halo, there are a few halo models to choose from, including isothermal sphere, exponential or Hernquist. Other models can also be tested, such as Navarro, Frenk and White (NFW), King and de Vaucouleurs models (see Binney & Tremaine, 2008).

The two DM models that fit well most frequently were, in particular, the isothermal sphere and, to some degree, the exponential model. We use the isothermal sphere here for reasons of consistency – we are not trying to assess which halo model is best, only to find halo parameters that are comparable to each other.

Isothermal sphere halo model

The density profile of the isothermal sphere is shown in equation 3.12:

$$\rho_{iso}(r) = \rho_0(1 + (\frac{r}{R_C})^2)^{-1} \tag{3.12}$$

where ρ_0 is the central density of the DM halo and R_C is the core radius of the halo. This translates to a rotation curve of the shape in Equation 3.13 (see e.g. de Blok et al., 2008):

$$v_{iso}(r) = \sqrt{4\pi G\rho_0 R_C^2(1 - \frac{R_C}{r}arctan\frac{r}{R_C})} \tag{3.13}$$

3.6 Summary

Rotation curves were created for 13 galaxies for which we have privately provided and public HI data cubes, using the tilted ring method on 2D Gaussian fitted velocity fields. These cubes (and a few additional ones) were later modelled using GalAPAGOS (see Chapter 4) and the two methods were compared to each other (see the first half of Chapter 5). By deriving the contribution to the rotation curve from the gas emission and the stellar contribution (divided up into the contribution from the disk and the bulge), mass models were created for the 11 galaxies for which SDSS data currently (2010) exist. These results are shown and discussed in the second half of Chapter 5.

Chapter 4

Methods and analysis: HI modelling

4.1 Background

4.1.1 Why model galaxies?

With regard to small-scale features, no two galaxies are alike. This is due to the many individual characteristics of galaxies, such as evolutionary history, star formation rates, and other contents of the galaxy. On a larger scale, however, there are similarities both in structure and in kinematics. This makes it possible to classify galaxies by morphology (using optical data), as was first done by Hubble (1926), and also by kinematic behaviour (connecting kinematic features with other galaxy characteristics was first attempted by Rubin et al. (1985)), as is the approach in this thesis.

In order to better assess the characteristics of a galaxy, making a model of it using its observational data as input is a practical approach. This model will illuminate the properties of a galaxy on both large and small scales. First, a model based on the HI content will describe for example a galaxy's gas density distribution and rotation, and could thus be a tool for constraining the DM content, star formation theory and the interstellar medium

structure. Second, fine structure anomalies that deviate from these global characteristics of the galaxy, and that may be of ambiguous origin, can potentially be well–assessed by subtracting a model from the observed data to illuminate these anomalous structures (e.g. Miller & Bregman, 2005; English, Fiege, Wiegert, Koribalski, Kerzendorf, & Freeman, 2010). An example of such structures is HI arcs. These are believed to come from either of two origins: they could be tidal debris due to galaxy interaction (e.g. Toomre & Toomre, 1972), or they are shells/filaments which are the results of star formation processes in the galaxy (e.g. King & Irwin, 1997; Irwin & Chaves, 2003).

As has been outlined here and in Fiege et al. (in prep.), we can see that a useful galaxy model not only needs to be simple (i.e. illuminating the global characteristics of the galaxy), it also needs to be sufficiently detailed in its parametric description to allow for all varieties of rotation curves and surface density distributions. Additionally, due to computational time and power constraints, the model would need to be able to describe an entire galaxy by as few parameters as possible and still meet the above requirements.

4.1.2 Methods

A few different methods have been used to create galaxy models in the literature. They are usually either based on the tilted-rings method (Rogstad et al., 1974) or on an analytic approach, where a set of equations will describe the behaviour of the modelled galaxy. Both will be briefly described here and illustrated by a few examples of software that utilize these methods.

The most common method makes use of the "tilted-ring" model, where elliptical annuli are used to describe the galaxy at increasing radial increments from its centre. Each such "ring" is fit to the emission at that particular radius (with a pre-defined annular width for the ellipse) and is described by parameters, including for example the position angle parameter. The variation of the position angle makes a "tilt" in the rings, which can

automatically describe a galaxy warp and has given the method its name.

An example of a software that uses the tilted-ring method is the GALMOD task in the GIPSY package (van der Hulst et al., 1992). GALMOD builds a model from user-supplied input parameters that describe the tilted rings. The input data to GALMOD are found through the tilted-ring fitting task ROTCUR , which requires a two dimensional velocity field. The input cube which the model will be based on is not used in the actual modelling process other than for copying the dimensional information for the output cube.

Recently a new code for modelling galaxies, TiRiFiC (Józsa et al., 2007) was developed, which still utilizes the tilted ring model, but expands it to apply to the entire three dimensional cube, rather than the more common 2D representation by a velocity field. This is a welcome approach since the 2D velocity field severely limits the ability to accurately find a good fit. For instance, high-inclination galaxies or galaxies with large warps lead to situations where the line-of-sight intersects the disk more than once, resulting in an ambiguity when deriving the velocity field. Beam smearing affecting the velocity field is another problem (e.g. Swaters, 1999; Teuben, 2002), and thus a direct fit of the 3D cube is preferred in the case of HI data (Józsa et al., 2007).

Going beyond tilted rings, another approach is to find a global description of the galaxy, using analytic expressions describing the galaxy behaviour as a whole. An example of such a code is CUBIT which can be used in the astronomical software package AIPS (Irwin & Seaquist, 1991). CUBIT fits up to 15 parameters by a χ^2 minimization process, where the best model is found by comparing with the observational data. CUBIT looks for the parameter set which yields the solution with the lowest χ^2, i.e. the best fit to the data (see section 4.2.1 for more information on χ^2 minimization). CUBIT as well as TiRiFiC, requires a fair amount of user interaction. Similar to rotation curve fitting processes such as ROTCUR in GIPSY, CUBIT needs to fit some parameters one at a time in an iterative process. While parameterising a galaxy quickly can become a hard task computationally

due to the high number of parameters involved, the number of parameters in CUBIT is kept down by allowing only preset profiles for rotation curves and surface densities, as well as not taking warps into account.

Modelling difficulties

The more parameters that are present in any type of model, whether it be tilted-rings or analytic, the harder and more time consuming it is to find a solution. Increasing the number of parameters, in combination with the presence of noise in the observational input data, considerably increases the risk of 'getting trapped' in local minima (i.e. finding what appears to be a best-fit solution, but is really not the minimum in the global parameter space solution). Thus we see that the choice of optimization method plays a large role for the success of the modelling. The examples CUBIT and TiRiFiC mentioned above use local optimization techniques (Levenberg–Marquardt and Monte Carlo, respectively) which in both cases introduce the need for a good initial guess, and iterative user-interaction throughout the run. The use of a global optimizer (searching all parameter space), would make it possible to evade local minima without user–interaction, and allows for a complicated analytic model. This is the motivation for developing GalAPAGOS[1].

4.2 GalAPAGOS

In this thesis, emphasis has been placed on a software which at a brief glance looks somewhat like CUBIT i.e. a 3D method using a parametric model rather than tilted-rings. The model is based on a HI disk including a flexible density profile and a warp. It uses the global optimizer Ferret (Fiege et al., 2004), which is a powerful genetic algorithm

[1]Note that the name of this software will be changed from GalAPAGOS to another name in future publications, since the name is already in use for another application in published papers.

(GA). GAs were made popular through the work of Holland (1975), and have since then further evolved.

A GA, just as any conventional optimizer, is a computational search technique used to find either an exact or an approximate solution to a specific optimization problem by systematically choosing values for parameters (within allowed limits). What distinguishes a GA is the optimization process: for a GA, the systematic search of values to find a best fit to a problem is similar to biological evolution. The GA will evolve a solution set of parameters by inheritance, mutations, natural selection (survival of the best fit) and crossover (doing a direct exchange of a part of the 'genome', or in this case, parameter set, of the parents to create the genome for the next generation, i.e. mating). GAs are particularly useful for more difficult optimization problems, since they cover the entire, (i.e. global), parameter space. Thus the risk of getting caught in local optima (a false optimal solution) is minimised, and instead the GA will in principle find the best global solution.

The approach of implementing Fiege's GA Ferret into a software called GalAPAGOS, has been developed by Dr. J. Fiege and his team at the University of Manitoba. As a member of that team, I am here presenting my contributions to GalAPAGOS as a user of this software. This usage affected development of the software (e.g. analytic descriptions of rotation curve and density profile). The major effort included testing the software on artificial data (see section 4.4), 'bug'-detection as well as analysis of the results.

GalAPAGOS is an abbreviation of **Gal**axy **A**strophysical **P**arameter **A**cquisition by **G**enetic **O**ptimization **S**oftware. Basically, GalAPAGOS constructs a model by using parameters fed from the optimizer, and converts the parameters into a modelled data cube based on user–defined equations. The parameters are found by comparing the modelled cube with the observational data cube and searching for the best fit.

This code, written in MATLAB, allows for great flexibility in modelling the HI disks

of galaxies, for instance:

- Kinematics: The equation defining the shape of the rotation curve can be modified into any of the many rotation curve descriptions available in the literature (see § 4.2.2).

- HI structure: The HI density distribution is modelled using a global distribution equation. Smaller scale variations in the density are added by modulating this global structure using a preset number of parameters (see § 4.2.2).

- Warp: A warped disk is included in the model, which is optional and can be turned off for example for low resolution data (see § 4.2.2).

Due to the powerful global optimizer that is used, the fitting process runs autonomously, without a need for an initial guess or further user interaction. Another useful feature of GalAPAGOS is the built-in error analysis that comes as a result of outputting all models with a χ^2 fit[2] which is found within the noise level of the input data. That is, instead of only one best-fit solution, GalAPAGOS delivers a family of equally valid solutions, which basically delineate uncertainty boundaries for each parameter. We can also find degeneracies in parameters, when two or more parameters 'trade off' against each other (for an example, see § 4.5.2).

GalAPAGOS has been developed at the University of Manitoba since 2005, and rigorous testing took place in 2008/2009. In this chapter, the function and tests of the software are described, followed by a discussion of the results, and a justification for the use of the code for subsequent parts of this thesis. GalAPAGOS, as well as its interaction with the genetic algorithm, is introduced and described in greater detail in Fiege et al. (in prep.). This chapter will focus more on my usage and testing of the software.

[2] χ^2 determines the deviation of the model from the input data, see Equation 4.1

4.2.1 Structure and function

The galaxy model consists of 18 standard parameters, as well as an optional number of additional parameters to modulate the surface density profile (usually five, see § 4.2.2). Nine of the standard parameters describe the primary structure of the disk and its kinematics, and the warp is described by three additional parameters. The remaining parameters describe properties such as orientation, location and receding velocity of the galaxy (heliocentric velocity). Table 4.1 lists all parameters and their properties, while much of this section describes how these parameters are defined.

GalAPAGOS builds a galaxy on a 3D grid, based on a parameter set chosen by the optimizer Ferret. This model galaxy is compared to the observational data via a fitness function which calculates the χ^2 value by summing over the difference between the model and the data in every voxel[3], weighted by the noise. That is, the best (reduced) χ^2 value one would expect to achieve is close to unity when the difference between the model and the data equals the noise, following equation 4.1:

$$\chi^2 = \frac{\sum_{i=1}^{N} \left(T_{b,i}^{model} - T_{b,i}^{data}\right)^2}{(N-M)\sigma^2(T_b)} \tag{4.1}$$

$T_{b,i}$ is the brightness temperature of a voxel, N is the number of voxels to be summed over, M is the number of parameters, and $\sigma(T_b)$ is the rms noise of the data cube. The optimiser Ferret then experiments with the values of the parameters based on the results, following a process which is similar to biological evolution with mutations, crossovers and natural selection, and delivers new solutions for evaluation. The first basic need in this optimization problem - to search the entire parameter space - can be satisfied, due to the coupling of the random nature of mutations with the non-random nature of crossovers

[3]a voxel is a 3-dimensional 'volume-pixel' of a data cube, where in this case the third dimension constitutes the velocity axis.

and natural selection (Holland, 1975). Tools to observe the progression of solutions as well as analyze solutions and export a single solution into the FITS format are included in the GalAPAGOS package.

The function of GalAPAGOS and its integration with the GA Ferret is described in a flowchart shown in Figure 4.1. Note that this flowchart also includes the names of some of the scripts and processes in the software. These are however not described further in this thesis beyond the information given in the flowchart. More information is available in the manual for Qubist (of which Ferret is a part)[4] and from the GalAPAGOS team led by J. Fiege.

Without sufficient computational power, an optimization problem of 23 parameters such as this will still pose a serious challenge, and yield unpractically long run times. There are many features that help with this. One example is 'linkage learning', a feature that identifies how different parameters are naturally linked to each other and divides up the problem into nearly independent sub-problems, which later get reassembled into a global solution. Run times can thus be shortened considerably, and linkage learning can even make a very difficult problem easier (Fiege et al., in prep.).

4.2.2 The parametric models

Analytic functions are used to describe the kinematic behaviour and density distribution of a HI disk with a warp applied to it. Table 4.1, described in detail in § 4.2.2, lists the 23 parameters that were used in the majority of the tests. This current secion presents some of the most important parameters and how they are applied.

For practicality, as well as for computational reasons, radii such as the turnover radius and disk scale height, are scaled to the value of the radius of the galaxy r_{out} in the

[4]http://www.nqube.ca

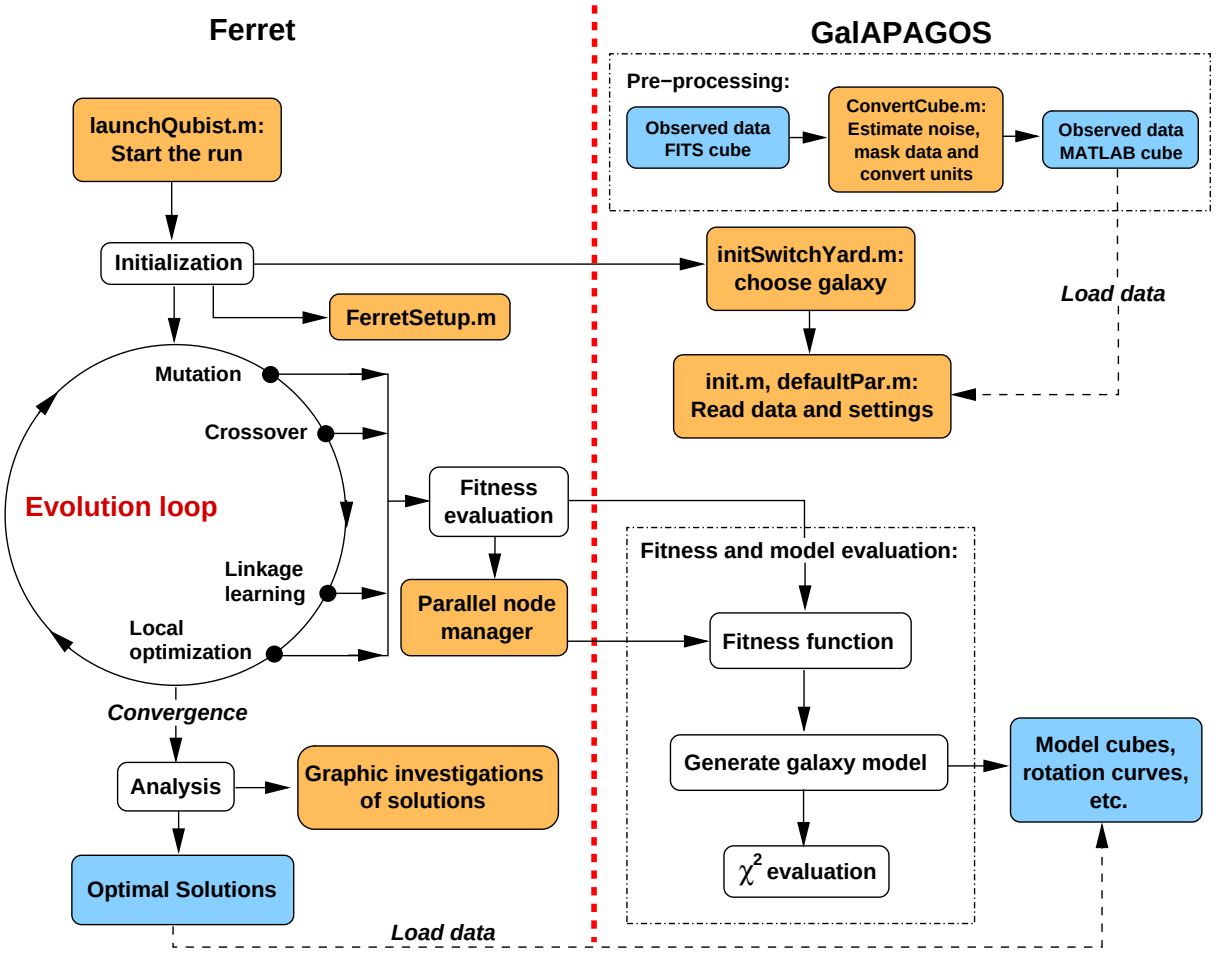

Figure 4.1: We constructed a flowchart describing the function of GalAPAGOS and its connection with the GA Ferret. Blue boxes denote handling of data, orange boxes denote processes that the user will interact with before (and after) a run and white boxes denote processes that are internal to the software.

fitting procedure. Thus the relative structure of the galaxy is maintained. Moreover, angles are converted to radians and the HI emission is converted from units of Jy/beam into brightness temperatures (K). This removes dependence on the individual beam size. Equation 4.2 (see e.g. Wrobel & Walker, 1999) shows this relationship, where c is the speed of light, k_B is the Boltzmann constant, ν is the rest frequency of hydrogen, S is the emission (flux density measured in $Jy/beam$) and Ω is the solid angle.

$$T_b = \frac{c^2}{2k_B\nu^2}\frac{S}{\Omega} \tag{4.2}$$

By modeling the solid angle (i.e. the beam) as

$$\Omega = \frac{\pi}{4\ln 2}\, b_{maj} \times b_{min}, \tag{4.3}$$

where b_{maj} and b_{min} are the major and minor axes of the beam, respectively, Equation 4.2 translates to

$$T_b = 1540.8 \cdot \lambda^2 S \frac{1}{\frac{\pi}{4\ln 2}\, b_{maj} \times b_{min}} \tag{4.4}$$

Kinematics

The tilted ring method described in Chapter 3 uses annuli at different radii and finds a rotation curve where each point is separate from the next. Attempts have been made to more uniformly describe the rotation curve, using analytic expressions. Different versions of analytic expressions of rotation curve were used by for example Persic & Salucci (1990, the 'Universal Rotation Curve'), Courteau (1997, an arctan based function) and Vogt et al. (2004, a four parameter exponential form)

The modelling equation in GalAPAGOS can be defined by the user. Here, the velocity behaviour of the galaxy is fitted to Equation 4.5, which describes the rotation curve of

the galaxy by four parameters:

$$v = v_0 \tanh\left(\frac{r}{r_{0,v}}\right)\left[1 + a_v\left(\frac{r}{r_{out}}\right)\right] \tag{4.5}$$

where v_0 is the maximum rotation velocity of the galaxy. $r_{0,v}$ is the radius at which the increasing *tanh* function bends or turns over, and is the equivalent of the rotation curve turnover radius. a_v is the asymptotic outer slope at radii beyound $r_{0,v}$, which will yield a flat rotation curve for $a_v = 0$ and rising or falling for positive and negative values of a_v, respectively. r_{out} is the outer radius of the galaxy where the surface density falls off, as shown in Figure 4.2.

Equation 4.5 very simply captures the global properties of the kinematics. Early in the development of GalAPAGOS, another form of the rotation curve was tested. This form included a second quadratic term, as well as the linear term slope a_v (within the square brackets of Equation 4.5), initially based on the form used in Vogt et al. (2004). It was however found that these two slope parameters took part in a 'trade off' against each other, where a model featuring a high linear term and low quadratic term would be similar to a model with the opposite scenario, i.e. a low linear term and a high quadratic term.

One could argue that the current form might not allow for rotation curves of shapes such as from a strongly barred galaxy (sometimes shown as a 'hump' on the turnover radius before the asymptotic behaviour) and that consequently a too low a_v value might be found. Also, there is a question whether the inner part of the rotation curve can adequately be described by only the turnover radius parameter. This will be discussed at a later stage in this thesis (see Chapter 7) along with basic modelling results.

Surface density structure and scale height

A rough approximation of the variation of HI surface density with radius could be a flat distribution, truncating at r_{out} (see curve a) of Figure 4.2). This primary structure is shown in Equation 4.6, a sigmoid function that falls off at r_{out} over a transition region Δr_{out}.

$$N_H(r) = \frac{N_{H,0}}{2}\left[\tanh\left(\frac{r_{out}-r}{\Delta r_{out}}\right)+1\right] \tag{4.6}$$

In reality, the distribution often has a lower density (a 'hole') in the centre, and is seldom flat beyond the central depletion. This is accounted for by a numerically interpolated spline function $SDM(r,\mathbf{a})$, which modulates the surface density. a_i are the surface density modulation parameters (hereafter called SDM-coefficients) which adjust the primary structure up or down at equally spaced radii. The first SDM coefficient controls the 'hole' in the centre. Thus the model for the HI density distribution follows Equation 4.7:

$$N_H(r) = \frac{N_{H,0}}{2}\left[\tanh\left(\frac{r_{out}-r}{\Delta r_{out}}\right)+1\right]\cdot SDM(r;\mathbf{a}) \tag{4.7}$$

Figure 4.2 shows a schematic of the surface density profile, including the modulation. There are two treatments of SDM coefficients. An initial treatment is described starting § 4.5.1 and a more robust version in § 4.5.2

The scale height H of the galaxy is defined as the σ of a Gaussian function, and this Gaussian function can be used to describe the vertical structure of the galaxy (the z-direction) (see e.g. King & Irwin, 1997). The surface density $N_H(r)$ (Equation 4.7) multiplied with this Gaussian thus defines the volume density of the galaxy and introduces the scale height H, following Equation 4.8:

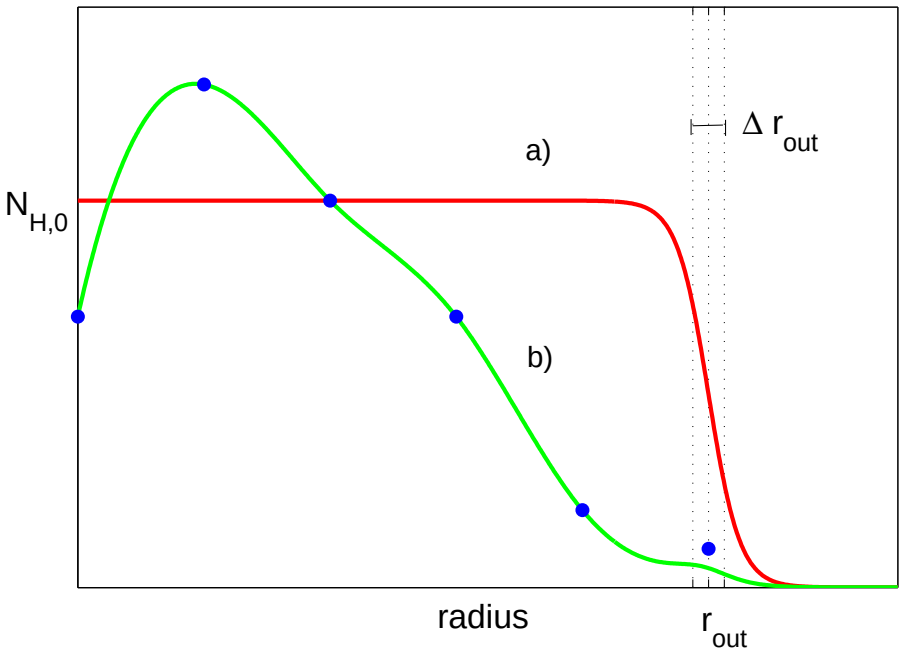

Figure 4.2: A schematic of the surface density profile. The figure shows (a) the basic sigmoid function as well as (b) the surface density profile modified by a spline function, described in Equations 4.6 and 4.7. The locations of the SDM coefficients a_i are indicated on the curve.

$$n_H(r,z) = N_H(r) \times \frac{1}{\sqrt{2\pi H^2}} \exp\left(-\frac{z^2}{2H^2}\right) \tag{4.8}$$

Warp

While the tilted ring models by design automatically incorporate warps, analytic models such as those in GalAPAGOS need a more sofisticated description of the warp. The GalAPAGOS warp can still be imagined as a number of tilted rings, but with the difference that they are connected rather than independent, and the warp is managed by a single function, that gives each "ring" a tilt throughout the disk. The warp is described by three parameters; an inclination angle, a phase and a maximum twist angle. The amount with which the warp alters the inclination angle i as a function of radius, is given by Equation 4.9:

$$\Delta i(r,\phi) = i_{warp}\left(\frac{r}{r_{out}}\right)^{\alpha_{warp}} \cos\left(m_{warp}\phi - \phi_{warp} - \phi_{twist}\right) \tag{4.9}$$

where $\phi \equiv \tan^{-1}(y/x)$ with x and y denoting respectively the semi-major and semi-minor axes of the galaxy and

$$\phi_{twist} = \phi_{twist,max}\left(\frac{r}{r_{out}}\right) \tag{4.10}$$

The inclination corresponds to the maximum tilt angle of the midplane of the galaxy measured at the outer radius r_{out}. Using the brim of a hat as an analogy to attempt to visualize the effect of the warp parameters, the warp inclination describes how much the brim of the hat is tilted, seen from the side. Using $\alpha = 1$ in Equation 4.9, the brim would be bent as a "U", using $\alpha = 2$ (used here), the bend would be "S"-shaped, and with $\alpha = 3$, the shape would be that of an extended "S". With m_{warp}, ϕ_{warp} and ϕ_{twist} at zero, the

"rings" tilt in the same direction as the disk inclination. The phase is the rotation of the warp, such that with positive values of the phase angle ϕ_{warp} the warped disk is rotated counter-clockwise, when viewing it from above. The twist is an angle applied onto the phase that describes how much the "rings" of the disk are being turned (twisted) as a function of radius. The maximum twist angle is the maximum value of the twist at the outer radius r_{out} (i.e. at short radii, the twist angle is small, and as radius increases, the twist angle increases until it reaches its maximum).

Note that Equation 4.9 is a complete description of the warp equation, as is given in Fiege et al. (in prep.). For the purposes of this thesis, a simpler version of the warp equation (equation 4.11) has been used, with the power law set to second order ($\alpha = 2$), and the azimuthal wave number m_{warp} set to zero (m_{warp} enables simulating higher order harmonic disk perturbations), following:

$$\Delta i(r) = i_{warp} \left(\frac{r}{r_{out}} \right)^2_{warp} \cos\left(0 - \phi_{warp} - \phi_{twist}\right) \tag{4.11}$$

The parameters

Table 4.1 lists all parameters currently used in GalAPAGOS. The first nine are physically important parameters describing the galaxy structure. The warp, described by the next three warp parameters, is optional and can be turned off, for example, for low resolution data sets for which a warp would be hard or impossible to discern. The remaining parameters describe non-physical properties such as orientation, location and systemic velocity. The number of parameters controlling the radial surface density (SDM coefficients) is optional as well and can be turned off. A parameter describing an angle is cyclic in nature, and is controlled by periodic boundary conditions.

Other galaxy modelling softwares such as TiRiFiC require a reasonable initial guess for their parameters. Rather than initiating the modelling with an estimated value per pa-

rameter, GalAPAGOS only requires a sensible observed value range per parameter. These ranges are set to accommodate all possible observed types of HI disks and span the parameter space in which the optimizer Ferret is allowed to search. The ranges are dimensionless as described in additional comments below.

#	parameter	description & unit	typical range
1	r_{out}	outer radius [*arcsec*]	$[0.5, 1.5]\times$ measured semi-major axis.
2	v_0	rotational velocity scale [*km/s*]	$[-350, 350]$
3	$r_{0,v}$	rotation curve turnover radius [ ]	$[0.01, 1]$
4	σ_v	1-dimensional velocity dispersion [*km/s*]	$[5, 100]$
5	a_v	rotation curve slope parameter [ ]	$[-1, 1]$
6	$N_{H,0}$	number density of disk [m^{-2}]	$[10^{20}, 10^{30}]$
7	Δr_{out}	width (disk outer edge) [ ]	$[0.005, 0.1]$
8	H	disk scale height (Gaussian σ) [ ]	$[0.005, 0.25]$
9	T_{spin}	Spin temperature [K]	$[1, 10^4]$
10	i_{warp}	maximum warp inclination [*radians*]	$[0, 1]$
11	ϕ_{warp}	warp angle offset [*radians*]	$[0, 2\pi]$ (cyclic)
12	$\phi_{twist,max}$	maximum twist angle [*radians*]	$[0, 2\pi]$ (cyclic)
13	k_D	distance multiplier	$[0.75, 1.25]$
14	v_{sys}	systemic velocity [*km/s*]	$[0, 10^4]$
15	i	inclination angle [*radians*]	$[0, \pi/2]$
16	PA	position angle [*radians*]	$[0, 2\pi]$ (cyclic)
17	Δx	model centre offset in x [*arcsec*]	$[-0.25, 0.25]\times$ map Δx
18	Δy	model centre offset in y [*arcsec*]	$[-0.25, 0.25]\times$ map Δy
19-23	$a_1 ... a_5$	surface density modulation (SDM) coefficients	$[-1, 1]$

Table 4.1: A list of all parameters, their units and their search ranges. Parameters 1 through 9 control the structure and velocity behaviour of the model galaxy (physical parameters). Parameters 10 through 12 control the warp, and 13 through 18 control the orientation (non-physical parameters). All length or radius parameters have been scaled to r_{out} and hence have empty unit brackets. Search ranges are designed to be large enough to accommodate any galaxy. Some parameters have additional comments below, which are enumerated according to the number in the table.

Additional comments on some of the parameters

1. r_{out} is the outer radius of the galaxy measured in arcseconds, and is used to scale all other distances in the model. All other lengths are therefore dimensionless and scaled by

this parameter. Thus this is a convenient parameter to scale the size of galaxy without changing its relative structure. r_{out} is defined as the point where the emission is indistinguishable from the noise, over a transition radius defined by parameter #7, Δr_{out}.

2-3, 5. See equation 4.5.

4. The 1-dimensional velocity dispersion is defined somewhat differently in GalAPAGOS than the usual definition of velocity dispersion (the dispersion of velocities at a certain line-of-sight radius): v_σ is here defined as the dispersion of velocities in a certain volume element on the galaxy disk. In other words, the FWHM of the Gaussian consisting of the velocities in a volume element is measured and the variation of the peak velocity of all these volume elements along a line of sight gives the velocity dispersion at this radius. The galaxy's average of this velocity dispersion is used as a constraint on the "local" 1D velocity dispersion.

8. The scale height of the disk is defined as the 'sigma' of the Gaussian used to model the vertical structure of the disk. See Equation 4.8.

13. The distance multiplier attempts to assess the uncertainty in distance.

14. The systemic velocity is easy to observe from the input HI data, but is included as a parameter to be optimized in order to fine-tune the systemic velocity and define the velocity range. This is to ensure that the model is centred in the cube with regard to the both the velocity axis and the spatial axes. Additionally, it has been found to be a good control parameter to verify that a modelling session is working well at an early stage of the run, since it is easy to find and usually converges early during a run. Thus it can have a very wide search range to accommodate any galaxy in the galaxy sample explored in this thesis.

17-18. This spatial offset of up to 25% of the size of the map, is used to fine-tune the exact location where the centre of the model galaxy will be placed.

19-23 The SDM coefficients control the secondary structure of the radial surface density

(see $SDM(r;\mathbf{a})$ in Equation 4.7). A small number of coefficients ($\sim$5) results in a very gradually varying solution similar to analytic models, while a larger number (>10) is comparable to the resolution of a tilted ring model.

4.2.3 The output

The result obtained from a GalAPAGOS run consists of all solutions that are found within a specified rms value (usually 1 σ of the level of noise of the cube), contained in a single observed data cube. These solutions are designated 'optimal' solutions. That is, for each GalAPAGOS run modelling input HI data, there is a large number of solutions, and each solution consists of the set of 23 parameters listed in Table 4.1. The number of solutions within an 'optimal solutions' set depends on the noise of the data (data with low S/N will allow for a larger variety of solutions) as well as how long GalAPAGOS is allowed to run. These solutions can be compared, and used for error analysis. Any parameter set making up a single solution can be output into a FITS file, which we call the model cube, making it compatible for use with various astronomy software packages in the community.

4.3 Beam convolution

The resolution of data is not determined by pixel size in its data cube, but by the size of the beam with which it was observed. Therefore, it is important that the model also is convolved with this beam, for a completely comparable result. Otherwise the model might exhibit small scale details (smaller than the beam size) that are not present in the original data. Beam information, i.e. the full width half maximum (FWHM) of each axis of its Gaussian shape and position angle, is acquired from the data header or entered manually, and the Gaussian–shaped beam is subsequently convolved with the model cube.

4.4 Testing GalAPAGOS

No modeling software will be able to model every galaxy equally well. For instance, low inclination (face-on) will always be an obstacle for the velocity characteristics while the ability to define the surface density profile will be a challenge for a highly inclined (edge-on) galaxy. An extensive number of artificial datasets were constructed in order to properly develop and test the function of GalAPAGOS. GalAPAGOS was tested not only for its ability to recover known individual parameters in an artificially generated "data" cube, but also to examine how the quality of the model is correlated with parameters such as inclination.

4.4.1 Artificial galaxies

The test galaxies were intentionally made with a low resolution to minimize run times, and were created using the same parameters that GalAPAGOS searches for. Thus the results of a GalAPAGOS run could be directly compared to the parameters of the artificial galaxies. Parameters that were deemed to be critical for the quality of a GalAPAGOS run were varied (e.g. inclination, rotation curve slope, surface density profile, warp) while other less important parameters such as those shown to be easily found by GalAPAGOS (e.g. position angle, typical radii), were kept constant throughout the runs. Figure 4.3 shows a typical artificial galaxy cube, and the settings used to create it are listed in Table 4.3. § 4.5.1 presents the different settings for the artificial galaxies used in the tests. The resolution of the cube is 16 by 16 pixels with 11 velocity channels. Each artificial galaxy had a signal-to-noise ratio (S/N, mean emission of the galaxy over its rms noise) of 25, except for one set designed specifically to test the effect of the S/N. In order to make a fair comparison, each artificial galaxy was run for exactly 1000 generations before analysis.

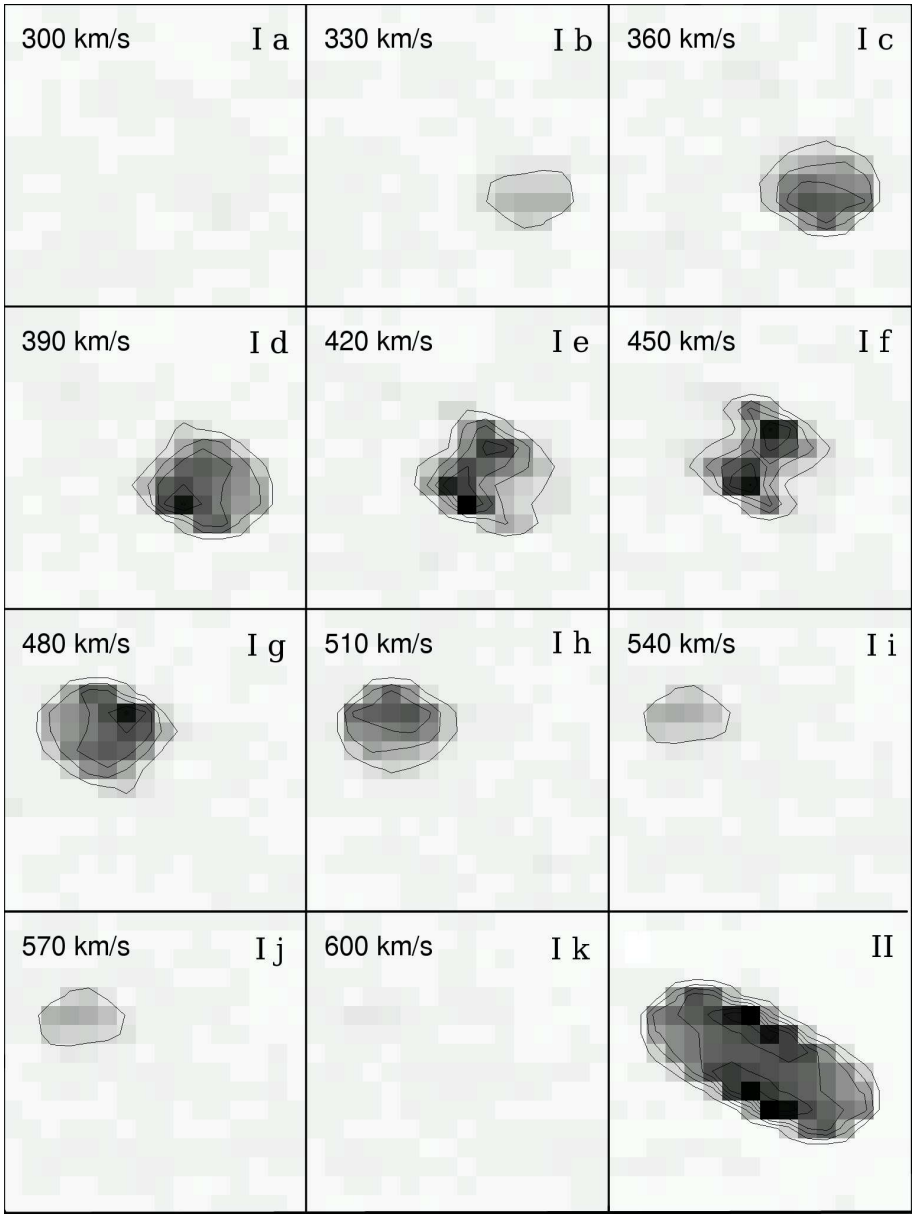

Figure 4.3: I a to I k show the individual channel maps for an example of an artificial galaxy cube. One of the solutions found by GalAPAGOS is overlaid as a contour map. II shows the integrated emission map (moment 0) of the artificial galaxy.

4.5 Results

141 artificial galaxies were created and tested on GalAPAGOS with a variety of different parameter settings. The lower the value of χ^2, the better the solution (see Equation 4.1). While a perfect match between model and data corresponds to a χ^2 of zero, we expect the best solutions to be found near unity. A histogram of the χ^2 values achieved for the models (see Figure 4.4) shows that the recovery of parameters is excellent.

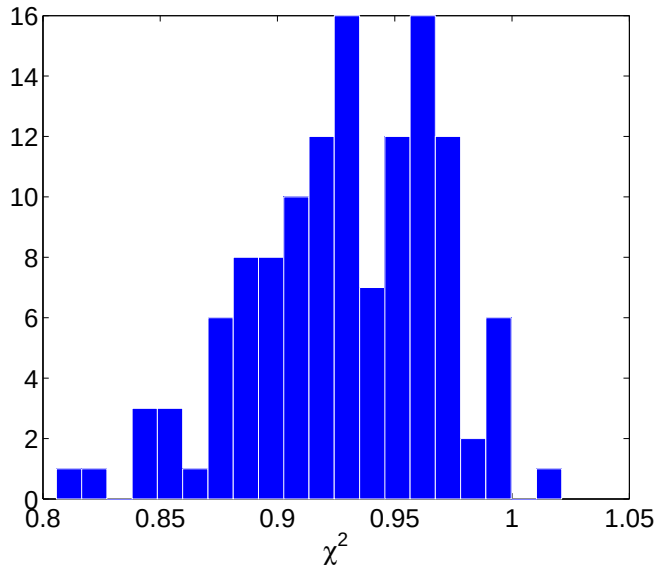

Figure 4.4: A histogram of the best fitness values achieved using 107 artificial galaxies. These runs include all artificial galaxy sets which test parameter retrieval, i.e. sets 1 through 6 in Table 4.2, but exclude sets 7 and 8 (which test stablity under other conditions) as well as multiple runs of the same artificial galaxy. That is, we are plotting a sub-sample of our 141 tests galaxies.

4.5.1 Artificial data: The GalAPAGOS "menagerie"

The tests were performed on sets of artificial galaxies (see Table 4.2), where each set was constructed to test the recovery of specific parameters and investigate how these parameters affect the quality of the models. Each artificial galaxy set is named after a

member of the local fauna of the Galàpagos islands. Figure 4.5 displays the results of all runs that were varied by inclination, i.e. sets 1 through 4 in Table 4.2. The general tendencies of variation for individual parameters can easily be discerned from the plots.

#	**Set**	**# of artificial galaxies**	**Investigation of**
1	Tortoise	9	the general inclination dependency
2	Penguin	27	three different density profiles
3	Flightless Cormorant	27	three different rotation curves (flat, declining, increasing)
4	Marine Iguana	45	the inclination of the warp
5	Bluefooted Booby	11	the phase of the warp
6	Redfooted Booby	15	the twist of the warp
7	Sea Lion	18	a variety of signal-to-noise-ratios
8	Lava Lizard	16	higher resolution and beam convolution

Table 4.2: Sets of artificial galaxies used in GalAPAGOS tests. Note that some of these sets overlap, e.g. the Tortoise set is used as one of the density profiles in the Penguin set. Thus the total number of artificial galaxies is slightly smaller than the sum of the sets.

Tortoises: inclination variation and initial sensitivity analysis

The first artificial data set varied only in inclination, from 10 to 90 degrees, with the goal of determining if any model parameters were significantly affected. It was found that the surface brightness profile parameters can be hard to constrain at higher inclinations, which is expected due to difficulty discerning a profile for an almost edge-on galaxy. Conversely, rotation curve parameters such as the slope (a_v, not plotted in Figure 4.5, but evaluated in § 4.5.1 and associated figures), the turnover radius ($r_{0,v}$, see Figure 4.5G) as well as the scale height (H, see Figure 4.5H) are sensitive to low inclinations. Table 4.3 gives an overview of the parameter settings, and the statistical ranges associated with each parameter in the Tortoise artificial data set.

The retrieval of the inclination parameter itself shows an expected correlation with

inclination (see Figure 4.5D, where Δincl is the difference between the original and the modelled inclination). Its maximum deviation for almost face-on artificial galaxies is however only six degrees, implying that GalAPAGOS finds this parameter well. The standard deviation measurements (given as a variation in percentage) for the parameters in Table 4.3 show that 11 parameters are easy to constrain regardless of inclination. Some parameters are retrieved with ease partially because they are well-defined in the modelling equations. A number of critical parameters such as those controlling the rotation curve (a_v, $r_{0,v}$), the radial fluctuations of the density distribution (a_i) as well as the warp show a large variation and need to be further investigated.

For the distance multiplier k_D, GalAPAGOS is set to search a range of 25 % above and below the provided (by the user) distance value. In panel L of Figure 4.5, we can see that the solutions found by GalAPAGOS fill the entire range for the scale factor (0.75 to 1.25), and thus do not constrain an estimate of the distance uncertainty. k_D might therefore be removed from future versions of GalAPAGOS.

Penguins: surface density profiles

The number density of the disk ($N_{H,0}$) is well constrained by GalAPAGOS. However the surface density modulation (SDM) coefficients (a_i) have a large range of values. We test the impact of this range using the Penguin artificial galaxy set. Three different distributions of HI, corresponding to three different sets of SDM coefficients, were tested. These profiles were chosen in order to encompass the range of possible profiles observed for HI gas in spiral galaxies. Each profile was used to create 9 artifical galaxies, each with a different inclination, in the range from 10 to 90 degrees. This yielded a total number of 27 runs. The three original profiles, hereafter referred to as SDM1, SDM2 and SDM3, are shown in Figure 4.6 along with profiles obtained by the GalAPAGOS modelling of each artificial galaxy.

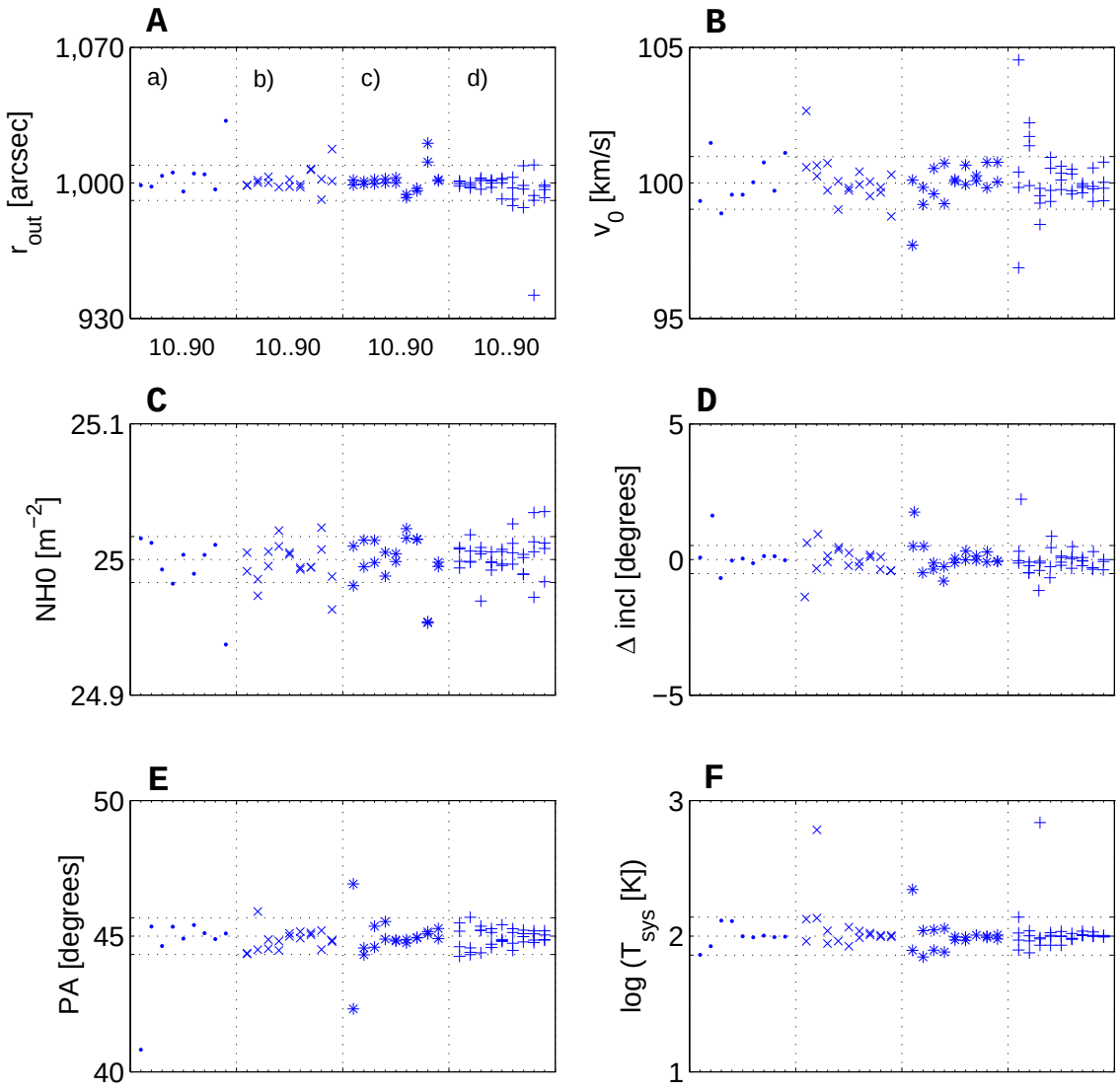

Figure 4.5: The performance of GalAPAGOS as a function of inclination: each plot shows how well GalAPAGOS has managed to find the individual parameter (on the y-axis). In each plot are shown, from left: a) Tortoises (dots), b) Penguins (x), c) Flightless Cormorants (*), and d) Marine Iguanas (+) (see Table 4.2 for descriptions of the different artificial data sets). Each of these bins spans an inclination range of 10 ° to 90 ° as shown in plot A. The actual value for a parameter is shown by a dotted horizontal line, flanked by lines delimiting its standard deviation.

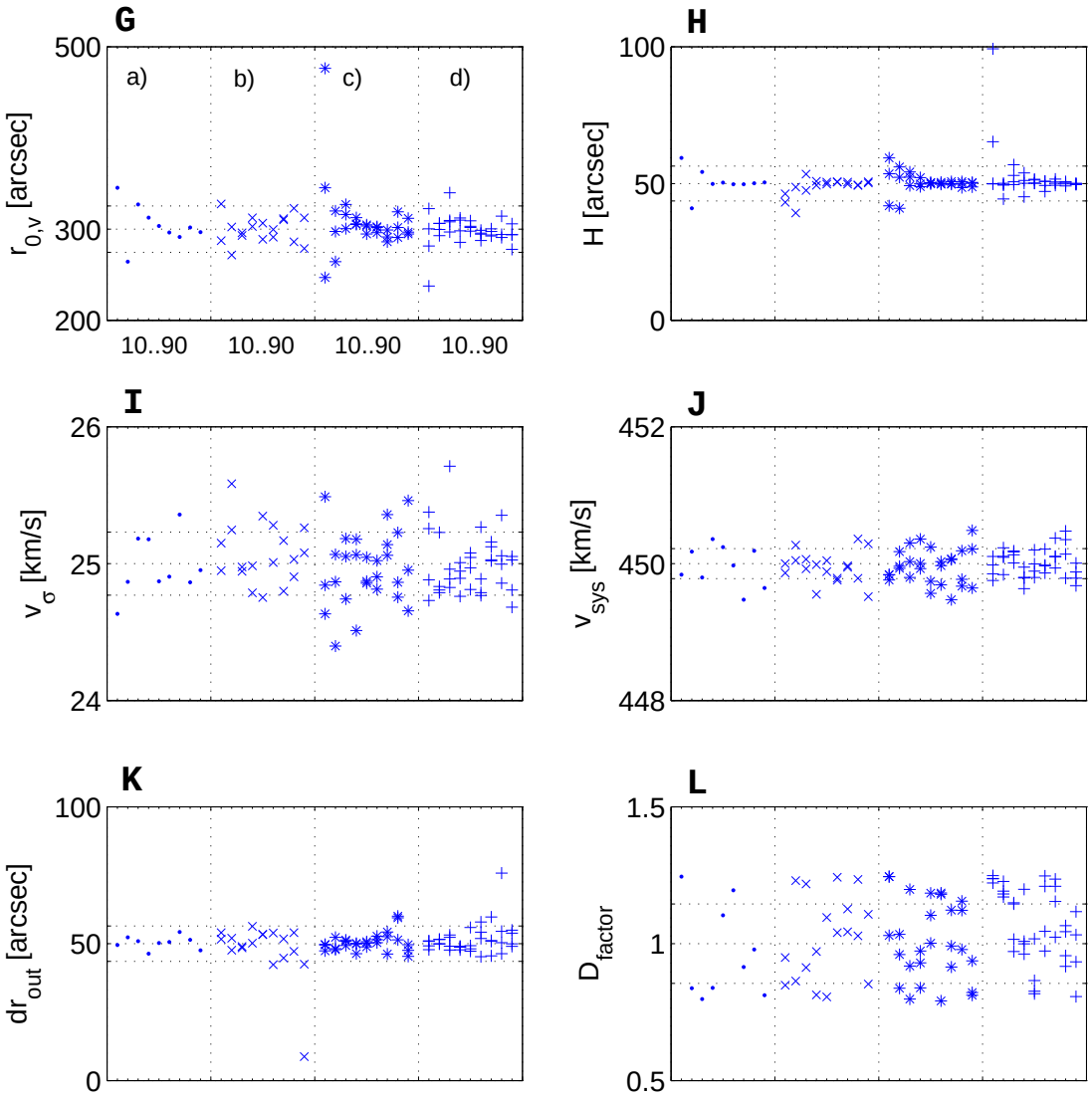

Figure 4.5 (continued)

Parameter	unit	original	min	max	variation (%)
r_{out}	[″]	1000	995.5	1032	1.1
v_0	$[km/s]$	100	98.88	101.5	0.9
$r_{0,v}$	[″]	300	264.4	345.3	7.6
σ	$[km/s]$	25	24.63	25.53	0.9
a_v	[ ]	0.2	-0.0002	0.471	65
$logN_{H,0}$	$[m^{-2}]$	25	24.93	25.02	0.1
Δr_{out}	[″]	50	46.35	54.29	4.8
H	[″]	50	40.93	59.36	9.6
$logT_{spin}$	$[K]$	2	1.860	2.115	4.0
i_{warp}	[°]	20	19.66	20.90	2.2
ϕ_{warp}	[°]	45	43.14	62.62	14
$\phi_{twist,max}$	[°]	45	30.61	47.35	14
k_D	[ ]	1	0.798	1.245	17
v_{sys}	$[km/s]$	450	449.4	450.4	0.1
PA	[°]	45	40.81	45.40	3.2
Δx	[″]	0	-0.001	0.000	0.0
Δy	[″]	0	0.000	0.000	0.0
a_1	[ ]	0.4	0.012	0.997	66
a_2	[ ]	0.1	-0.043	0.207	64
a_3	[ ]	-0.2	-0.388	-0.131	36
a_4	[ ]	-0.4	-0.434	-0.363	5.2
a_5	[ ]	-0.2	-0.977	-0.116	130

Table 4.3: Tortoises: Tests of effects of varying the inclination. See Table 4.1 for description of the different parameters. The inclination parameter was varied between 10 and 90 degrees. The variation is the standard deviation of all values in the optimal solutions set, divided by the original (input) value.

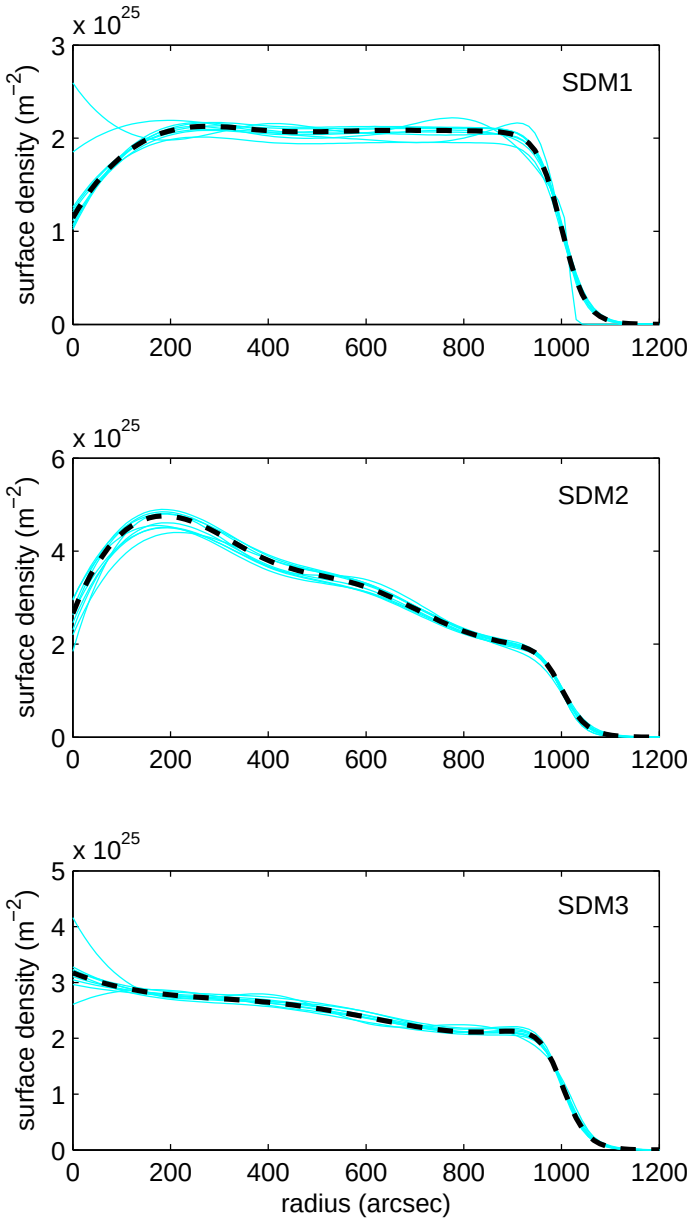

Figure 4.6: Three different density profiles (dashed black line) and the corresponding GalAPAGOS fits (thin solid grey lines) to artificial galaxies of inclinations 10-90°. High inclination artificial data sets of 80 and 90 degrees are harder for GalAPAGOS to fit, particularly near the centre (see SDM1 and SDM3).

The density profile $N_H(r)$ is given in Equation 4.6. The error between the original profile such as SDM1 and the profile acquired from the best GalAPAGOS model for each artificial galaxy can be assessed by:

$$error = \frac{\int |N_H(r)_{model} - N_H(r)_{original}|\, dA}{\int N_H(r)_{original}\, dA}. \tag{4.12}$$

By integrating over an area element dA, a measure of the error of the total HI mass in the galaxy is given. The integration was performed numerically using the trapezoid rule and MATLAB. The errors for each of the three profiles are listed in Table 4.4

We find that although there might be a rather large dispersion in the values found for the SDM coefficients a_i, an acceptable fit to the density profile is still delivered. The maximum error in total HI mass is 6% with a standard deviation of 1.4% in the errors. With one exception, the profiles are found to be imprecise only for high inclinations. At these inclinations, the SDM coefficients that have the largest deviations are a_1 and to some extent a_5. Thus, a poor fit to the inner regions of a galaxy can be due to inclinations 70 ° and above.

incl	**profile**	**HI mass error (%)**	**profile**	**HI mass error (%)**	**profile**	**HI mass error (%)**
10	*SDM1*	1.3	*SDM2*	3.6	*SDM3*	3.4
20		6.0		3.2		1.5
30		1.3		2.1		1.0
40		1.1		2.4		2.9
50		2.3		1.8		0.9
60		1.6		2.3		1.3
70		1.9		3.5		1.9
80		4.7		3.7		1.4
90		6.0		3.0		4.4

Table 4.4: Error estimates for the three density profiles that were tested with GalAPAGOS.

Note that a slight change to the handling of the SDM parameters was adopted in a later version of GalAPAGOS which (after additional testing) was used on observed HI data. The change is described in § 4.5.2. These tests are however still valid concerning the ability of GalAPAGOS to model the surface density profile.

Flightless Cormorants: Rotation curves

The Flightless Cormorants consist of 27 artificial galaxies that test three different rotation curves for nine inclinations ranging 10 ° to 90 °. The three rotation curves are increasing, flat and decreasing, respectively, which is accomplished by setting the slope parameter a_v (see Equation 4.5) to zero (flat), positive values (increasing) or negative values (declining). In order to examine effects on this slope, the other three parameters controlling the rotation curve, v_0, $r_{0,v}$ and r_{out}, are kept constant. Note that Figure 4.5 show that these other three controlling parameters will have little effect on the rotation curve. The exception is the case where the turnover radius is a significant fraction of the value of the outer radius allowing for a much greater range of a_v values.

Figure 4.7 shows the three different rotation curves that were tested, overlaid with the best fits retrieved by GalAPAGOS.

As was previously shown (i.e. Table 4.3), a_v is one of the most imprecise parameters in the optimization problem. Figure 4.8 displays our attempts to retrieve a_v from the artificial galaxies. It is clear that an accurate description of the rotational behaviour is hard to achieve for galaxies of inclination 30 ° and lower. Table 4.5 shows the expected accuracy when only higher inclination galaxies are taken into account, with a standard deviation of 15% of the original value for the increasing slope.

For inclinations of 30 degrees and above, GalAPAGOS has little to no problem finding the velocity parameter v_0 or turnover radius $r_{0,v}$ (see Figure 4.5), however, caution should be used when determining rotation curves for galaxies with inclinations less than 40 °.

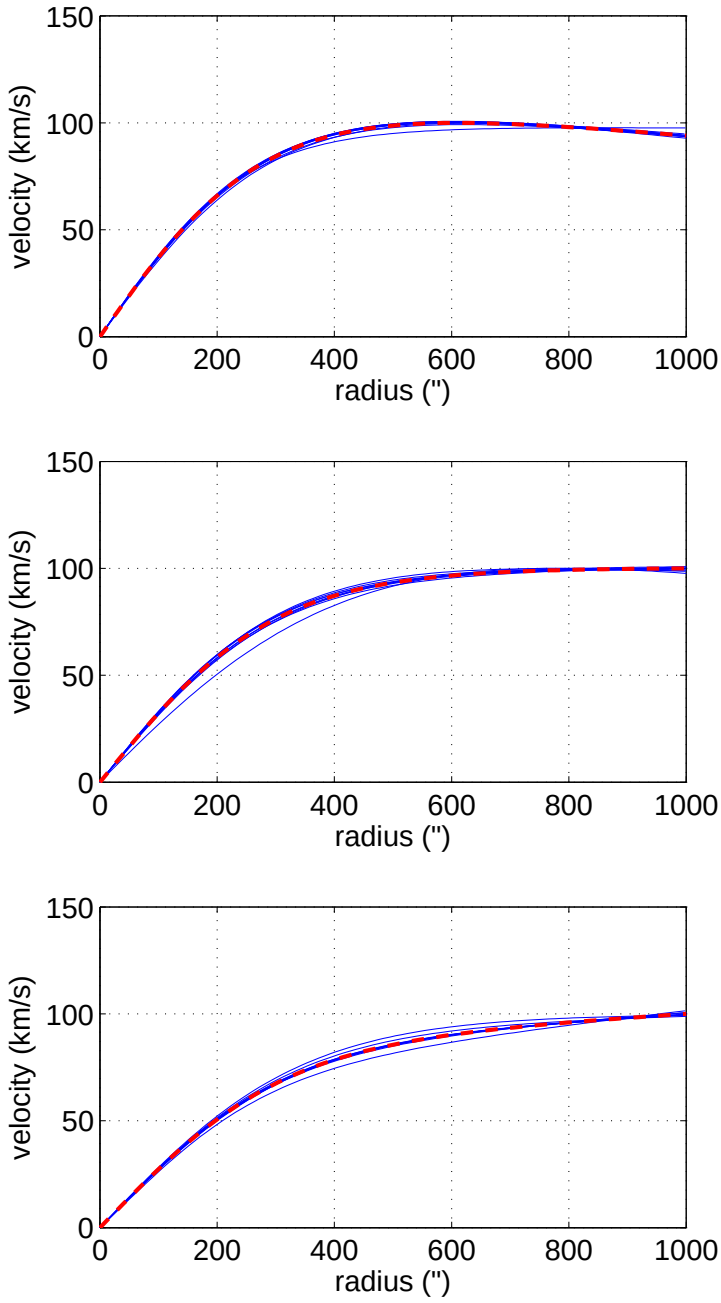

Figure 4.7: Rotation curves based on the four parameters v_0, r_{out}, $r_{0,v}$, and a_v. The rotation curve corresponding to the input parameters of the artificial galaxy is shown as a dashed red line, and the GalAPAGOS fits are shown in blue. The three different shapes feature from the top a declining, flat and increasing rotation curve. Note also that the less accurate results from the face-on inclinations (10-30 degrees) were included in these plots.

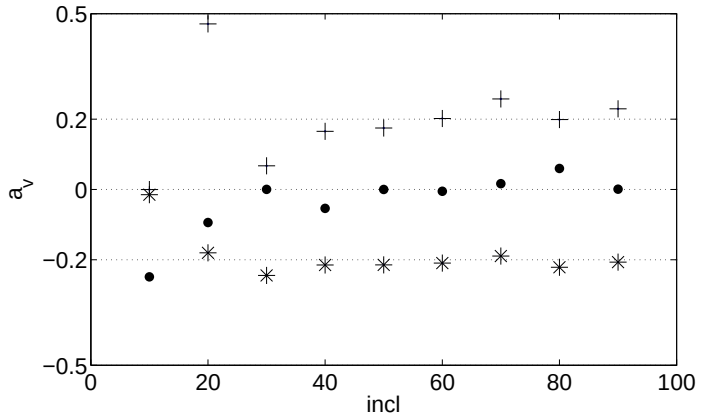

Figure 4.8: GalAPAGOS fits for three different a_v at values of -0.2 (decreasing slope, represented by asterisks), 0 (flat slope, represented by dots) and 0.2 (increasing slope, represented by + signs). Reliable fits are achieved for inclinations above 30°.

type	**original value**	**min**	**max**	**std**
declining a_v	-0.2	-0.22	-0.19	0.01
flat a_v	0	-0.05	0.06	0.04
increasing a_v	0.2	0.17	0.26	0.03
$r_{0,v}$	$300''$	246.8	476.3	38.3
v_0	100 km/s	97.71	101.5	0.769

Table 4.5: For the a_v parameters, only results from artificial data runs of inclinations 40° and higher were considered.

Marine Iguanas, Blue- and Redfooted Boobies: warp inclination, phase and twist

The Marine Iguana set is used to test five warp inclinations ranging from 0° to 40°. Each warp inclination is tested for nine galaxy inclinations (10° to 90°). For example, we constructed five artifical galaxies with inclination 90° but with a warp inclination of 0°, 10°, 20°, 30° and 40°. Recall that GalAPAGOS solves for all parameters simultaneously. GalAPAGOS was run to determine if the correct warp inclination could be recovered for each artificial galaxy (with the phase and maximum twist both created to be 45° in the artificial galaxy).

The result is displayed in Figure 4.9, wherein we find that GalAPAGOS has no difficulty finding the warp at any inclination.

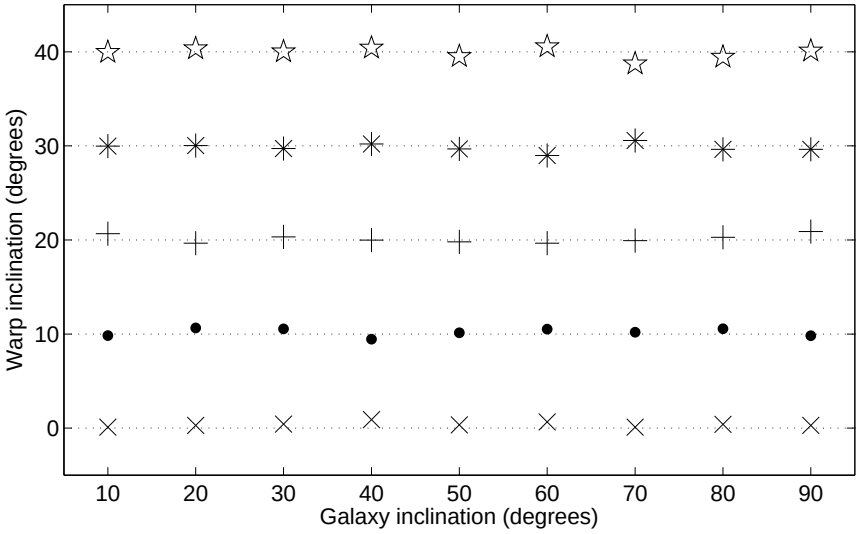

Figure 4.9: Warp inclinations of 0 (no warp) to 40 degrees were tested for the full range of galaxy inclinations, where 0° is represented by x signs, 10° by dots, 20° by + signs, 30° by asterisks, and 40° by stars). GalAPAGOS was found to have no difficulty discerning the warp at any inclination.

For a review of the warp parameters phase and maximum twist, see § 4.2.2. The

phase of the warp in the Bluefooted Booby set and the maximum twist of the warp in the Redfooted Booby set were tested for only galaxy inclination 60°. That is, GalAPAGOS was run on numerous artificial galaxies constructed with a galaxy inclination of 60°, but with a large range of phase and twist values. The results are displayed in Figure 4.10. We find that the phase, although showing larger deviations for large values, exhibits a maximum error of 4°. The scatter of the twist is also less than 4°.

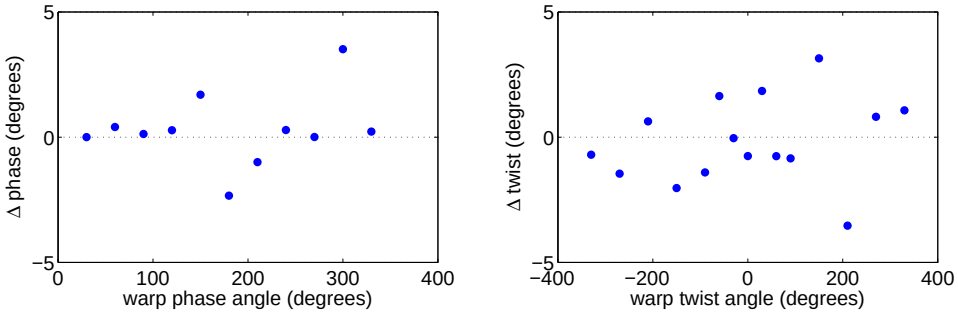

Figure 4.10: Left: The Bluefooted Booby artificial data set tests the ability to find the phase of the warp. The figure shows $\Delta phase$, i.e. the difference between the fitted phase and the original phase on the y-axis, plotted against the original phase. Right: The Redfooted Booby artificial data set tests the ability to find the twist. The figure shows $\Delta Twist$, i.e. the difference between the fitted twist and the original twist on the y-axis plotted against the original twist.

Although it is harder for GalAPAGOS to constrain the warp phase and maximum twist, than the warp inclination, it is found that the results for the phase and twist are satisfactory with differences to the input values of only a few degrees.

Sea Lions: S/N ratios

The χ^2 value is acquired by essentially dividing the difference between a model and the data in each voxel, by the noise level (see Equation 4.1). This has some implication for the interpretation of the χ^2 value achieved during a run. There are in particular two cases where caution in interpreting the χ^2 value has to be taken, since the value might be

misleading:

- For data with high S/N, the low noise in the denominator might cause high χ^2, even for a good fit.
- For data with low S/N, a GalAPAGOS run will return a larger range of models, since more possibilities will fit the noisy data. The returned χ^2 values will however be low, due to the high noise.

The Sea Lion artificial galaxies were created in order to test the range of S/N that GalAPAGOS can operate within, and in particular the high limit of S/N. The Sea Lion set spans a range of S/N values[5] from 2 to 10^6. Figure 4.11 shows that the fits are stable, even for low S/N ratios (although the reason for the constant χ^2 is unclear). Only above uncommonly high S/N, e.g. 5000, the χ^2 results become unreliable.

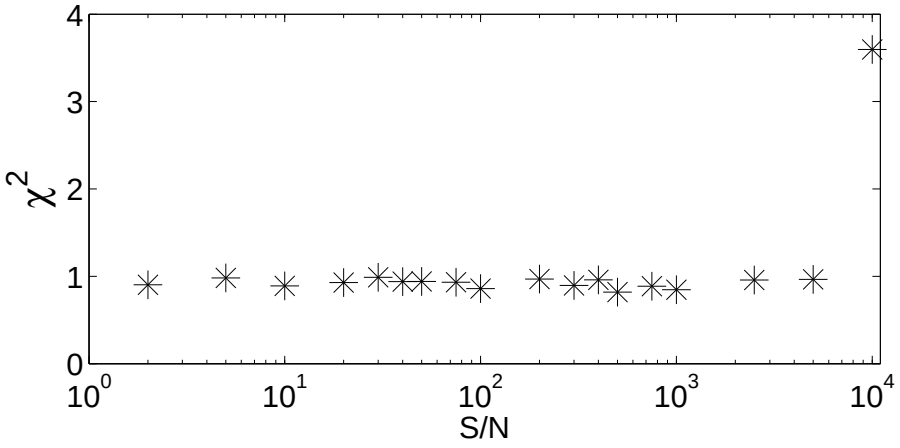

Figure 4.11: Low or high S/N does not become a problem for the χ^2 minimization, as long as it is found within the range 2 to 5000.

Another side effect due to the noise in the denominator of the χ^2 evaluation is that the fitness result of the very first evaluation (the first generation) of the GalAPAGOS run

[5]Recall that the S/N in the artifical cube is defined as the mean emission (signal) over the rms noise

is proportional to the S/N ratio. Thus data with low S/N ratio will yield a low χ^2 value already by its first generation. We note that caution thus should be taken in interpreting the fitness values for low S/N ratio data, until it has reached values sufficiently close to unity. This especially applies to data with S/N lower than 10.

Lava Lizards: resolution and beam convolution

16 artificial data sets were dedicated to testing the addition of beam convolution (see § 4.3). Eight of them were based on the same artificial data set (one of the Tortoises using a 60 ° inclination), while the remaining eight were randomly picked from the GalAPAGOS fauna, one from each artificial data set. For all of these 16 test sets, the following settings were tested: beam sizes (major and minor axes variation as well as increasingly larger sizes), beam angle, galaxy location in the cube (centred and offset), resolution (achieving higher resolution by decreasing the pixel size). There were no surprises among the results; all χ^2 values were less than unity, and the results for the eight artificial data sets are similar to previous tests.

4.5.2 GalAPAGOS tested on actual data

15 observed data cubes of galaxies were modelled with GalAPAGOS. A few of these galaxies were available in more than one survey, making it possible to evaluate whether inherent characteristics of a dataset due to the instrument (VLA and Westerbork) would have an impact on a model. Additionally, the capacity/robustness of GalAPAGOS on high and low resolution datasets were tested using a couple of galaxies available both in the THINGS and in the HIPASS survey. The results for all 15 galaxies, including NGC 3556, are evaluated in Chapter 5, with an emphasis on the rotation curves. Here we present the results from NGC 3556, which is one of the cubes that had been provided to us in the beginning of this investigation and on which we performed all initial data tests due to its

appropriate size.

Surface density modulation change

Note that there is a small change in how the surface density modulation was described earlier in this chapter, and what was later adapted before the data runs. The reason for this is a minor typo in the code describing the surface density, which was discovered at a later stage. A change was subsequently made to make the surface density modulation more robust: A pivot point was included in the vector, such that the density distribution will "pivot" around this static point. The value in this point will be that of the surface density without the modulation applied, i.e. $N_{H,0}$ (In Figure 4.2, the pivot point would be the third point from the centre (r=0)). The location of the pivot point is set by the user. It is important to place the point at a radius where there is HI emission. By default, the pivot is placed at the third position in the vector, i.e. at a location about halfway between the centre and the outer radius of the galaxy. For galaxies such as NGC 4258, the position might have to be changed due to the paucity of HI emission in this area.

11 additional tests were performed on artificial galaxies with similar surface density distributions as shown in Figure 4.6, before the revised software was used on HI data cubes.

It was found that the tests previously performed in this chapter still give a valid picture of the performance of GalAPAGOS and its ability to retrieve the SDM parameters with no effect on other parameters. That is, the original error in the code did not have an effect on GalAPAGOS's ability to retrieve the parameters.

NGC 3556

Most of the initial testing of GalAPAGOS during its developmental stages was made using HI data of NGC 3556, provided by J.Irwin. NGC 3556 is a highly inclined (i=78 °) spiral

galaxy classified as SB(s)cd. The disk of NGC 3556 has a warp, and there is a a prominent gas extension in the northeast corner. There is no apparent bulge in the optical, and the nucleus is displaced from the kinematic centre (Irwin et al., 2000). Its adopted distance is 11.6 Mpc (King & Irwin, 1997). The HI data used here were observed by King & Irwin (1997) with the Very Large Array (VLA) using the C-array configuration. The cube is naturally weighted with a beam resolution of 21.7 x 17.2 arcsec and with 23 channels, each with a velocity width of 20.7 km/s. See King & Irwin (1997) for more details.

In order to achieve feasible run times with GalAPAGOS (∼1-2 weeks on an 8 core computer), HI cubes often have to be binned in spatial and velocity resolution. In doing so, great care was taken to attempt to maintain the individual characteristics in the HI gas distribution.

NGC 3556 was binned in spatial resolution from an original pixel size of 4″/pixel to 12″/pixel (0.7 kpc/pixel), which is roughly equivalent to half a beam per pixel. The velocity resolution was kept unchanged. The GalAPAGOS run was kept going for 1200 generations and resulted in 1636 solutions in the set of optimal solutions.

Figure 4.12 displays the original data cube with the contours of the lowest χ^2 solution overlaid. Figures 4.13, 4.14 respectively show the resulting rotation curves and density profiles allowed by the optimal solutions, weighted by χ^2 value. A rotation curve calculated using the standard method GIPSY described in § 3.2 is overlaid with the GalAPAGOS rotation curves shown in Figure 4.13. There is a difference in how far out the rotation curve reaches for the two different methods; the GalAPAGOS rotation curve is shorter than the one measured with GIPSY. This is due to the gas extension in the north east corner of NGC 3556, which is discarded in the GalAPAGOS model as an anomaly. In the GIPSY rotation curve the gas extension on the approaching side was included in the rotation curve. Thus a declining rotation curve is reasonable for NGC 3556, if we exclude the extraneous gas cloud. The potential decline was also reported by King & Irwin

(1997), who also modelled this galaxy using CUBIT. Table 4.6 compares the parameters the two softwares have in common, and finds a strong similarity between them. The velocity dispersion v_σ is the radial dispersion for CUBIT (i.e. measured along a line-of-sight), while the GalAPAGOS dispersion is measured using a volume element (see § 4.2.2), and the methods give comparable results. The systemic velocity v_{sys} is the parameter with highest discrepancy. Our measurements using GIPSY gives a similar result to that of GalAPAGOS (678 km/s) while the literature (HyperLEDA) lists a systemic velocity closer to that of CUBIT (697km/s). The difference is however only on the order of one channel width.

Parameter	**CUBIT**	**GalAPAGOS**
PA	77.8±0.8	77 (0)
incl	78.3±0.8	78 (0)
v_{sys}	695.2±0.7	677 (0)
v_0	154±2	155 (3)
v_{sigma}	21±3	22 (0.1)

Table 4.6: Common parameters in CUBIT and GalAPAGOS (using the lowest χ^2 solution) compared for NGC 3556. The bracketed value in the GalAPAGOS column is the standard deviation using all the solutions in the optimal solutions set. Note that the standard deviation is small and rounded to zero where appropriate. See the text for a discussion on the difference between systemic velocities.

Notes regarding additional data tests

For some low resolution and/or low sensitivity data sets, particularly with a shorter r_{out}, sometimes a trade-off between $r_{0,v}$, and a_v can be noticed (such as HIPASS data, see Chapter 2 for description). The short r_{out}, especially in combination with a long turnover radius $r_{0,v}$, allows for a larger range of a_v, making it hard to classify the rotation curve properly in such cases. Additionally, among the high resolution data (THINGS) there is a tendency for galaxies with high rotational velocity and short turnover radius to result

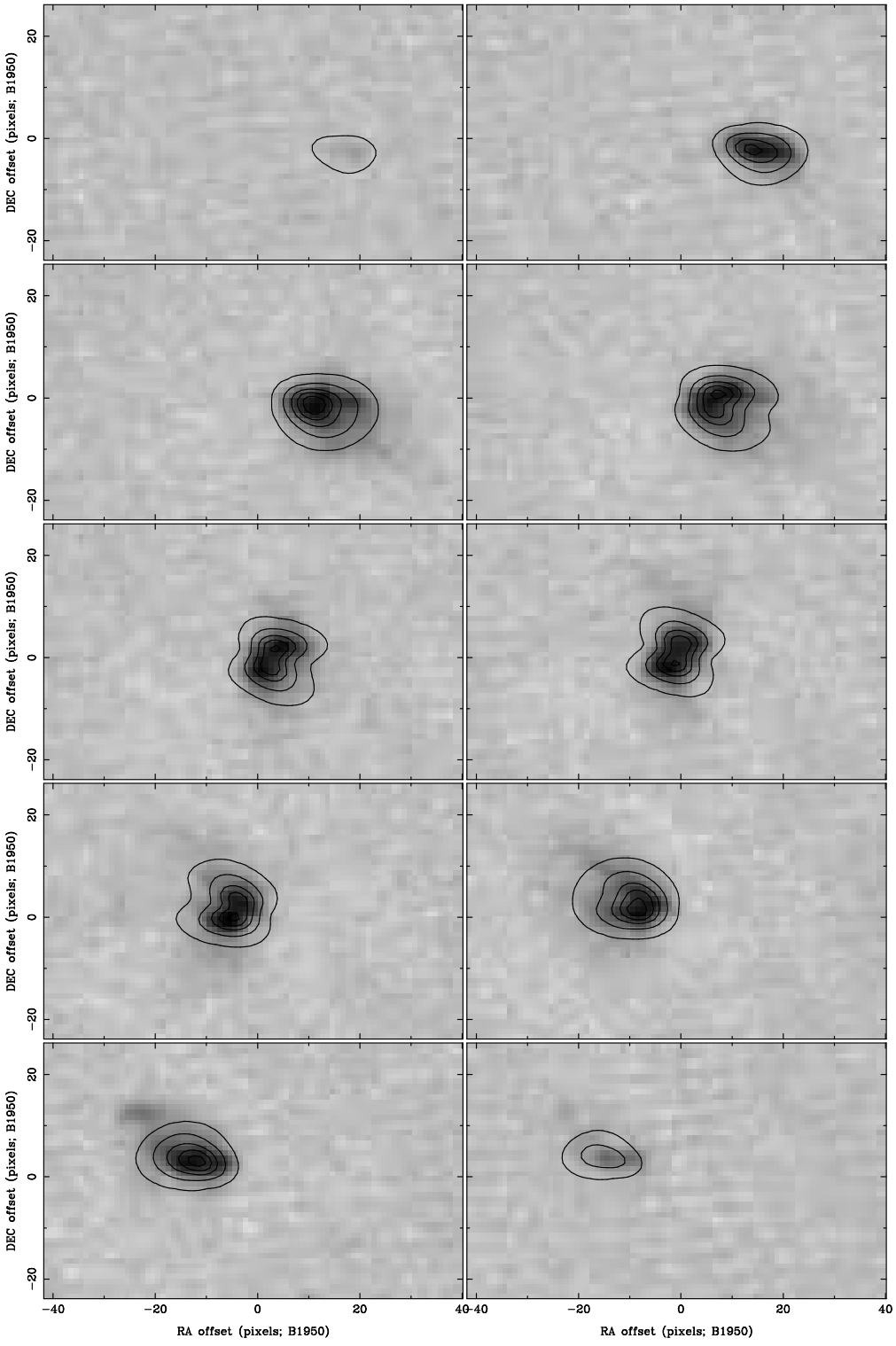

Figure 4.12: Channel map of NGC 3556 with contours of the lowest χ^2 GalAPAGOS model overlaid (roughly every two channels of the 23 channels are shown in this figure).

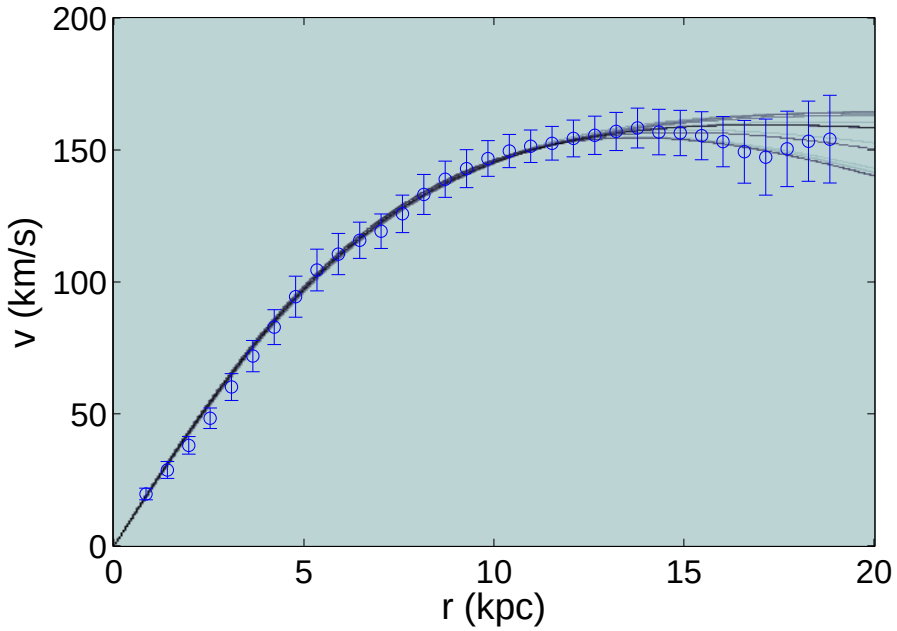

Figure 4.13: NGC 3556: Rotation curves as given by the optimal solution set, which includes 1636 models. The greyscale value of the curve is weighted by χ^2, such that dark lines have lower χ^2. A rotation curve measured with GIPSY's tilted ring method is overlaid for comparison. The errorbars indicate the velocity dispersion at that particular radius. The outer radius of the galaxy as found by GalAPAGOS is 16 kpc.

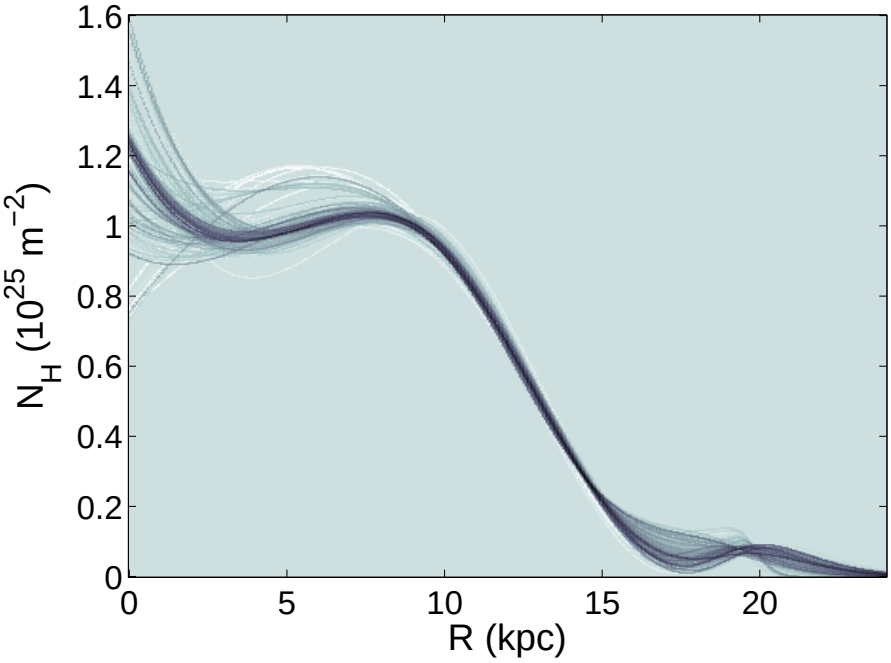

Figure 4.14: NGC 3556: The allowed density profiles as given by the optimal solution set of 1636 models, with greyscale values weighted by χ^2 as in Figure 4.13.

in GalAPAGOS models with a much shorter turnover radius than expected. This issue is discussed in more detail in Chapter 5.

4.6 Conclusions

In order to avoid complexities of using the tilted ring method, including the inaccuracies generated by using 2D velocity fields, a software package called GalAPAGOS was developed by J. Fiege and his team. GalAPAGOS uses a powerful genetic algorithm optimiser called Ferret, also created by Fiege. The main user and driver of this software (so far) is the author of this thesis.

GalAPAGOS offers a parametric model (typically using 23 parameters) with flexible rotation curves and surface density profiles, that include a warp, and is based on evaluating the full 3D cube. Additionally,

- There is no need for user interaction after starting a run.
- The global optimizer diminishes the risk of false minimum entrapment.
- The set of optimal solutions received after a run provides a built-in error analysis.
- Multiple runs on the same test cube show that results are consistent.

The artificial galaxy tests show that GalAPAGOS overall manages very well to constrain the parameters, with one exception; the distance multipler k_D, cannot be constrained in any of the setups of tests that were investigated. Additionally, caution needs to be taken for extreme inclinations. This is true in particular for low inclinations.Below an inclination of 30 °, GalAPAGOS is not reliable for the rotation curve parameters $r_{0,v}$ (turnover radius) and a_v (the slope of the rotation curve beyond $r_{0,v}$). Conversely, surface density profiles will be less reliable for high inclinations of 80 ° and above, albeit mainly the inner radii close to the galaxy centre are affected.

In conclusion, GalAPAGOS is found to be suitable for the purposes of this thesis, which concentrates on deriving the kinematic properties of highly inclined galaxies (including one not so highly inclined) in a range between 42 ° and 80 °. The results from GalAPAGOS modelling of these galaxies are presented and evaluated in Chapter 5.

Chapter 5

Results: rotation curves and mass models

5.1 Introduction

The first part of this chapter presents the rotation curves (RC) for each galaxy in the observed sample of 14 of mostly highly inclined disk galaxies, selected from the 16 galaxies presented in § 2.2.2. Two methods are used:

- The tilted ring method (Begeman, 1989) using a software package called GIPSY. Hereafter we refer to these rotation curves as 'GIPSY RCs'
- The GalAPAGOS software. This produces HI models as well as derives rotation curve families for each galaxy. Hereafter we refer to rotation curves derived with GalAPAGOS as 'GalAPAGOS RCs'.

The object of the first part of this chapter is to evaluate the quality of 14 GalAPAGOS models (§ 5.2). As an initial step, this was done by visually confirming that the model is indeed a plausible fit to the input data. Subsequently, the individual parameters given

in the solutions were scrutinized. In the following presentation, the emphasis is on the kinematic parameters of the model. This is because the values for parameters determining the kinematic behaviour (maximum rotational velocity v_0, turnover radius $r_{0,v}$ and outer slope of the RC a_v) are used in the analysis in Chapter 6, where a kinematic classification scheme is developed. Additionally, GalAPAGOS models of galaxies acquired from different data sets are compared, in an effort to discern whether it is possible to acquire sufficiently good HI models using data from low resolution single dish surveys (such as HIPASS), and whether any remarkable differences exist for galaxies measured in different surveys (such as WHISP and THINGS).

Recall that we are using a revised treatment of the surface density modulation (SDM) parameters for the GalAPAGOS runs used on observed data – see § 4.5.2.

The last part of this chapter, § 5.3, presents mass models for 11 galaxies derived using both GalAPAGOS RCs and GIPSY RCs. The results thereof are also used in Chapter 6.

5.2 Evaluation of GalAPAGOS applied to observations

18 data sets measured for 14 individual galaxies were used as input data for GalAPAGOS (see Chapter 4 for details about the modelling procedure and § 5.2.1 for modelling details for the individual galaxies). The data used in these runs (Tables 5.1 and 5.2) were chosen from the THINGS and WHISP surveys, except in the case of NGC 2903, where we also used archival VLA data collected and reduced by J. Irwin. Additionally, two galaxies from the HIPASS survey were modelled. See § 5.2.1 for a discussion on the results produced when using different input datasets of the same galaxy.

In order for the computationally demanding GalAPAGOS to manage modelling large

high resolution data cubes in a feasible timescale (on the order of 1-2 weeks per galaxy using 8 processors), it was necessary to bin most of the data cubes to a lower spatial and velocity resolution. This was done carefully so as to not lose any vital information that could deteriorate the retrieval of parameters. However, as we shall see later in this chapter, the binning appears to cause GalAPAGOS to find shorter turnover radii than expected for a few galaxies (see § 5.2.2).

The parameters from the resulting models are presented in Tables 5.1 (see § 4.2.2 for parameter definitions) and 5.2. These tables list the parameters for the (one) solution in the solution set ("family" of solutions) with the lowest χ^2 value, including the standard deviation of all the values retrieved for a parameter within the solution set. The distance multiplier has been excluded from the tables since tests in Chapter 4 found it unreliable. The two centre offsets were also excluded since they are only used to centre the galaxy in the cube and are thus not physically relevant in this context.

We found that for two datasets from the WHISP survey, NGC 4096 and NGC 4258, GalAPAGOS had some difficulty finding solutions, such that none of the parameters were sufficiently constrained during the course of a normal run. This was possibly due to the low sensitivity of these data. Therefore, instead of searching for a *set* of valid solutions for these two galaxies, GalAPAGOS was set up to find only *one* best-fit solution. Due to this, there is no standard deviation listed for the parameters for these two galaxies.

Parameters in units of angular distances are converted to parsecs to enable better comparisons in Table 5.3. Distances listed in Table 2.1 are used for this conversion.

In order to evaluate the results, visual comparisons are made between the original data cube and the model to gain an overall idea of whether the results are plausible. Individual parameters are thereafter checked, to see if they fall within expected ranges. For example, the disk scale height H for the Milky Way galaxy is 500 pc (Dickey & Lockman, 1990), and we thus expect the scale height H to be found to be of the same

Galaxy	r_{out} [″] (1)	v_0 [km/s] (2)	$N_{H,0}$ $\times 10^{20} cm^{-2}$ (3)	$incl$ [°] (4)	PA [°] (5)
NGC 925	500 (19)	126 (9)	3.2 (0.2)	69 (5)	112 (3)
NGC 2403	1400 (152)	141 (5)	4.0 (1.3)	61 (2)	124 (1)
NGC 2613	341 (5)	307 (1)	1.9 (0.1)	80 (0)	114 (0)
NGC 2841	873 (68)	322 (7)	1.6 (0.2)	71 (2)	147 (1)
NGC 2903	633 (9)	206 (0)	2.8 (0.1)	64 (0)	20 (0)
NGC 3198	547 (42)	155 (1)	3.9 (0.3)	70 (1)	37 (0)
NGC 3351	382 (176)	202 (210)	3.3 (38)	45 (10)	12 (81)
NGC 3521	552 (44)	245 (1)	4.9 (0.7)	63 (4)	165 (1)
NGC 3556	353 (8)	155 (3)	4.9 (0.3)	77 (0)	78 (0)
NGC 3621	729 (11)	146 (2)	6.6 (0.8)	55 (2)	0 (0)
NGC 4096	186	147	9.7	72	2
NGC 4258	675	206	3.6	75	148
NGC 5055	891 (145)	214 (4)	4.4 (0.5)	66 (5)	100 (1)
NGC 7331	493 (22)	254 (4)	5.9 (0.5)	76 (1)	170 (1)
Galaxy	a_v (6)	T_s [K] (7)	$r_{0,v}$ [″] (8)	H [″] (9)	v_σ [km/s] (10)
NGC 925	0.02 (0.29)	23 (2700)	170 (3.0)	5.4 (0.6)	15 (0.6)
NGC 2403	0.20 (0.20)	46 (3700)	120 (7.0)	32 (3.0)	9.8 (1.8)
NGC 2613	-0.17 (0.01)	8900 (3700)	35 (0.0)	6.9 (0.0)	14 (1.6)
NGC 2841	-0.20 (0.07)	35 (4100)	9.0 (2.0)	22 (0.3)	15 (5.3)
NGC 2903	-0.13 (0.01)	16 (1)	40 (0.0)	40 (0.0)	9.7 (0.5)
NGC 3198	-0.07 (0.03)	880 (2600)	60 (0.3)	13 (0.1)	14 (0.4)
NGC 3351	-0.15 (0.59)	9200 (3800)	3.9 (63)	21 (14)	12 (13)
NGC 3521	-0.22 (0.02)	170 (2400)	7.6 (0.3)	19 (0.2)	19 (2.2)
NGC 3556	-0.42 (0.11)	9500 (3000)	196 (0.4)	10 (0.0)	22 (0.1)
NGC 3621	-0.09 (0.04)	61 (2800)	61 (0.1)	74 (0.1)	13 (0.8)
NGC 4096	0.01	38	2.9	13	16
NGC 4258	0	7800	7.1	16	14
NGC 5055	-0.20 (0.12)	8600 (4100)	12 (3.0)	21 (2.1)	16 (3.0)
NGC 7331	-0.14 (0.20)	72 (2100)	22 (2.0)	12 (0.1)	17 (4.0)

Table 5.1: GalAPAGOS results for 14 galaxies for which the solution with the lowest χ^2 is listed, with standard deviation of all solutions in the solution set listed in brackets. 20 of the 23 parameters defining each galaxy are listed here (the distance multiplier and the two centre offsets have not been included). Column (1) is the outer galaxy radius, (2) maximum rotational velocity, (3) column density of the HI disk, (4) inclination, (5) position angle, (6) slope of the rotation curve at radii beyond the turnover radius, (7) spin temperature, (8) turnover radius, (9) disk scale height, and (10) velocity dispersion. Table 5.2 lists the remaining 10 parameters.

Galaxy	v_{sys} [km/s] (11)	Δr_{out} [″] (12)	i_{warp} [°] (13)	ϕ_{warp} [°] (14)	$\phi_{twist,max}$ [°] (15)
NGC 925	553 (1)	50 (0.8)	48 (19)	240 (61)	-52 (160)
NGC 2403	131 (2)	140 (6.0)	7 (2)	75 (110)	-167 (290)
NGC 2613	1673 (0)	2.6 (0.2)	2 (1)	290 (94)	-270 (94)
NGC 2841	627 (2)	4.5 (2.7)	22 (9)	50 (94)	28 (300)
NGC 2903	557 (0)	63 (0.3)	8 (0)	6 (170)	69 (10)
NGC 3198	681 (1)	55 (1.7)	4 (2)	300 (100)	32 (310)
NGC 3351	781 (7)	38 (6.0)	7 (19)	76 (110)	214 (240)
NGC 3521	801 (1)	55 (1.4)	37 (17)	320 (65)	38 (58)
NGC 3556	677 (0)	35 (0.1)	4 (0)	240 (10)	360 (4)
NGC 3621	734 (1)	73 (0.4)	30 (3)	260 (14)	89 (22)
NGC 4096	593	18	42	96 n/a	-67
NGC 4258	443	67	6	200 n/a	-123
NGC 5055	503 (3)	89 (5.0)	22 (13)	240 (140)	-125 (224)
NGC 7331	819 (2)	4 (0.9)	6 (3)	81 (99)	-148 (296)
Galaxy	SDM_1 (16)	SDM_2 (17)	SDM_3 (18)	SDM_4 (19)	SDM_5 (20)
NGC 925	-0.07 (0.66)	-0.32 (0.40)	-0.80 (0.08)	-0.94 (0.18)	-0.99 (0.84)
NGC 2403	0.73 (0.78)	0.99 (0.48)	-0.69 (0.52)	-0.76 (0.58)	0.28 (0.77)
NGC 2613	-0.42 (0.30)	-0.37 (0.06)	-0.81 (0.03)	-0.95 (0.05)	-0.99 (0.90)
NGC 2841	0.07 (0.75)	0.99 (0.27)	-0.39 (0.14)	-0.99 (0.44)	0.53 (0.78)
NGC 2903	0.99 (0.05)	0.38 (0.12)	-0.63 (0.03)	-0.82 (0.02)	-0.20 (0.72)
NGC 3198	-0.99 (0.78)	0.61 (0.11)	-0.37 (0.09)	-0.54 (0.09)	0.99 (0.85)
NGC 3351	-0.43 (0.71)	-0.16 (0.64)	-0.54 (0.71)	-0.77 (0.62)	-0.99 (0.74)
NGC 3521	-0.03 (0.65)	0.99 (0.42)	-0.79 (0.06)	-0.29 (0.20)	0.99 (0.79)
NGC 3556	0.30 (0.19)	0.002 (0.02)	-0.75 (0.05)	-0.87 (0.01)	-0.13 (0.72)
NGC 3621	0.96 (0.80)	0.49 (0.33)	0.02 (0.33)	-0.75 (0.14)	0.99 (0.76)
NGC 4096	0.95	-0.56	-0.64	-0.43	0.23
NGC 4258	-0.86	-0.51	-0.80	-0.03	0.99
NGC 5055	0.99 (0.78)	0.99 (0.19)	-0.17 (0.57)	0.38 (0.72)	0.99 (0.80)
NGC 7331	-0.51 (0.74)	0.06 (0.45)	-0.81 (0.15)	-0.92 (0.21)	-0.96 (0.82)

Table 5.2: GalAPAGOS results for 14 galaxies for which the solution with the lowest χ^2 is listed, with standard deviation of all solutions in the solution set listed in brackets. Table 5.1 lists the first 10 parameters. Column (11) is the systemic velocity, (12) is the width of the outer edge of the disk, (13) maximum warp inclination, (14) warp angle offset, (15) maximum warp twist angle, (16) ... (20) are surface density modulation parameters. Note that NGC 4096 and NGC 4258 only has one solution each and there is thus no standard deviation listed for the parameters of these galaxies.

Galaxy	r_{out} [kpc] (1)	$r_{0,v}$ [kpc] (8)	H [pc] (9)	Δr_{out} [kpc] (12)
NGC 925	22.1 (0.8)	7.5 (0.1)	240 (27)	2.2(0.0)
NGC 2403	21.6 (2.3)	1.8 (0.1)	500 (46)	2.1(0.1)
NGC 2613	42.8 (0.6)	4.4 (0.0)	870 (4)	0.3(0.0)
NGC 2841	59.7 (4.6)	0.6 (0.1)	1500 (21)	0.3(0.2)
NGC 2903	27.3 (0.4)	1.7 (0.0)	780 (13)	2.7(0.0)
NGC 3198	36.6 (2.8)	4.0 (0.0)	870 (6)	3.7(0.1)
NGC 3351	17.3 (8.0)	0.2 (2.8)	950 (630)	1.7(0.3)
NGC 3521	22.7 (1.8)	0.3 (0.0)	780 (8)	2.3(0.1)
NGC 3556	19.9 (0.4)	11 (0.0)	560 (2)	2.0(0.0)
NGC 3621	23.1 (0.3)	1.9 (0.0)	2400 (3)	2.3(0.0)
NGC 4096	9.2	0.1	640	0.9
NGC 4258	25.3	0.3	600	2.5
NGC 5055	31.1 (5.1)	0.4 (0.1)	730 (70)	3.1(0.2)
NGC 7331	34.7 (1.5)	1.5 (0.1)	850 (7)	0.3(0.1)

Table 5.3: Angular sizes converted to linear size. Column numbers match those of Tables 5.1 and 5.2. Column (1) is the outer galaxy radius, (8) turnover radius, (9) disk scale height and (14) is width of the outer edge of the disk.

order for our galaxies (e.g. 100-1000 pc). As can be seen in Column (9) of Table 5.3, the H values seem acceptable. One possible exception is NGC 3621, which suffers from some other issues as well (see more in § 5.2.1). NGC 2841 also has a somewhat higher H value. Comparing with values dedrived in Bagetakos et al. (2011), where galaxies NGC 2403, NGC 2841 and NGC 3521 have HI scale heights of 360 pc, 480 pc and 330 pc, we can see that the results for NGC 2841 should be treated with caution. This is confirmed in the discussion later in the following section, where the rotation curves of NGC 2841 are found to be inaccurate due to the inner region being inadequately sampled.

A number of parameters, such as position angle, inclination, systemic velocity and rotational velocity, can easily be compared to literature and databases. Table 5.4 lists the GalAPAGOS model values with values from the HyperLEDA[1] database (Paturel et al.,

[1]http://leda.univ-lyon1.fr

2003). This catalogue was chosen since the geometrical parameters are homogenized to the RC2 system (de Vaucouleurs et al., 1976). The inclination column in Table 5.4 also includes the optical inclination, calculated from the standard equation, Equation 5.2

$$\cos^2 i = \frac{(b/a)^2 - q_0^2}{1 - q_0^2} \tag{5.1}$$

This equation assumes the galaxy disk to be an oblate spheroid with an intrinsic axial ratio q_0. We use $q_0 = 0.13$ for an Sc galaxy here (Giovanelli et al., 1994). In reality, this value varies with morphological type, but the resulting uncertainty in inclination will generally be less than 2.5% for the galaxies in our sample ranging from types Sb to Sd. The parameters a and b are respectively the semimajor axis and the semiminor axis, and these values were acquired from the NASA/IPAC Extragalactic Database (NED)[2].

As is expected, the systemic velocity is easily found (i.e. its standard deviation in Table 5.2 is low), and is in agreement with values in Table 5.4. In Table 5.4 the slightly larger differences in maximum rotational velocity (up to 21%) is a matter related to the method of derivation used by different authors, in combination with galaxy inclination. The position angle is a close match, except for a few cases (NGC 3621 and NGC 4096). Possible reasons for this are evaluated in the discussions about individual galaxies which follow in the next section, § 5.2.1.

Overall, we find that parameters seem to be found within plausible ranges (see later discussion) with the exception of the spin temperature T_s, for which the uncertainties are large. Based on the testing of GalAPAGOS the expectation was to be able to distinguish between orders of magnitude of temperatures. The temperature uncertainties can partly be explained by the radiative transfer functions for HI which are used to calculate T_s

[2]http://nedwww.ipac.caltech.edu/

Galaxy	v_{sys}		v_0		PA		i		
NGC 925	553	554	126	102	112	111	69	57	61
NGC 2403	131	141	141	122	124	125	61	57	60
NGC 2613	1673	1677	307	292	114	113	80	78	90
NGC 2841	627	636	322	319	147	149	71	65	68
NGC 2903	557	555	206	210	20	22	64	63	56
NGC 3198	681	662	155	148	37	40	70	67	70
NGC 3351	781	778	202	178	12	12	45	22	42
NGC 3521	801	800	245	233	165	158	63	63	66
NGC 3556	677	697	155	153	78	82	77	77	68
NGC 3621	734	728	146	133	0	163	55	55	66
NGC 4096	593	570	147	146	1.7	20	72	79	77
NGC 4258	443	454	206	208	148	150	75	68	72
NGC 5055	503	508	214	215	100	99	66	56	56
NGC 7331	819	818	254	245	170	167	76	71	75

Table 5.4: Comparison of 4 GalAPAGOS parameters with values presented in literature: systemic velocity, maximum rotation velocity, position angle and inclination. The value on the left side in each column is modelled by GalAPAGOS and the right side value is from the HyperLEDA database. The centre value in the inclination column is the optical inclination, calculated using Equation 5.2.

in GalAPAGOS. For high temperatures, there will be high uncertainties. This can be seen using the Planck intensity B_ν (Equation 5.2) (Binney & Merrifield, 1998; Mihalas & Binney, 1981), and expanding the exponential (Equation 5.3, this is possible because HI is emitted in radio frequencies so that $\frac{h\nu}{kT} \ll 1$):

$$B_\nu = \frac{2h\nu^2/c^2}{e^{h\nu/kT_s} - 1} \tag{5.2}$$

$$e^{h\nu/kT_s} \approx 1 + \frac{h\nu}{kT_s} \tag{5.3}$$

Substituting Equation 5.3 into Equation 5.2, there is a clear problem when the spin temperature T_s increases and brings the denominator in Equation 5.4 to zero:

$$B_\nu = \frac{2h\nu^2/c^2}{\frac{h\nu}{kT_s}} \tag{5.4}$$

This is, however, just a part of the explanation, since we can see that even at lower temperatures of tens of degrees, the uncertainties are large.

In the following section, we make comparisons between RCs derived by GalAPAGOS (using a parametric method based on a 3D cube) and RCs derived using GIPSY (using the tilted ring method based on a 2D velocity field). While both methods are imprecise at low inclinations, the tilted ring method can also be imprecise at high inclinations. This is due to the use of 2D data - at such inclinations, a large range of velocities will be present in the line-of-sight, which makes it difficult to measure the typical rotational velocity as a function of radius. In particular, measurements can be inaccurate for high inclination galaxies due to warps, causing the line of sight to cross the disk more than once. Additionally, velocity points far from the major axis will suffer from larger deprojection errors.

5.2.1 Rotation curves - GalAPAGOS vs tilted rings

Figures 5.1, 5.2 and 5.3 show the rotation curves from all the solutions acquired for each galaxy. The greyscale of the curves is weighted by their χ^2 value, where darker curves correspond to lower χ^2. Overlaid on (most) figures are the corresponding rotation curves derived using the tilted ring method task ROTCUR in the software package GIPSY, described in § 3.2. The error bars correspond to the velocity dispersion in each ring. Briefly, the technical differences between GalAPAGOS and ROTCUR are that the former is using the entire 3D data cube and fits a user-defined parametric model to this cube, while the latter uses the 2D velocity field and measures the velocities directly using the tilted ring method (see previous chapters). Note that the figures are cut off at the outer radius (r_{out}) determined by the GalAPAGOS model. Cases where this is drastically different from the outer radius found in the tilted ring method will be noted individually for each galaxy.

Each galaxy is individually commented on below. The focus here is on differences be-

tween the outer RC slope (a_v) and the turnover radius ($r_{0,v}$) for each method. To quantify the outer slope, rather than looking at the slope value alone (defined in Equation 4.5), we look at the percentage difference in velocity between the velocity directly after the turnover and the velocity at r_{out}. Doing this will enable distinguishing between slopes that have been given negative values but might be flat, and slopes with an actual declining behaviour. Velocity changes less than 10% will not be considered large enough to warrant the label "declining" or "increasing". The term "observable parameters" used in some of the individual galaxy discussions refers to parameters that can easily be compared in literature and databases, such as inclination, position angle and systemic velocity.

In a number of the GalAPAGOS RCs, the inner part differs drastically from that of the GIPSY RC, in that the modelled turnover radius has a shorter value than expected. This short turnover radius is an interesting artefact that, as we shall see later, seems to be a common phenomenon for galaxies which also have a short turnover radius in the GIPSY RC. This is discussed in the summary (§ 5.4).

Rotation curves have also been derived for the THINGS data by the THINGS team (de Blok et al., 2008), using the same method (GIPSY) as was used in this thesis on the same data cubes. Their RCs correspond well to ours with regards to turnover radius, maximum velocity and uncertainties, for all galaxies in the sample. However, in some cases their 3σ cutoff results in a much shorter outer radius, disregarding the faint emission in the outer part of the galaxy. Nevertheless, we consider these GIPSY RCs comparable, and will use the ones derived in this thesis for the comparisons that follow.

Technical data on the GalAPAGOS runs are listed in Table 5.5. The number of generations is a measure of the amount of time the run was searching for solutions, but is not a measure of the quality of the solutions – usually, the solutions start to converge after a few 100 generations. The χ^2 value is only indirectly a measure of quality since it is highly dependant on the sensitivity of the input data. Thus low sensitivity data (WHISP)

can easily reach low χ^2 values due to their high noise, while it is harder to reach low χ^2 values using high sensitivity data (THINGS) (see also § 4.5.1). Thus the χ^2 value cannot be used to compare the goodness of fit of runs on different data cubes (unless the input data cubes have the same sensitivity).

Galaxy	Generations	Lowest χ^2	# solutions
NGC 925 (W)	2000	1.9	10635
NGC 925 (T)	2000	2.6	5650
NGC 2403 (T)	1375	1.8	10856
NGC 2613 (I)	2000	3.4	3938
NGC 2841 (T)	1500	1.9	4544
NGC 2903 (T)	2000	3.6	8411
NGC 2903 (W)	2000	1.4	90267
NGC 2903 (I)	1550	26	2112
NGC 3198 (T)	1800	2.9	8501
NGC 3351 (T)	1575	0.8	23330
NGC 3521 (T)	875	7.2	1243
NGC 3556 (I)	1200	53	1636
NGC 3621 (T)	1125	8.8	2354
NGC 3621 (H)	1500	20	2472
NGC 4096 (W)	325	1.0	1
NGC 4258 (W)	700	1.3	1
NGC 5055 (T)	1500	2.3	6769
NGC 7331 (T)	2000	1.9	11076
NGC 7793 (T)	1500	2.5	5926

Table 5.5: Technical data for the GalAPAGOS runs. (W) refers to WHISP data, (T) to THINGS data, (H) to HIPASS data and (I) to individually donated data (Irwin).

For a few galaxies, data from multiple surveys were available. GalAPAGOS is applied to these in order to investigate the software's ability to use low resolution data and still get solutions similar to those from higher quality data. Also the possibility of using HI data from single dish surveys such as HIPASS was alluring. Obviously, with lower resolution data, parameters such as the geometrical size (r_{out}) will have an uncertainty increase directly related to the beam resolution. A higher uncertainty in the solution set was also expected. However, would the parameters be retrieved as precisely as the low resolution

artificial galaxies investigated in Chapter 4? Data from THINGS, WHISP, and HIPASS, as well as privately donated VLA data (J. Irwin) for galaxies NGC 925 (THINGS and WHISP), NGC 2903 (THINGS, WHISP, Irwin), NGC 3621 and NGC 7793 (both THINGS and HIPASS) were used for these additional comparisons. Figures 5.3 and 5.4 display the RCs of these galaxies.

To summarise, this section compares and attempts to explain differences between

- RCs generated by GalAPAGOS and GIPSY for each data set.
- GalAPAGOS RCs generated using different resolution and sensitivity data cubes (from different surveys) for the same object.

NGC 925 (i=60°)

NGC 925 has an intermediate inclination of 60°, an inclination for which the GIPSY RC is considered to be reliable. Its existence in two HI surveys made it possible to model NGC 925 in two versions; one for data from the THINGS catalogue, and one for data from the WHISP catalogue (see Chapter 2). This was done in order to evaluate whether inherent characteristics of a data set due to the instrument would have an impact on a model. The two different data sets are described in Chapter 2.

For these GalAPAGOS runs, both cubes were binned to the same spatial resolution of 30″per pixel. Despite this low resolution – one pixel covers 5 VLA beams or 2.3 WSRT beams, or 1.3 kpc – the large turnover radius allows the inner region to be well sampled, and the GalAPAGOS RCs compare well with the GIPSY RCs. GalAPAGOS was allowed to run for 2000 generations for each of the data cubes.

Panels a and b of Figure 5.3 show the results from runs on data from the WHISP and the THINGS survey respectively. The GIPSY RC is derived from THINGS data in

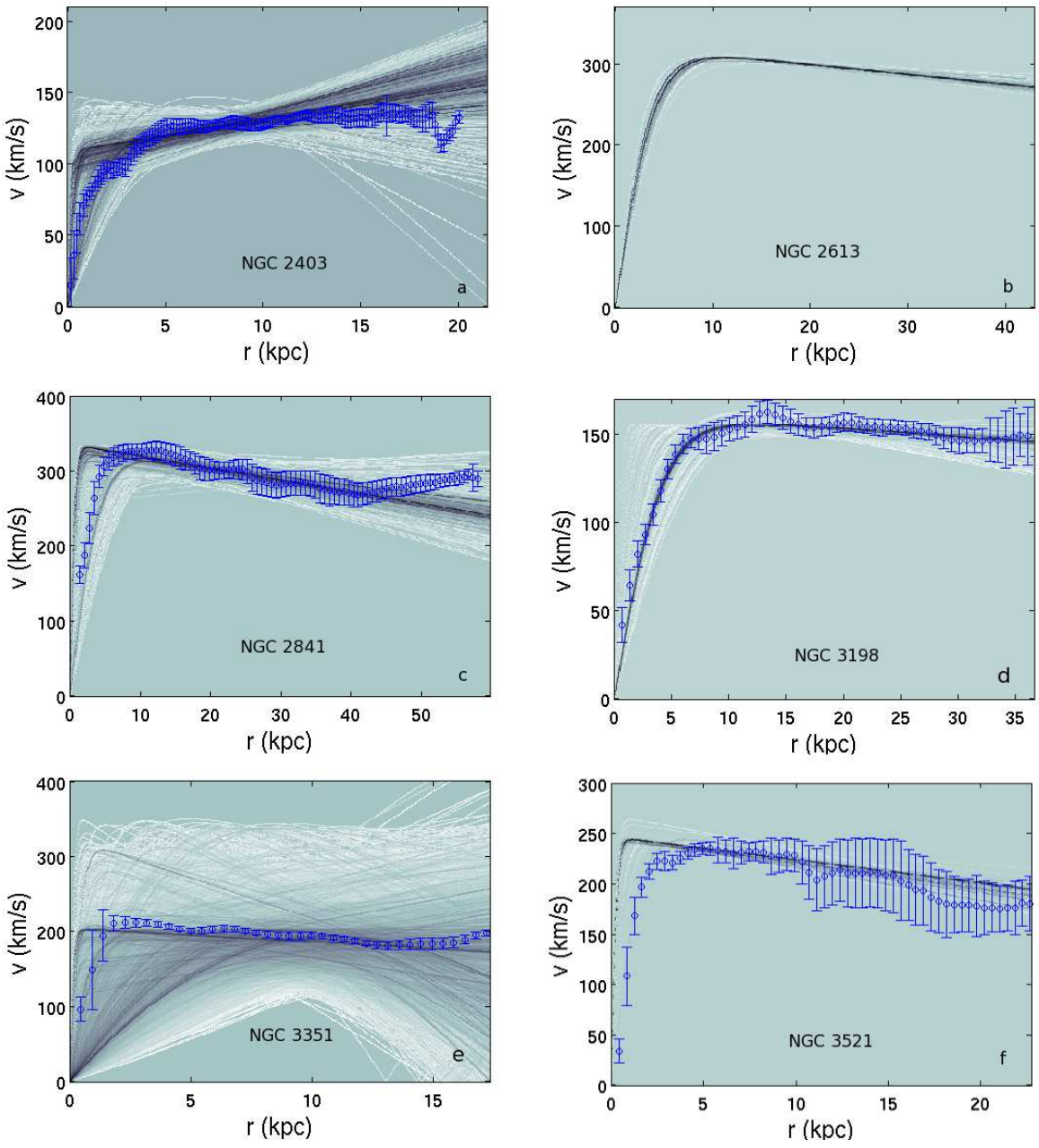

Figure 5.1: Rotation curve families from GalAPAGOS overlaid with the tilted ring RC (with error bars) from GIPSY. The shade of the curve is weighted by χ^2 value, so that darker curves have a lower χ^2. The radius is cut off at the r_{out} value found by GalAPAGOS. (Recall that the GIPSY errorbars are represented by velocity dispersion instead of the formal least square errors given by the fitting software, as described in § 3.2.3

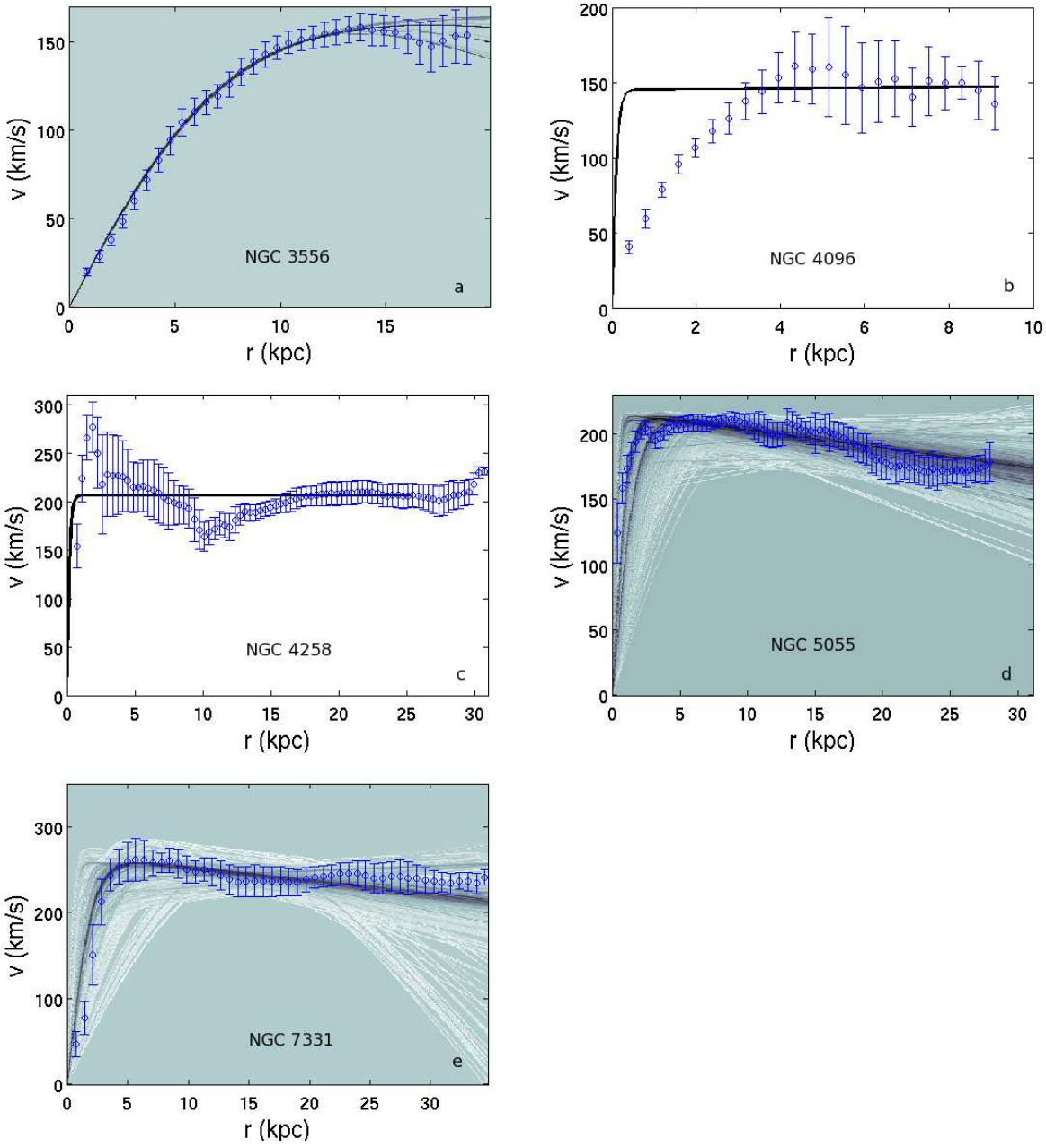

Figure 5.2: See caption of Figure 5.1. Galaxies NGC 4096 and NGC 4258 only have one solution each.

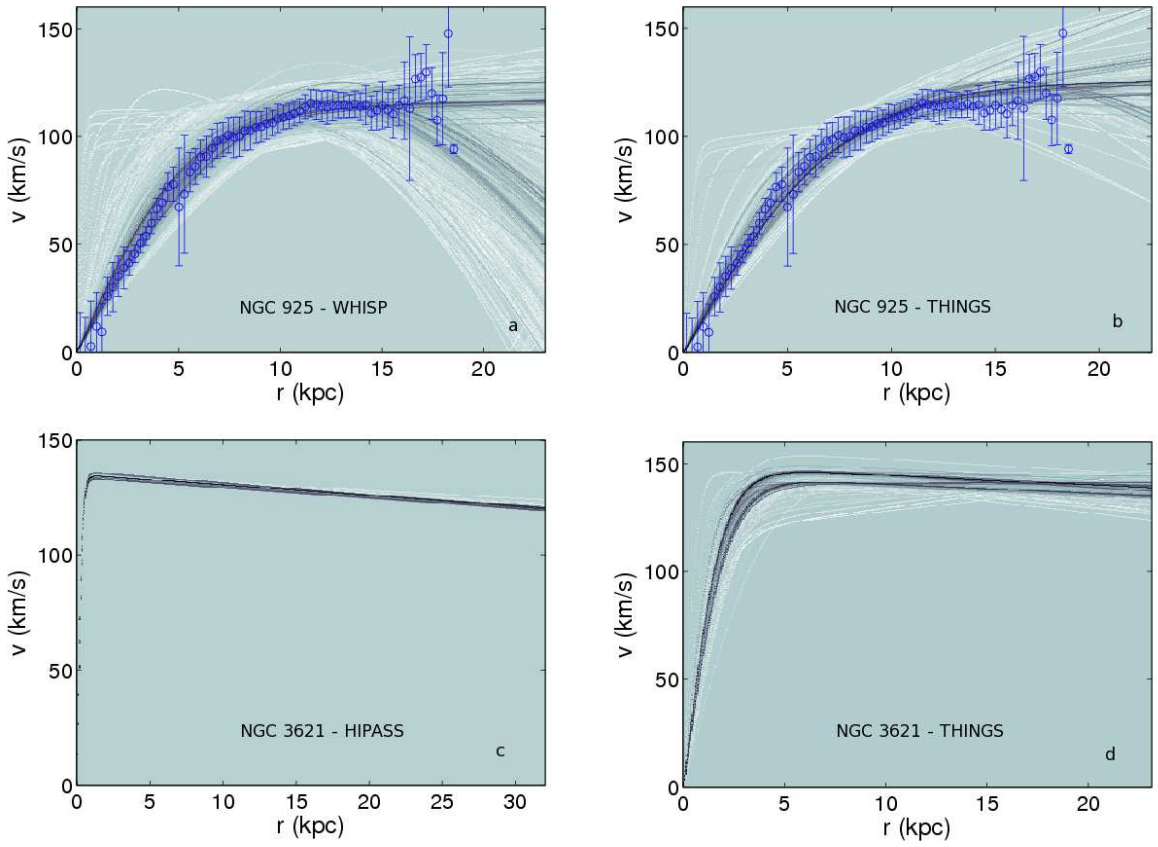

Figure 5.3: Rotation curves from GalAPAGOS runs performed on galaxies from different data cubes.

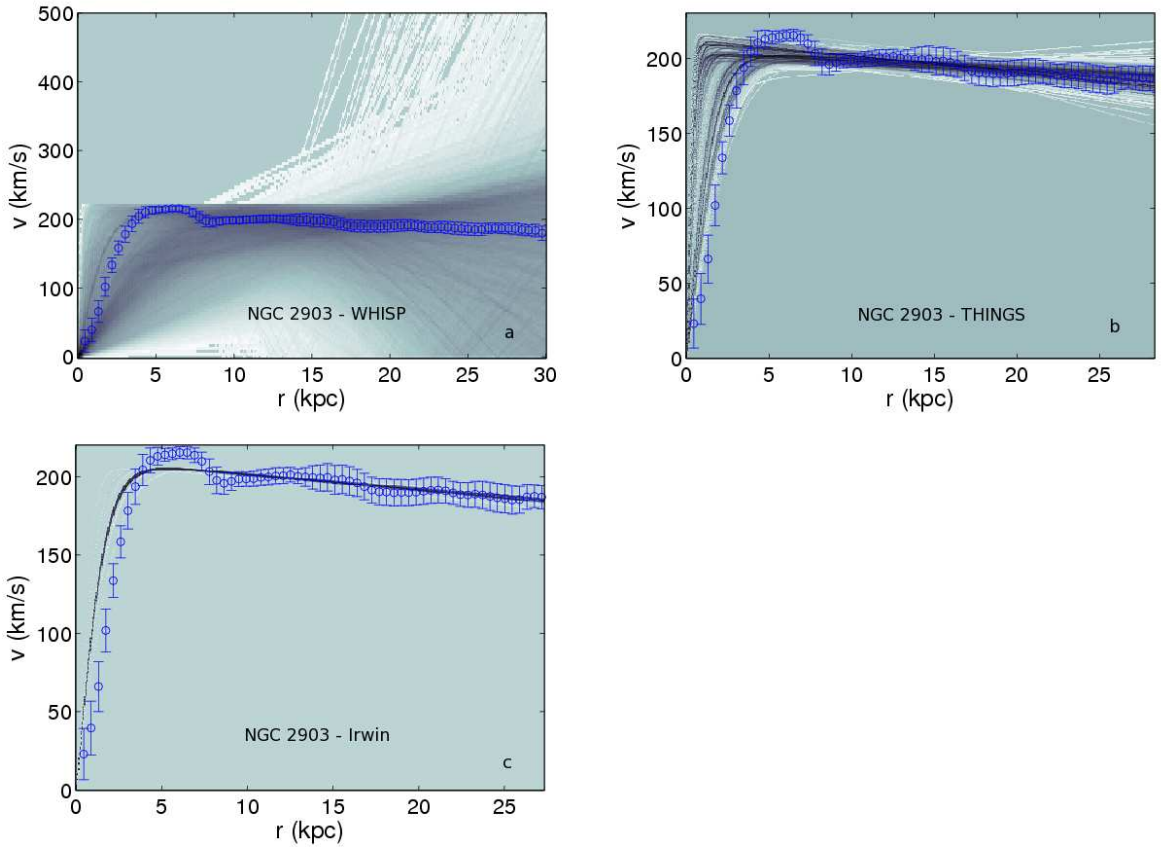

Figure 5.4: Rotation curves from GalAPAGOS runs performed on galaxies from different data cubes.

both panels. The GIPSY RCs and the GalAPAGOS model RCs are similar apart from the longer r_{out} found by GalAPAGOS in both cases.

The lowest χ^2 parameter results are similar for both runs for all parameters except the spin temperature T_s. Table 5.6 lists the kinematic parameters for the best χ^2 solutions for the two runs. Both GalAPAGOS results seem to favour a flat outer slope with a slope parameter a_v close to 0.

parameter	**THINGS**	**WHISP**
outer radius r_{out} [″]	500 (19)	510 (17)
max velocity v_0 [km/s]	126 (9)	125 (4)
outer slope a_v [ ]	0.02 (0.29)	-0.01 (0.40)
turnover radius $r_{0,v}$ [″]	169 (3)	171 (5)

Table 5.6: Kinematic parameters for NGC 925 using two different data cubes.

NGC 2403 (i=62°)

Figure 5.1, panel a. This THINGS cube was binned to a resolution of 30″/pixel (i.e. 0.5 kpc/pixel) before the GalAPAGOS run.

As mentioned above, at the intermediate inclination of ∼60°, the tilted ring rotation curve from GIPSY is expected to be reliable. This makes NGC 2403 a good comparison galaxy for the GalAPAGOS results. Indeed, the lowest χ^2 RC shape follows the GIPSY RC well (the lowest χ^2 solution is hidden in the figure by the GIPSY RC), with regards to turnover radius and rotational velocity. There is a somewhat higher slope increase for the GalAPAGOS solution (13%) than that of GIPSY (5%, not including the anomalous velocities between 18 and 20 kpc). However, there are also many GalAPAGOS RCs that seem to favour an increasing slope in the outer parts (beyond 13 kpc), while the GIPSY RC shows tendencies towards a flattening RC.

There is a large number of solutions in the family which favour a shorter turnover radius than the lowest χ^2-solution. A discussion of why the inner region of the models

are not well constrained for some of the galaxies is included below in § 5.2.2. In the case of NGC 2403, there might be a connection between the short turnover radii and the increasing slopes, while the lowest χ^2 solutions show results more similar to the GIPSY RC (longer turnover radii and flatter slopes).

NGC 2613 (i=80°)

Figure 5.1, panel b. The cube was binned by a factor of 3 to a resolution of 9″/pixel. Due to its late addition to the sample, a GIPSY RC has not been derived. However, the rotation curve derived by Chaves & Irwin (2001) agrees very well for all kinematic parameters (outer radius, maximum velocity, turnover radius and slope). The GalAPAGOS RC has a decline of 12% from flat. Other observable parameters also show an excellent agreement with those modelled by Irwin & Chaves (2003) using CUBIT and in databases. These include inclination, position angle, systemic velocity and maximum rotational velocity. This galaxy is included out of interest to show how well GalAPAGOS RCs can compare with RCs in the literature.

NGC 2841 (i=73°)

Figure 5.1, panel c. The cube was binned by a factor of 15 to 22.″5/pixel and in velocity by a factor of 2, giving 10.5 km/s/channel. A large number of its solutions feature a short turnover radius, and similar to NGC 2403, the outer GIPSY RC initially declines and then increases. However, this increase comes from an area of faint gas in outer region in the northern part, which likely has anomalous velocities. Indeed, de Blok et al. (2008) truncate the disk of this galaxy at a radius of 46 kpc, i.e. just before our GIPSY rotation curve changes its direction. The GalAPAGOS RC has a decline of 19%. The GIPSY RC declines by 15% out to 40 kpc, but the curve flattens out in the (warped) faint region beyond this radius and the decline is 10% at r_{out}.

When visually comparing the modelled cube channel by channel with that of the original input datacube, one can see that the GalAPAGOS model provides a beautiful fit to the warp in the outer edge of the galaxy.

NGC 2903 (i=62°)

Figure 5.4, all panels. This is the only galaxy for which we have three different data cubes. Of these, the WHISP cube with the lowest S/N is also the one which is hardest for GalAPAGOS to constrain, which can be seen in the large range of solutions within the optimal solutions set. Nevertheless, its lowest χ^2 solution is similar to those of the other cubes. The geometric and kinematic parameters (see Table 5.7) are also comparable. The THINGS and Irwin cubes are both observed with the VLA, albeit in different configurations (resulting in a better resolution for the THINGS cube). The results are similar, with one exception: the THINGS results exhibit the smaller turnover radius as was also seen for NGC 2841.

Since the cube only has four pixels across the inner region, it is not well enough sampled for the GalAPAGOS run. Therefore we choose to use the GalAPAGOS model derived from the less binned Irwin cube in the analysis in the remainder of this thesis.

All three GalAPAGOS RCs show a decline between 11% and 14%, consistent with that of the GIPSY RC, if the higher velocities of the 'hump' after the turnover radius are not taken into account. The decline would be more substantial if the hump is included in the change in velocity, but the hump seems to be a local anomaly (possibly connected to the bar of the galaxy) and is not consistent with the behaviour of the outer slope. Both the THINGS and the WHISP data were binned to the same pixel resolution of 30″/pixel before the GalAPAGOS runs, and the donated (reduced by J. Irwin) VLA cube (which provided the best results of the three) was binned to 8″ per pixel. Implications of different resolutions are discussed in § 5.2.2.

parameter	THINGS	WHISP	other (VLA)
outer radius r_{out} [″]	657 (23)	700 (230)	633 (8.5)
max velocity v_0 [km/s]	211 (4)	208 (191)	206 (0.4)
outer slope a_v [ ]	-0.15 (0.03)	-0.18 (0.60)	-0.13 (0.0)
turnover radius $r_{0,v}$ [″]	8.9 (0.7)	42 (78)	40 (0.0)

Table 5.7: GalAPAGOS kinematic parameters for NGC 2903 using three different data cubes.

NGC 3198 (i=72°)

Figure 5.1, panel d. The GalAPAGOS and GIPSY RCs visually agree well, and observable parameters are also in agreement with differences less than 5%. The galaxy exibits a flat RC, with a minor 4.5% difference in velocity at the outer radius. The data cube was binned to a spatial resolution of 22.″5/pixel, corresponding to 1.5 kpc/pixel, with five pixels spanning the inner radius (centre to turnover). This demonstrates that it is possible to find an excellent RC agreement even though it is only sampled by five pixels across the inner region.

NGC 3351 (i=41°)

Figure 5.1, panel e. Although this galaxy is not highly inclined (the inclination is just above the inclination limit of 40° we found in the GalAPAGOS tests), we included it here to increase the size of the sample and confirm results of the artifical data tests in Chapter 4.

The cube was binned to 19.″5/pixel before the GalAPAGOS run. The low inclination of this galaxy provides a challenge for GalAPAGOS, which is evident on the solution set, and the standard deviation for each parameter which is very large. Nevertheless, the lowest χ^2 model shows a good agreement with observable parameters (see Table 5.4), and the kinematic parameters provide a plausible RC in the outer region. An exception is the turnover radius, which, similar to NGC 2841, is shorter than that of the corresponding

GIPSY RC (see discussion later in this section).

The outer slope declines with 13% (GIPSY RC) to 14% (GalAPAGOS RC) until it, again similar to NGC 2841, starts to increase at 15 kpc radius. This shows that models at the lower inclination limit of 40° can be modelled, albeit yielding large uncertainties for the kinematic parameters.

NGC 3521 (i=71°)

Figure 5.1, panel f. Despite plausible results for all parameters, including close correspondence with observable parameters, this is another example of a galaxy RC featuring a shorter turnover radius than expected. The cube was binned to a pixel resolution of 15″/pixel. The resulting RC shows a declining outer slope of -21% from the turnover velocity, for both the GIPSY and the GalAPAGOS RCs. There is however a slight flattening of the GIPSY RC at the outermost radii (20 kpc and beyond), but no increase such as the one found by de Blok et al. (2008). Thus, further investigation is necessary before unequivacally labeling this galaxy as declining.

NGC 3556 (i=76°)

Figure 5.2, panel a. This cube was binned to 12″/pixel. The GalAPAGOS RC is well constrained in the inner region and has plausible model parameters. The lowest χ^2 solution has a slope that follows that of the GIPSY RC, excluding the flattening beyond 17 kpc. The velocity behaviour beyond that radius is due to a cloud in the southeast corner of the galaxy with higher velocity, which is not included in the GalAPAGOS model. It is hard to conclusively determine the outer slope, due to its large turnover radius and the small extent of the galaxy detected beyond the turnover. Thus, even though the model has a large negative a_v value (Table 5.1), the decline is not more than 5% at 17 kpc radius, or 9% at the outer radius in the GalAPAGOS model.

NGC 3621 (i=66°)

Figure 5.3, panels c and d. This galaxy is interacting, shown in its moderately distorted HI distribution. The reason it is included in our analysis is to compare the use of low resolution data from HIPASS with high resolution data from THINGS. NGC 3621 is not used elsewhere in this thesis. The results for the THINGS cube (binned to a 22.″5/pixel) show a fair comparison with the velocity parameters in Table 5.4. GalAPAGOS incorporates a warp to account for the distorted morphology and this warp is the cause of the anomalous discrepancy (Table 5.4) in the position angle and inclination values, parameters that usually are easy to constrain. Also the scale height H is unrealistically high for this galaxy, possibly another result of the asymmetric HI distribution.

The solution from the HIPASS data exhibits a short turnover radius, which likely is the result of the resolution being too low to show the kinematic behaviour in the inner part of the disk. Indeed the extent of the HIPASS galaxy is characterised by only 4 beams across, which also gives a large uncertainty to the outer radius parameter. Velocity parameters such as systemic velocity and maximum rotational velocity are however well constrained and match the THINGS results and tabulated values to within 7%.

NGC 4096 (i=76°)

Figure 5.2, panel b. This data cube from the WHISP survey, as well as NGC 4258, has a low sensitivity and it proved to be very challenging for GalAPAGOS to converge on plausible solutions. Therefore, instead of finding a family of solutions, we set GalAPAGOS to search for a single best solution. The data was not binned due to the small angular size, so the pixel resolution remains at 5″/pixel. Similar to NGC 3621, the GalAPAGOS solution has incorporated a strong warp which accounts for what is normally seen as a larger position angle, which explains the differences listed in Table 5.4. Note that the

high inclination of this galaxy also provides a challenge for the GIPSY method, and quite possibly neither rotation curve is to be fully trusted. The short turnover radius of the GalAPAGOS RC is an enigma since the inner radius is well spanned by ∼18 pixels and 6 beams.

NGC 4258 (i=69°)

Figure 5.2, panel c. As for NGC 4096, GalAPAGOS was set to search for a single best solution. The cube was binned to 15″/pixel. There is nothing abnormal with the parameters for this solution. The short turnover radius here is plausible in comparison with the GIPSY RC. The GalAPAGOS RC is an average of the rotational behaviour of the galaxy along its radius, as expected, yielding a flat slope. The main noticeable difference is that GalAPAGOS truncates the HI disk at a shorter radius (25 kpc) than GIPSY (30 kpc).

NGC 5055 (i=65°)

Figure 5.2, panel d. This THINGS cube was binned to 30″/pixel. The GalAPAGOS solution set features some interesting solutions that are seemingly divided up in three groups of RCs. The lowest χ^2 solution is included in the group with shortest turnover radius, although the other two groups include solutions of very similar χ^2 values. Comparing these to the tilted ring RC, the groups harbouring longer turnover radius seem more probable, and indeed the tilted ring RC is considered credible at this inclination (∼60°). For this reason we have chosen to use one of the solutions from the centre group of solutions for future analysis in this thesis. The GalAPAGOS RC shows a decline of 20% and the GIPSY RC of 16%, making NGC 5055 another candidate in the group of galaxies with declining RC. However, we note that the GIPSY RC flattens out in the faint region close to r_{out}, similar to NGC 2841 and NGC 3521.

NGC 7331 (i=76°)

Figure 5.2, panel e. This is another "spot on" galaxy, for which the parameters in Table 5.4 and the RCs from both methods agree very well, especially at inner radii. There is a slight difference in the slope at outer radii – is the curve flattening out as the tilted ring RC suggests, or is the GalAPAGOS favoured decline a real decline? Both RCs decline with ∼10% (9% for the GIPSY RC and 12% for the GalAPAGOS RC), and this galaxy is thus a border line case.

5.2.2 Discussion and summary of assessing GalAPAGOS models

Out of the 14 galaxies presented here, at least five have solutions favouring a short turnover radius (followed by a sharp turnover), different to what is expected by comparison with rotation curves derived using the tilted ring method in GIPSY. It is appropriate to keep in mind that there are limitations to the tilted ring method as well, especially for higher inclinations where the line-of-sight crosses a large range of velocities and it becomes difficult to find the actual rotation velocity at a certain radius. Thus, we should not accept these RCs as indisputable. However, intermediate inclinations around 60 degrees are generally considered reliable as has been noted for NGC 2403 and NGC 5055, two galaxies for which the lowest χ^2 solution shows good likeness with the tilted ring solution.

Since the inclinations for the "problematic" galaxies lie in a range spanning 45° to 71° (disregarding NGC 4096 for which the solution overall seems questionable), it does not appear that their GalAPAGOS RCs are affected by inclination.

The galaxies in question all have in common a high rotational velocity (larger than 200 km/s) in combination with a declining slope at outer radii, and a short GIPSY turnover radius. This is, however, also true for NGC 2613 and NGC 7331, which do not display short GalAPAGOS turnover radii. That is, a declining slope and a large velocity amplitude

do not predict a short and sharp turnover. In the case of NGC 3351, its low inclination may very well be the reason for greater uncertainty for the turnover radius as well as the other parameters, as has been described. It does indeed have many solutions with a much higher turnover radius as well, unlike NGC 3521, for which all solutions generate short turnover radii.

As is the case for the HIPASS galaxy NGC 3621, we suspect that a lack of resolution in the inner regions might be the culprit. Although the THINGS galaxies in particular have an excellent beam resolution, we notice that the short (GIPSY) turnover radius for some galaxies will only be spanned by a few pixels due to the unfortunate necessity of binning the data cubes so that GalAPAGOS runs in a reasonable amount of time. The estimated GIPSY turnover radii for each galaxy and the resulting number of pixels covering these radii are listed in Table 5.8. As well, we list the number of beams covering the turnover radius for each galaxy (see Chapter 2 for beam sizes). This shows that while the beam size is not so much of an issue for GalAPAGOS (c.f. NGC 2613 and NGC 2903 from Irwin), it is necessary to ascertain that the distance from the galaxy's centre to the turnover radius is spanned by *at least* 5 pixels in order to capture the characteristics of the inner region. Note that the GIPSY RCs are derived from non-binned data, so we feel inclined to trust their turnover radii.

Apart from the issue of short turnover radii for a few galaxies, the GalAPAGOS models seem to be consistent with expectations in all other aspects. The scale height H is 500 pc for the Milky Way galaxy (Dickey & Lockman, 1990), and so we expect H to be of the same order for these galaxies as well. This is true for all cases with the exception of NGC 3621 (the interacting galaxy). NGC 2841 also has a larger H, the reason for which is uncertain.

Additionally, the 1D velocity dispersion v_σ have plausible values, between 10 and 20 km/s, which is consistent with the order of magnitude found in the literature.

Galaxy	**GIPSY turnover** [″]	**# beams**	**# pixels**
NGC 925 (W)	170	12	6
NGC 925 (T)	170	28	6
NGC 2403 (T)	324	41	11
NGC 2613 (I)	56	1.4	6
NGC 2841 (T)	88	8	4
NGC 2903 (I)	116	2	14
NGC 2903 (T)	116	8	4
NGC 2903 (W)	116	7	4
NGC 3198 (T)	120	11	5
NGC 3351 (T)	55	7	3
NGC 3521 (T)	49	4	3
NGC 3556 (I)	178	9	15
NGC 3621 (T)	126	10	6
NGC 4096 (W)	91	6	18
NGC 4258 (W)	53	4	4
NGC 5055 (T)	72	8	2
NGC 7331 (T)	67	11	4

Table 5.8: Estimated turnover radius based on the GIPSY rotation curve, and the number of beam elements and pixels that cover this region in the binned data cubes used for GalAPAGOS runs. Galaxies in boldface denote galaxies for which a large part of the GalAPAGOS solutions include rotation curves with unexpectedly short turnover radii. (W), (T), and (I) denote data cubes from WHISP, THINGS, and Irwin, respectively.

Three candidates for declining rotation curves are found; NGC 2841, NGC 3521 and NGC 5055.

With the exception of the spin temperature, the parameter results are comparable to the tests performed in Chapter 4 with regards to the ability to retrieve parameters, and there are no inconsistencies in the results. Inclination effects (i.e. how the parameters vary with inclination) are, however, not possible to perceive, as the inclination range for the data cubes only covers a small region of the range used in the tests.

When visually examining the model cube found by GalAPAGOS and comparing it to the input data, the model follows the disk but misses anomalies present in the data that will affect the (GIPSY) RC (if including the outer radii when measuring the RC).

Less successful GalAPAGOS results are found when using low sensitivity cubes (NGC 4096 from WHISP) or low resolution data cubes. One example was investigated in this chapter; NGC 3621 from the HIPASS survey (see § 5.2.1). Other HIPASS galaxies were also tested, such as NGC 7793's HIPASS dataset which was compared to its THINGS dataset. The HIPASS resolution was however too low to give any constrained results. One of the HIPASS cubes, NGC 55 (an SBm galaxy, not presented in this thesis) with a larger angular size and consequently better resolution, is an exception. Its GalAPAGOS model is an excellent fit to observable parameters and published HI rotation curve. Thus we conclude that GalAPAGOS requires a beam resolution greater than 4 beams across the disk, such as is the case for the NGC 55 cube. In the remaining analysis, HIPASS galaxies will not be used due to this limitation.

In summary, comparison with GIPSY RCs demonstrate that the best χ^2 solutions from GalAPAGOS reasonably trace the region beyond the turnover radius and are less perturbed by anomalies. The quality of the models are less affected by the original data resolution and more by binning of the data required to run the code in a reasonable amount of time, which affects the inner regions of the RC. Additionally, the current models produced

by GalAPAGOS deliver reasonable values for physical parameters (such as scale height, inclination, velocity dispersion etc.) and are revealing about the outer disk and, therefore, can be used to calculate the DM content. There is a risk that short turnover radii are over-emphasized in a few families of solutions. However, comparison between GalAPAGOS and GIPSY modelling programs demonstrates that galaxies with large turnover radius will not be assessed as having short turnover radius by GalAPAGOS. Therefore the current model parametrisation and results are adequate for the continued analysis in this thesis.

5.3 Mass models

The second part of this chapter presents the mass models of 11 galaxies. For these, a predefined halo model is chosen and tested in combination with the other galaxy components (gas, stars in bulge and disk) to add up to the observed kinematic rotation curve derived from the HI data, following Equation 3.1. There are a number of physically motivated theoretical halo models to choose from. For example the isothermal sphere model and the Navarro Frenck and White model (Navarro et al., 1996), which is based on simulation. (See more discussion in § 3.5.)

Here we choose to concentrate on the isothermal sphere, which is the model that we find most often provides a good fit to the observed kinematic rotation curve behaviour. We base the choice on the need for consistancy: since the goal is not to assess which halo type fits a mass model better, but to derive halo parameters that are comparable, we need one halo type to consistently assess the characteristics of the halo for each galaxy. The results can also be compared to results in the literature, in which most investigations include the isothermal halo model.

5.3.1 Stellar mass-to-luminosity ratios

The largest margin of error comes from the wide range in mass-to-light ratio, M/L, that can be used to fit the stellar component of the mass model.

The widest limits on the stellar M/L are usually in between the so-called *maximum disk* and *minimum disk* fits. We adopt the definition of maximum disk to be when the stellar matter supplies 85%±10% of the total velocity at a radius of 2.2 times the disk scale length R_d (Sackett, 1997). (Another approach would be to use the sub-maximal disk (see § 3.1), however, we wanted to explore a wide range of possible M/L values.)

The minimum disk is adopted to be the situation in which the stellar component is reduced to a minimum while it is still possible to obtain a good fit to the rotation curve (Swaters, 1999). The "best fit" will be located anywhere in between these extremes. The "best fit" refers to the case when the mass model fitting algorithm is allowed to vary the stellar M/L for the bulge and disk in order to find stellar M/L values that provide the smallest difference between the total (modelled) RC and the observed HI RC in a χ^2 minimization process.

There are ways of narrowing the range of the stellar M/L, using stellar synthesis population models. This has not been done in this thesis, but the literature indicates that there is a correlation between M/L and galaxy morphology. The reason is that the stellar population differs for different Hubble types: Early-type galaxies (S0, Sa) have large bulges, and consist of older stars, which means that there are fewer high mass stars. Since the bulk of the stellar mass generally comes from low-luminosity, low-mass stars (which live longer), while the luminosity comes from bright high-mass stars (which live shorter), the mass in early type galaxies is represented by fainter luminosities. This means S0 and Sa galaxies have higher M/L values. In contrast, later type galaxies (Sc, Sd) have more star formation, and thus more high luminosity stars, so there is more light emitted

by less mass, or in other words a lower M/L value.

Portinari et al. (2003) present I-band stellar M/L values based on the present and past star formation rate in a galaxy (a relationship shown by Kennicutt et al., 1994) in combination with the initial mass function, which in its turn is correlated with morphological galaxy type. Using their Figures 1 and 2, we adopt the M/L correlation with Hubble type listed in Table 5.9. These values are based on a Salpeter initial mass function[3] (Bell and De Jong 2001), and hereafter in this chapter, the mass models derived with a stellar disk M/L fixed to this value, will be referred to as a "Salpeter model". The I-band is sufficiently close to the SDSS i-band that is used here, making these values appropriate in this context. Note that in the following mass models, we only apply this predicted Salpeter M/L to the disk, and let the bulge M/L be a free parameter.

Morphology	**b**	$(M/L)_I$
Sa	0.1	2.9
Sab	0.2	2.5
Sb	0.4	2.2
Sbc	0.9	1.6
Sc	1.0	1.42
Scd	1.7	1.75

Table 5.9: Hubble type with corresponding birthrate parameter $b = SFR/ < SFR >$ (the ratio between present and past average star formation rate, also called star formation history) and I-band M/L ratio for a Salpeter initial mass function. From Portinari et al. (2003).

5.3.2 Mass model fits: total M/L ratios and halo parameters

The mass model fits were constructed in the following order (see details in Chapter 3):

1. The HI rotation curve was derived using two different techniques: 1) the tilted

[3]The initial mass function (IMF) empirically describes the relation between the distribution of mass in a stellar population and the initial mass (i.e. the mass they were formed with).

ring technique utilizing the GIPSY software package, 2) using analytic GalAPAGOS models (see Chapters 3 and 4). The RCs are presented and evaluated in Section 5.2.

2. The HI data were also used to assess the contribution to the total rotation curve by the mass of the gas. The HI gas was scaled by 1.4 to account for the mass of primordial He throughout the mass model fits.

3. Photometry from near IR i-band data from SDSS was analysed to provide the stellar mass contribution to the total rotation curve.

4. A disk-bulge decomposition was performed on the stellar mass, in which the bulge was fit with a Sérsic profile and the disk with an exponential disk (see results below).

5. Rotational velocities due to the mass in each luminous constituent were calculated; HI layer, stellar disk and bulge. The bulge and disk contributions were either automatically scaled by best fit M/L ratios in the fitting procedure, or fixed (disk only) by the user to the value in Table 5.9.

6. Mass models comprised of the luminous constituents and a dark matter halo, were fit to both the GalAPAGOS and GIPSY rotation curves. The contribution from the DM halo was assessed by adding an isothermal sphere model to the sum of the luminous components and fitting all components to the kinematic RC. A "best fit" model, a model based on a Salpeter M/L, a Maximum disk model, and a Minimum disk model were tested. The "best fit" and Salpeter fit results for each of the two rotation curves are presented in Tables 5.11 and 5.12.

Disk-Bulge decomposition

The bulge-disk decomposition allows two different M/L values to occur in the stellar component of the galaxy. Without the decomposition the bulge and the disk are forced

to share a common stellar M/L value across the full extent of the disk. We fit the stellar contribution with an exponential disk (Equation 3.11) for the disk component, and a Sérsic bulge (Equation 3.9) for the bulge component using a script written by J.Fiege for the Ferret GA optimizer. Details on the disk-bulge decomposition method are given in Section 3.4.1. The parameters derived from the decomposition are listed in Table 5.10. Figures 5.5 and 5.6 display the SDSS i-band luminosity profiles and the Sérsic bulge fit and exponential disk fit for the 11 galaxies.

Galaxy	$logI_0$ $[L_\odot]$ (2)	R_d $['']$ (3)	$logI_e$ (4)	R_e (5)	n (6)	z [kpc] (7)
NGC 2403	5.5	105.8	5.8	26.7	0.52	0.33
NGC 2841	5.8	64.8	9.98	13.3	1.37	0.87
NGC 2903	6.3	59	8.98	9.97	0.92	0.51
NGC 3198	4.9	55.4	7.06	7.18	1.03	0.74
NGC 3351	6.1	45.9	9.31	8.27	0.79	0.42
NGC 3521	4.6	109.1	9.99	49.2	2.03	0.90
NGC 3556	5.2	60.4	6.08	4.28	0.67	0.68
NGC 4096	4.8	52.6	6.79	6.20	0.74	0.52
NGC 4258*	4.3	244	10.0	15.3	1.65	0.80
NGC 5055	5.0	113.5	9.49	50.0	1.87	0.79
NGC 7331	4.8	91.2	9.82	28.1	1.67	1.28

Table 5.10: Parameters derived in the disk-bulge decomposition (Equations 3.9 and 3.11). Column (2) is the logarithm of the intensity at r=0, column (3) is the exponential disk scale length, column (4) is the logarithm of the intensity at the effective radius R_e in Column (5). Column (7) is the scale height (z) of the disk (derived in the exponential disk fit), which is used in the conversion from luminosities to rotation velocities.*) The bulge and the disk parameters were fitted in two separate runs for NGC 4258 - one for the full disk to get the disk parameters, and one where the disk was only measured out to $300''$, to get a more accurate fit to the bulge.

Note that there is an artifact present at the end of the disk for many of the fitted exponential disk rotation curves, where the curve has a little flattening before the decline (this is visible in the stellar rotation curve displayed in the mass model figures, Figures 5.5 and 5.6). This is due to the truncation of the exponential disk (see a disscussion on this

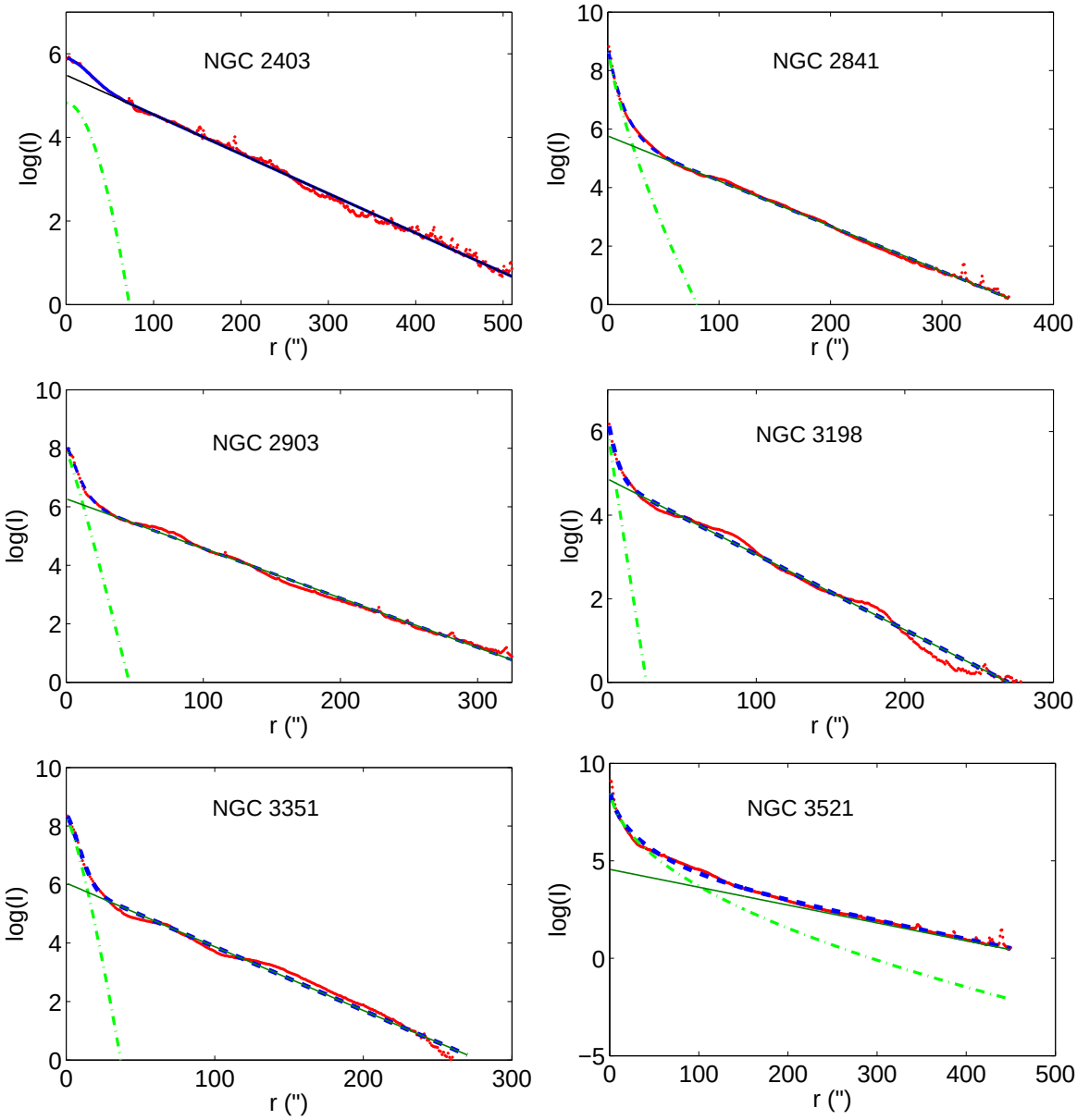

Figure 5.5: Disk-bulge decompositions for 6 of the 11 galaxies. The panels show the bulge and disk fits overlaid on the luminosity profile. Thick solid line (red) is the luminosity profile, dash dotted line (light green) is the bulge fit, solid thin line (dark green) is the disk fit and dashed blue line is the sum of the bulge and disk fit.

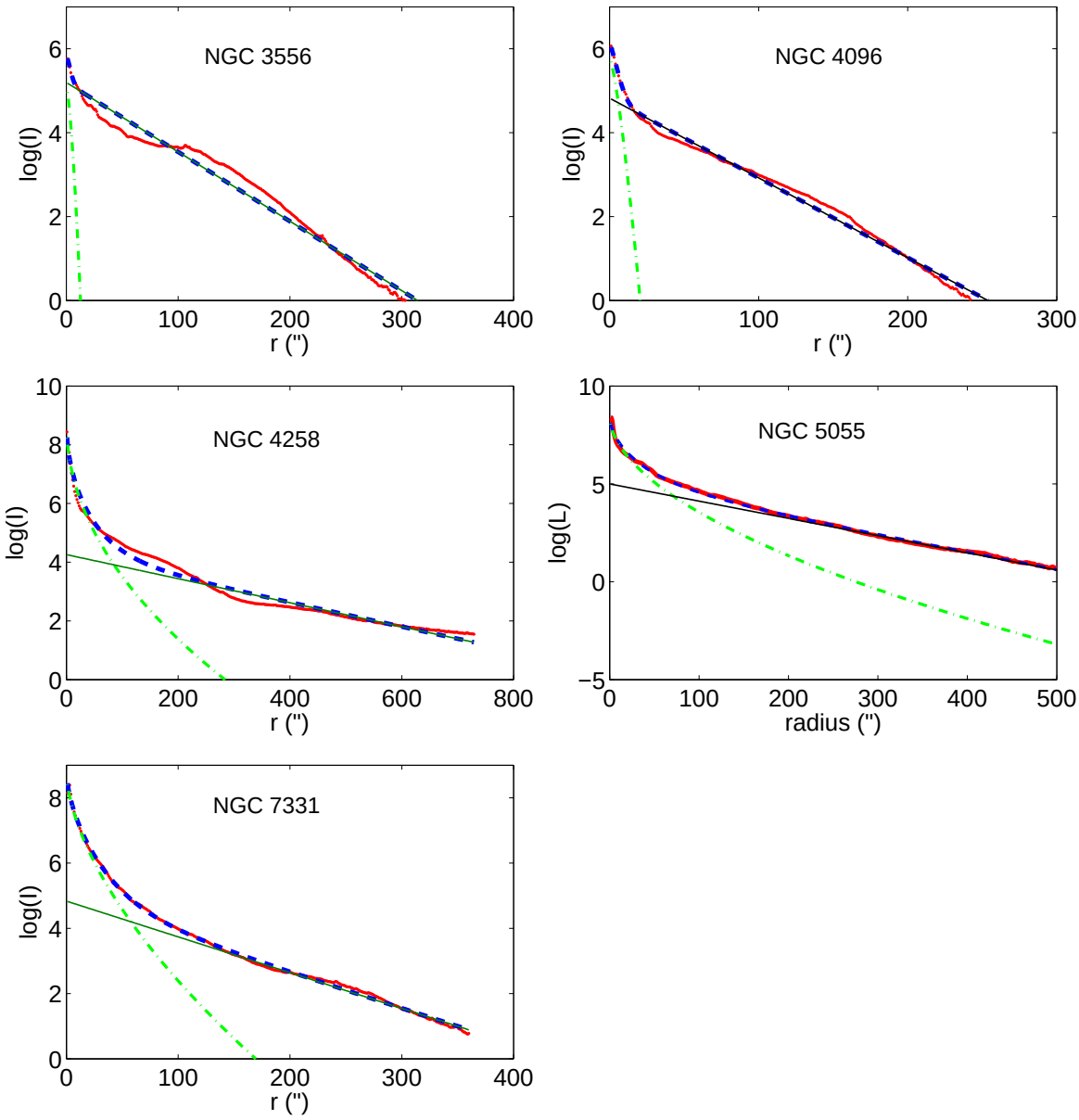

Figure 5.6: Disk-bulge decompositions cont'd for the remaining 5 galaxies. The panels show the bulge and disk fits overlaid on the luminosity profile. Thick solid line (red) is the luminosity profile, dash dotted line (light green) is the bulge fit, solid thin line (dark green) is the disk fit and dashed blue line is the sum of the bulge and disk fit.

in Casertano, 1983).

5.3.3 The mass models

For both the GIPSY and GalAPAGOS HI rotation curves, we have tested several mass models: the "best fit", maximum and minimum disk, and a fit using the Salpeter IMF predicted M/L values (see definitions in § 5.3.1).

To represent the stellar disk, we investigated two cases: the exponential fit of the disk (§ 5.3.2) and the total luminosity profile with the bulge component subtracted. Generally there was no difference in the mass model results using these two disk representations, except that in some cases the bulge-subtracted luminosity profile could explain small scale behaviour (bumps) of the rotation curve at inner radii.

The mass model results for each galaxy are presented below, including a figure consisting of:

- The HI distribution displayed in a 0th moment map (top left panel).
- The Gaussian fitted HI velocity field that was used to derive the GIPSY RC (top right panel).
- A graph of the mass model derived using a GIPSY RC (bottom left panel).
- A graph of the mass model derived using a GalAPAGOS RC (bottom right panel). This RC is the lowest χ^2 RC unless otherwise noted.

In the individual discussions, the goodness of fit of a mass model is based on the χ^2 value provided by the fitting program ROTMAS (not to be confused with the GalAPAGOS χ^2). When referring to a model as having a "best fit" in the following sections, the χ^2 value is the lowest among the models tested for each HI RC. The χ^2 value is however only used as an indication of goodness of fit for one RC at a time and have no relevance as a measure

of goodness of fit between models generated by different RCs, so we do not list the χ^2 values for the models.

The fitted stellar M/L values and isothermal halo parameters are displayed in Tables 5.11 ("best fit" i.e. free stellar M/L ratios) and 5.12 (using a Salpeter derived M/L for the stellar disk). Note that a flat rotation curve for the halo component, which can occur in cases with a small stellar contribution, is represented by very short values for the core radius and very large values for the density.

NGC 2403

Figure 5.7 shows the HI distribution and velocity field of NGC 2403, a well studied relatively nearby Scd galaxy, as well as the two mass models fitted to the two differently derived rotation curves. The GalAPAGOS RC is derived from the lowest χ^2 result in the GalAPAGOS run using THINGS HI data. The THINGS data were also used to derive the GIPSY RC, following the procedure outlined in Chapter 3. The rotation curve derivation was straightforward, aided by its intermediate inclination of 62 degrees and symmetric behaviour. The SDSS i-band data had a large amount of foreground star contamination which were carefully removed so as to not contaminate the surface brightness distribution measurement. The stellar emission was traced out to $510''$(7.9 kpc), which is approximately 40% of the HI disk.

The "best fit" to the GalAPAGOS RC produces an unphysical negative bulge. Instead, we set a maximum bulge contribution to find the bulge M/L in the model, while letting the software optimize the remaining parameters for the disk M/L and the halo.

The modelling of NGC 2403 demonstrates that there is a large range of plausible M/L values for this galaxy. While both the maximum disk and Salpeter models are very close to the "best fit" model, it is also possible to fit a plausible minimum disk model to the RCs.

Galaxy	**RC**	Free stellar M/L				$\sim$
		$(M/L)_B$	$(M/L)_D$	R_C	ρ	
	(2)	(3)	(4)	(5)	(6)	(7)
NGC 2403	Gip	7.4	1.4	2.4 ± 0.6	60 ± 26	max/sal
	Gal	4.0	1.0	1.7 ± 0.2	110 ± 26	max/sal
NGC 2841	Gip	1.3	7.5	35 ± 3.4	2.4 ± 0.2	max
	Gal	3.8	2.2	0.5 ± 0.1	5000 ± 2500	
NGC 2903	Gip	0.04	2.9	8.4 ± 1.1	10 ± 2	max
	Gal	0.6	3.2	13 ± 0.9	5.3 ± 0.4	max
NGC 3198	Gip	1.1	4.0	9.6 ± 1.2	32 ± 2.2	max
	Gal	1.0	2.7	3.6 ± 0.3	27 ± 4.3	max
NGC 3351	Gip	0.4	1.5	0.3 ± 1	6700 ± 46000	
	Gal	5.2	3.2	8.3 ± 0.6	10 ± 0.9	
NGC 3521	Gip	2.8	6.9	0.7 ± 3.9	340 ± 3600	max
	Gal	5.6	1.9	6 ± 2.2	15 ± 9.9	
NGC 3556	Gip		0.7	8.5 ± 1.3	13 ± 2.8	min
	Gal		0.25	4.1 ± 0.4	33 ± 7	
NGC 4096*	Gip		1.2	1.2 ± 0.1	330 ± 75	sal
	Gal	37	1.5	0.6 ± 0.04	790 ± 92	
NGC 4258	Gip	12	0.7	8.4 ± 2.3	16 ± 8	min
	Gal	5.3	0.3	0.7 ± 0.03	1500 ± 100	
NGC 5055	Gip	4.2	3.8	6.7 ± 7.9	8.1 ± 16.8	
	Gal	3.8	4.6	16 ± 2.8	2.6 ± 0.5	
NGC 7331	Gip	0.4	0.3	1.1 ± 2	860 ± 3160	min
	Gal	3.1	1.4	2.6 ± 0.2	99 ± 12	

Table 5.11: Mass model and halo results for the isothermal sphere halo for "best fit" models. That is, the stellar (disk and bulge) M/L are left as free parameters in the fit. In some cases (noted in the text for the individual galaxy) the bulge M/L is constrained to provide a plausible result when the inner rotation curve ($r < r_{0,v}$) is poorly defined. The naming convention "Gip" and "Gal" in in Column (2) refer to use of GIPSY and GalAPAGOS RCs respectively. Column (3) is the Bulge M/L, (4) is the disk M/L, (5) is the halo core radius in units of kpc, and (6) is the halo density in units of $10^{-3} M_{\odot}/pc^3$. Column (7) lists which other model this "best fit" model is similar to, where max, min, and sal denote the maximum, minimum and Salpeter models. *) NGC 4096 has unreliable rotation curves, an unrealistic bulge M/L, and will not be used in subsequent analysis in this thesis. Unrealistic halo value parameters are considered in the following individual galaxy discussions.

		Salpeter M/L_D				
Galaxy	**RC**	$(M/L)_B$	$(M/L)_D$	R_C	ρ	$\sim$
NGC 2403	Gip	6.7	1.75	3.0 ± 0.1	38.8 ± 1.5	max, BF
	Gal		1.75	2.6 ± 0.04	50.4 ± 1.2	
NGC 2841	Gip	0.02	2.2	0.67 ± 0.09	3064 ± 800	
	Gal	3.8	2.2	0.5 ± 0.1	4991 ± 2450	
NGC 2903	Gip	0.02	1.6	1.3 ± 0.1	331 ± 58	min
	Gal	0.06	1.6	-0.7 ± 0.01	1000 ± 39	
NGC 3198	Gip	0.1	1.42	1.8 ± 0.1	120 ± 13	min
	Gal	0.03	1.42	2.0 ± 0.03	101 ± 3	min
NGC 3351	Gip	0.4	2.2	0.3 ± 1	5140 ± 34500	BF
	Gal	4.6	2.2	1.3 ± 0.05	245 ± 17	
NGC 3521	Gip	2.6	1.6	0.8 ± 1.2	838 ± 2545	min
	Gal	5.6	1.6	5.5 ± 0.3	17.7 ± 1.6	
NGC 3556	Gip		1.75	29 ± 55	4.0 ± 1.7	
	Gal		1.75	16 ± 2	4.9 ± 0.3	max
NGC 4096	Gip		1.75	1.3 ± 0.1	271 ± 30	BF
	Gal	11.3	1.75	0.04 ± 0.001	160000 ± 10000	
NGC 4258	Gip	11.2	1.6	13.3 ± 1.7	7.0 ± 1.2	
	Gal	6.2	1.6	1 ± 0.1	517 ± 56	
NGC 5055	Gip	3.9	1.6	1.4 ± 0.7	224 ± 215	min
	Gal	2.8	1.6	0.7 ± 0.2	926 ± 435	
NGC 7331	Gip	0.2	1.6	1.1 ± 2.3	760 ± 3100	
	Gal	1.9	1.6	1.0 ± 0.3	704 ± 460	BF

Table 5.12: Mass model and halo results for the isothermal sphere halo, using a disk M/L constrained to a value derived from the Salpeter IMF dependent on morphological type of the galaxy. The naming convention "Gip" and "Gal" in in Column (2) refer to use of GIPSY and GalAPAGOS RCs respectively. Column (3) is the Bulge M/L, (4) is the disk M/L, (5) is the halo core radius in units of kpc, and (6) is the halo density in units of $10^{-3} M_{\odot}/pc^3$.Column (7) lists which other model this "best fit" model is similar to, where max, min, and BF denote the maximum, minimum and "best fit" models. Unrealistic halo value parameters are considered in the following individual galaxy discussions.

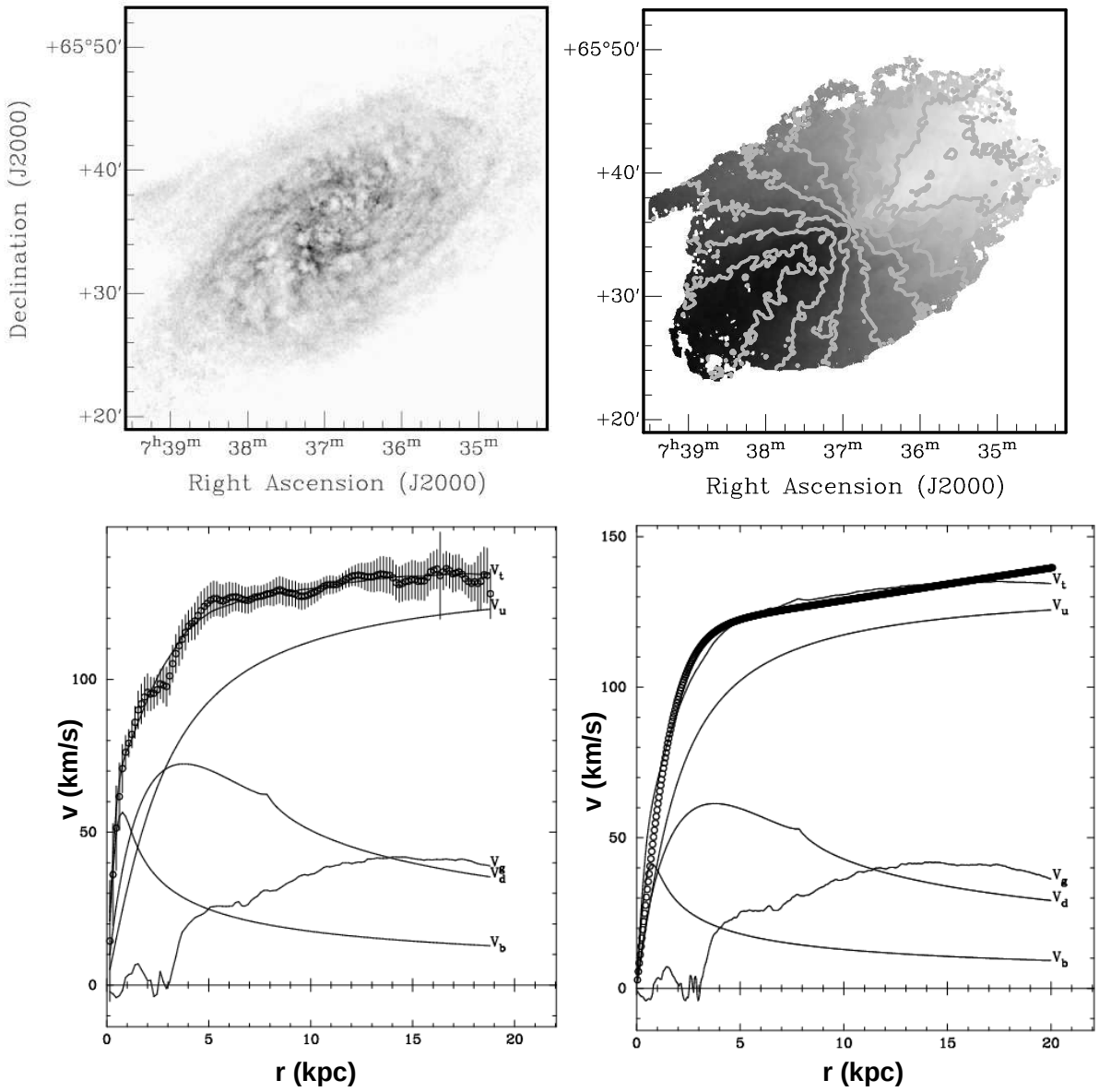

Figure 5.7: NGC 2403, Top left: The HI density distribution shown in a zeroth moment map (see Chapter 3). Top right: The velocity field with isovelocity curves overlaid ("spider diagram"). Bottom left: "best fit" mass model using the tilted ring (GIPSY) rotation curve. Bottom right: "best fit + maximum bulge" mass model using one (the lowest χ^2) of the GalAPAGOS rotation curves. v_g, v_d, v_b refer to the rotation curve contributions from the gas (HI+He), the disk and the bulge respectively. v_u refers to the user-supplied halo model, here the isothermal sphere, and v_t is the total fitted rotation curve, consisting of the individual components added together following Equation 3.1.

NGC 2841

NGC 2841 is a highly inclined Sb galaxy with a strong warp. For the GIPSY derivation of its rotation curve, the position angle was only fixed out to a radius of 300″, and beyond that it was let free, allowing the PA increase to follow the warp. The major difference between the GIPSY and GalAPAGOS RCs is that the latter exhibits a shorter turnover radius (see § 5.2.1 earlier in this chapter).

The best fit mass models require the inclusion of the bulge component. Figure 5.8 shows the "best fit" models for both rotation curves. For the GIPSY RC, this is the maximum disk fit. However, the bulge M/L (which should be higher than the disk M/L due to its older stellar population) is unphysically low. This could potentially be due to too much luminosity being assigned to the bulge in the bulge/disk decomposition, but we do not believe that to be the case (see Figure 5.5). Additionally, there is no bar that could be the cause of such a scenario. Another option is that a too small bulge contribution (i.e. scaled with a too low M/L) is being fit in the mass model. This could be caused by the lack of rotational information in the centre, due to the depletion of HI in that region.

Additionally, it is hard to match the minimum disk, and the Salpeter models to the HI RC, regardless of the size of the bulge contribution.

NGC 2841 is one of three galaxies for which the GalAPAGOS RC suffers a too short turnover radius (the other two are NGC 3521 and NGC 3351), which leads to an incorrect fit of the bulge component. This is likely the cause of the unrealistically large central density halo parameter. Therefore we choose to use the GIPSY RC mass model for this galaxy, despite the M/L issue.

Note that we could have chosen another model from the solution set (as was done for NGC 5055). This will be done for future publications (combined with new GalAPAGOS runs with increased pixel resolution).

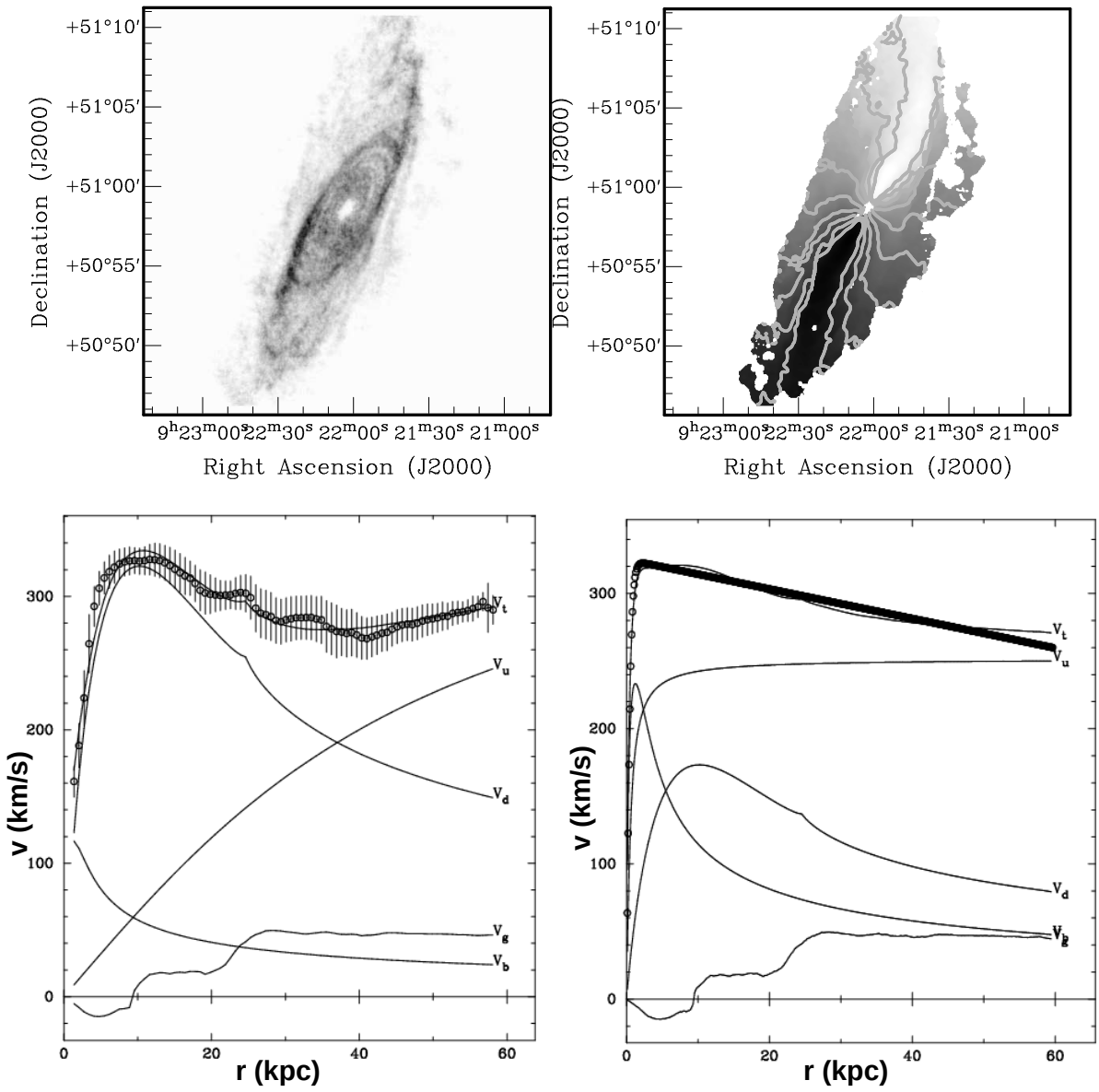

Figure 5.8: NGC 2841. Top left: The HI density distribution shown in a zeroth moment map (see Chapter 3). Top right: The velocity field with isovelocity curves overlaid ("spider diagram"). Bottom left: "best fit" mass model using the tilted ring (GIPSY) rotation curve. Bottom right: "best fit" mass model using one (the lowest χ^2) of the GalAPAGOS rotation curves. v_g, v_d, v_b refer to the rotation curve contributions from the gas (HI+He), the disk and the bulge respectively. v_u refers to the user-supplied halo model, in this case the isothermal sphere, and v_t is the total fitted rotation curve, consisting of the individual components added together following Equation 3.1.

NGC 2903

Figure 5.9. Similar to NGC 2841, this barred Sbc galaxy also exhibits a strong warp, and for the GIPSY RC derivation, the position angle was left unfixed to allow for the warp. The rotation curve shows a 'hump' after the turnover radius which is indicative of a barred galaxy. We used the THINGS data for the GIPSY RC, but the GalAPAGOS RC from the Irwin VLA data for the GalAPAGOS RC mass model, since its GalAPAGOS model has a better determined inner region than the GalAPAGOS model from the THINGS data (see § 5.2.2). The top panels of Figure 5.9 show maps derived from the THINGS data. The mass model fits require a small bulge contribution to explain the inner parts, which however still is hard to fit, possibly due to the presence of the bar. Indeed, the M/L of the bulge is too low, which is probably due to too much luminosity being assigned to the bulge component due to the bar, affecting both mass models.

. In contrast, the outer rotation curve is easily matched. Diminishing the disk contribution towards a Salpeter disk increases the halo contribution. The maximum disk model is also the "best fit" model, and the minimum disk model fit is similar to the Salpeter fit model, using a $M/L_{I,D}$ of 1.6.

NGC 3198

NGC 3198 is an Sc galaxy featuring a small bulge. The HI content extends to twice the radius of the optical disk.

The luminosity profile at outer radii does not follow an exponential disk behaviour perfectly, so rather than using the fitted exponential disk from the disk-bulge decomposition, we subtracted the fitted Sérsic bulge from the luminosity profile to provide the data for the RC of the disk component. Due to the small bulge contribution, it is possible to achieve a good fit to the GIPSY RC both with and without the bulge. The disk RC curve

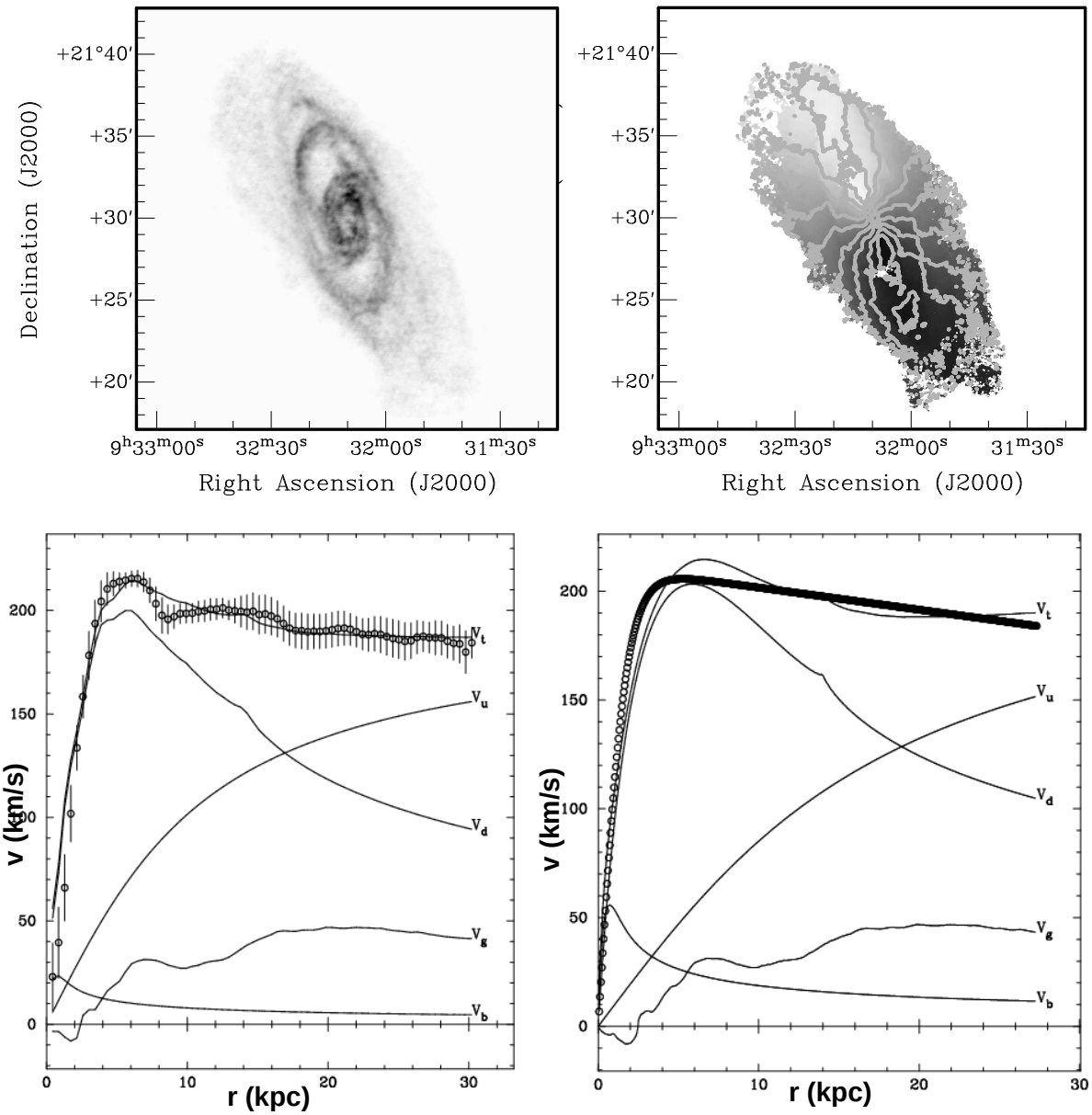

Figure 5.9: NGC 2903. Top left: The HI density distribution shown in a zeroth moment map (see Chapter 3). Top right: The velocity field with isovelocity curves overlaid ("spider diagram"). Bottom left: "best fit" mass model using the tilted ring (GIPSY) rotation curve. Bottom right: "best fit" mass model using one (the lowest χ^2) of the GalAPAGOS rotation curves. v_g, v_d, v_b refer to the rotation curve contributions from the gas (HI+He), the disk and the bulge respectively. v_u refers to the user-supplied halo model, in this case the isothermal sphere, and v_t is the total fitted rotation curve, consisting of the individual components added together following Equation 3.1.

behaviour seems to correspond to the "wiggles" of the GIPSY RC at optical radii, i.e. out to ∼20 kpc. The "best fit" model is also the maximum disk model, while the Salpeter model corresponds to the minimum disk model.

The GalAPAGOS RC mass models can be fit well with any size of bulge or no bulge, so we opt to set the bulge to a maximum bulge, which corresponds well to the GIPSY RC model. The maximum disk model is comparable to the "best fit" (and maximum disk) model of the GIPSY RC fit, while the Salpeter model is the same as the minimum disk model.

Similar to NGC 2903, NGC 3198 is barred, which might explain the low M/L of the bulge in both mass models (also found by de Blok et al. (2008)).

Since the GalAPAGOS RC is based on a model, the RC lacks the "wiggles" visible in the GIPSY RC, but regardless of which disk contribution is chosen (the luminosity profile with the bulge subtracted, or the fit to an exponential disk), the results are the same.

NGC 3351

Figure 5.11. Morphologically, this galaxy is classified as an Sb galaxy with a ring and a strong bar. It is different from the other galaxies in the sample in that it is a UV bright starburst galaxy, most of which usually are classified as irregular or peculiar (Conselice et al., 2000). It also has a much lower inclination than the rest of the galaxies in the sample ($\sim 41\,^{\circ}$). NGC 3351 appears to be symmetric and regular, without any tidal features (Conselice et al., 2000). Thus we assume it to be non-interacting, even though is is not present in the Catalogue of Isolated Galaxies (Karachentseva, 1973).

The GIPSY RC fitting was sensitive to inclination and position angle, and had to be carefully derived in many steps before settling on the final rotation curve. Similar to NGC 3198, the luminosity distribution could not be fitted perfectly to an exponential disk, and the fitted bulge was therefore subtracted from the data to provide the data for the disk

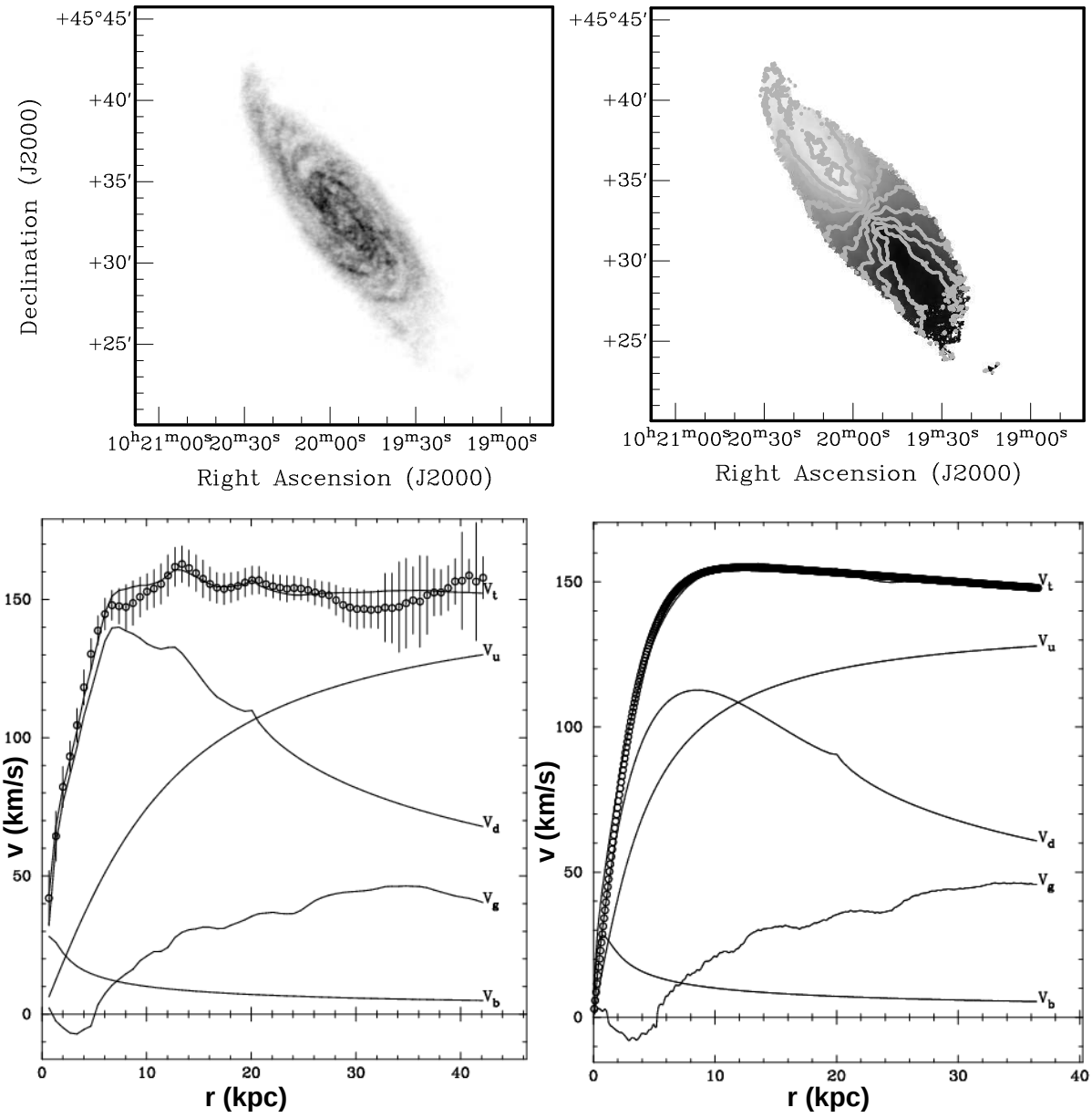

Figure 5.10: NGC 3198. Top left: The HI density distribution shown in a zeroth moment map (see Chapter 3). Top right: The velocity field with isovelocity curves overlaid ("spider diagram"). Bottom left: "best fit" mass model using the tilted ring (GIPSY) rotation curve. Bottom right: "best fit" mass model using one (the lowest χ^2) of the GalAPAGOS rotation curves. v_g, v_d, v_b refer to the rotation curve contributions from the gas (HI+He), the disk and the bulge respectively. v_u refers to the user-supplied halo model (isothermal sphere), and v_t is the total fitted rotation curve, consisting of the individual components added together following Equation 3.1. Note that the disk contribution in the massmodels of the two lower panels is the data with the bulge subtracted for the the GIPSY RC fit, while the fitted exponential disk has been used for the GalAPAGOS RC fit.

RC. Fitting a mass model was far from straightforward for this galaxy. The depletion of HI in the centre may have caused the centre to be incorrectly determined, possibly affecting the rotation curve derivation. This depletion also caused the error bars in the centre to be large, and in order to fit the inner parts correctly, uniform weighting rather than the uncertainty values had to be used in the ROTMAS fitting process (otherwise the bulge would be allowed to take improbably high M/L values). The "best fit" to the GIPSY RC does however have a too low bulge M/L, as well as an unrealistically high central density of the halo, which we attribute to the overall badly fitted mass model, likely due to the low inclination of the galaxy.

The GalAPAGOS RC has a shorter turnover radius in comparison to the GIPSY RC which we earlier discovered likely is due to too few pixels spanning the inner region. We will use the GIPSY RC results in analysis later in this thesis.

NGC 3521

Figure 5.12. Despite the designated Sbc morphological type which implies an intermediate size bulge, the initial mass calculations (where an M/L of 1 is assumed) indicate that the bulge consists of as much as 50% of the total stellar mass. There is a disagreement in the literature of the rotation curve for this galaxy; de Blok et al. (2008) find higher inner velocities but not as much of a decline at the outer radii compared to Casertano & van Gorkom (1991). Our tilted ring rotation curve agrees perfectly with that of de Blok et al. (2008) out to a radius of 25 kpc (which is the extent of their rotation curve), after which there is an agreement with the decline found by Casertano & van Gorkom (1991).

In the derivation of the GIPSY RC, we decided to use two values (343 ° at inner radii and 339 ° at outer radii, where the angle is measured from north to the receding side of the galaxy) for the position angle to accommodate the small warp, with the change taking place at a radius of 230″(9.5 kpc).

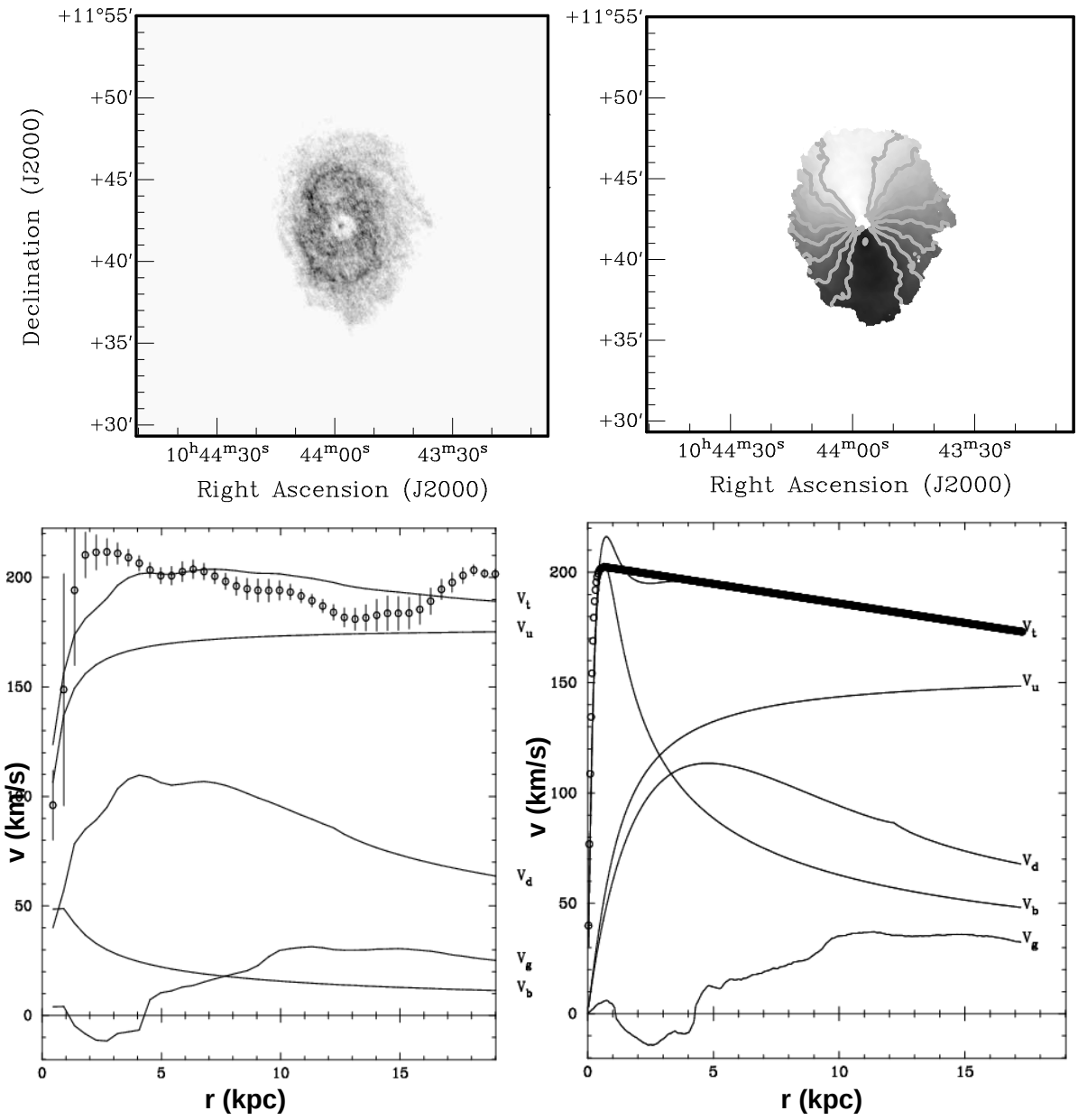

Figure 5.11: NGC 3351. Top left: The HI density distribution shown in a zeroth moment map (see Chapter 3). Top right: The velocity field with isovelocity curves overlaid ("spider diagram"). Bottom left: "best fit" mass model using the tilted ring (GIPSY) rotation curve. Bottom right: "best fit" mass model using one (the lowest χ^2) of the GalAPAGOS rotation curves. v_g, v_d, v_b refer to the rotation curve contributions from the gas (HI+He), the disk and the bulge respectively. v_u refers to the user-supplied halo model (isothermal sphere), and v_t is the total fitted rotation curve, consisting of the individual components added together following Equation 3.1. The luminosity profile data with the bulge subtracted was used for the tilted ring mass model in the bottom left panel, while the exponential disk fit was used for the disk in the GalAPAGOS model in the bottom right panel.

Due to the shape of the GIPSY rotation curve, all mass model fits incorporate a dominating stellar contribution. The minimum disk model is the same as the Salpeter model. The disk M/L ranges between 6.9 ("best fit") and 8.3 (maximum disk). The bulge contribution remains the same throughout all fits to this RC. Its M/L is however unrealistically low, due to too much luminosity being attributed to the bulge in the disk-bulge decomposition. In Figure 5.5, the bulge is too extended and should have been fit in several steps (similar to the procedure for NGC 4258, see below). This issue could have arisen due to structure such as a bar or a ring in the inner region causing an extra bend in the luminosity profile.

The short turnover radius of the GalAPAGOS rotation curve constrains the mass model considerably, which causes the bulge to dominate the inner region of the mass model. The best fit is close to the Salpeter fit, which is also the minimum disk. It is not possible to fit a maximum disk model with this rotation curve. Note however that the GalAPAGOS RC is considered less reliable for this galaxy, due to its short turnover radius (see § 5.2.2) and we will use the mass model of GIPSY RC in analysis later in this thesis.

NGC 3556

NGC 3556 has a very small to no bulge and a disk-bulge decomposition is not necessary in the mass model for this late-type Scd galaxy. The rotation curve is interesting in that it has a large turnover radius (50% of its total HI radius), and there is an indication of a decline just after the turnover. The discrepancy between the GIPSY RC and the GalAPAGOS RC at radii > 17 kpc is likely due to the gas extension in the northeast corner of the galaxy.

The HI disk in the data on hand does not reach much further out than the optical disk. Fitting a mass model is difficult for this highly inclined galaxy. There seem to be two options of mass models: a) a Salpeter model, or b) a minium disk model where the halo

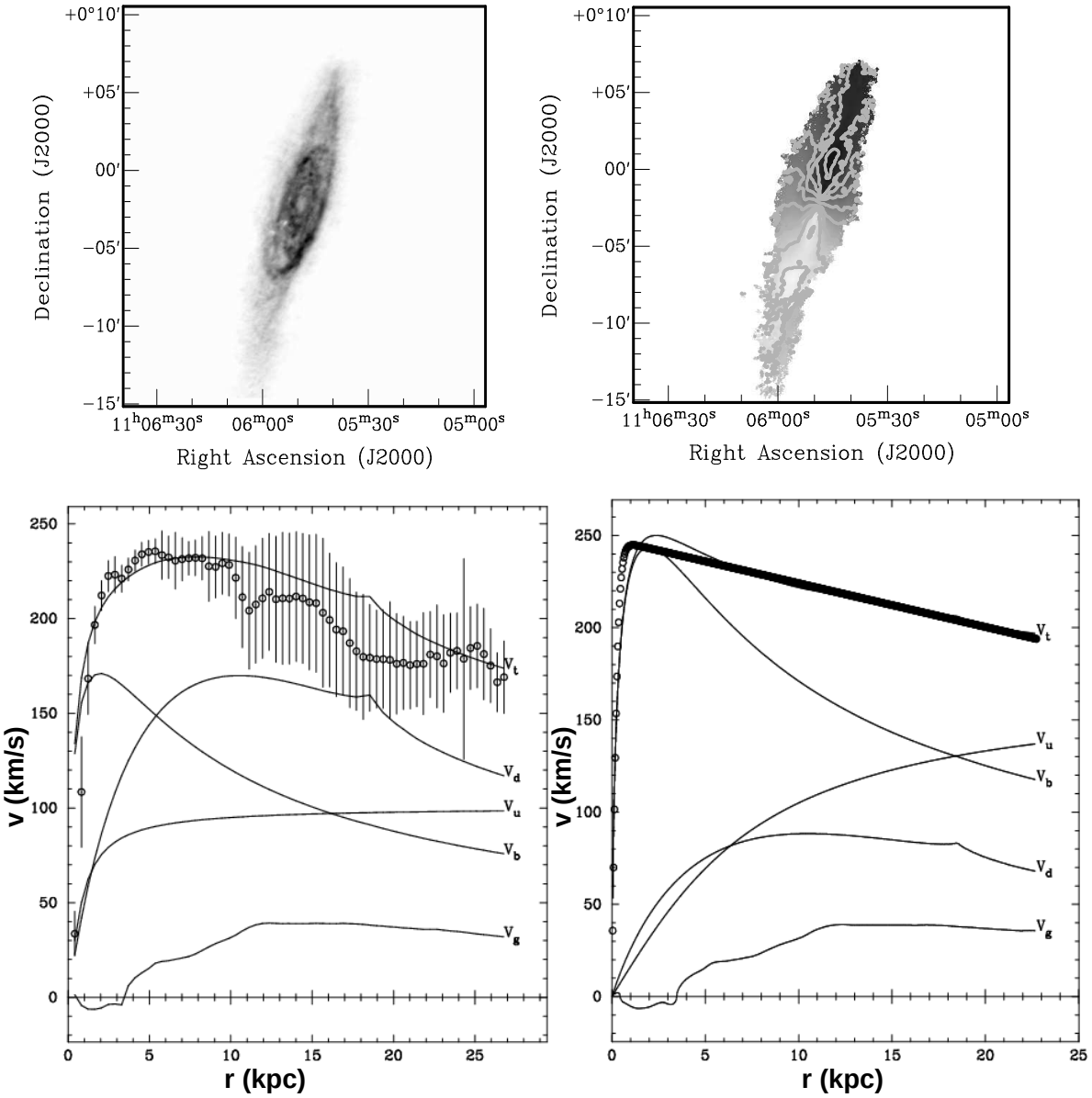

Figure 5.12: NGC 3521. Top left: The HI density distribution shown in a zeroth moment map (see Chapter 3). Top right: The velocity field with isovelocity curves overlaid ("spider diagram"). Bottom left: "best fit" mass model using the tilted ring (GIPSY) rotation curve. Bottom right: "best fit" mass model using one (the lowest χ^2) of the GalAPAGOS rotation curves. v_g, v_d, v_b refer to the rotation curve contributions from the gas (HI+He), the disk and the bulge respectively. v_u refers to the user-supplied halo model (isothermal sphere), and v_t is the total fitted rotation curve, consisting of the individual components added together following Equation 3.1.

alone is responsible for the kinematics. The "best fit" model is similar to the minimum disk model. The models presented in the two bottom panels of Figure 5.13 are "best fit" (i.e. minimum disk) disk models.

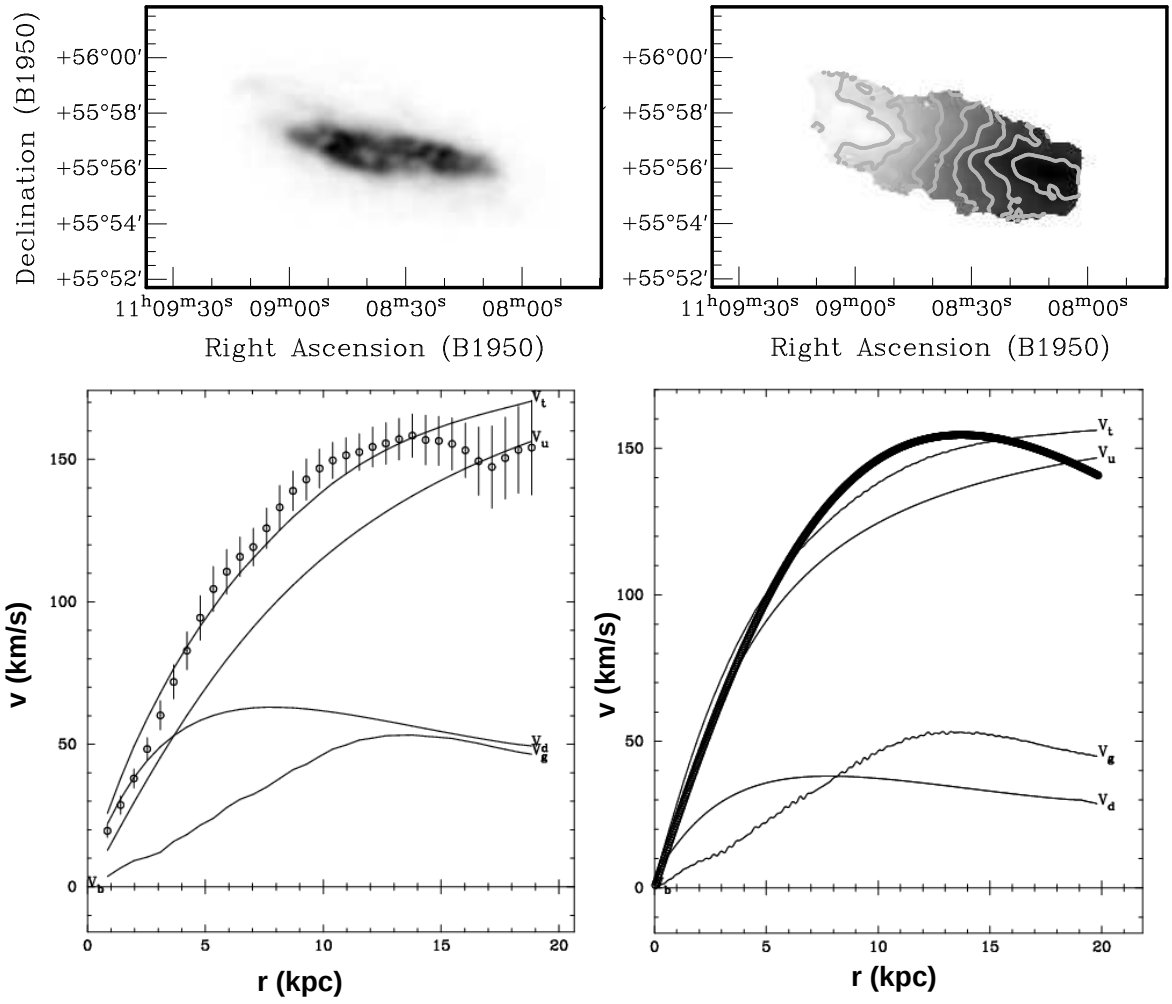

Figure 5.13: NGC 3556. Top left: The HI density distribution shown in a zeroth moment map (see Chapter 3). Top right: The velocity field with isovelocity curves overlaid ("spider diagram"). Bottom left: "best fit" disk mass model using the tilted ring (GIPSY) rotation curve. Bottom right: "best fit" disk mass model using one (the lowest χ^2) of the GalAPAGOS rotation curves. v_g, v_d, v_b refer to the rotation curve contributions from the gas (HI+He), the disk and the bulge respectively. v_u refers to the user-supplied halo model (isothermal sphere), and v_t is the total fitted rotation curve, consisting of the individual components added together following Equation 3.1.

NGC 4096

Similar to NGC 3556, this Sc galaxy is highly inclined. Its HI content traces the kinematic behaviour 30% further out than the optical radius. In the optical data, the stellar disk is elongated along the major axis on the south side of the galaxy, which might indicate recent interaction (although this has not been confirmed or addressed in the literature). It is problematic to fit a mass model to NGC 4096. The two rotation curves have dramatically different turnover radii even though GalAPAGOS was run on a well-resolved cube (see Table 5.8). NGC 4096 has a small angular size, and the data set has the lowest sensitivity in the sample, so even though GalAPAGOS has been shown to handle low S/N ratio data well in artificial galaxy tests (§ 4.5.1), caution should be used with the results for this galaxy. Better data are needed in order to make any conclusions on the validity of these two options.

Figure 5.14 shows the maps and mass models of NGC 4096. The mass model of the GIPSY RC prefers to exclude the bulge. If we do include the bulge, the galaxy is dominated by stellar mass and the halo is brought to a minimum for all models. The situation is the opposite for the GalAPAGOS RC fit. The short turnover radius requires either a low disk constribution combined with a large halo, or a very massive bulge with large M/L. This seems however unlikely due to the morphology of NGC 4096.

NGC 4258

Also known as M106, this large Sb or Sbc galaxy has an HI disk that closely follows the spiral arms, and thus exhibits large holes in its HI distribution. Also the centre has an HI depletion, which makes it difficult to pinpoint the centre of the galaxy. We smoothed the data to twice the beam size to discern the faint emission and also applied Hanning smoothing in the velocity direction for the HI analysis.

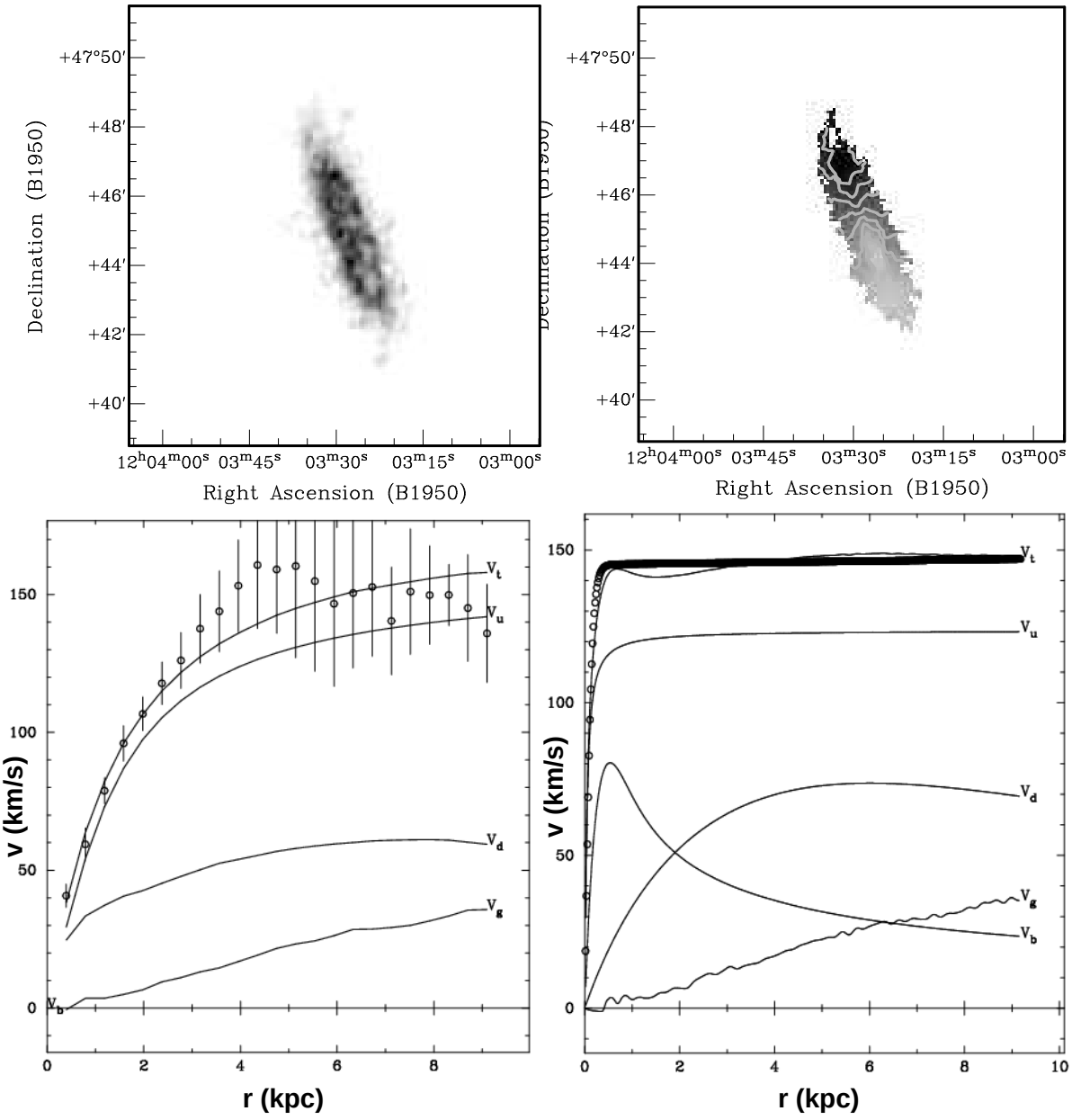

Figure 5.14: NGC 4096. Top left: The HI density distribution shown in a zeroth moment map (see Chapter 3). Top right: The velocity field with isovelocity curves overlaid ("spider diagram"). Bottom left: "best fit" mass model using the tilted ring (GIPSY) rotation curve. Bottom right: Salpeter mass model using one (the lowest χ^2) of the GalAPAGOS rotation curves. v_g, v_d, v_b refer to the rotation curve contributions from the gas (HI+He), the disk and the bulge respectively. v_u refers to the user-supplied halo model (isothermal sphere), and v_t is the total fitted rotation curve, consisting of the individual components added together following Equation 3.1

The stellar disk seems to consist of two components (apart from the bulge), one ranging out to $\sim$300″ (11.2 kpc), and the other beyond this radius (see Figure 5.6). This makes a disk-bulge decomposition difficult, unless only taking the "inner disk" into account when deriving the bulge components. The disk scale length of the inner disk component is 108″ while the average disk scale length of the entire disk is 244″. The exponential disk fit of the inner disk is thus not accurate beyond 300″, and instead we have subtracted the bulge off the luminosity profile to represent the disk component instead of using the disk fit.

The behaviour of the "two disks" can also be seen in the GIPSY RC, which ressembles two RCs overlaid on each other, where the inner disk exhibits a declining slope and the outer disk is flat. The mass model of the GIPSY RC exhibits a very large bulge contribution, even for a maximum disk model. This might be due to the uncertain behaviour near the centre of the galaxy, and the inner part of the RC, which is very hard to fit a model to. NGC 4258 is barred, and this might be a reason for the disturbed velocities. The minimum disk and the "best fit" models produce the same parameters.

A potentially more reliable mass model for the average kinematic behaviour of NGC 4258 is achieved by the fit to the GalAPAGOS RC. However, it still suffers from shortcomings, due to issues with the GalAPAGOS model related to the holes in the HI distribution. The "best fit" model here favours a small disk contribution and a massive (flat RC) halo contribution. The massive halo results in a flat shape of the velocity curve of the halo contribution which generates an unrealistically large halo density, with a short core radius.

NGC 5055

NGC 5055, an Sbc galaxy also known as M63, is called the 'Sunflower Galaxy'. It is part of the M51 group, but does not seem to be showing any signs of interaction. The 'petals' of the sunflower makes for an extensive exercise in preparing the extended velocity field (see top right of Figure 5.16). As can be seen in the velocity field, the position angle (PA)

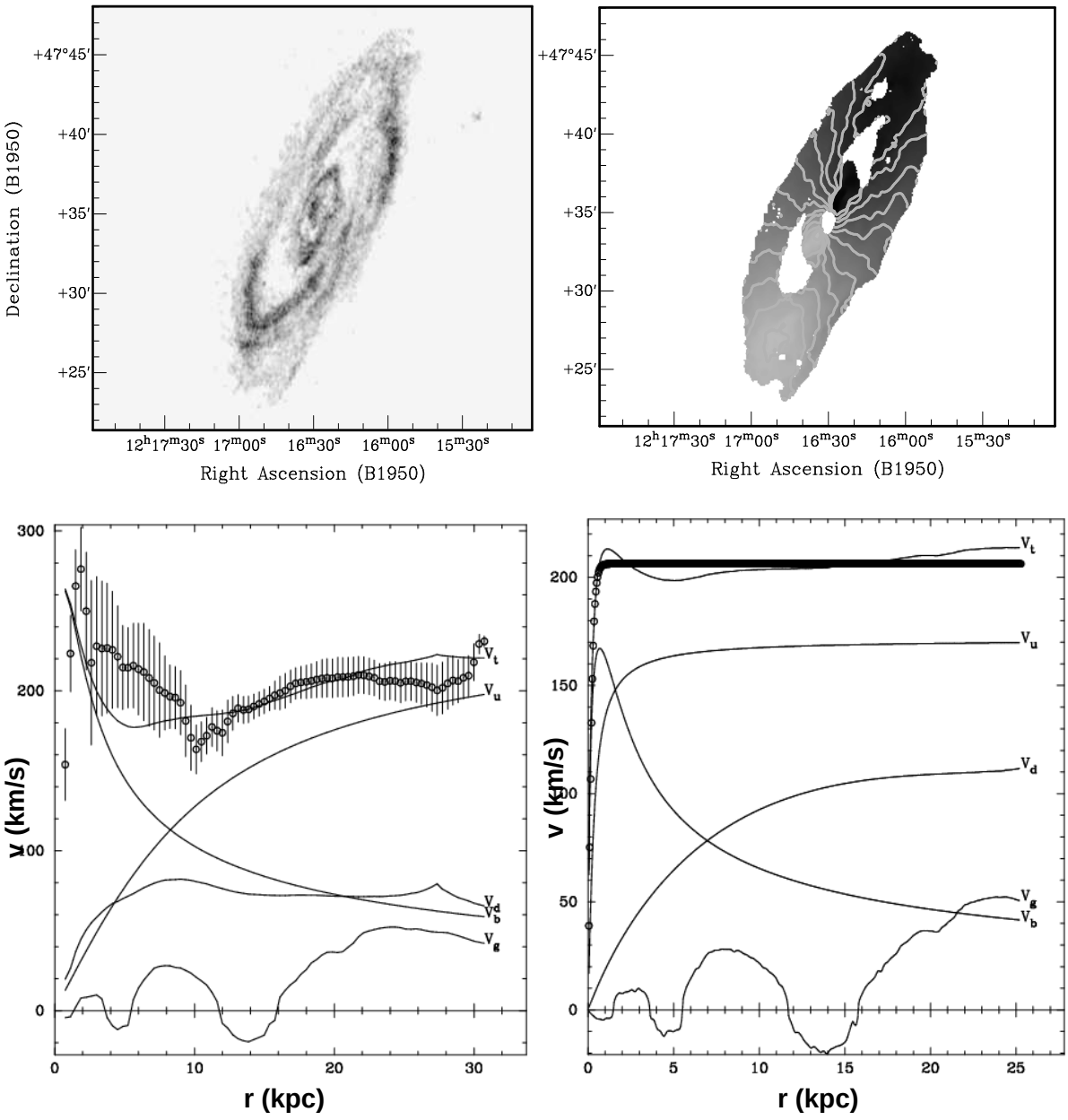

Figure 5.15: NGC 4258. Top left: The HI density distribution shown in a zeroth moment map (see Chapter 3). Top right: The velocity field with isovelocity curves overlaid ("spider diagram"). Bottom left: "best fit" mass model using the tilted ring (GIPSY) rotation curve. Bottom right: Salpeter mass model using one (the lowest χ^2) of the GalAPAGOS rotation curves. v_g, v_d, v_b refer to the rotation curve contributions from the gas (HI+He), the disk and the bulge respectively. v_u refers to the user-supplied halo model (isothermal sphere), and v_t is the total fitted rotation curve, consisting of the individual components added together following Equation 3.1.

changes at a radius of 420″. In the GIPSY RC derivation, we kept the PA fixed to 98 ° inside this radius, and to 101 ° in the fitting of the outer disk. Also the inclination changes at this radius, and we adopt an inclination of 65 ° within the radius and 57 ° outside of it for the derivation of the GIPSY RC.

The mass models fit well to the GIPSY RC. The minimum disk model is similar to the Salpeter model using a disk M/L of 1.53 (Salpeter M/L for an Sbc galaxy is 1.6), and a maximum disk model brings it up to 5.7, but with a worse fit. The bulge contribution remains approximately the same for all model fits, for both RCs.

The solutions from GalAPAGOS find the RCs appearing in three groups where the main difference is the turnover radius. The solution with the lowest χ^2, which is usually the one chosen for this analysis, is in a smaller group of solutions featuring RCs with too short turnover radii in comparison with the GIPSY RC. Instead we chose to use the RC with the lowest χ^2 from the 2nd (centre) group, which contains the bulk of the solutions.

The "best fit" GalAPAGOS RC model is similar to the GIPSY RC model, and the disk M/L takes the value of a maximum disk model.

NGC 7331

The process of analysing the data for this Sb (or possibly Sbc) galaxy was straightforward, and its luminosity profile is well–fit by the disk-bulge decomposition. Yet the mass model fits (see Figure 5.17) to the GIPSY RC are difficult to fit. Although the shape of the RC suggests a larger bulge component, this can only be applied at the cost of a good fit in the outer part. The resulting high central density in the halo is not credible.

There is no plausible maximum disk fit to the GIPSY RC, and the "best fit" model is similar to a minimum disk model. Thus we deem the GIPSY RC mass model to be unreliable.

The slightly shorter turnover radius for the GalAPAGOS RC makes it easier to find

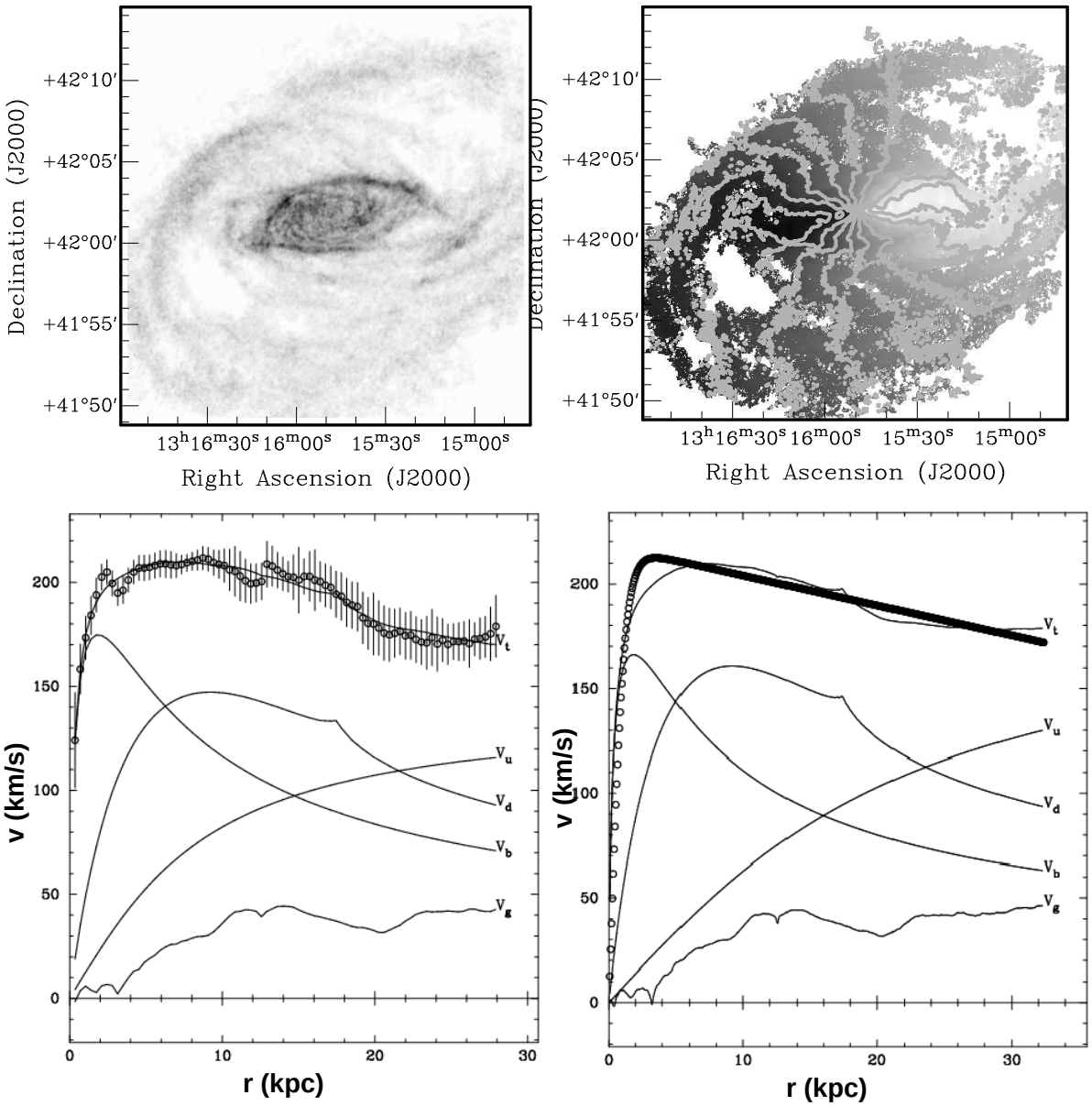

Figure 5.16: NGC 5055. Top left: The HI density distribution shown in a zeroth moment map (see Chapter 3). Top right: The velocity field with isovelocity curves overlaid ("spider diagram"). Bottom left: "best fit" mass model using the tilted ring (GIPSY) rotation curve. Bottom right: "best fit" mass model using one (the lowest χ^2) of the GalAPAGOS rotation curves. v_g, v_d, v_b refer to the rotation curve contributions from the gas (HI+He), the disk and the bulge respectively. v_u refers to the user-supplied halo model (isothermal sphere), and v_t is the total fitted rotation curve, consisting of the individual components added together following Equation 3.1.

good mass model fits. The "best fit" model is similar to the Salpeter model, which agrees with the I-band M/L found by Bottema (1999) (1.6 ± 0.7) for this galaxy. It should be noted that the right bottom panel of Figure 5.17 shows a "best fit" model with a maximum bulge applied, making the outer disk fit better, at the cost of a somewhat higher χ^2 value. The resulting mass model has a disk M/L slightly lower than the Salpeter one (1.4 as opposed to 1.6). A minimum disk model which lets the bulge, gas and halo alone create the total rotation curve is also possible for the GalAPAGOS RC.

5.3.4 Implications of different rotation curves

As we can see visually from the mass models displayed in § 5.3.3, the GalAPAGOS and GIPSY rotation curves will deliver similar best fit halo models. We can however also see from Tables 5.12 and 5.12, that there is a certain variation in the derived mass model parameters for the two different RCs.

Since, unlike the GIPSY RCs, GalAPAGOS RCs are extrapolated in the central region to the centre (v=0, r=0), a large range of bulge M/L is allowed when fitting GalAPAGOS RC mass models. We have in most cases opted to use a maximum bulge in the GalAPAGOS mass model, which also agrees well with the GIPSY mass models.

Thus we can see that the mass model parameters are very sensitive to small changes, and in particular to the fit in the central region of the galaxy.

Additionally, for the three cases of potentially declining rotation curves, the GIPSY RC flattens out in the outer region of the galaxy, while the parameterisation of the GalAPAGOS does not allow for flexibility beyond the turnover radius. This is an indication that it might be necessary to adapt the parametrised rotation curve form we are using in GalAPAGOS (§ 4.2.2).

For the continued analysis, we will disregard NGC 4096 due to its inconclusive results, and we will only use the mass models based on GIPSY RCs for the galaxies suffering from

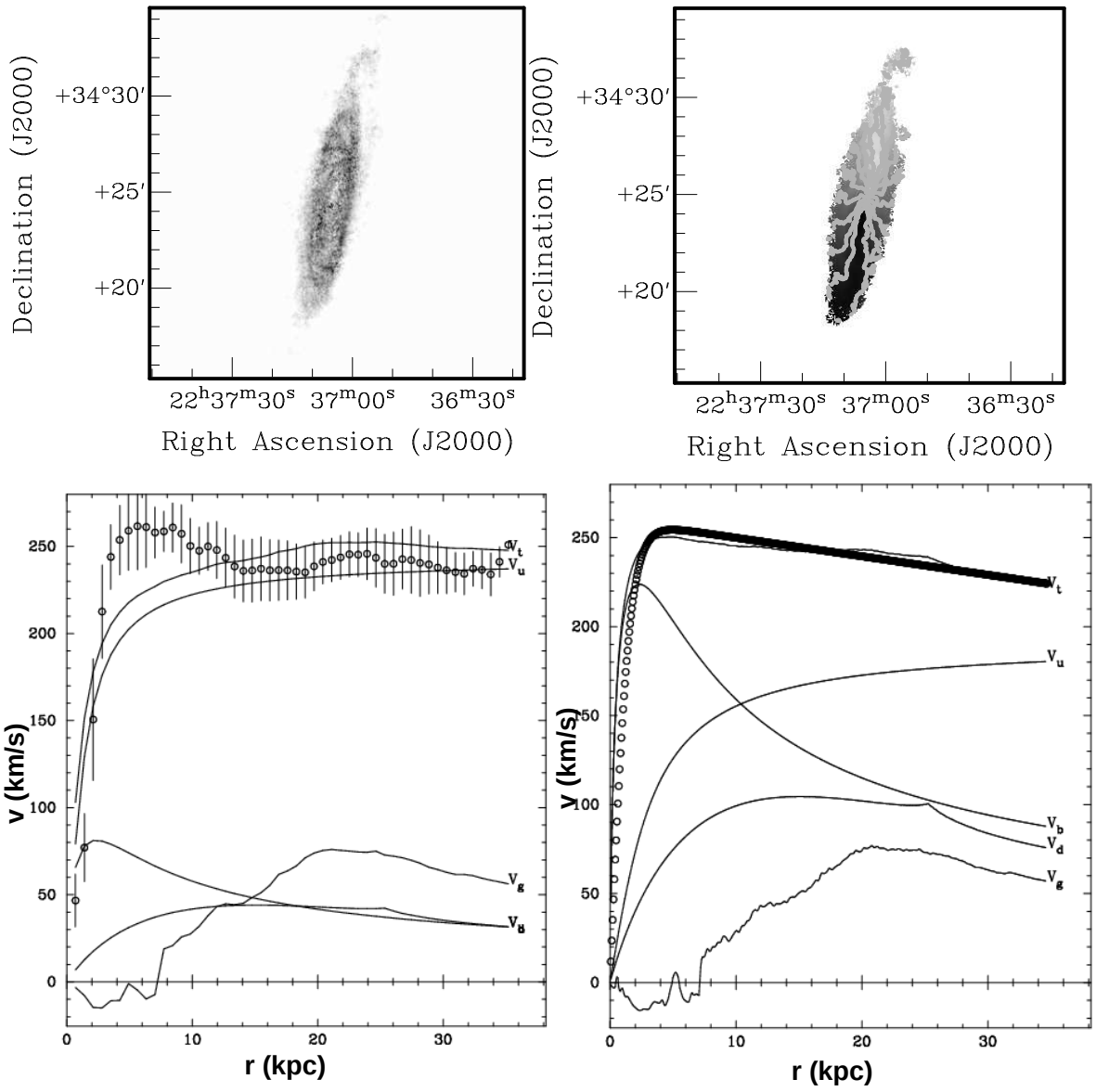

Figure 5.17: NGC 7331. Top left: The HI density distribution shown in a zeroth moment map (see Chapter 3). Top right: The velocity field with isovelocity curves overlaid ("spider diagram"). Bottom left: "best fit" mass model using the tilted ring (GIPSY) rotation curve. Bottom right: "best fit" mass model (with maximum bulge) using one (the lowest χ^2) of the GalAPAGOS rotation curves. v_g, v_d, v_b refer to the rotation curve contributions from the gas (HI+He), the disk and the bulge respectively. v_u refers to the user-supplied halo model (isothermal sphere), and v_t is the total fitted rotation curve, consisting of the individual components added together following Equation 3.1.

the issue with the short turnover radius (described in § 5.2.2); NGC 2841, NGC 3351 and NGC 3521.

For the remaining galaxies, we will use the "best fit" mass models to the GalAPAGOS RC, and include all the models (Salpeter, Maximum and Minimum disk models, both for GIPSY and GalAPAGOS RCs) in the uncertainties.

It is common that the "best fit" mass model will coincide with the maximum disk model, and the Salpeter model with the minimum disk model (this has been noted in Tables 5.11 and 5.12). Table 5.13 lists the derived M/L values for bulge and disk, as well as the corresponding stellar masses.

5.3.5 Halo masses and mass ratios

We derive the dynamical mass at the outer radius by using Equation 5.5:

$$M_{dyn}(r) = f \cdot \frac{r v^2(r)}{G} \tag{5.5}$$

Here, r is the radius within which the mass $M_{dyn}(r)$ is calculated, and $v(r)$ is the velocity at this radius. G is the gravitational constant, which takes the value $4.31 \times 10^{-6}\,\mathrm{kpc\,km^2/s^2}$ (using units of kpc and km/s for r and v). The scaling constant f was introduced by Lequeux (1983), who showed that it has a value between 0.6 and 1, depending on the distribution of the mass. $f = 1$ corresponds to a spherical, halo dominated distribution, while $f = 0.6$ corresponds to a disk like-mass distribution. We initially adopted $f = 0.7$ which corresponds to a mass distribution with a flat rotation curve (based on Figure 1 of Lequeux (1983)), and used the limits for the uncertainties. However, a factor of 1 might be more appropriate when the spheroid component (DM) is more dominant, which is likely the case for our galaxies. The dynamical masses are thus closer to the upper limit listed in Table 5.14. These values are later used in Chapter 6 as ratios (e.g. dynamical

mass over luminosity), in which case the scaling parameter does not impact the general correlations or results.

Table 5.13 lists HI mass (derived in GIPSY's ROTMOD task) and the mass model derived i-band M/L values for disk and bulge, as well as their corresponding masses. The dynamical mass is listed in Table 5.14, as well as the total dynamical M/L of the galaxy derived using the i-band, the halo mass (corresponding to dynamical mass with the baryonic mass (gas, bulge and disk) subtracted), the fraction of gas mass over stellar mass and the ratio of the halo mass over the baryonic mass.

Note that five of the mass models exhibit unrealistically low bulge M/L values. For some, this is caused by too much luminosity being assigned to the bulge through a problematic disk-bulge decomposition (due to the presence of a bar or ring). For others, the cause could be unreliable velocities due to depletion of HI gas in the inner region.

We can also note that three galaxies, NGC 2841, NGC 3521, and NGC 5055, have a low ratio of halo mass over baryon mass, which is consistent with these three galaxies being candidates for declining rotation curves (see § 5.2.2 and further discussion in § 6.8).

5.4 Summary of the results

This chapter has two parts. In the first part, we evaluated the results from GalAPAGOS on 14 galaxies. We evaluated the entire parameter set, then we concentrated on the parameters included in the rotation curve, and we also compared data sets of different sensitivity and resolution. We find that:

- The spin temperature T_s is not well constrained in the GalAPAGOS HI models
- It is necessary to have enough pixel resolution to adequately characterise the inner region within the turnover radius for galaxies that are candidates for a short turnover

Galaxy	M_{HI} $[\times 10^9 M_\odot]$ (2)	M_{gas} $[\times 10^9 M_\odot]$ (3)	$(M/L)_{bulge}$ (4)	$(M/L)_{disk}$ (5)	M_{bulge} $[\times 10^9 M_\odot]$ (6)	M_{disk} $[\times 10^9 M_\odot]$ (7)
NGC 2403	3.3	4.6	$4.0^{+3.4}_{-4.0}$	$1.0^{+1.0}_{-1.0}$	$0.4^{+0.3}_{-0.4}$	$3.9^{+3.9}_{-3.8}$
NGC 2841	13	1.9	$1.0^{+0.3}_{-0}$	$7.5^{+0.1}_{-0}$	$8.0^{+2.4}_{-0}$	$290^{+3.9}_{-0}$
NGC 2903	6.0	8.4	$0.6^{+0}_{-0.6}$	$3.2^{+0}_{-1.6}$	$0.8^{+0}_{-0.8}$	68^{+0}_{-34}
NGC 3198	7.7	10.7	$1.0^{+0.1}_{-1.0}$	$2.7^{+1.3}_{-1.28}$	$0.21^{+0.02}_{-0.19}$	30^{+14}_{-14}
NGC 3351	2.0	2.8	0.4^{+0}_{-0}	$1.5^{+0.7}_{-0}$	0.7^{+0}_{-0}	$17^{+7.8}_{-0}$
NGC 3521	3.5	4.8	$2.8^{+0}_{-0.2}$	$6.9^{+1.4}_{-5.3}$	$36^{+0}_{-2.6}$	$77^{+16}_{-5.9}$
NGC 3556	5.0	7.0	n/a	$0.25^{+1.5}_{-0}$	n/a	3.3^{+20}_{-0}
NGC 4258	5.8	8.1	$6.2^{+5.8}_{-0.9}$	$1.6^{+0.7}_{-1.3}$	$13^{+12}_{-1.8}$	59^{+26}_{-48}
NGC 5055	7.4	10.4	$3.9^{+0.4}_{-2.2}$	$4.6^{+0}_{-3.0}$	$30^{+3.1}_{-17}$	63^{+0}_{-41}
NGC 7331	14	19.7	$3.1^{+0}_{-2.7}$	$1.4^{+0}_{-1.1}$	61^{+0}_{-53}	41^{+0}_{-32}

Table 5.13: Masses for the baryonic components of ten galaxies. Column (2) is the HI mass, Column (3) is the total gas mass (HI scaled by 1.4 following § 1.3.1), Column (4) is $(M/L)_i$ of the bulge, Column (5) is the $(M/L)_i$ of the disk (both derived from the mass models), Column (6) is the mass of the bulge in $M_\odot$, and Column (7) is the mass of the disk in $M_\odot$. The uncertainties are derived from the mass models. Unrealistic bulge M/L values are considered in the individual galaxy discussions.

Galaxy	M_{dyn} $[\times 10^{10} M_\odot]$ (2)	L_i $[\times 10^9 L_\odot]$ (3)	$(M_{dyn}/L)_i$ (4)	M_{gas}/M_* (5)	M_{halo} $[\times 10^{10} M_\odot]$ (6)	M_{halo}/M_{baryon} (7)
NGC 2403	$7.0^{+3.0}_{-1.0}$	4.0	$18^{+7.5}_{-2.5}$	$1.1^{+58}_{-0.5}$	$6.1^{+3.4}_{-1.4}$	$6.9^{+14}_{-3.3}$
NGC 2841	79^{+34}_{-11}	47	$17^{+7.3}_{-2.4}$	0.06^{+0}_{-0}	48^{+34}_{-12}	$1.5^{+1.1}_{-0.4}$
NGC 2903	$15^{+6.5}_{-2.2}$	23	$6.7^{+2.9}_{-1.0}$	$0.12^{+0}_{-0.04}$	$7.3^{+3.2}_{-2.2}$	$1.0^{+0}_{-0.3}$
NGC 3198	$13^{+5.6}_{-1.9}$	11	$12^{+4.9}_{-1.6}$	$0.36^{+0.32}_{-0.12}$	$8.9^{+7.0}_{-3.3}$	$2.2^{+3.7}_{-1.2}$
NGC 3351	$14^{+6.1}_{-2.0}$	13	$11^{+4.7}_{-1.6}$	$0.16^{+0}_{-0.05}$	$12^{+6.1}_{-2.8}$	$6.0^{+3.0}_{-2.7}$
NGC 3521	$12^{+5.4}_{-1.7}$	24	$5.2^{+2.2}_{-0.7}$	$0.04^{+0.05}_{-0}$	$0.6^{+12}_{-0.6}$	$0.1^{+2.1}_{-0.0}$
NGC 3556	$6.4^{+2.7}_{-0.9}$	13	$4.8^{+2.1}_{-0.7}$	$2.12^{+0}_{-1.82}$	$5.4^{+2.7}_{-2.9}$	$5.2^{+2.7}_{-4.4}$
NGC 4258	$18^{+7.4}_{-2.5}$	39	$4.5^{+1.9}_{-0.6}$	$0.11^{+0.26}_{-0.04}$	$9.5^{+12}_{-6.2}$	$1.2^{+6.2}_{-0.9}$
NGC 5055	$16^{+6.7}_{-2.2}$	21	$7.3^{+3.1}_{-1.0}$	$0.11^{+0.2}_{-0}$	$5.2^{+4.3}_{-2.5}$	$0.5^{+0.2}_{-0.3}$
NGC 7331	$28^{+12}_{-4.0}$	49	$5.8^{+2.5}_{-0.8}$	$0.19^{+0.99}_{-0}$	$16^{+21}_{-4.1}$	$1.3^{+8.8}_{-0.3}$

Table 5.14: Masses and mass ratios. Column (2) is the dynamical mass using the scaling constant $f = 0.7$, with the lower uncertainty using $f = 0.6$ and the higher using $f = 1.0$. Column (3) is the galaxy luminosity measured in $L_\odot$, Column (4) is total M/L of the galaxy derived using the i-band, Column (5) is the ratio of the gas mass and the stellar mass. Column (6) is the mass of the halo and Column (7) is the ratio of the halo mass and the baryonic mass of the galaxy.

radius. At least 5 pixel elements are necessary in order for GalAPAGOS to find a plausible turnover radius.

- Low resolution galaxies such as HIPASS are only useful to constrain velocity parameters, unless the disk is covered by more than 4 beams. This might still not be enough for fast rotators (see previous bullet).

- GalAPAGOS may have difficulties properly constraining low sensitivity data sets such as the WHISP data for NGC 4096.

- Three galaxies have declining slopes measuring a velocity decline of ∼20%: NGC 2841, NGC 3521 and NGC 5055. We note however that two of these (NGC 2841 and NGC 5055) also have solutions within the solution set with flat RCs. Additionally, the GIPSY derived RCs show a flattening of the curve just before the outer radius.

- GalAPAGOS generates rotatation curves suitable for continued analysis (taking the above caveats into consideration).

We should also note that while it is necessary to have a high enough (pixel) resolution in the inner part, it is also important not to use too detailed data, since they might result in unrealistic models. One reason for this might be that GalAPAGOS endeavours to use the warp to account for smaller scale irregularities in the cube. Its effort to do this overshadows the effort to pinpoint the global characteristics of the galaxy and the results are unrealistic. This is to our knowledge only a problem for data with very high beam resolution (such as THINGS). In order to balance the need for resolution in the inner part, with the need for less details overall, the data could be smoothed or weighted to produce lower beam resolution.

In the second part, we present a preliminary investigation of mass models derived for the two rotation curves (from GIPSY and GalAPAGOS) for 11 galaxies. In order to delineate uncertainties, we investigate 4 different mass model setups: Maximum and minimum disk, the "best fit" found by the program and a Salpeter IMF derived disk M/L.

- Mass models are highly dependent on how well the inner region is constrained. The M/L of the bulge is highly dependent on the quality of the RC in the central region of the galaxy, and affects the disk M/L and consequently the halo mass. It is thus imperative that the inner region is well determined in order to find reliable mass models.

- It is hard to constrain GalAPAGOS models due to the bulge being able to take almost any value for each mass model. Thus we set the bulge to a maximum bulge in all cases (which is consistent with GIPSY RC models), before searching for a "best fit" model to the disk and halo parameters.

- Halo parameters are sensitive to even small changes in M/L values for bulge and disk. In some cases, an unrealistically low bulge M/L value has been assigned. This can be due to too much luminosity being attributed to the bulge due to a bar or a ring, and consequently affecting the disk-bulge decomposition. Also, unreliable velocities in the inner region due to depletion of HI gas in that region can affect the bulge fit in the mass models. Unfortunately, the effect on the halo parameters is too substantial to be able to use these parameters to examine correlations in Chapter 6 (see § 6.7).

- Often the "best fit" and the Salpeter models will be either the minimum or maximum disk. In four cases, the "best fit" model corresponds to the Salpeter model, but more often, the "best fit" corresponds to the maximum disk model, and the Salpeter model corresponds to the minimum disk model.

- We can improve upon the RC modelling equation used in GalAPAGOS by accounting for changes in slope in the outer region (see discussion in Chapter 7).

- We used GalAPAGOS RCs for all mass models except for three which had unrealistically short turnover radius. Instead we used the GIPSY RC for NGC 2841, NGC 3351 and NGC 3521. We exclude NGC 4096 altogether from the analysis since we do not trust either of its RCs.

Initially, the plan was to use the range of GalAPAGOS rotation curves to delinate the uncertainties of the mass model parameters. However, as we have been able to see here, the fitting of mass models will yield a variety of fits only by varying the M/L ratio of the stellar components, and the differences between a GalAPAGOS RC and a GIPSY RC alone will deliver quite different results. Indeed, including the full range of GalAPAGOS rotation curves from a set of optimal solutions will only widen the range rather than constraining it (see the first part of this chapter).

Our attempt to use predicted values dependent on morphology type in Table 5.9 is a revealing experiment. Only in a few cases do the Salpeter predictions agree with the "best fit" models. One might expect a better agreement, such as the one of de Blok et al. (2008), who used 3.6 μm near IR data on the THINGS galaxies (of which 7 are present in our galaxy sample) and found a remarkably good agreement between their "best fit" models and their mass models using the predicted stellar M/L. Recall, we use SDSS i-band data since more of the galaxies in our sample are available in the SDSS survey than in the Spitzer survey. We note that another way of constraining stellar M/L, instead of using the morphological type, is to use the colour of the galaxy following Bell & de Jong (2001). We recommend that this strategy be used in future work.

Chapter 6

Analysis: development of a classification scheme

6.1 Introduction

The shape of a galaxy's rotation curve reveals more characteristics of a galaxy than an immediate first glance reveals. A straight-forward example is the Tully-Fisher relation which shows a correlation between the maximum rotation velocity of a galaxy and its intrinsic luminosity (Tully & Fisher, 1977), providing a way to derive the distance to a galaxy. As has been mentioned in previous chapter (see chapter 3), the dark matter content in the galaxy is given by the flat rotation curve behaviour at outer radii (e.g. Bosma, 1981a)). Moreover, a 'kink' in the rotation curve just after the turnover radius might indicate the presence of a bar.

It is illuminating to acquire a better picture on exactly which galaxy characteristics affect the rotation curve, and how they affect it. This has been investigated since rotation curves first were measured. Initially, only optical rotation curves were used, measured from the Hα emission line and slit spectroscopy. These rotation curves only show the

velocity behaviour of radii covering the stellar disk, and will thus show the inner kinematic behaviour of the galaxy. Later, the rotational behaviour at outer radii, beyond the stellar disk, could be probed by using 21 cm line spectroscopy of the HI content.

The inner rotation curve shape

Generally, a correlation with the central light concentration is found (e.g. Corradi & Capaccioli, 1990; Chattopadhyay & Chattopadhyay, 2006). This translates to occurrences where galaxies with highly concentrated stellar light (such as S0 and Sab galaxies) have rotation curves with a rapid rise, reaching their turnover radius quicker (a few hundred parsecs from the centre) than galaxies with small bulges and relatively diffuse light distribution. In other words: dynamics in the central regions seem to be dominated by the stellar mass, as is also confirmed in HI studies (Noordermeer et al., 2007).

This behaviour - a steep rise and a short turnover radius - is usually followed by a flat stretch at outer radii and is generally seen for high-luminosity galaxies. In contrast, low-luminosity galaxies exhibit rotation curves with a longer turnover radius and a rising curve at outer radii (Rubin et al., 1985), implying that the dark matter fraction in galaxies increases as luminosity decreases.

Based on the above, and still using optical rotation curves, Persic et al. (1996) developed a universal form for rotation curves (URC), dependent solely on the galaxy luminosity for 1100 galaxes of diverse Hubble types. The URC has, however, been debated by e.g. Bosma (1999) since many galaxies do not fit the URC form (Verheijen, 1997), and most investigations point towards multi parameter dependencies (e.g. Noordermeer et al., 2007) as a more likely scenario.

Other than the disk/bulge luminosity ratio correlation, authors have found that there does not seem to be any connection between kinematic behaviour and morphological Hubble type (Rubin et al., 1985; Burstein & Rubin, 1985). Additionally, de Jong (1996)

find that the near infrared (K-band) bulge-to-disk scale length ratio does not correlate well with Hubble type, further supporting this.

Another method of probing the inner rotation curve is to use sub-millimeter observations of CO emission, as a complement to HI observations which often show little amounts of HI in the centre of galaxies. An attempt for this was made in this study for NGC 925, but this turned out to be a challenging galaxy with very low amounts of CO.

In this thesis we focus however on the outer rotation curve shape, adopting only one parameter (turnover radius) to define the inner shape.

The outer rotation curve shape

With the advent of HI observations, a better view of the rotation curve behaviour at larger radii could be achieved. The feature that was originally expected for rotation curves but rarely found - a decline in the outer part - is in almost all cases also absent in the HI rotation curves, which instead continue to show a flat shape. There are however a few cases where a subtle decline can be perceived. The cause for this is still under debate: Are declining rotation curves a general trend for high surface brightness galaxies with short disk scale length (Casertano & van Gorkom, 1991) and galaxies with a big bulge? Or do they only appear when the galaxy is, or previously has been, interacting with another galaxy, which could result in tidal stripping of the halo (as has been shown to be the case for galaxies in clusters by Whitmore et al., 1988)? Furthermore, Elmegreen & Elmegreen (1990) report a correlation between declining curves and grand design spiral arm structures of galaxies. As a reminder, a schematic of common rotation curve characteristics is shown in Figure 6.1. Note that curve A in the figure also commonly exhibits a flat outer shape. However it seems to be more common that curves with short turnover radius (such as A) will exhibit tendencies of decline. A notable exception is NGC 7793, a galaxy with a longer turnover radius, and a declining slope, as found both by GalAPAGOS (not presented in

the thesis) and by Dicaire et al. (2008).

This schematic corresponds to the rotation curve classes that were found by Corradi & Capaccioli (1990) in their kinematic classification scheme within optical radii (R25).

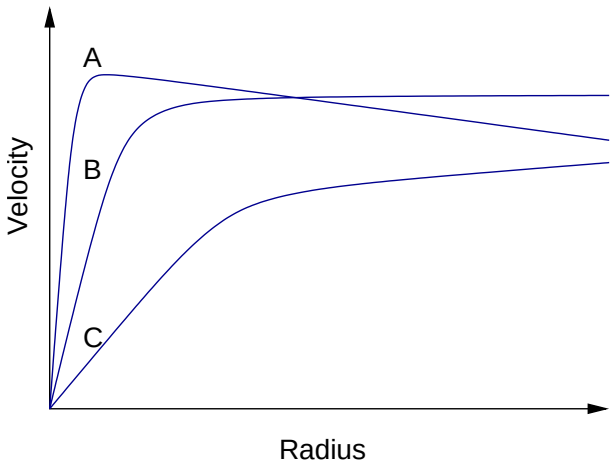

Figure 6.1: A schematic figure of (A) a rotation curve exhibiting steep rise/short turnover radius followed by a decline, (B) a flat rotation curve and (C) a shallow rise/long turnover radius followed by a rise.

Rotation curve classification

Table 6.1 summarizes a number of correlations investigated in the literature and their effect on the galaxy rotation curve. Chattopadhyay & Chattopadhyay (2006) used principal component analysis to deduce which characteristics are more important in affecting the rotation curve shape. Their correlations are listed in Table 6.1 as well, the most notable ones being that while the overall shape is determined by the central surface brightness, the outer RC (beyond the stellar disk) is mainly determined by the size of the disk.

There are still a few ambiguities and/or uncertainties in the results, as has been outlined above. A number of reasons can contribute to this. For example, many of the investigations using HI data have small numbers of galaxies, leading to low number statistics. Additionally, often a particular galaxy group is targeted, such as late-type and

low-luminosity or dwarf galaxies (Swaters, 1999; Carignan & Freeman, 1985). Noordermeer et al. (2007) provide one of few investigations that target early-type galaxies. To our knowledge, there are no HI investigations that only examine isolated, non-interacting galaxies.

We assume that it would be possible – with a large enough set of rotation curves – to define a rotation curve classification scheme, based on a number of parameters. Then this classification scheme could be used to search for relationships between the observables of the galaxies.

This chapter describes such an attempt, which combines employing a mathematical approach with visual evaluation, to find features in a database. For the division into rotation curve groups, the parameters describing the observed velocity behaviour, such as the maximum velocity, the turnover radius, and the behaviour of the curve at large radii assessed by the RC slope, are taken into account. These divisions are then examined for correlations with the "secondary" parameters, such as of those listed in Table 6.1. In order to discern the intrinsic properties of rotation curves, emphasis is placed on using data from isolated non-interacting galaxies.

This chapter is divided into two parts: In the first part, the mathematical approach, which uses a clustering algorithm, is described, tested and used on the parameters used to describe an analytic form of the rotation curve. In the second part, the classification scheme is correlated with a number of additional galaxy characteristics.

6.2 Mathematical approach: clustering algorithms

A clustering algorithm is capable of taking many parameters into account simultaneously and searching for commonalities in the data in order to divide them into groups (clusters).

RC behaviour	Galaxy characteristic	nature of correlation	References
General correlations	Hubble type	None	(1), (2)
	Hubble type	None (outer RC)	(7)
	Hubble type	Strong	(3)*, (14)
	Spiral arm pitch angle		(4)
	Central surface brightness	overall shape of RC	e.g. (5)*
	Disk scale length	overall shape: weak	(5)*
	Central halo density	high: increasing RC	(5)*
	Inner Lindblad resonance	weak	(5)*
	Bar	weak	(5)*
	Light distribution	within optical radius	(6)
	Overall mass distribution	outside optical radius	(7)
	Maximum velocity		(8)
	Luminosity dependence only	Strong	(9)
	Luminosity	None (outer RC)	(7)
Flat slope	Intermediate max velocity	v_{max}= 100 to 180 km/s	(7)
Increasing slope	Luminosity (M_B, M_I)	Faint galaxies	(1), (9), (10), (5)*, (2)
	Low maximum velocity		(9)
	Dwarf galaxies		(15)*, (16)*
Declining slope	Luminosity (M_B, M_I)	Bright, compact galaxies	(1), (9), (10), (13)* (4), (3)
	Luminosity	To intermediate radii (with flattening in the outer region)	(13)*
	Grand design spiral arms	(for optical radii)	(11)
	Lack of massive halo		(12)*
	Interacting galaxies		(17)
Turnover radius	Early type and large bulge	shorter turnover radius	e.g. (14)
	Less concentrated light distribution	longer turnover radius	(14)

Table 6.1: Rotation curve behaviour correlations with galaxy characteristics from the literature. Note that most of these relations were found using rotation curves derived from optical data. Starred references denote investigations using HI data. The references are: (1) Rubin et al. (1985), (2) Burstein & Rubin (1985), (3) Casertano & van Gorkom (1991)*, (4) Seigar et al. (2003), (5) Chattopadhyay & Chattopadhyay (2006)*, (6) Kent (1987)*, (7) van Albada & Sancisi (1986), (8) Tully & Fisher (1977), (9) Persic et al. (1996), (10) Vogt et al. (2004), (11) Elmegreen & Elmegreen (1990), (12) Honma & Sofue (1999)*, (13) Noordermeer et al. (2007)*, (14) Corradi & Capaccioli (1990) (15) Carignan & Freeman (1985)*, (16) Swaters (1999)*, (17) Whitmore et al. (1988).

There are different techniques e.g. in how the 'distance'[1] between parameters is defined, as well as in interpretation of the results. Thus it is necessary to choose a technique that best suits the needs of this exploration. There are a number of popular algorithms. K-means is considered to be the simplest, with a user defined number of centroids, one for each cluster. Fuzzy c-means is a method of clustering which allows one piece of data to belong to two or more clusters. 'Mixture of Gaussians' is a model-based approach, which uses certain models for clusters and attempts to optimize the fit between the data and the model (gaussians for instance). Hierarchical clustering assigns one item per cluster, then merges the most similar clusters in iterative steps.

We find that a hierarchical clustering method is the best one for this investigation, due to its flexibility and ease of interpretation. Its display of the results in a hierarchical tree is especially useful for finding subcluster structures and discerning relationships.

6.2.1 Hierarchical clustering

The basic process of hierarchical clustering (based on Johnson, 1967) on a set of N n-dimensional items is the following:

1. Each item in the set is assigned to its own cluster. Thus the set contains N clusters, each containing just one item. The distances - or similarities in parameter space - between the clusters are equal to the distances between the items that each make up one cluster.

2. The most similar (i.e. the closest) pair of clusters is found by calculating all the distances. These two clusters are merged into a single cluster, diminishing the

[1]The similarities between items to be clustered are defined by their 'distances'. By distance, we refer to how far away one item is from another item, where the items are defined by a number of parameters. In a 3D parameter space, where one item is defined by (x_1, y_1, z_1) and another item by (x_2, y_2, z_2) the Euclidean distance between these two points is defined as $d = \sqrt{(x_2 - x1)^2 + (y_2 - y_1)^2 + (z_2 - z_1)^2}$.

number of clusters by one.

3. The distances are recalculated between the new cluster and each of the old clusters.

4. The second and third step are now repeated until all the items are clustered into a single cluster containing all N items.

There are a number of ways to calculate the distances between the clusters in the 3rd step. We use *Single linkage* which measures the shortest distance between any member of the cluster to any member of another cluster.

For the explorations presented here, we have used the MATLAB statistics toolbox. This toolbox includes functions that can perform hierarchical clustering on an n-parametric dataset. In particular, we used the functions *pdist* (to calculate the euclidian distances between items), *linkage* (to link items into clusters) and *dendrogram* (to visualize the results). Other tools are available to evaluate the results. I also developed a number of scripts to streamline the input of data and to visualize the results. An example of clustering 5 datapoints in 2 dimensions is shown in Figure 6.2

The result of the clustering is a reversed tree, where all items branch together to one single trunk. The cluster tree can be viewed in a *dendrogram*, which is probably the easiest way of understanding the hierarchy for the data points. Figure 6.3 shows a schematic dendrogram of the clusters in Figure 6.2. This 2D example can be extended to any number of dimensions. Here, we only needed to extend our parameter space to three dimensions, as described in § 6.3.

The algorithm will attempt to find all naturally occurring clusters in the data set, but one can also set a fixed number of clusters for it to search for. However, there are cases where a user might want to define a more sparsely populated area of the dataset as a cluster, which the automated process might have difficulties finding. A careful visual inspection can therefore be an important step in the clustering process. This is important

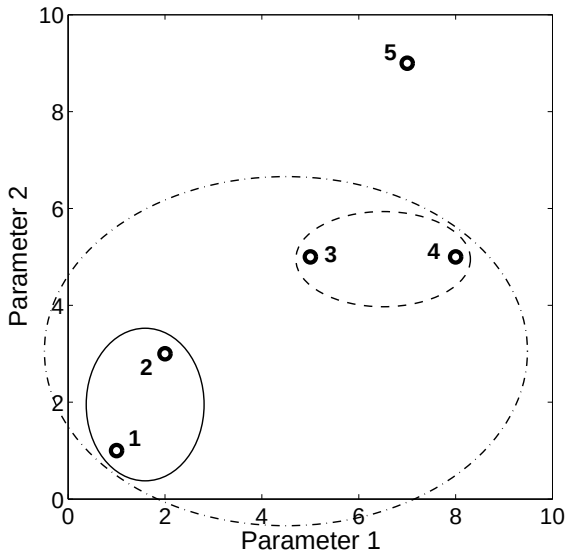

Figure 6.2: A schematic figure of how hierarchical clustering works. Data points 1 through 5 are clustered based on the distances between the points. The first clusters consist of each point individually. The second cluster consists of point 1 and 2 (solid ellipse), and the third cluster consists of points 3 and 4 (dashed ellipse). The fourth cluster consists of the 2nd and 3rd cluster (points 1-4, dash-dotted ellipse) and the last cluster consists of all points in the set. The sizes of the ellipses are arbitrary in this figure and are only used to illustrate the clusters.

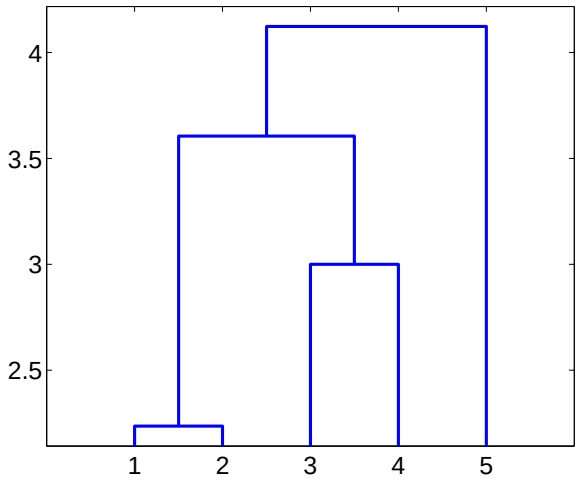

Figure 6.3: A dendrogram visualizing the cluster tree. The numbers along the horizontal axis are the indices of the data points shown in Figure 6.2. The data are connected by lines shaped as an upside-down U. The height of the U-shape represents the Euclidian distance between the objects in parameter space, given by the values on the vertical axis.

in this experiment as well, in order to confirm any natural clusters as well as potential subclusters.

6.3 Parameterised rotation curve

As has been described in chapter 4, a galaxy's rotation curve can be parameterised in the following manner:

$$v = v_0 \tanh\left(\frac{r}{r_{0,v}}\right)\left[1 + a_v\left(\frac{r}{r_{out}}\right)\right] \tag{6.1}$$

Eq. 6.1 is the same rotation curve form as is used in GalAPAGOS (see chapter 4), and includes four parameters; the maximum velocity v_0, the turnover radius $r_{0,v}$, the slope a_v of the rotation curve beyond the turnover radius, and the radius to the last data point, r_{out}. To make the rotation curves individually comparable, we scale the turnover radius by the galaxy radius r_{out}. This leaves us with 3-dimensional data to cluster. This manoever

does however require r_{out} to be sufficiently well determined (see further discussion on this in section 6.5.3).

6.4 Clustering tests on artificial data sets

To test MATLAB's hierarchical clustering functions and assess the efficiency of the algorithm, artificial data sets were created. In these datasets, numbers of parameters (i.e. the dimensionality) as well as total number of data points (i.e. number of galaxies) and number of clusters were varied. Both randomly generated clusters and clusters with predefined boundaries (but with random data within each cluster) were tested. The values of the mock data were chosen to mimic the three parameters of the analytic rotation curve. The goal was to assess how well the algorithm finds the clusters, and how many data points (galaxy rotation curves) that are required to discern potential clusters. It was found that while the clustering algorithm works well at low numbers of datapoints, it is much harder to discern potential clusters if the number of galaxies go below 60.

Figures 6.4 and 6.5 show an example of test results of a run using 60 data points in three dimensions designed with three clusters.

6.5 Data used for developing a rotation curve classification scheme

The tests in § 6.4 demonstrated that at least 60 galaxies are required to discern clusters. Since only 14 galaxies in total are analysed in this thesis, we supplemented this dataset with rotation curves culled from the literature.

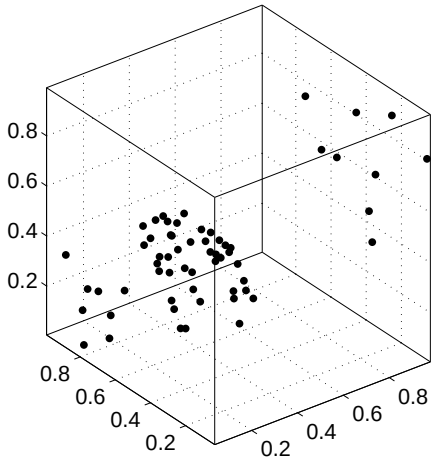

Figure 6.4: A 3D view of the artificial test data used to explore the hierarchical clustering algorithm. All three axes display normalised values.

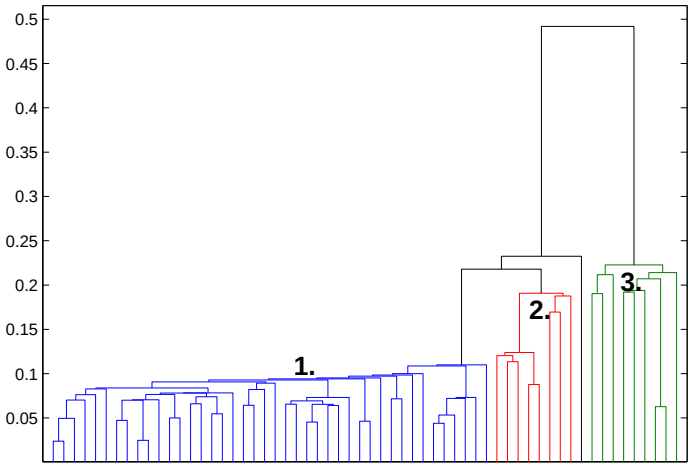

Figure 6.5: Dendrogram showing the hierarchical clustering of artificial test data displayed in Figure 6.4. The largest (1, blue) group is the centre cluster in Figure 6.4, with the closest neighbour cluster in the low left corner in red (2) and the top right cluster in green (3) at the far right in the dendrogram.

6.5.1 Sample selection

HI rotation curves for 105 spiral galaxies were initially collected from the limited number of published articles which present such curves. For the purpose of this investigation, it was important to use isolated spiral galaxies (Sa through Sd), with no history of interaction which might have substantially altered the intrinsic rotational behaviour of the galaxy. Galaxies indicated in the literature to be interacting were removed from the sample. Distorted spiral galaxies were also excluded.

After removing all clearly interacting galaxies and those that appear in data sets more than once, the resultant set (including our own data) consists of 79 galaxies. Some galaxies appear both in literature and in the data used in this thesis, making it possible to assess uncertainties in the extracted rotation curve parameters (see § 6.5.3). The galaxies were selected from the papers listed in Table 6.2.

Note that the galaxy rotation curves collected in one of these papers (Sanders (1996)) is not using original data but is a collection of rotation curves collected by the author from several references. We reference this paper here since we use the rotation curves as presented therein to derive the rotation curves for this work. Please see Sanders (1996) for references to the *original* data for each galaxy in the sample.

The literature claims that 42 of these galaxies are isolated or non-interacting. We designate these as Sample 1. The 17 galaxies of Sample 2 are well documented yet lack mention of isolation or interaction, and were deemed to be potentially non-interacting in spite of the mention of a nearby companion or an asymmetric morphology. We note that if there are asymmetries in a galaxy's rotation curve, this might be an echo of the galaxy's recent interaction history making it possible to distinguish an isolated galaxy from an interacting one. However, a large number (up to 50%) of apparently isolated field galaxies might show significant rotation curve asymmetries and lopsided HI profiles

Sample	Reference	# of RCs	Comments
a ...	Sanders (1996)	18	
b ...	García-Ruiz et al. (2002)	18	Edge-on galaxies
c ...	Sanders & Verheijen (1998)	23	Ursa Major galaxies
d ...	de Blok et al. (2008)	13	The THINGS survey
e ...	Hoekstra et al. (2001)	3	
f ...	Bottema & Verheijen (2002)	1	NGC 3992
g ...	Fraternali et al. (2005)	1	NGC 891
h ...	This work	14	GalAPAGOS rotation curves

Table 6.2: Rotation curves were extracted from these samples. Note that a galaxy might appear more than once in each sample, so the total number of individual galaxies (79) is less than the total in this list.

(e.g. Haynes et al., 1998; Richter & Sancisi, 1994). Thus, asymmetries in the rotation curve might not always be an implication of (recent) interaction, and the galaxies in Sample 2 exhibiting asymmetries might still be valid for our exploration. The remaining galaxies lacked sufficient information about interactions. Based upon their seemingly undisturbed morphology and lack of companions, these 20 were collected into Sample 3. The clustering algorithm was applied on Sample 1 alone as well as on all three samples together. Comparisons of these runs are in § 6.6.

Tables 6.3, 6.4, and 6.5 list these three samples including their references and the extracted rotation curve parameters.

6.5.2 Extracting rotation curve parameters from literature rotation curves

The values for the rotational velocity as a function of radius were carefully extracted from published plots[2] for all the galaxies in the samples. The analytical form of the

[2]using the 'rpp' method: ruler, pencil and patience

Name	ref	v_0	a_v	$r_{0,v}$
M33	a	115.16	0.6030	0.1158
NGC 0055	a	86.35	-0.0011	0.3484
NGC 0247	a	112.76	0.9471	0.1153
NGC 0300	a	95.87	0.2280	0.1949
NGC 0891	g	228.86	-0.0431	0.0061
NGC 0925	h, d	126	0.0200	0.3400
NGC 2403	h,d	141	0.1900	0.0800
NGC 2613	h	307.5	-0.1700	0.1000
NGC 2683	a	205.41	-0.3389	0.0575
NGC 2841	d,h	322	-0.2000	0.0100
NGC 2903	h,d	206	-0.1300	0.0600
NGC 2915	a	88.98	0.1893	0.0981
NGC 2976	d	82.62	0.0016	0.5557
NGC 2998	a	208.41	0.0267	0.0325
NGC 3198	h, d	155	-0.0700	0.1100
NGC 3351	h,d	202.2	-0.1500	0.0100
NGC 3510	b	88.17	0.0020	0.4001
NGC 3521	h,d	245	-0.2200	0.0140
NGC 3556	h	154.6	-0.4000	0.5600
NGC 3621	d, h	155.35	0.1958	0.0704
NGC 3877	c	168.92	-0.0302	0.2881
NGC 3917	c	134.12	-0.0983	0.3035
NGC 3972	c	128.78	-0.0016	0.3563
NGC 3992	c	267.89	-0.1417	0.1304
NGC 4096	h	147	0.0120	0.0160
NGC 4100	c	194.58	-0.3262	0.1908
NGC 4138	c	186.38	-0.3271	0.0955
NGC 4144	b	73.59	-0.0009	0.2671
NGC 4258	h	206	0.0000	0.0110
NGC 5033	a	224.48	-0.1270	0.0097
NGC 5055	h,d	212	-0.2100	0.0345
NGC 5371	a	221.53	0.0017	0.0124
NGC 5533	a	289.22	-0.2282	0.0041
NGC 5585	a	92.3	0.1272	0.2442
NGC 5907	a	226.05	-0.0807	0.0577
NGC 6503	e	115.77	0.0030	0.0390
NGC 6674	a	272.88	-0.1891	0.0443
NGC 7331	d,h	254	-0.1400	0.0400
NGC 7793	h,d	124	-0.029	0.3800
UGC 0128	a	132.79	0.1702	0.1638
UGC 7089	b	79.92	0.8858	0.1889
UGC 9242	b	96.61	0.6257	0.2892

Table 6.3: Sample 1 – 42 galaxies known to be isolated and/or non-interacting. The references are defined in Table 6.2 and refer to the paper with the published rotation curves which were used to derive the three RC parameters in columns (3), (4) and (5), which are velocity amplitude, RC slope and turnover radius, respectively.

Name	**ref**	v_0	a_v	$r_{0,v}$
NGC 0801	a	223.17	0.0019	0.0245
NGC 1003	a	115.28	0.3008	0.0784
NGC 1560	e	80.29	0.4549	0.2505
NGC 2770	b	165.71	-0.4147	0.6249
NGC 3600	b	94.81	0.2039	0.1111
NGC 3726	c	166.58	0.1015	0.1328
NGC 3949	c	169.34	0.0862	0.2727
NGC 3953	c	223.46	-0.0007	0.2045
NGC 4010	c	126.23	0.0047	0.3980
NGC 4013	c	190.19	-0.1464	0.0092
NGC 4051	c	168.41	0.4595	0.0626
NGC 4217	c	189.76	-0.1266	0.1872
NGC 5301	b	149.75	-0.1273	0.4155
NGC 6946	a,d	164.84	-0.0010	0.1372
UGC 2459	b	149.77	-0.1547	0.1204
UGC 2885	a	299.16	0.0912	0.0026
UGC 3909	b	76.31	-0.0027	0.2458

Table 6.4: Sample 2 – 17 well-documented galaxies with no mention of interaction. These are placed in Sample 2 due to an apparent companion or asymmetry, which might be signs of interaction.

Name	**ref**	v_0	a_v	$r_{0,v}$
NGC 3118	b	101.52	-0.0026	0.4195
NGC 4157	c	192.49	-0.0961	0.1078
NGC 4183	c	109.91	0.0000	0.1336
NGC 4389	c	107.87	-0.0287	0.9027
NGC 5023	b	84.38	-0.0638	0.2864
NGC 5229	b	53.97	0.0786	0.2037
UGC 1281	b	54.65	-0.3282	0.7850
UGC 2259	e	93.25	0.3538	0.1099
UGC 3137	b	106.84	-0.0885	0.1509
UGC 5459	b	130.93	-0.1604	0.2584
UGC 6399	c	87.85	0.0010	0.4170
UGC 6446	c	85.11	0.2697	0.1251
UGC 6667	c	87.7	0.1776	0.3415
UGC 6818	c	74.52	-0.0441	0.7455
UGC 6917	c	110.87	0.2965	0.2333
UGC 6930	c	110.38	0.1485	0.1817
UGC 6983	c	108.96	0.0492	0.1737
UGC 7321	b	104.07	-0.0781	0.3621
UGC 7774	b	88.47	-0.0721	0.3510
UGC 8246	b	62.78	0.2194	0.2648

Table 6.5: Sample 3 – these 20 galaxies appear to be non-interacting but lack sufficient information to determine conclusively whether they really are isolated and non-interacting.

rotation curve in equation 6.1 was fitted to these data, using a simple unconstrained linear optimization method, *fminsearch*, available in MATLAB. This fitting procedure finds the best fit of a function of several variables to a number of data point values. For each galaxy, the extracted RC data points were fed into a script which I designed to call the *fminsearch* optimizer. *fminsearch* was given an initial guess to start iterating, and the resulting parameters – v_0, $r_{0,v}$ and a_v – were saved in a matrix which subsequently was fed into the script handling the clustering algorithm.

The galaxies and their fitted rotation curve parameters are listed in Tables 6.3, 6.4, and 6.5.

Figure 6.6 shows 74 of the rotation curves from the literature. These are overlaid with the analytical rotation curves that were fitted to them. 12 RCs from the literature are included to be compared to those from GalAPAGOS in order assess uncertainties. An additional five RCs are derived using GalAPAGOS and are not included in the figure.

6.5.3 Uncertainties

Datasets of the same galaxy available from different sources were used to assess errors introduced due to e.g. low number of datapoints in the rotation curve, different cut-off for the rotation curves (due to different values of the HI radius r_{out}) as well as measurement errors. Table 6.6 lists comparisons between GalAPAGOS parameters, with the corresponding parameters from published rotation curves in the same samples that were utilised in this survey. Some galaxies have more than one additional reference, and in those cases we have chosen to compare to de Blok et al. (2008) since the same data (THINGS) were used in both their and our analyses. In the future, it would be valuable to compare with additional publications for parameters such as velocity amplitude, turnover radius and outer radius. But we note, for example, that the outer radius of NGC 7793 by Dicaire et al. (2008) is 480″, which is consistent with the 7% uncertainty listed in Table 6.6.

		v_0 (km/s)		a_v		$r_{0,v}$ (scaled)		r_{out} ($''$)		
Galaxy	Ref	TW	Other	TW	Other	TW	Other	TW	Other	%
NGC 55 (H)	(a)	86	86	0.11	0.00	0.21	0.35	1330	1263	5
NGC 925	(d)	126	116	0.02	0.00	0.34	0.52	500	291	42
NGC 2403	(d)	141	137	0.19	0.19	0.08	0.08	1400	1160	17
NGC 2841	(d)	322	316	-0.20	-0.16	0.01	0.04	872	512	41
NGC 2903 (I)	(d)	206	210	-0.13	-0.20	0.06	0.06	658	672	2
NGC 3198	(d)	155	148	-0.07	0.00	0.11	0.06	547	568	4
NGC 3521	(d)	245	225	-0.22	-0.28	0.014	0.09	915	598	35
NGC 3621	(d)	146	155	-0.09	0.20	0.08	0.07	728	812	12
NGC 4096 (W)	(c)	147	149	0.01	0.00	0.05	0.22	186	210	13
NGC 5055	(d)	212	208	-0.2	-0.20	0.03	0.05	928	980	6
NGC 7331	(d)	254	253	0.14	0.12	0.04	0.06	493	351	29
NGC 7793	(d)	115	113	-0.29	-0.34	0.38	0.27	440	410	7

Table 6.6: TW refers to This Work and Other refers to the literature referenced in column (2) (following the references in Table 6.2). v_0 is half of the velocity amplitude, or the maximum rotational velocity, a_v is the slope of the rotation curve and $r_{0,v}$ is the turnover radius which is scaled to r_{out}, the outer radius. The letter after the galaxy name in column (1) refers to those cases when other data than THINGS data were used for the analysis in this work: (H) is HIPASS, (I) is VLA data donated by J. Irwin and (W) is data from WHISP.

Outer radius The radius of the HI disk is uncertain, in that it is hard to determine how individual authors have chosen this radius. Ideally, we would like to define r_{out} to a certain column density similar to how the size of a galaxy is defined using a faint isophote for optical data (e.g. D_{25}). That is, we would select the furthest radius associated with a low column density (e.g. $5\times10^{19}cm^{-2}$, based on a common column brightness sensitivity). Obviously this is not possible when relevant information is not available in the literature data.

The maximum deviation in the value of r_{out} has (surprisingly) been found in comparing the rotation curves derived in this work with those of de Blok et al. (2008) - for which the same data have been used. Upon examining this discrepancy in detail, we found that for a few galaxies, the THINGS team have chosen to discard extended faint emission in the outskirts of the galaxy, while it was included in this work. This might be due to their cutoff in the velocity fields at the 3σ level (3 times the rms noise). GalAPAGOS has however chosen a shorter r_{out} for NGC 3621. This is a galaxy for which the outer HI gas is very distorted and thus GalAPAGOS considers it to be anomolous gas that cannot be included in the galaxy model. For the most discrepant cases, NGC 925 and NGC 2841, the reasons for the high differences are not clear. The GIPSY analysis performed for NGC 925 also resulted in a higher outer radius ($\sim400''$), similar to that of Pisano et al. (1998).

While the slope a_v and the rotation amplitude v_0 can be mildly affected by r_{out}, the largest impact is on the turnover radius $r_{0,v}$, since we have chosen to scale it by the outer radius. An increase in r_{out} leads to a decrease in $r_{0,v}$, in terms of percentage.

Turnover radius Typically, the difference between our estimate and that from literature is 44%. Apart from the effect on the turnover radius by r_{out}, $r_{0,v}$ is obviously also sensitive to the number of data points tracing the turnover in the rotation curve.

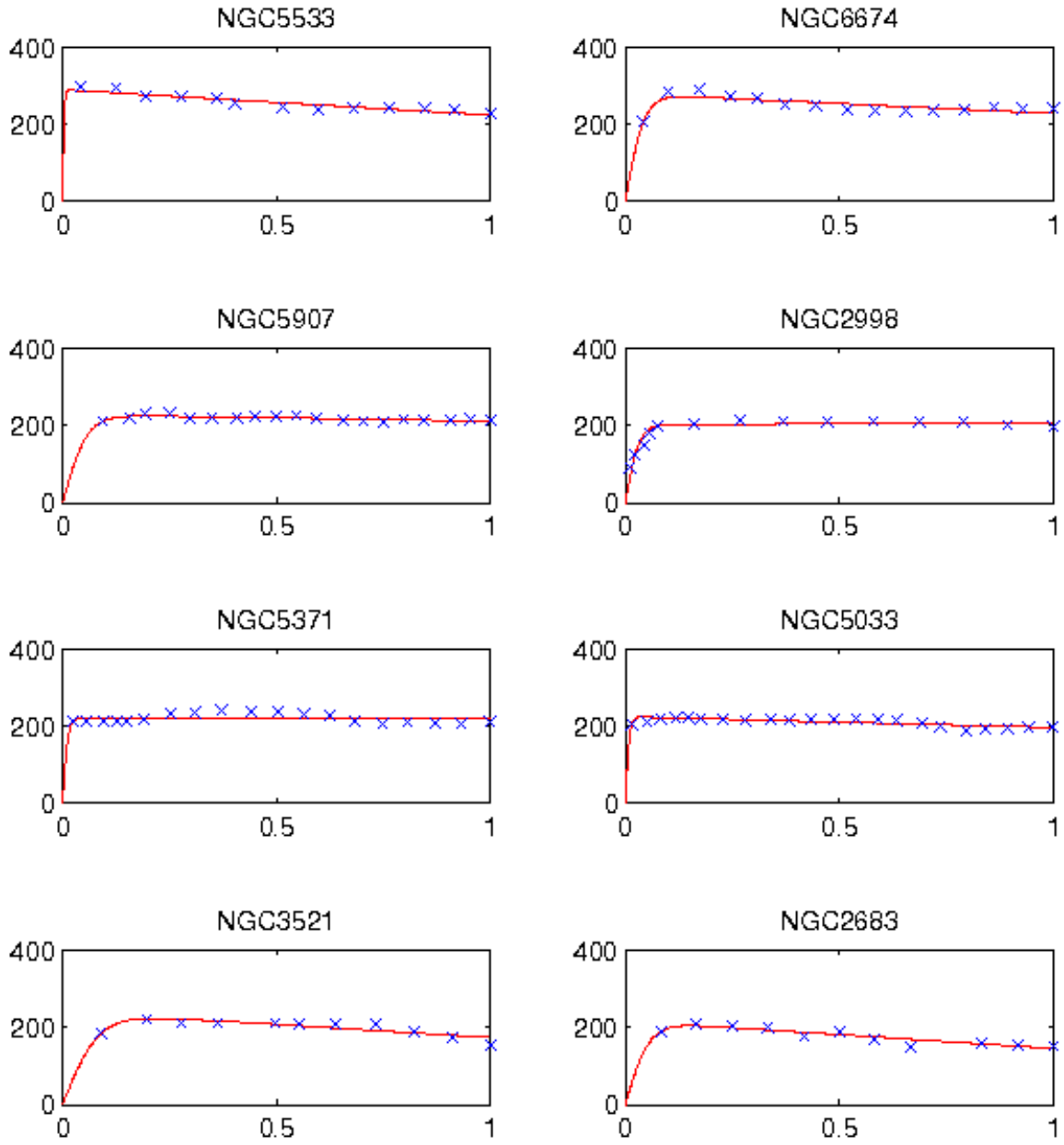

Figure 6.6: The rotation curve function in eq. 6.1 is fitted to the rotation curve data points for the galaxies listed in tables 6.3, 6.4 and 6.5. The horizontal axis is the radius, normalised to the last measured datapoint (r_{out}. The vertical axis is the velocity in units of km/s.

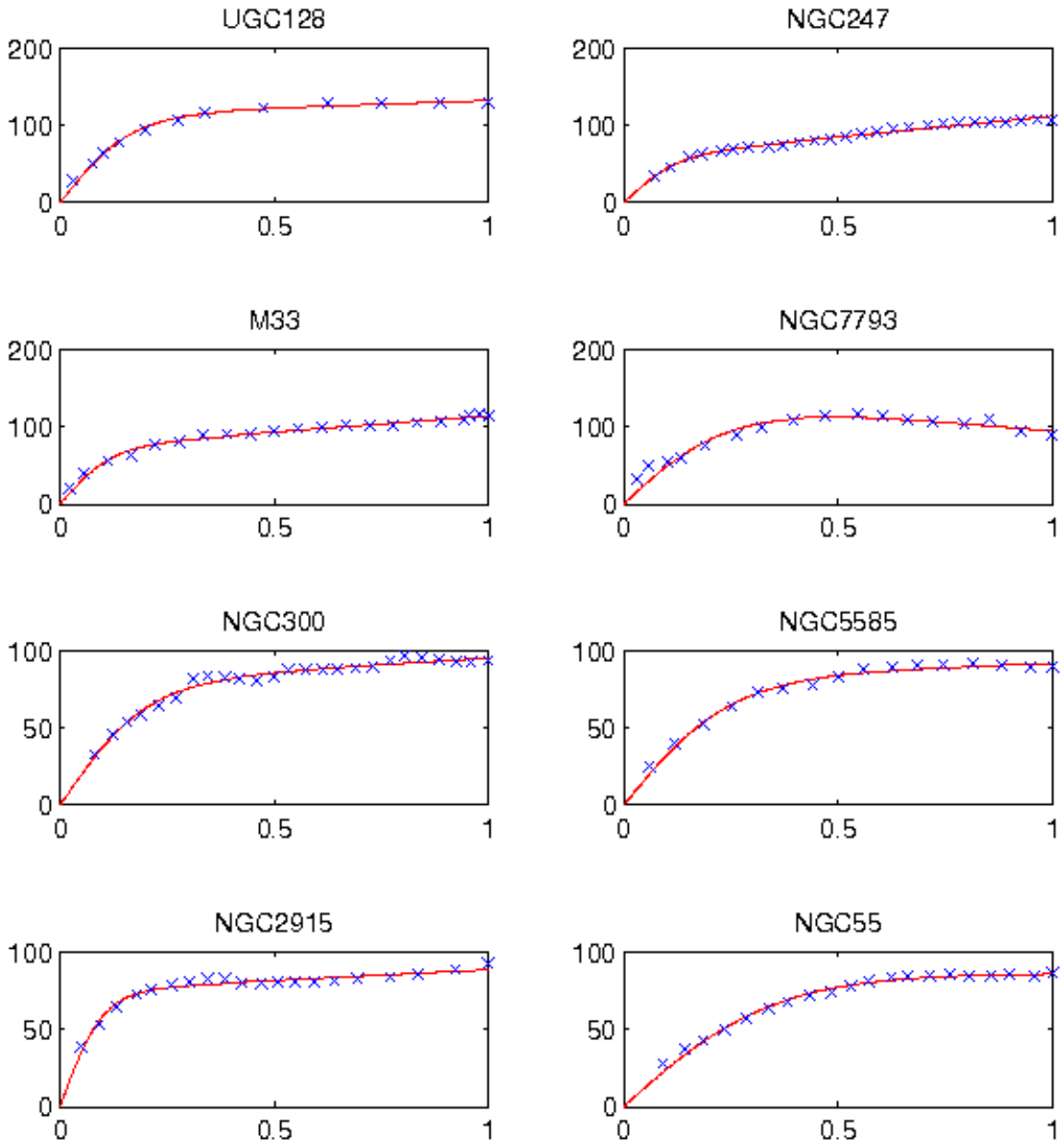

Figure 6.6 (continued)

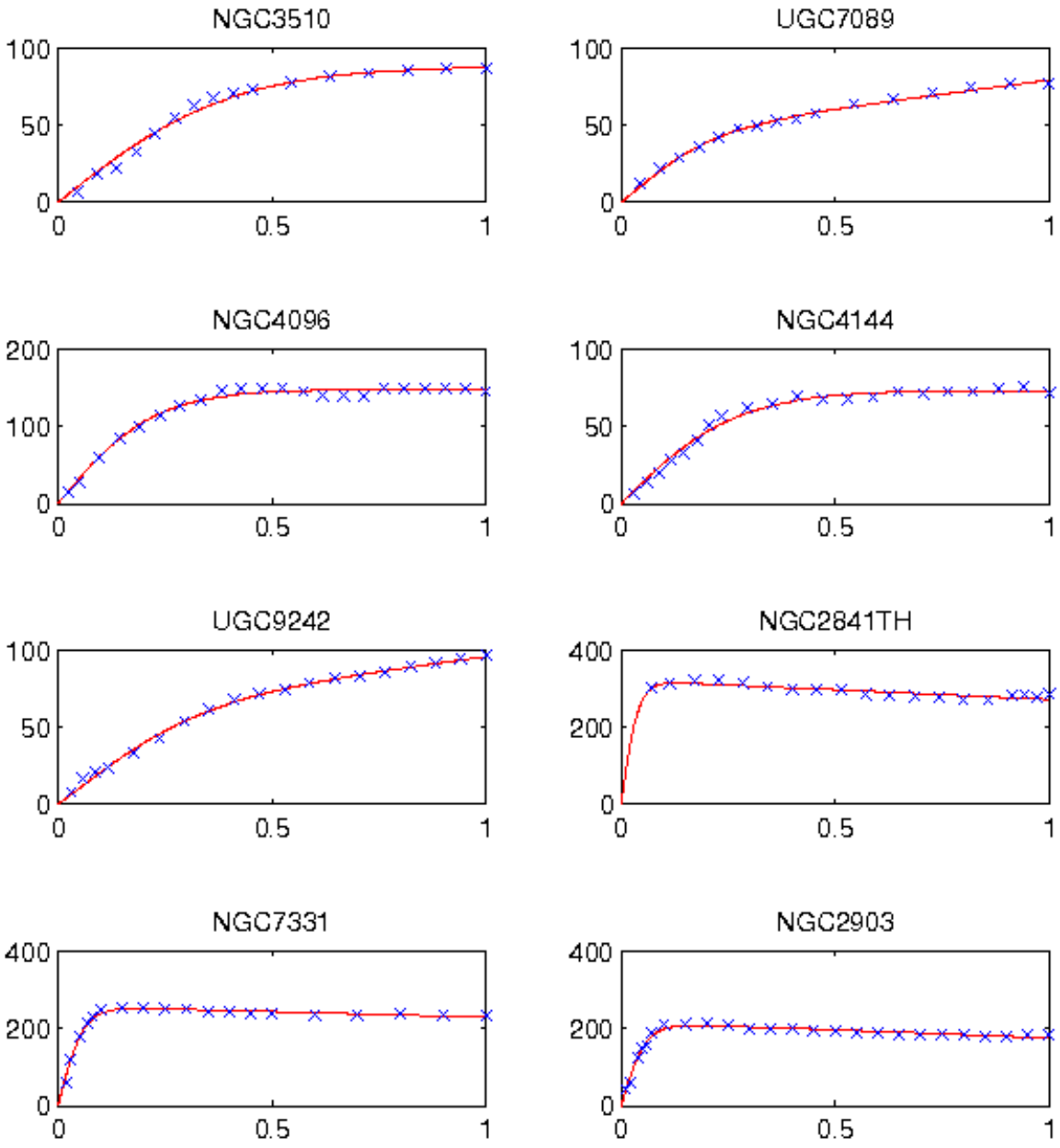

Figure 6.6 (continued)

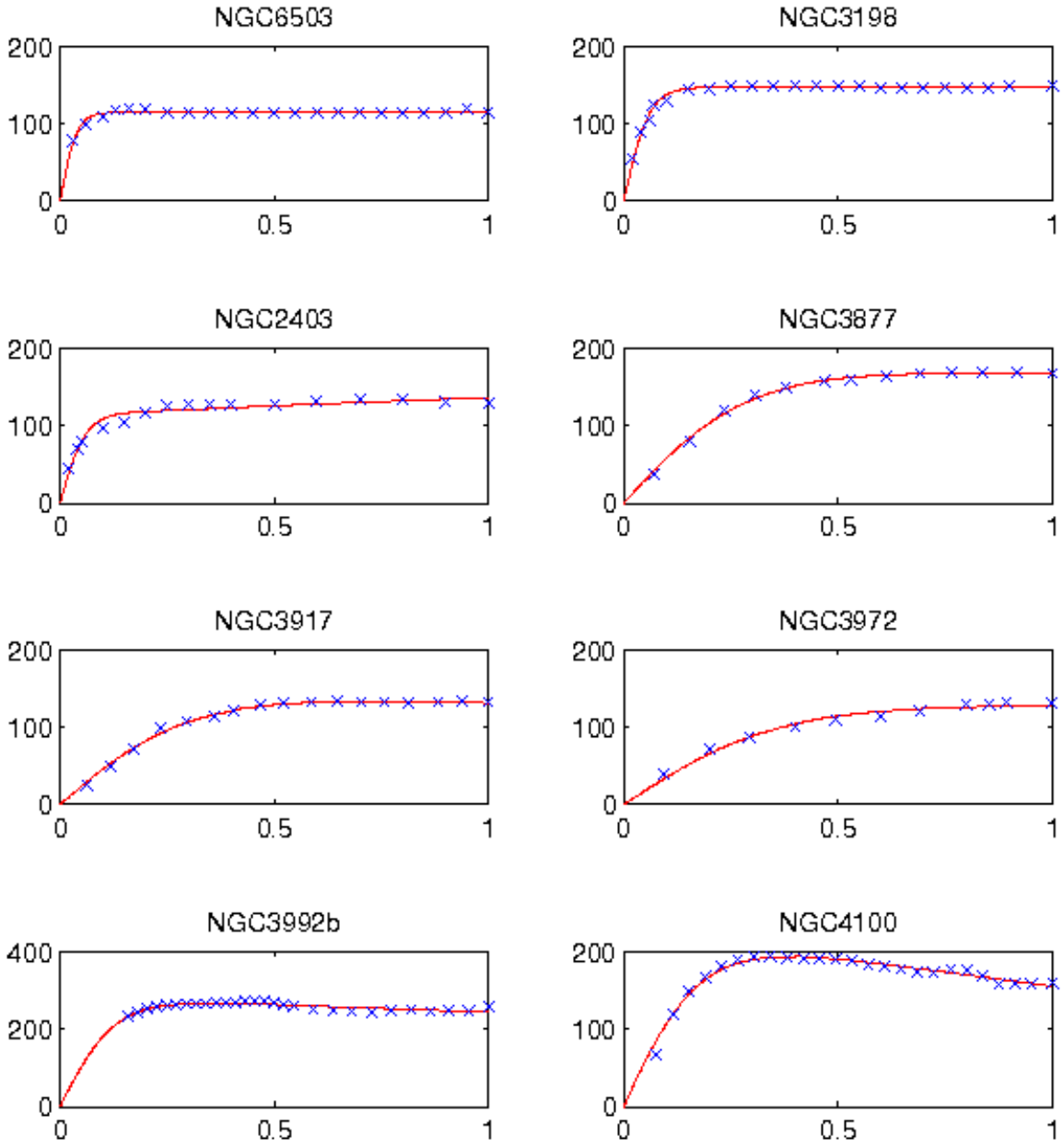

Figure 6.6 (continued)

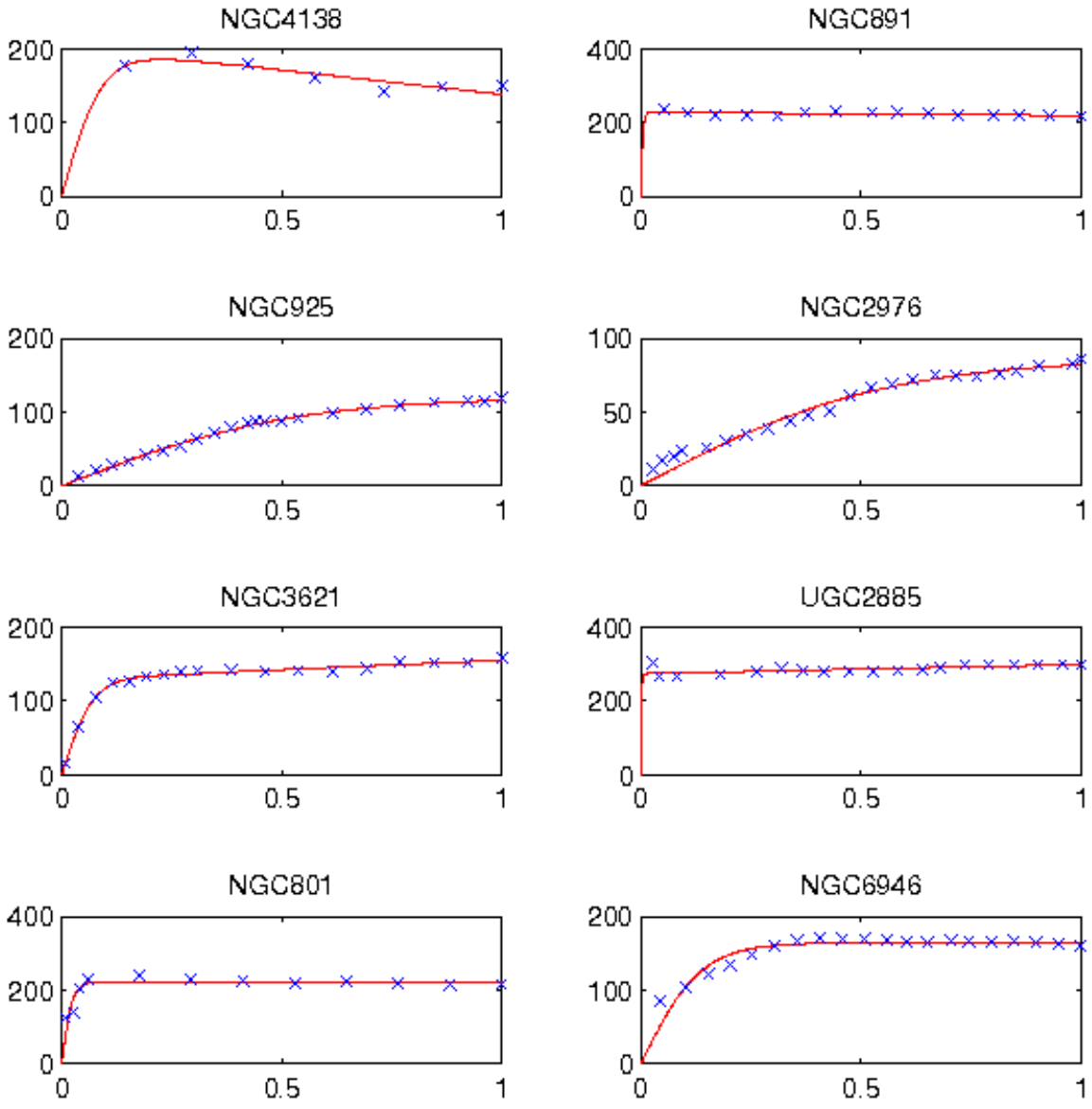

Figure 6.6 (continued)

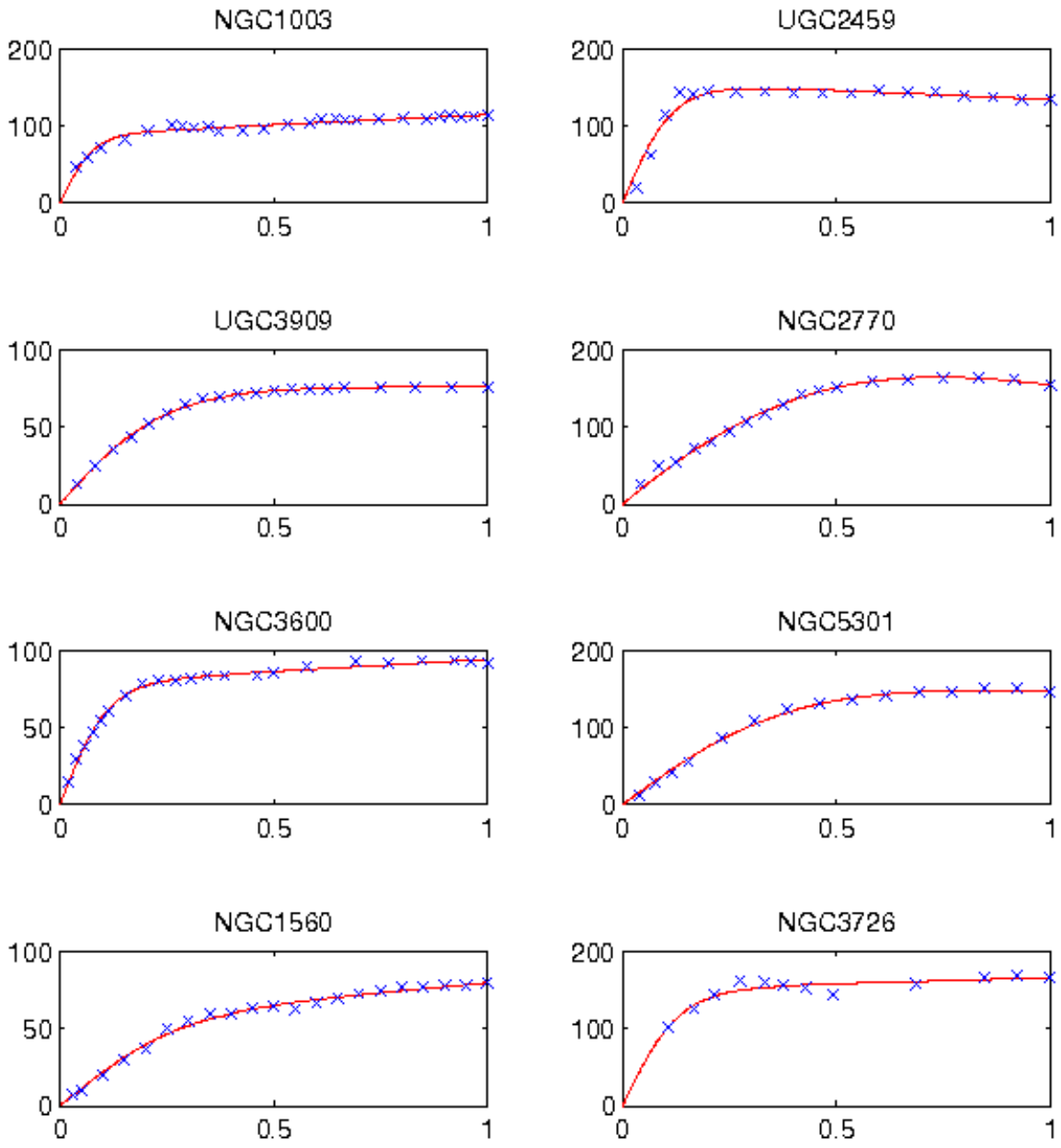

Figure 6.6 (continued)

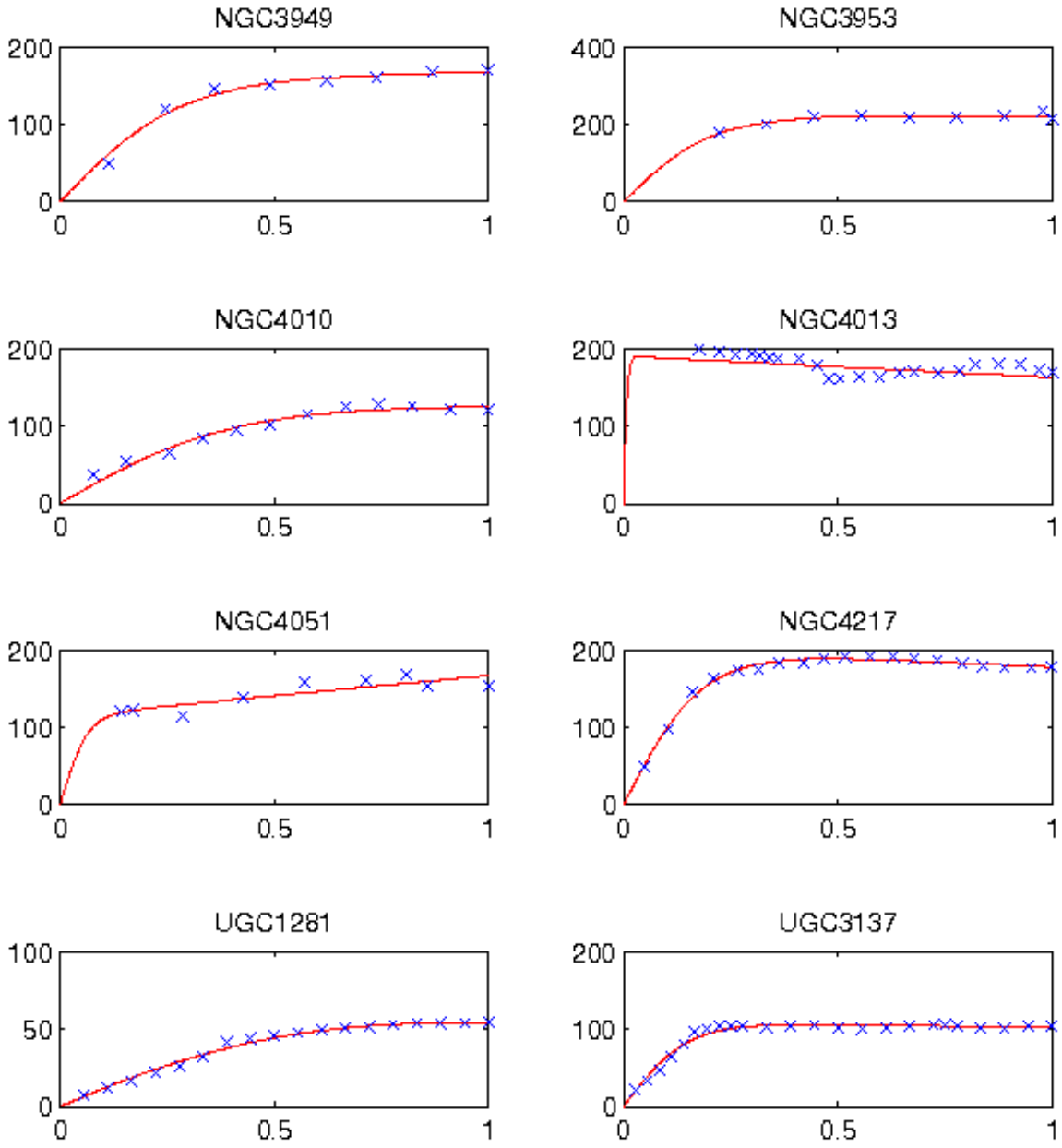

Figure 6.6 (continued)

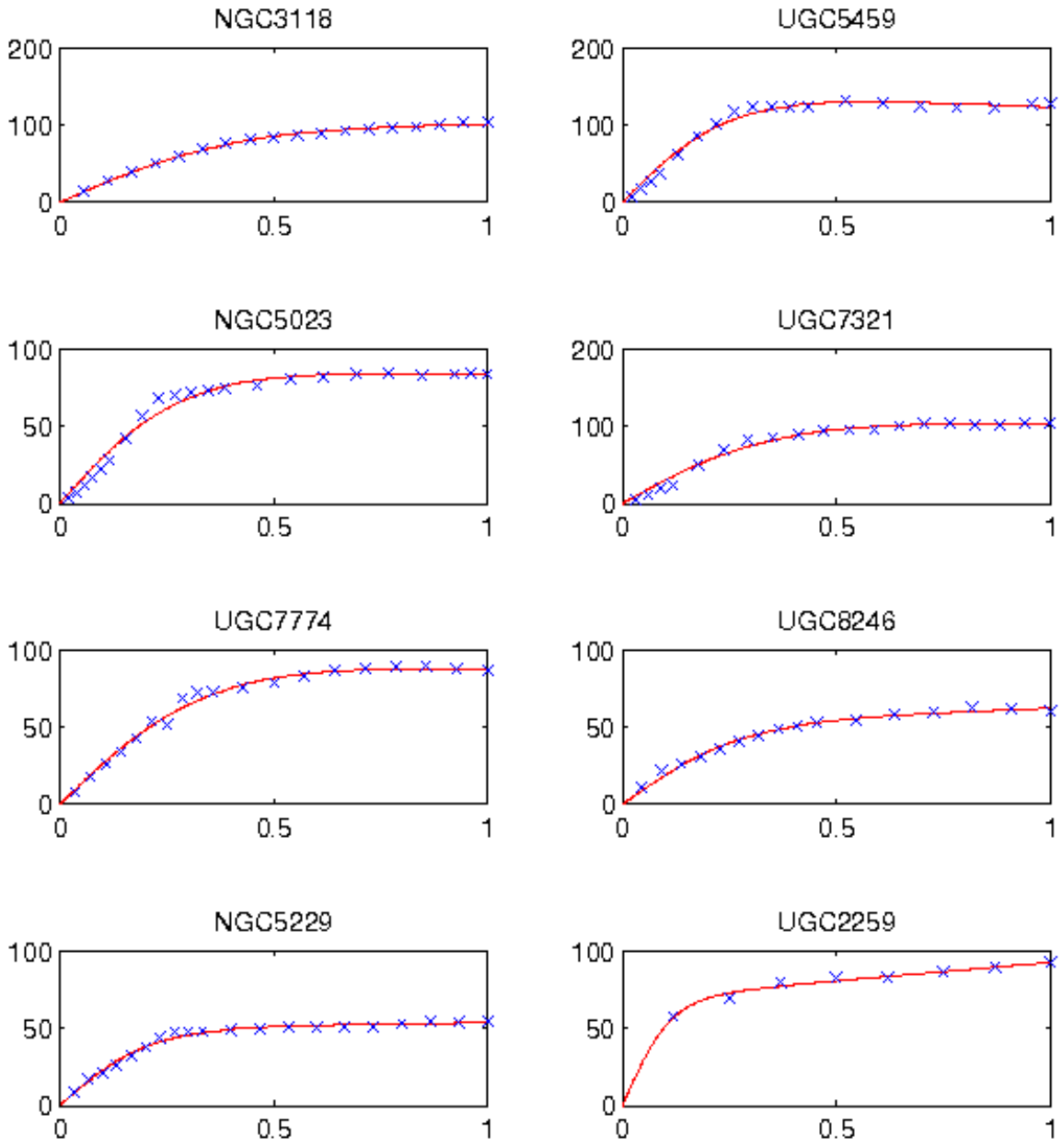

Figure 6.6 (continued)

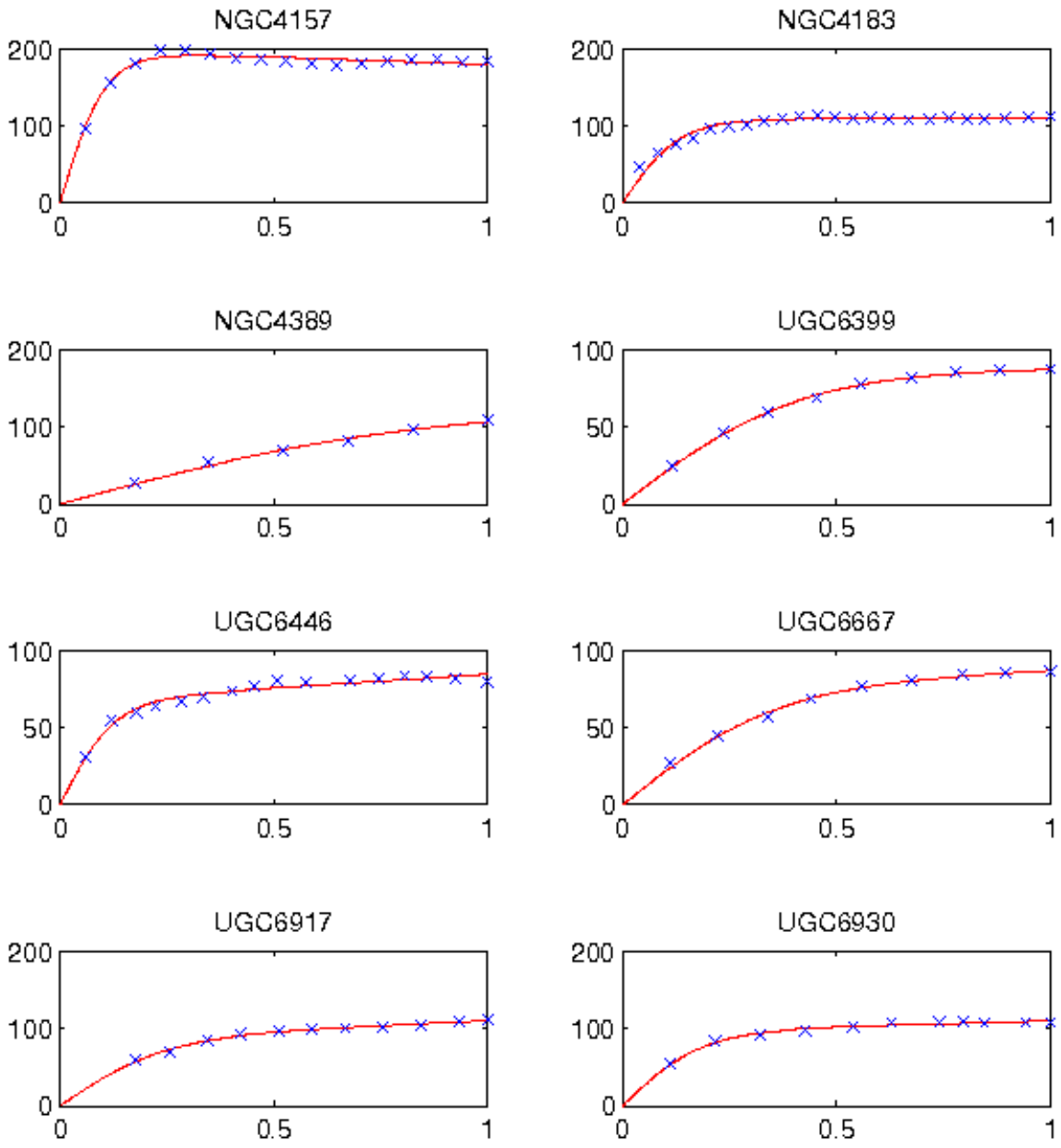

Figure 6.6 (continued)

NGC 4013 is an illustration of such a case. For most galaxies in our samples, the centre is however well enough described to avoid this problem. Another factor that could potentially have a large impact is the ability to find the centre of the galaxy while measuring the rotation curve from HI data. The difference between the rotation curves for NGC 2903 measured by Hoekstra et al. (2001) and de Blok et al. (2008) might suffer from this scenario, partly resulting in an uncertainty of almost 50% for the turnover radius. Note that the short turnover radii for galaxies NGC 2841 and NGC 3521 are due to a badly defined inner region due to binning (see Chapter 5), and these values have not been used in the classification. Instead we used GIPSY derived values, which agree more with the literature values.

Velocity We find that the value of maximum velocity v_0 generally varies by 3%. If it is very different, such as in the case of NGC 6946 that we measured using data by Carignan et al. (1990b) (from the Sanders (1996) sample), and de Blok et al. (2008), where the difference in $v0$ is as high as 19%, a choice was made based on which method is considered most reliable. A subsequent comparison was made to see if a change in this parameter resulted in a change of RC classification. The result was that the ranges of the classes were slightly altered, but the classification remained. In the case of NGC 6946, the cause of the discrepancy is believed to be due to different choices of galaxy inclination when measuring the rotation curve (de Blok et al., 2008). Another versions of this rotation curve exists measured by Boomsma (2007), with values similar (within 3%) to that of the Carignan et al. (1990b) data which is the one we adopt. Generally, inclinations are well defined, and situations like this are uncommon. NGC 6946 is an almost face-on galaxy ($32^\circ - 38^\circ$ inclination) which might explain the difficulty in constraining the inclination and consequently the velocity.

Slope a_v, the parameter that describes the slope at radii beyond the turnover radius, is the parameter most sensitive to correctly transcribing the published rotation curves. The sensitivity is also inversely proportional to the length of the turnover radius. In other words: the longer the turnover radius, the larger the range of slope values that can be allowed without considerably affecting the resultant rotation curve fit. Thus caution should be noted when looking at a slope value alone to define the behaviour of a galaxy - it should at least always be accompanied by the turnover radius as well. For instance, NGC 3556 is a galaxy with a negative A_v value. It is however also accompanied by a large turnover radius (more than 50% of the HI radius). The behaviour after the turnover radius might in fact only be an apparent decline due to the bar, possibly causing a 'hump'.

6.6 Classification - clustering classes

The hierarchical clustering was performed on the extracted rotation curve parameters by letting a script feed the parameters (after normalisation) into the 'pdist' function in MATLAB, as described in § 6.2.1. Pdist calculated the distances between the data points after each call of the 'linkage' function which linked the clusters, one by one, until the entire linkage tree could be displayed using the function 'dendrogram'. The results could then be analysed, using both the matlab analysis tools, as well as visual inspection

The script was run on the the galaxies from all three samples listed in Tables 6.3, 6.4 and 6.5, as well as on the assumed non-interacting galaxies in Sample 1 alone.

Figures 6.7 and 6.8 display the result of the clustering of the full set of 79 galaxies. When displaying v_0, a_v and $r_{0,v}$ in three dimensions (Figure 6.8), the data points form a shape ressembling a scorpion. The most distinct cluster is the tail, which consists of high rotational velocity galaxies. We have designated this group A, where 'A' is the amplitude

of the velocity. Slightly lower velocities tend to spread out like a curved torso towards higher values of turnover radius and slope, making up two groups designated AS and AT ('S' for slope and 'T' for turnover). There are a few low velocity galaxies that visually indicate the presence of two 'claws', one for rotation curves with high slopes and one with long turnover radii. These claws are not designated a natural cluster by the clustering functions, since the points are fairly widely spread in these regions. Nevertheless we designate them T, for the turnover radius 'claw' and S for the slope 'claw'. Hereafter, we refer to the 3D structure formed by the data point distribution in v_0, a_v and $r_{0,v}$ as the 'scorpion plot'

Figures 6.10 and 6.9 show the cluster tree and the 3D figure (with the clusters marked in the same way as in Figure 6.7) of the 42 confirmed non-interacting galaxies in Sample 1. With the smaller sample, the A galaxies have remained the same. However, the difference between groups AS and AT is less visible, with the AT galaxies clustered as a sub-group of AS. Only one of the outliers is part of Sample 1, and has been given a C classification. The shape of the scorpion is otherwise the same, with each group represented in the less populated version. This encourages us to believe the structure of the version using all galaxies from the three samples, and the rest of the analysis is performed on the full set of galaxies.

The following classes were found, with characteristic values listed in Table 6.7

	v_0 (km/s)			$r_{0,v}(/r_{out})$			a_v		
Class	min	max	mean	min	max	mean	min	max	mean
A	186	322	229	0.004	0.19	0.05	-0.34	0.03	-0.15
AS	85	167	119	0.02	0.42	0.14	-0.15	0.35	0.11
AT	54	134	100	0.20	0.42	0.33	-0.29	0.08	-0.04
T	55	166	107	0.56	0.9	0.7	-0.41	0.002	-0.20
S	80	115	97	0.12	0.29	0.19	0.45	0.95	0.70

Table 6.7: Minimum, maximum and mean values of the rotation curve parameters of the galaxies in the different kinematic classes.

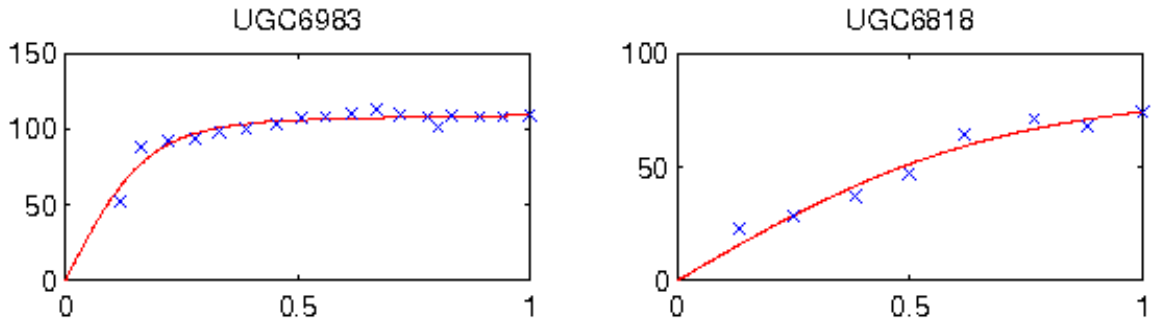

Figure 6.6 (continued)

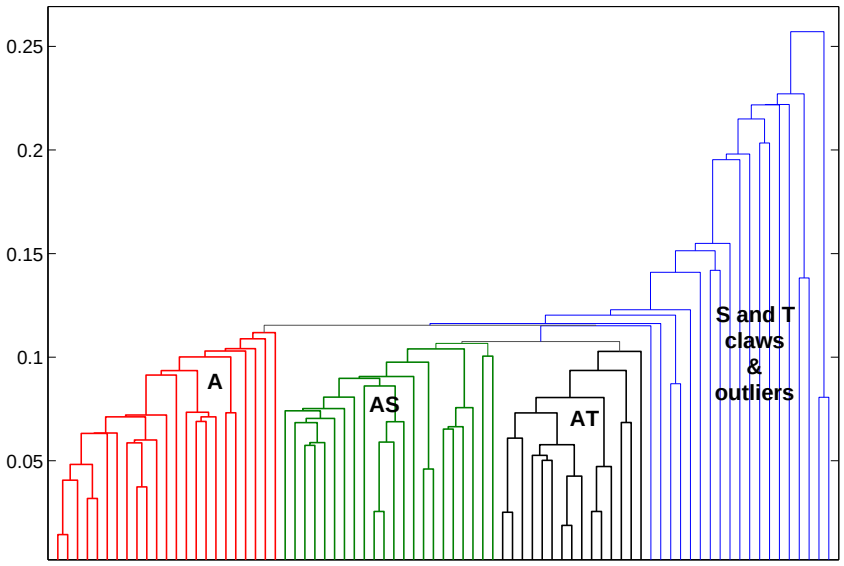

Figure 6.7: A cluster tree showing the similarities between the three rotation curve parameters of the 79 galaxies in the sample. Class A (red connectors) consists of galaxies with high rotational velocities, low slope values and short turnover radii. The "claws" are shown among the outliers (blue connectors)

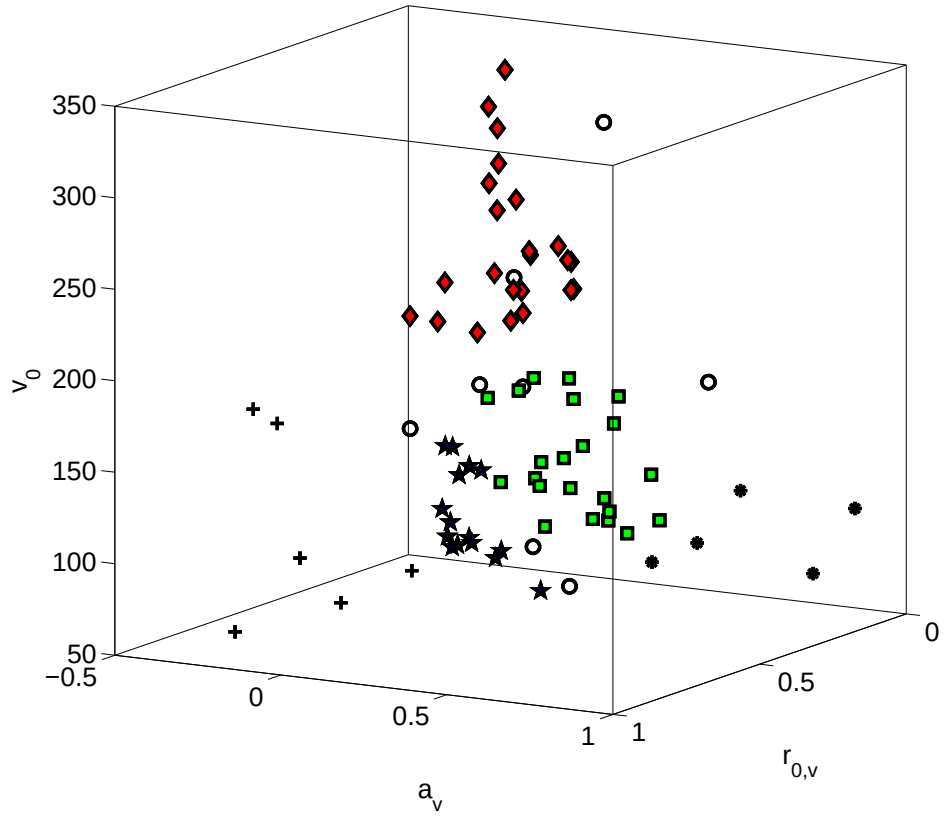

Figure 6.8: Division of galaxies into kinematical classes. Red diamonds ("tail of the scorpion") = Class A, green squares = Class AS, black stars = Class AT, '+'-sign = Class T, black dots = Class S. Circles are outliers.

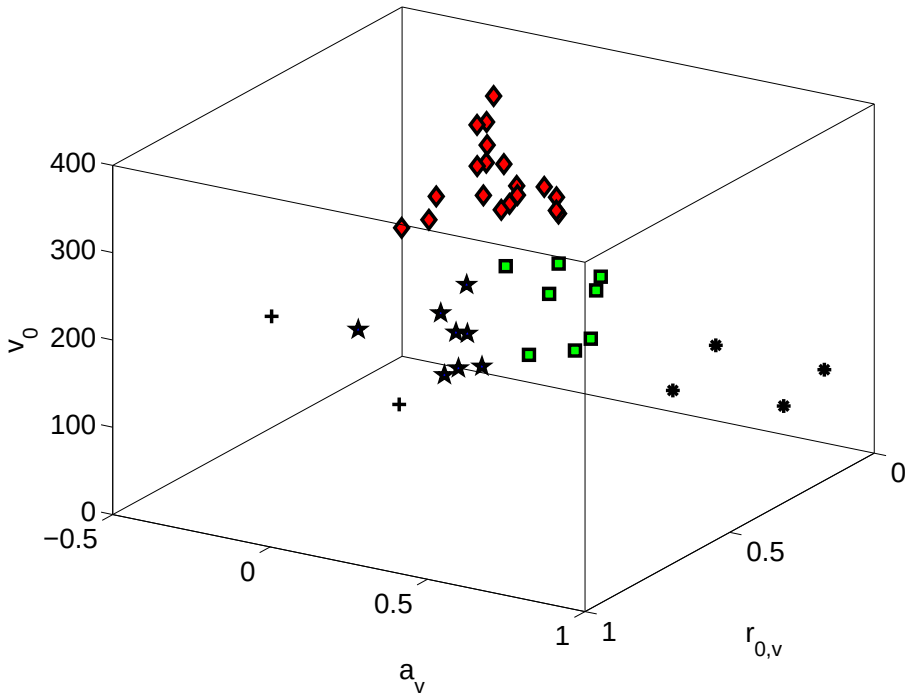

Figure 6.9: The three velocity parameters for each of the 42 galaxies documented to be isolated or non-interacting. The classes found by the clustering algorithm are indicated by symbols: Red diamonds = Class A, green squares = Class AS, black stars = Class AT, '+'-sign = T, black dots = S.

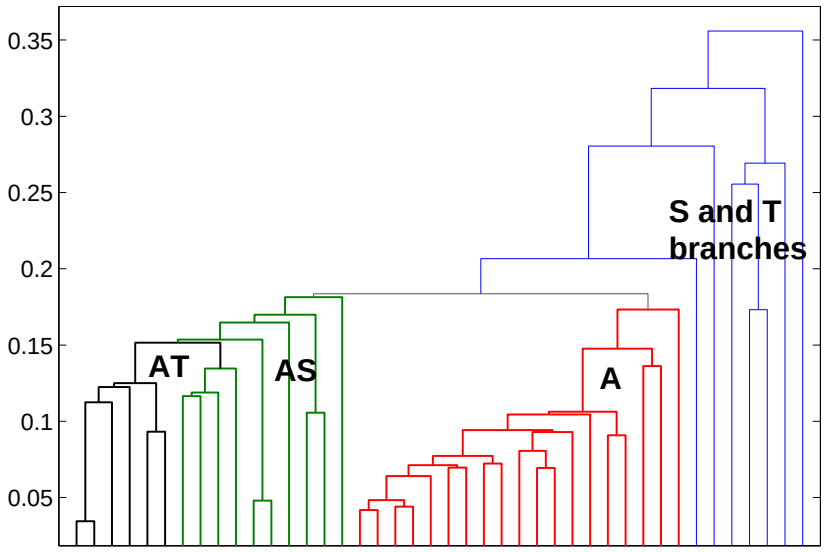

Figure 6.10: A cluster tree showing the similarities between the galaxies in Sample 1.

Class A The most distinct group is the "tail of the scorpion" which consists of fast rotating galaxies, with short turnover radii and the lowest slope values. All of these exhibit flat or even seemingly declining rotation curves, such that 70% of the group have an a_v value below -0.1, 30% below -0.2 and 13% below -0.3.

Class AS This group has lower velocities, flat rotation curves and somewhat longer turnover radii than the A class.

Class AT This class and the two 'claws' (S and T) have similar velocity ranges. Its galaxies have flat slopes and in some cases slightly negative a_v values. In contrast to A, the turnover radii are the longest of the three classes.

Class T This class could be seen as an extension to Class AT; low velocities, flat slopes with some negative a_v values, but very high turnover radii.

Class S Similarly, the slope branch could be interpreted as an extension to Class AS

albeit with lower velocities; intermediate turnover radii and highly increasing slopes.

Outliers The outliers are individually described in Table 6.8.

Galaxy	v_0 (km/s)	$r_{(0,v)}$	a_v	**Comment**
NGC3877	169	0.29	-0.03	close to AS and NGC 3949. Classified as a AT in Sample 1.
NGC3949	169	0.27	0.09	close to AS and NGC 3877
NGC3953	223	0.20	0	A with long turnover radius
NGC4051	168	0.06	0.46	High-velocity 'void' galaxy, close to slope branch
NGC5301	150	0.42	-0.13	AT or turnover branch
UGC2885	299	0.003	0.09	A with increasing rotation curve
UGC6667	88	0.34	0.18	'void' close to AT
UGC8246	63	0.26	0.22	'void', AT or AS

Table 6.8: Eight galaxies classified as outliers. The 'void' refers to the empty area between the S branch and T branch where galaxies with both high turnover radius and increasing slope would fall.

Is the scorpion shape a natural shape, or due to selection bias? There is a void in the centre between the two 'claws', where the galaxies exhibiting both large turnover radii in combination with strongly rising curves (high slope values) would exist. Galaxies with such rotation curves do exist - they are often irregulars, dwarfs or interacting (indeed, some of the interacting galaxies that were excluded from the sample presented here were pairs with such rotation curves, e.g. NGC 5107 from Sanders (1996), and NGC 3109 and DDO170 from Hoekstra et al. (2001)). There are at least 10 dwarf galaxies in our sample, which reside in classes AS, AT as well as S and T, some bordering the void. A few of the outliers listed in Table 6.8 are also present in the 'void'. As an answer to the question above, one guess could be that non-interacting galaxies avoid the void, while interacting ones are more commonly part of it. This needs however be confirmed by studying the RCs of a sample of galaxies confirmed to be interacting.

6.6.1 Cluster uncertainties

As was previously described (section 6.5.3), the uncertainty in r_{out} plays a large role for the value of the turnover radius, leading to an average uncertainty of 18%, with a the most extreme case at 44%. There is also an intrinsic uncertainty for both the turnover radius and the slope parameter originating in the fitting of the parameters to the rotation curve data points, but which is typically much lower, on the order of 1-5%. Applying these uncertainties to the data would leave the velocity axis at about the same values (uncertainty $\sim$ 3%), but result in a shifting in the $r_{0.v}$-a_v-plane. The shifting could affect classes AS and AT causing the already fine distinction between these two classes to disappear, and they might be considered one class. Although the "claws" would be affected in equal amounts, they would still be present.

6.7 Correlations between classifications and galaxy properties

A number of galaxy characteristics were explored in order to find or confirm correlations like those listed in Table 6.1 in § 6.1. For the bulk of the galaxies, these include: absolute B magnitude, luminosity class, size of optical disk D_{25}, morphological type, presence of bar, HI content and mass ratio of gas mass over dynamical mass. Additionally, the analysis in Chapter 5 gives us disk scale length and halo mass properties for 11 galaxies in the sample. Table 6.9 lists the galaxies according to their kinematic class, with the values used to investigate these correlations. The following sections describe these values and the correlations in more detail.

For a number of these correlation investigations, it is necessary to know the distance to the galaxy. It is used both for converting the galaxy radius to *kpc* as well as for

determining the HI mass and star formation rates. The distance is the source of the largest uncertainty in these calculations. We use Tully-Fisher determined distances for the galaxies from García-Ruiz et al. (2002), which they deemed to be more accurate than virgocentric inflow model distances. Still, García-Ruiz et al. (2002) estimate an uncertainty of up to 30% for these distances. For these and the other galaxies included in this analysis, the distances are listed and referenced in Table 6.2.

Table 6.9

Galaxy	Class	T	Bar	D_{25}	M_B	LC	SFR	M_{HI}	M_{dyn}	M_{ratio}
	(2)	(3)	(4)	(5)	(6)	(7)	(8)	(9)	(10)	(11)
NGC0801	A	5.3		64.2	-22.0		2.46	1.94	64.5	23.7
NGC0891	A	3		36.0	-20.2	5	0.64	0.27	20.7	53.9
NGC2613	A	3.2		57.4	-21.8	3	0.61	0.91	72.3	56.6
NGC2683	A	3		14.1	-21.1	4	0.04	0.03	9.7	203.6
NGC2841	A	3		28.3	-20.8	1	0.19	0.57	94.2	118.3
NGC2903	A	4	B	30.9	-20.9	2	1.04	0.27	21.5	56.2
NGC2998	A	5.2	B	47.6	-21.7	2.3	2.59	1.6	42.4	18.9
NGC3351	A	3.1	B	19.6	-20.2	3	0.11	0.07	12.0	115.9
NGC3521	A	4	B	20.6	-21.1	3	0.47	0.28	33.0	85.4
NGC3992	A	4	B	36.4	-21.2	1		0.3	38.8	93.3
NGC4013	A	3		22.0	-19.4	5	0.27	0.14	18.0	91.9
NGC4100	A	4.1		20.6	-20.6	2	0.35	0.18	11.7	46.5
NGC4138	A	-0.9		13.2	-18.7		0.14	0.08	8.4	73.7
NGC4157	A	3.3	B	28.1	-19.8	3	1.31	0.35	20.3	41.6
NGC4217	A	3		24.5	-20.0	5	0.85	0.12	10.6	63.5
NGC4258	A	4	B	38.2	-21.1	3.9	0.42	0.41	24.9	43.8
NGC5033	A	5.1		34.1	-20.9	2	0.51	0.38	30.9	57.7
NGC5055	A	4		24.8	-21.2	3	0.4	0.26	22.0	60.2
NGC5371	A	4	B	39.4	-22.1	1	1.42	0.75	41.5	39.3
NGC5533	A	2.4		45.0	-21.6	1.9	1.03	1.88	87.7	33.3
NGC5907	A	5.4		36.2	-21.0	3	0.19	0.42	34.1	58.5
NGC6674	A	3	B	57.1	-21.6			2.25	94.6	30
NGC7331	A	3.9		39.2	-21.6	2	1.36	0.67	4.1	4.3

Continued on next page...

Galaxy	Class	T	Bar	D_{25}	M_B	LC	SFR	M_{HI}	M_{dyn}	M_{ratio}
	(2)	(3)	(4)	(5)	(6)	(7)	(8)	(9)	(10)	(11)
NGC0300	AS	6.9		12.1	-19.2	6		0.22	2.5	8.1
NGC1003	AS	6		11.9	-19.5	5	0.05	0.35	9.5	19.3
NGC2403	AS	6	B	18.5	-19.7	5	0.02	0.18	9.9	40.1
NGC2915	AS	0.6		3.0		9		0.07	3.1	30.1
NGC3198	AS	5.2	B	25.9	-20.5	3	0.13	0.56	18.6	23.9
NGC3600	AS	1		6.2	-17.8		0.02	0.1	2.8	20
NGC3621	AS	6.9	B	18.8	-20.5	5.8	0.14	0.4	15.3	27.1
NGC3726	AS	5.1	B	23.8	-20.6	2	0.18	0.33	17.1	36.8
NGC4096	AS	5.3	B	16.8	-20.3	4	0.16	0.11	4.6	29.7
NGC4183	AS	5.9		19.3	-19.7	5.9	0.02	0.19	5.4	19.9
NGC5585	AS	6.9	B	9.4	-18.5	7.1		0.11	2.2	13.9
NGC6503	AS	5.9		9.0	-18.6	4.8	0.03	0.05		
NGC6946	AS	5.9	B	19.6	-20.9	1.3	0.19	0.74	17.7	17
UGC0128	AS	8.1		31.2				0.57	15.7	19.6
UGC2259	AS	7.8	B	4.7	-16.0	6		0.04		
UGC2459	AS	7.8		24.6			0.11	0.8	22.4	20
UGC3137	AS	4.3		37.4	-17.6	6		0.84	15.1	12.9
UGC6446	AS	6.6		6.4	-17.2	5		0.16	2.0	8.8
UGC6917	AS	8.8	B	11.3	-18.5	5		0.11	2.6	16.6
UGC6930	AS	6.6	B	6.4	-18.3	5		0.15	3.9	17.9
UGC6983	AS	5.8	B	8.6	-18.4	5		0.14	3.8	18.6
NGC0055	AT	8.8	B	13.9	-17.8	5.5		0.13	1.7	9.2
NGC0925	AT	7	B	28.4	-20.1	4	0.02	0.35	0.8	1.7
NGC3118	AT	4.1		13.1	-18.4		0.06	0.21	2.4	8.3

Continued on next page...

Galaxy	Class	T	Bar	D_{25}	M_B	LC	SFR	M_{HI}	M_{dyn}	M_{ratio}
	(2)	(3)	(4)	(5)	(6)	(7)	(8)	(9)	(10)	(11)
NGC3510	AT	8.6	B	4.0	-17.6	4	0.01	0.06	0.8	9.6
NGC3917	AT	5.8		20.8	-19.9	5.9		0.09	5.3	39.8
NGC3972	AT	4	B	16.6	-18.9		0.04	0.06	3.0	37.7
NGC4010	AT	6.9	B	13.8	-19.1		0.14	0.15	3.1	14.3
NGC4144	AT	6	B	9.1		5	0.01	0.03	0.6	13.4
NGC5023	AT	6		14.5				0.06	1.7	19.4
NGC5229	AT	6.8	B	8.6			0.05	0.08	0.7	6.4
NGC7793	AT	7.4		11.8	-18.9	6.3	0.01	0.06	3.8	47.2
UGC3909	AT	5.8	B	11.6	-17.1			0.19	1.9	7.2
UGC5459	AT	5.2	B	17.5	-19.4		0.11	0.2	6.8	25
UGC6399	AT	8.8		9.7	-17.7			0.05	1.2	19.3
UGC7321	AT	6.6		20.9				0.15	3.2	15.2
UGC7774	AT	6.3		12.0	-16.5			0.17	2.5	10.4
M33	S	5.9		15.2	-19.4	4		0.2	2.8	9.8
NGC0247	S	6.9	B	16.0	-18.6	6.9	0	0.08	2.9	25.9
NGC1560	S	7		8.3			0	0.03		
UGC7089	S	7.9		10.3	-17.8			0.04	0.9	14.7
UGC9242	S	6.6		15.4	-19.8			0.05	2.3	31.8
NGC2770	T	5.3		21.1	-20.7		0.2	0.26	6.8	18.8
NGC2976	T	5.2		6.0	-18.1	7	0.01	0.01	0.4	29.6
NGC3556	T	6	B	13.4	-20.7	5.9	0.86	0.34	9.2	19
NGC4389	T	4.1	B	11.3	-18.4	7	0.14	0.04	1.3	26.1
UGC1281	T	7.5		7.7				0.02	0.3	13.9
UGC6818	T		B	7.9	-16.3			0.06	0.8	8.8

Continued on next page...

Galaxy	Class	T	Bar	D_{25}	M_B	LC	SFR	M_{HI}	M_{dyn}	M_{ratio}
	(2)	(3)	(4)	(5)	(6)	(7)	(8)	(9)	(10)	(11)
NGC3877	O	5.1		24.2	-20.4	4	0.29	0.09	6.4	49.9
NGC3949	O	4		10.2	-19.9	5.9	0.84	0.17	4.1	17.4
NGC3953	O	4	B	27.7	-21.4	1.1	0.15	0.17	14.5	62.5
NGC4051	O	4	B	22.0	-20.0	3	0.67	0.16	5.8	26
NGC5301	O	4.7	B	25.9	-19.8	4	0.24	0.3	7.1	17
UGC2885	O	5.2		98.9	-22.0		1.92	3.38	149.6	31.6
UGC6667	O	5.9		5.6	-17.8			0.05	1.2	17.3
UGC8246	O	5.9	B	14.0	-17.1			0.12	0.9	5.1

Table 6.9: A list of the galaxies and their classes, with values for galaxy characteristics included in subsequent correlation analysis. Column (2): Kinematic class; (3) de Vaucouleurs revised morphological type from the Second Catalogue of Bright Galaxies (RC2); (4) Presence of bar; (5) optical diameter of galaxy, measured out to to the 25 mag/$''^2$ isophote [kpc]; (6) absolute B-band magnitude; (7) Luminosity class; (8) Derived star formation rate [$M_\odot$/yr]; (9) Derived HI mass [$\times 10^{10} M_\odot$]; (10) Derived dynamical mass [$\times 10^{10} M_\odot$]; (11) Ratio of dynamical mass over gas mass (where the gas mass is the HI mass scaled by 1.4 to correct for He and molecular gas content). Data in columns (3), (4), (5), (6) and (7) come from the extragalactic database HyperLEDA (Paturel et al., 2003). The derivation of the values in columns (8), (9), (10) and (11) is described in § 6.7.

Absolute B magnitude

The first investigation serves as a 'sanity check' of the rotation curve data – all literature, including of course the Tully-Fisher relation, agree on the correlation between the

rotational velocity of a galaxy and its luminosity, in which more luminous galaxies also have high rotational velocities. The absolute B magnitude is available in the extragalactic database HyperLEDA for all the galaxies in the sample except for nine. These values were added as a 4th dimension onto the 'scorpion' plot, by normalizing the values onto a 0–1 scale. A colour shade, corresponding to absolute magnitude, was assigned to each data point. The left side of Figure 6.11 shows this plot and features a clear correlation. The scatter would be even less if corrections for inclination and Galactic extinction were applied, however, this is adequate to see the trend.

Although not plotted, this correlation is also present for the luminosity class. Luminosity class is a classification based on galaxy luminosity in combination with the degree of development of spiral arms, a classification that was introduced by van den Bergh (1960). The values listed in Table 6.9 are on a scale from 1-11, where 1 = supergiant galaxy, 3=bright giant galaxy, 5 = normal giant galaxy, 7 =subgiant galaxy , 9 = dwarf galaxy.

Morphology

We investigate the potential correlation of the morphological type (Hubble type) and the rotation curve parameters. According to Noordermeer et al. there is disagreement whether there is a correlation between morphology and rotation curves. It has been shown that early type galaxies (Sa, Sb, and Sc) show a correlation with decreasing maximum rotational velocity (Rubin et al., 1985), but they did not find any correlation with any other rotation curve properties.

The morphological type is expressed in numbers in the de Vaucouleurs system (RC2). The galaxies in our sample range from -0.9 to 8.8, where -0.9 corresponds to early type S0, through Sa (1), Sab (2), Sb (3), Sbc (4) etc to later types Sc (5), Sd(7) and Sm (9, Magellanic type). The values in column (3) of Table 6.9 come from HyperLEDA.

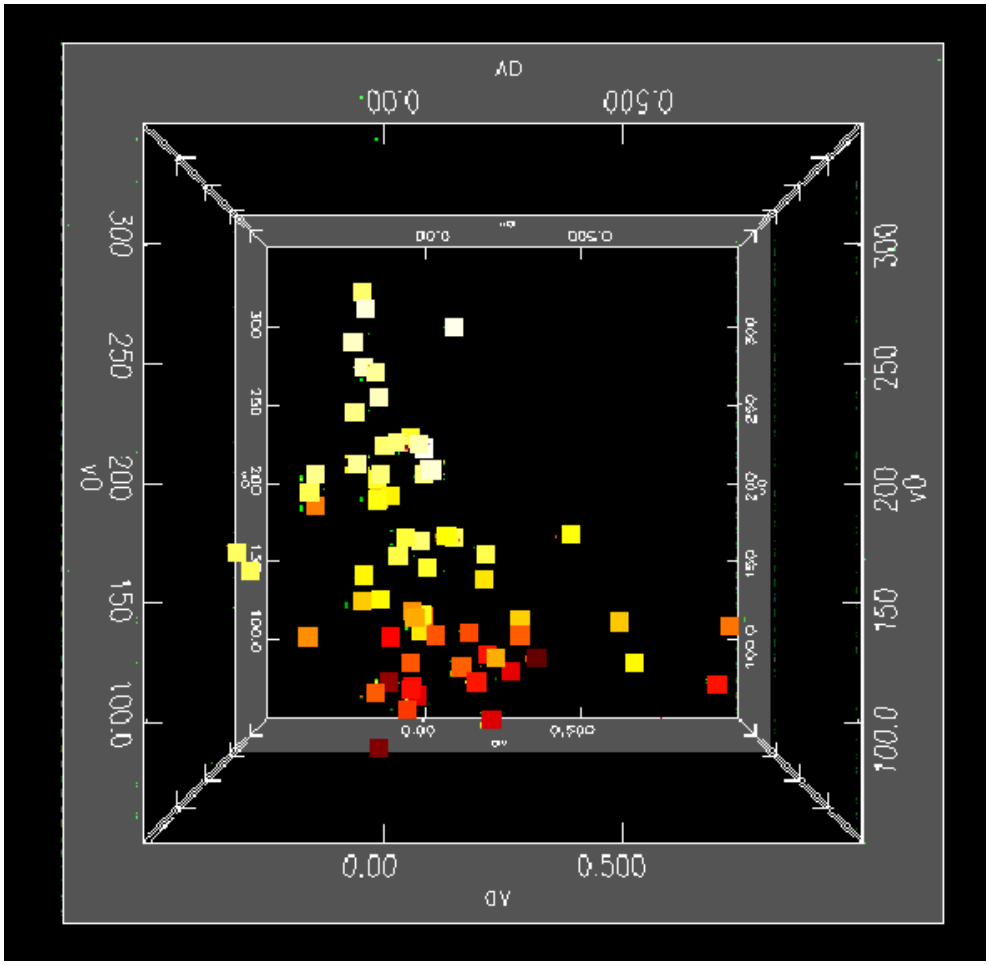

Figure 6.11: The 'scorpion' plot in 3 dimensions (vertical axis = v_0, horizontal axes = $r_{0,v}$ (side) and a_v (front)) with the data points coloured by the B magnitude. Light colour (white, yellow) correspond to bright galaxies and darker colours (red) correspond to fainter galaxies.

Figure 6.12 shows the morphology displayed as colours on 78 (the information is not available for one of the galaxies) of the datapoints of the 'scorpion' plot, where bright colours correspond to early-type (low values) galaxies and darker colours correspond to late-type (higher values) galaxies. The correlation with velocity is clear, but it is hard to say anything conclusive about the turnover radius and the slope. The majority of the A class galaxies are Sb. There is a bit of a scatter for the T class which includes Sbc to Sd galaxies. The AS, AT and S classes consist mainly of Scd galaxies with the surprising exception of two S0 galaxies in the AS class; NGC 3600 and NGC 2915. Figure 6.13 which shows morphology as a function of class further illustrates the results.

Size of optical disk D_{25}

A strong correlation between the size of the optical disk and rotation curve is found by Chattopadhyay & Chattopadhyay (2006). D_{25} is defined as the length of the projected major axis at the isophotal level $25 mag/''^2$ measured in the B-band. We retrieved the D_{25} values from the HyperLEDA database, measured as angular sizes for all galaxies in the sample. These values have not been corrected for galactic extinction. Using the galaxy distances listed in Tables 6.3, 6.4, and 6.5, the diameters were converted to units of kpc, and their values are visualized as the colours of the the data points in Figure 6.14.

We can confirm the strong correlation between D_{25} and the maximum velocity. Perhaps a more interesting parameter to investigate is the scale length – see a brief discussion in § 6.7

Bar

Despite the indication of a weak correlation between the presence of a bar and rotation curve shape found by Chattopadhyay & Chattopadhyay (2006), there was no such correlation noticed for these galaxies, as can be discerned directly from Table 6.9. Note however

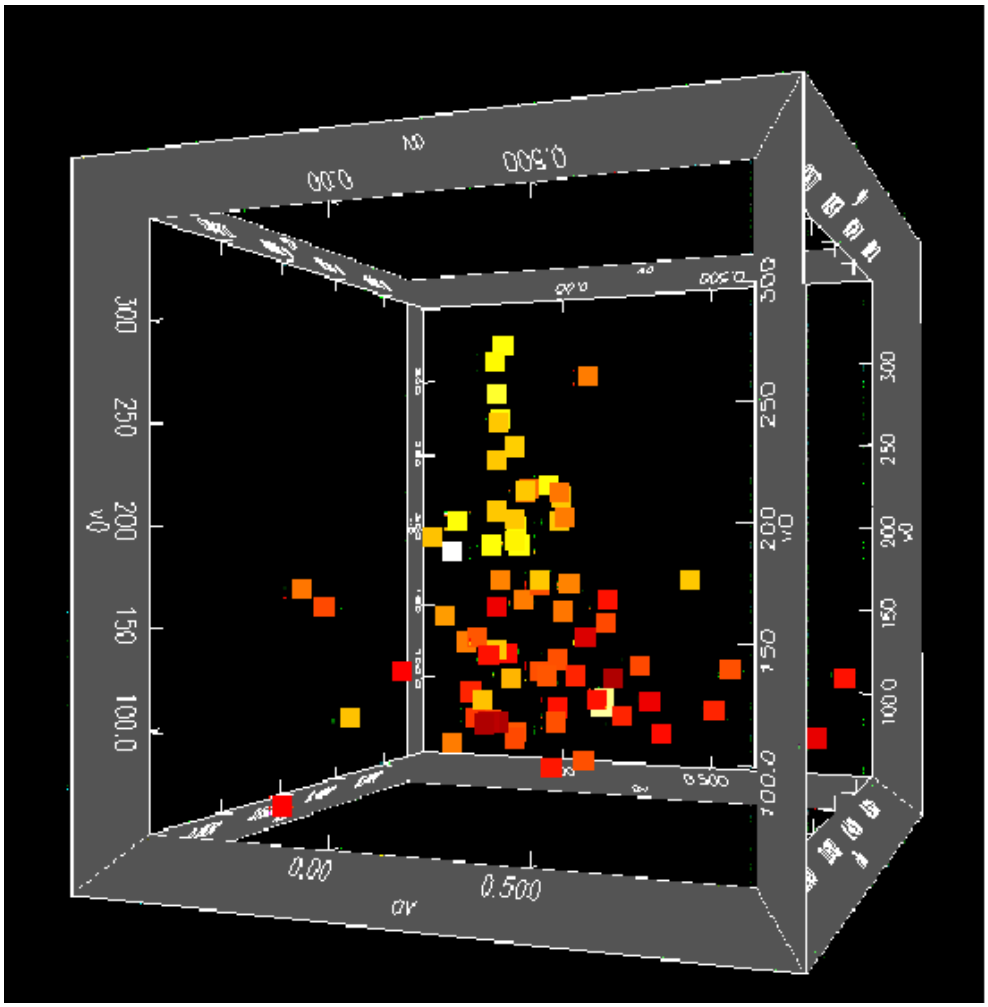

Figure 6.12: The 'scorpion' plot in 3 dimensions (vertical axis = v_0, horizontal axes = $r_{0,v}$ (side) and a_v (front)) with the data points coloured by the morphological type. Light colours (white, yellow) correspond to early type galaxies (Sa, Sb) and darker colours correspond to later type galaxies (Sc, Sd).

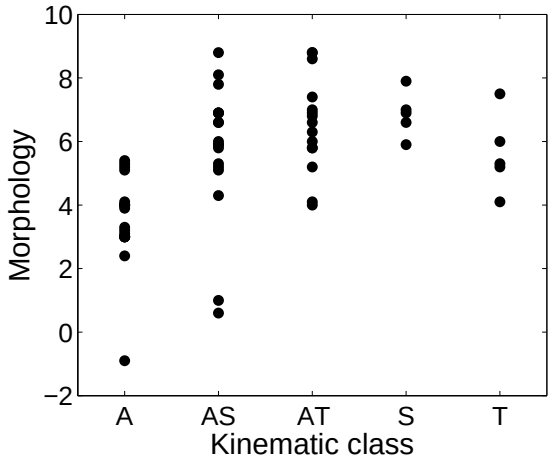

Figure 6.13: Kinematic class plotted against morphological type in the de Vaucouleurs RC2 system.

that we do not examine the inner part of the rotation curve (its slope) in detail. The inner part is here only determined by the turnover radius parameter. Also, the possible 'hump' at the turnover that can indicate a bar is not visible in the rotation curves of our samples due to low resolution (few data points). Therefore, while the classes do not appear to be sensitive to the effect investigated by Chattopadhyay & Chattopadhyay (2006), this is not conclusive.

HI content, dynamical mass and mass ratio

Since mass is the main ingredient of a galaxy's kinematic behaviour, this is one of the most interesting correlations to study. Unable to compare the DM content for these galaxies in a homogenous way (save the 11 in this thesis for which mass models have been constructed (Chapter 5)), we instead take a look at the dynamical mass calculated at the edge of the HI disk (r_{out}), which is an indication of the lower limit of the total (including DM) mass content. Additionally, we calculate the HI content, and investigate the mass ratios in the different kinematic classes.

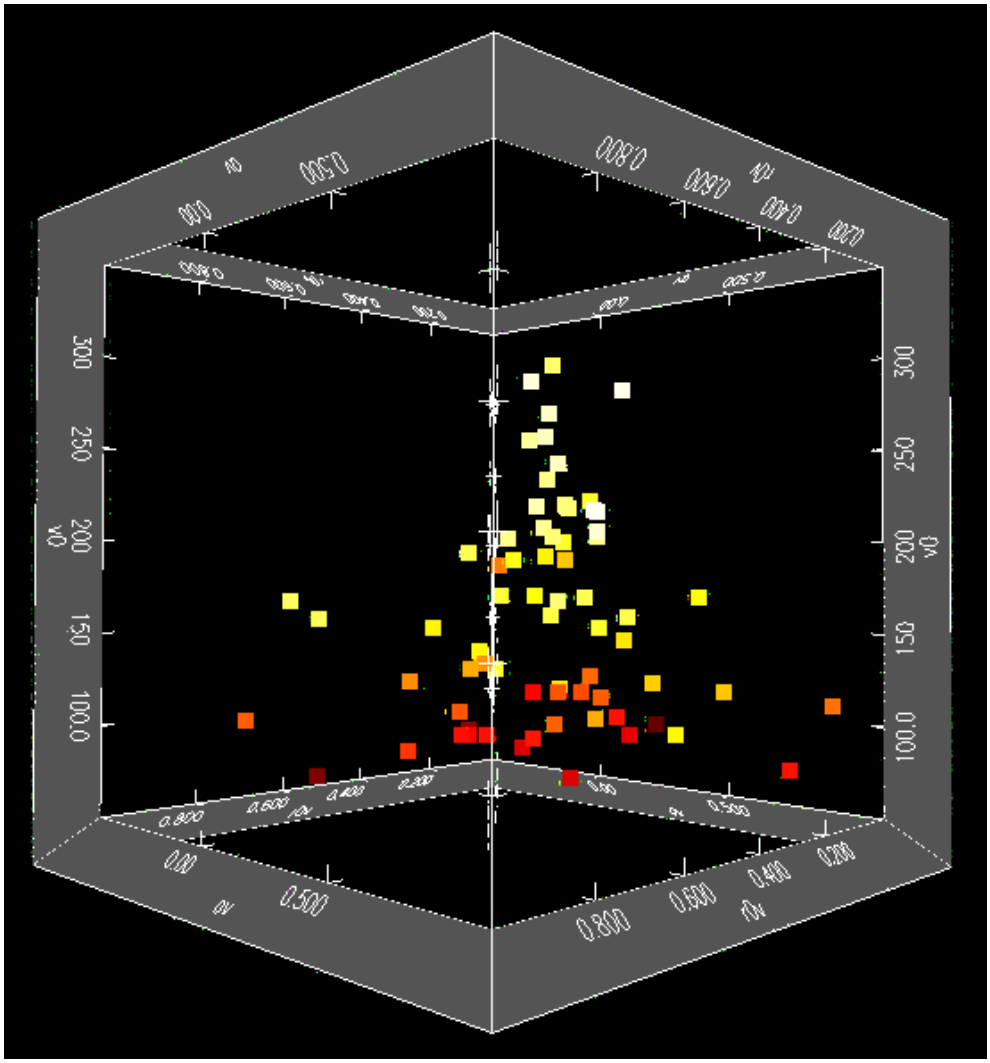

Figure 6.14: The colour of the data points are scaled to the value of the size of the optical disk, D_{25}. Light colours (white yellow) refer to a large disk diameter and dark colours correspond to a small disk diameter. Vertical axis = v_0, horizontal axes = $r_{0,v}$ (right side) and a_v (left side).

Column (10) in Table 6.9 is the dynamical mass of the galaxy at r_{out}, the outer radius measured for the rotation curves of these galaxies. It is derived by the simple relation in equation 6.2

$$M(r) = \frac{v(r)^2 r}{G} \tag{6.2}$$

where G is the gravitational constant and v is measured at $r = r_{out}$. In § 5.3.5 we use a constant f to scale the dynamical mass, according to rotation curve shape, where f ranges from 0.6 to 1 (Lequeux, 1983). Since we are only interested in looking at the ratio of the dynamical mass and the gas mass, we simply set the constant to 1 in this section.

Three galaxies from the Hoekstra et al. (2001) sample do not have values for r_{out} and are excluded.

The HI content was derived by taking the integrated HI flux (given in magnitudes in the de Vaucouleurs et al. (1991) RC3 catalogue) and converting it from magnitudes to the integrated flux following equation 6.3 (from RC3):

$$m_{HI} = -2.5 log S + 17.40 \tag{6.3}$$

where the integrated flux S is in units of Jy km/s. The flux was then converted to mass in units of $M_\odot$ by the standard formula (eq. 6.4):

$$M_{HI} = 2.36 \times 10^5 \cdot D^2 \cdot S \tag{6.4}$$

where D is the distance to the galaxy in Mpc.

For the galaxies collected from Sanders (1996) and Sanders & Verheijen (1998), some HI masses are available for comparison. Generally, our values are lower, with a mean difference of $2.6 \times 10^9 M_\odot$, or 32%.

Figure 6.15 shows the HI mass and Figure 6.16 the ratio of the gas mass (corrected

for He) over the dynamical mass.

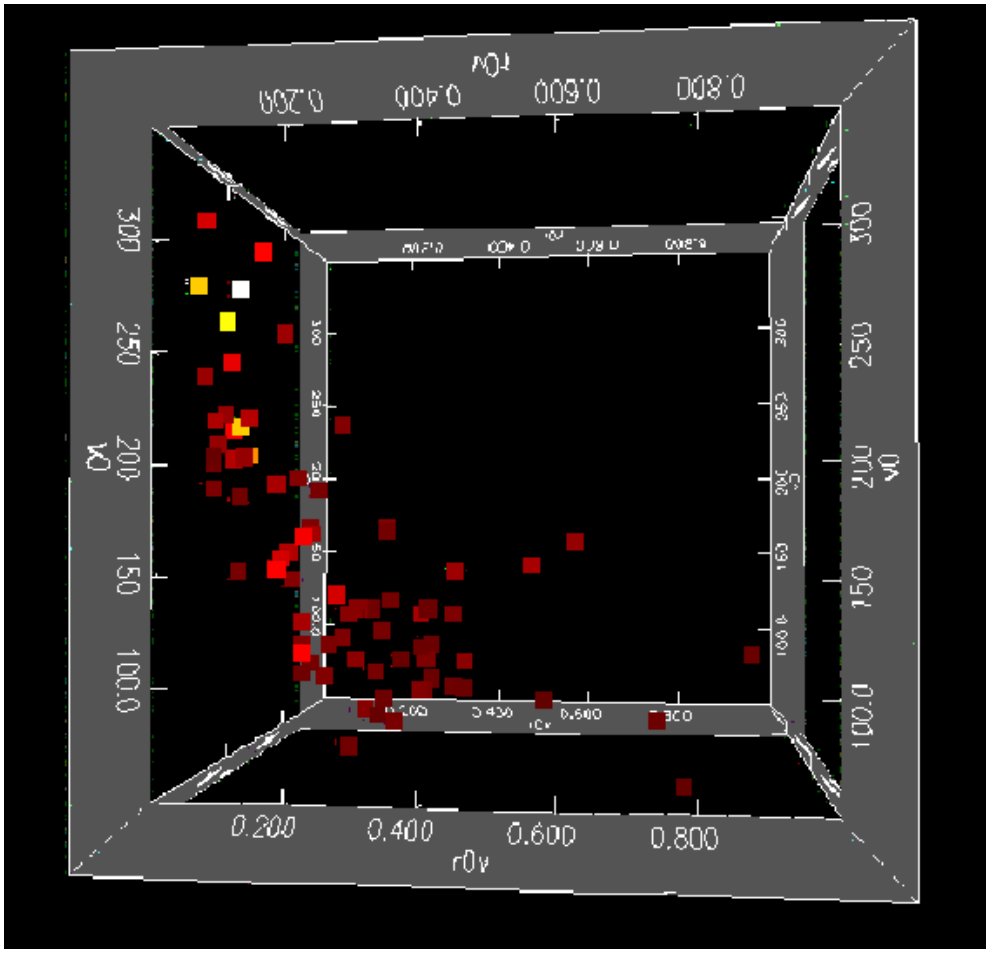

Figure 6.15: The colour of the data points are scaled to the value of the HI mass. Light colours (white, yellow) refer to larger amounts of mass and dark colours (red, dark red) refer to smaller HI masses. Vertical axis = v_0, horizontal axes = $r_{0,v}$ (front) and a_v (side).

There is an obvious correlation between the dynamical mass and velocity (see Equation 6.2 (not shown in figure). While there is no strong trend, it is notable that the highest HI mass and mass ratio values occur in the A class. Although there is a scatter in values for the A class, this group has a median mass ratio that is three times lower than the other classes with a value of 2%; the other classes each have a median mass ratio near 6%. It is likely that the dynamical mass in the ratio overshadows any other correlations, and

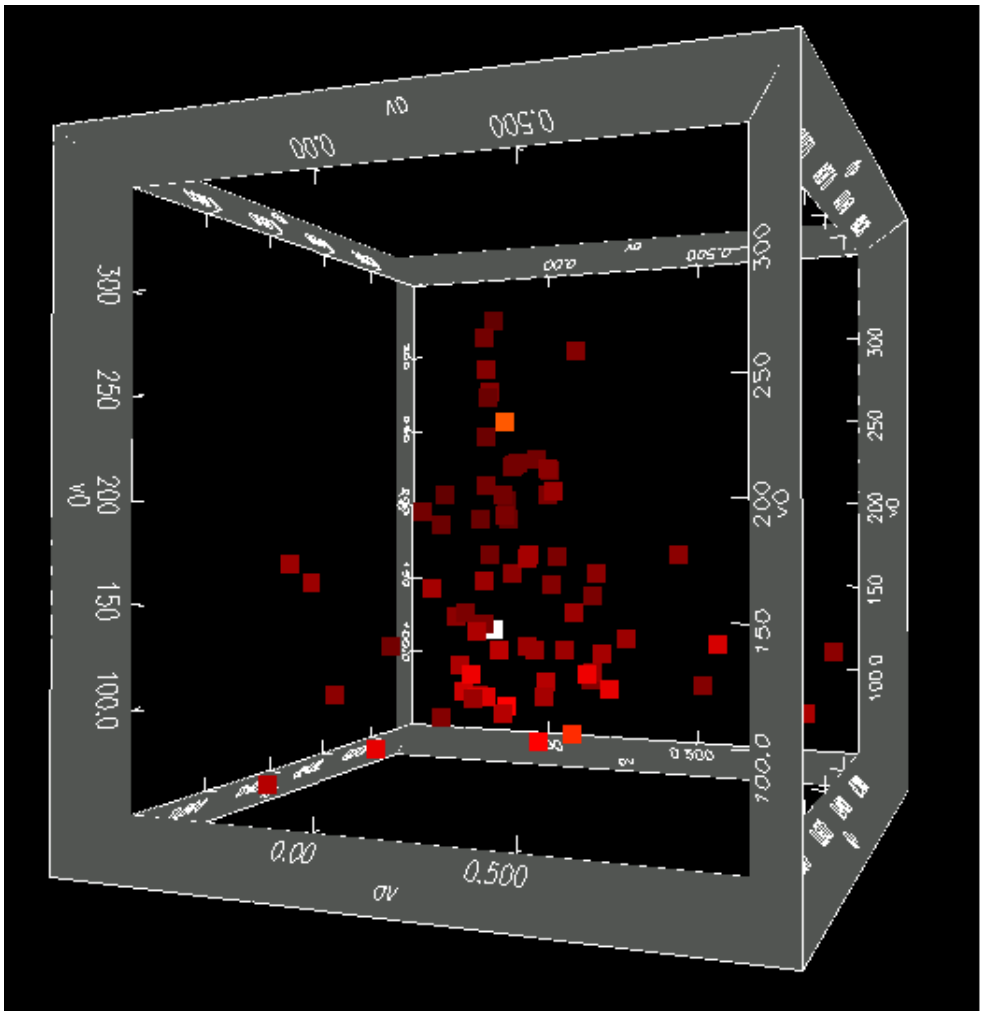

Figure 6.16: The colour of the data points are scaled to the value of the mass ratio (M_{gas}/M_{dyn}). Light colours (white, yellow) refer to a higher mass ratio and dark colours (red, dark red) refer to a lower mass ratio. Vertical axis = v_0, horizontal axes = $r_{0,v}$ (side) and a_v (front).

the correlation which is seen is simply the velocity component in the dynamical mass.

Star formation rate

Radio continuum emission at 20 cm wavelength can be used as a tracer of the star formation rate (SFR) in a galaxy. Condon (1992) describes in a review paper how the emission is produced by supernova remnants from massive (more than $8M_{\odot}$) and short lived (less than 3×10^7years) stars. This emission thus traces recent star formation activity in the galaxy. The observed flux densities are proportional to intrinsic luminosities since radio wavelengths suffer minimal extinction.

Integrated flux from 20 cm continuum data from the NRAO VLA Sky Survey (NVSS, Condon et al., 1998) is available for 55 of the 79 galaxies used for our explorations. Since NVSS only can properly image structures of angular size $10'$ or less, larger galaxies in our sample might be missing a significant fraction of the flux. This is an issue for eight galaxies in the sample which have an optical size (D_{25}) between $10'$and $20'$. Two of these 8 galaxies have such large angular sizes that we exclude them from the SFR analysis altogether (NGC 55 and M33).

The flux for the remaining 53 galaxies is translated to luminosity (for a particular frequency, in this case 1.4 GHz) using the inverse square law:

$$L_{\nu} = 4\pi D^2 \times Flux_{\nu} \tag{6.5}$$

Since the flux is given in mJy (where 1 Jy= $10^{-26}\frac{W}{m^2 Hz}$, and distance in Mpc (1 pc= $3.0857 \cdot 10^{16}$ m), a conversion has to take place in order to receive the luminosity in units of W/Hz. Equation 21 in Condon (1992) can then be used to translate the luminosity

into star formation rate, following:

$$SFR = \frac{L}{5.3 \cdot 10^{21} \cdot \nu^{-\alpha}} \tag{6.6}$$

where SFR refers to formation of stars with masses greater than 5 M_{sun} in units of $M_{sun}/year$, ν is the frequency of emission in GHz, and α is the radio spectral index (set to a typical value of 0.8). The resulting star formation rates are listed in Table 6.9

Plotting the kinematic parameters vs star formation rate, we find an indication of a correlation between Class A galaxies and higher SFR, and in particular with velocity amplitude v_0 and SFR. Figure 6.17 shows this correlation. Due to the lower number of data points, the S and T classes are not well represented, making it hard to distinguish any correlation with the slope or turnover radius.

Note that it is the galaxies of later-type morphology within the A class that have the higher SFR rates, which is expected. For example Portinari et al. (2003) show that Sc galaxies have the highest SFR, while early type galaxies with large bulges typically have low SFR.

It would here be interesting to show the relation of SFR and gas fraction as a function of kinematic class. Figure 6.18 shows the classes vs SFR, where the datapoints are coloured by gas fraction (M_{gas}/M_{dyn}). Here we can again see that the A class includes galaxies with the highest SFR. It is however only the galaxies within this class with high levels of gas fraction that exhibit high SFR rates, which is consistent with the morphological dependency described above. The other classes however have a higher ratio of galaxies with high gas fraction, but low SFR, possibly due to the lower rotational velocities.

It is expected that there is a relationship between high rotational velocity and SFR, due to the consequential higher angular velocity of density waves which creates conditions favourable for star formation, as mentioned by e.g. Zasov & Smirnova (2005). These

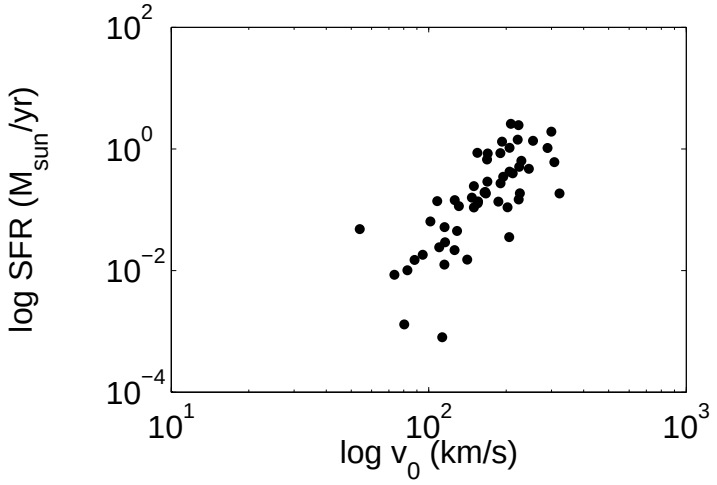

Figure 6.17: Star formation rates calculated for 53 of the galaxies in the sample are plotted against the velocity amplitude v_0 in this log-log plot.

results are consistent with expectations.

In addition, since we know that the 1D velocity dispersion plays a role in star formation laws (e.g. McKee & Ostriker, 2007) such as the Kennicutt-Schmidt law (Kennicutt, 1998), it would be illuminating to complement these data with 1D velocity dispersion data as well. GalAPAGOS constrains this 1D velocity dispersion as one of its parameters (see § 4.2.2), and thus we have this information for 15 of the galaxies in the sample. It is however hard to draw any conclusions with these few datapoints, as shown in Figure 6.19. Only a possible constraint can be seen (v_σ between 10 and 20 km/s), but there are no visible trends between velocity dispersion and SFR.

Halo mass and disk scale length

In Chapter 5, mass models were derived for 10 galaxies for which we had both HI (to derive the rotation curve and gas contribution) and NIR data (to derive the stellar contribution) available. The sample is limited by a number of selection criteria (see Chapter 2), of which the major criterium was that the galaxies need to be isolated and non-interacting.

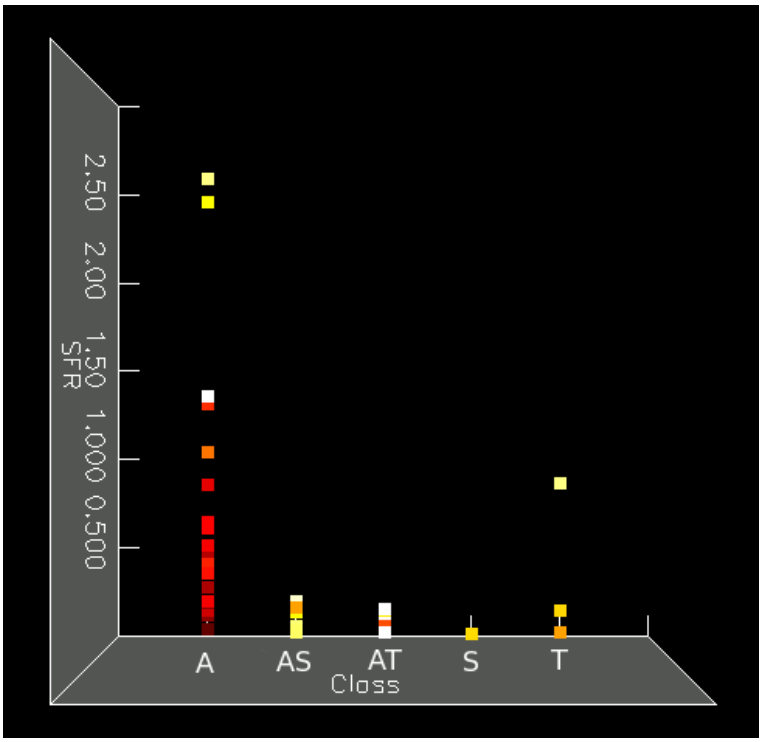

Figure 6.18: Relation between kinematic class, SFR and gas fraction (M_{gas}/M_{dyn}). The gas fraction is represented by the the colour shade of the data points, where bright colours (white, yellow) correspond to high mass ratios.

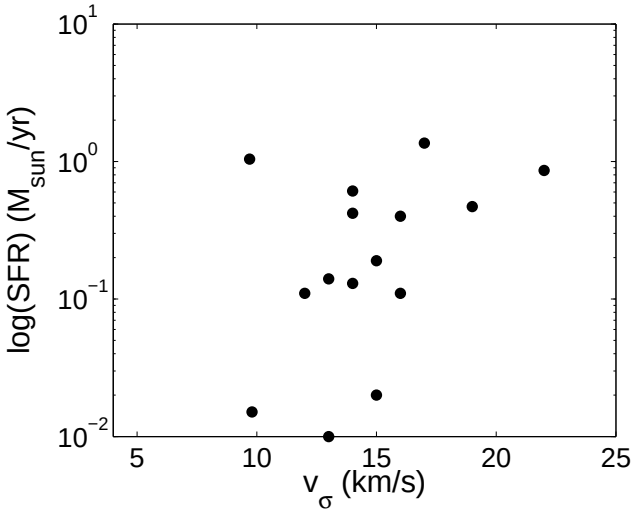

Figure 6.19: Star formation rates are plotted against the 1D velocity dispersion for 15 galaxies.

For ten of these galaxies, parameters pertaining to the halo were derived. Table 6.10 lists the parameters used in this section. The kinematic class is also listed and we note that 7 of the ten galaxies are from Class A, with two from Class AS and one from the T class. The disk scale length was derived from the luminosity profile (see § 5.3.2). Note that the values derived using the dynamical mass might be understated, due to a too low scaling factor used in the derivation in § 5.3.5. This will however not impact the general distribution of data points in e.g. Figure 6.20.

Galaxy	Class	Disk scale length [kpc]	$(M_{dyn}/L)_i$	M_{halo} $[\times 10^{10} M_\odot]$	M_{halo}/M_{baryon}
	(2)	(3)	(4)	(5)	(6)
NGC 2403	AS	1.6	$18^{+7.5}_{-2.5}$	$6.1^{+3.4}_{-1.4}$	$6.9^{+14}_{-3.3}$
NGC 2841	A	4.4	$17^{+7.3}_{-2.4}$	48^{+34}_{-12}	$1.5^{+1.1}_{-0.4}$
NGC 2903	A	2.6	$6.7^{+2.9}_{-1.0}$	$7.3^{+3.2}_{-2.2}$	$1.0^{+0}_{-0.3}$
NGC 3198	AS	3.7	$12^{+4.9}_{-1.6}$	$8.9^{+7.0}_{-3.3}$	$2.2^{+3.7}_{-1.2}$
NGC 3351	A	2.1	$11^{+4.7}_{-1.6}$	$12^{+6.1}_{-2.8}$	$6.0^{+3.0}_{-2.7}$
NGC 3521	A	4.5	$5.2^{+2.2}_{-0.7}$	$0.6^{+12}_{-0.6}$	$0.1^{+2.1}_{-0.0}$
NGC 3556	T	3.4	$4.8^{+2.1}_{-0.7}$	$5.4^{+2.7}_{-2.9}$	$5.2^{+2.7}_{-4.4}$
NGC 4258	A	8.7	$4.5^{+1.9}_{-0.6}$	$9.5^{+12}_{-6.2}$	$1.2^{+6.2}_{-0.9}$
NGC 5055	A	4.0	$7.3^{+3.1}_{-1.0}$	$5.2^{+4.3}_{-2.5}$	$0.5^{+0.2}_{-0.3}$
NGC 7331	A	6.4	$5.8^{+2.5}_{-0.8}$	$16^{+21}_{-4.1}$	$1.3^{+8.8}_{-0.3}$

Table 6.10: Parameters derived from mass models in Chapter 5. Column (2) is the kinematic class, Column (3) is the disk scale length, Column (4) is the mass-to-luminosity ratio of the dynamical mass over the i-band luminosity, Column (5) is the halo mass derived at the outer HI radius of the galaxy, and Column (7) is the ratio of the halo mass and the baryonic mass of the galaxy.

The two halo parameters describing the isothermal halo model, the halo density and the core radius, are available in Chapter 5 as well. These parameters are however very sensitive to small changes in the mass model. Even small changes in M/L ratios results in significant changes for the halo parameter values. Due to these uncertainties, the halo parameters are not useful for our correlation search at this stage. In the literature,

correlations between high halo central densities (combined with short core radii) and low-luminosity galaxies have been seen (Spano et al., 2008) and we thus expect that such correlations should be visible in this classification scheme using a larger set of galaxies, with well-derived mass models.

Since most galaxies in the sample are Class A galaxies, we concentrate on looking for correlations with the maximum rotational velocity v_0 (the parameter that varies most significantly for the A class). Figure 6.20 shows, in the left panel, a plot of the halo over baryon mass ratio (i.e. the sum of the stellar mass and the gas mass as calculated using the mass models in Chapter 5) and, in the right panel, the M_{dyn}/L_i. The velocity uncertainties are generally on the order of a few km/s (the size of the data points are larger than the uncertainties). The different kinematic classes are shown by different symbols.

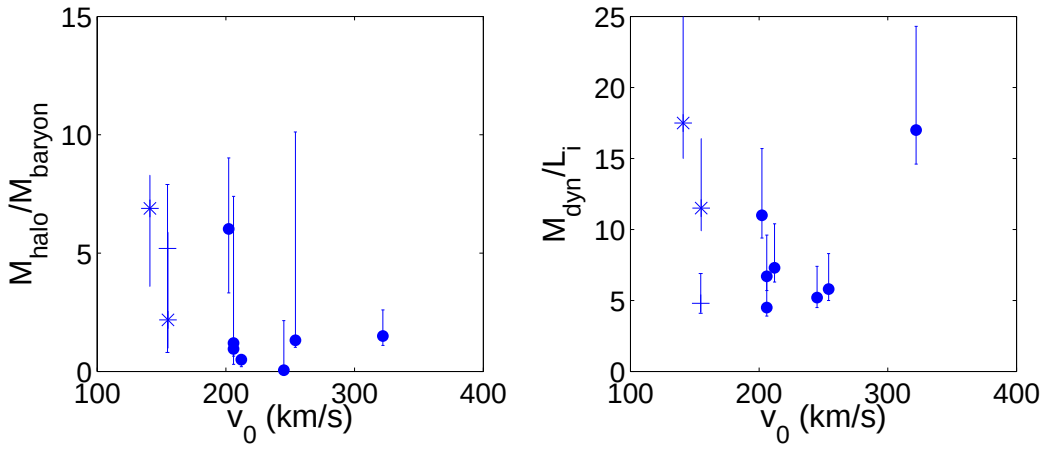

Figure 6.20: 10 mass modelled galaxies: Rotational velocity v_0 plotted against the halo mass over baryon mass ratio (left) and the dynamical mass-to-luminosity ratio in the i-band M_{dyn}/L_i (right). Data points displayed as dots are A class galaxies, asterisks are AS and the T class galaxy is shown with a '+'.

Due to the small number of galaxies in the sample, it is hard to conclusively discern trends. Nevertheless, we can use these results as indicators for future study.

The left panel of Figure 6.20 suggests that the halo mass is higher for galaxies with

lower velocities. This would be expected, since the fastest rotators are also the brightest galaxies, which we have seen usually have a smaller halo contribution in the mass models. Also, dwarf galaxies, which are slow rotators (this is true for all 10 dwarf galaxies in the galaxy sample which were included in the derivation of the classification scheme), normally have a large halo contribution (e.g. Swaters, 1999).

With the exception of NGC 2841 (right top corner in the right panel of Figure 6.20), the M_{dyn}/L_i is higher for galaxies with lower rotation velocity (i.e. not A class). This also agrees with the halo mass correlation in the left panel, since galaxies with a larger halo contribution should cause a higher M/L. The location of NGC 2841 in this diagram is intriguing. NGC 2841 is a Seyfert galaxy (i.e. featuring an active nucleus (AGN) and likely a supermassive black hole), but so is NGC 4258, which has a lower rotational velocity.

In Figure 6.21, we investigate the correlation between disk scale length and maximum velocity (left panel) and outer slope of the rotation curve (right panel). The three Class A galaxies with potentially declining rotation curves are shown in red.

In contrast to the results of Chattopadhyay & Chattopadhyay (2006), who found a weak correlation between disk scale length and the shape of the rotation curve, we find no such correlation with our limited sample.

6.8 Conclusions

In this chapter, an exploratory kinematic classification scheme was devised, based on three rotation curve parameters in a simple rotation curve model: the maximum rotational velocity v_0, turnover radius $r_{0,v}$ and outer slope a_v (beyond $r_{0,v}$). A hierarchical clustering method was used to discern natural clusters of these parameters. Combining this with visual inspection, we found that the 80 galaxies in our samples tend to be organized within

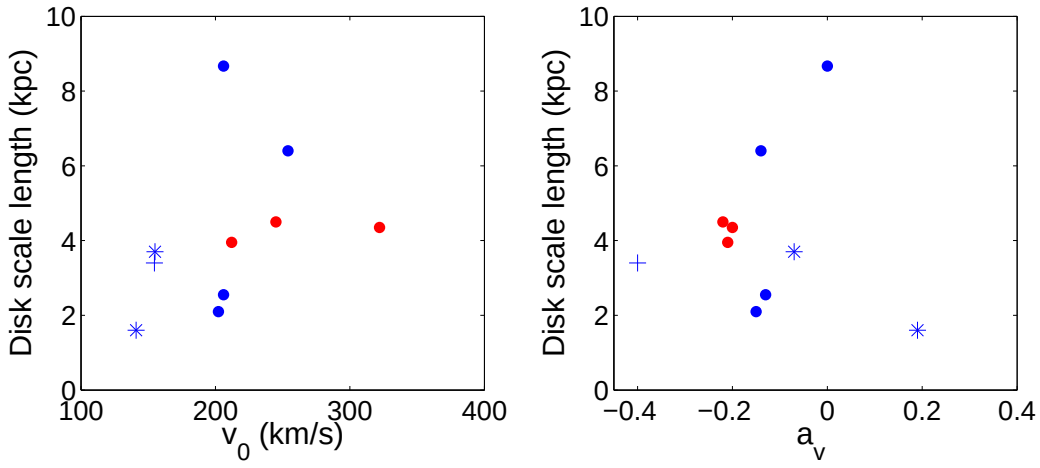

Figure 6.21: 10 mass modelled galaxies: Rotational velocity v_0 plotted against the disk scale length (left), and outer slope of the rotation curve (a_v) plotted against the disk scale length (right). Data points displayed as dots are A class galaxies, asterisks are AS and the T class galaxy is shown with a '+'. Note that the uncertainties for the disk scale length in this figure (although not shown) are at least 30%, mainly as a consequence of the distance to the galaxy which is used to convert the scale from units of arcseconds to kpc.

a 3D plot in a structure ressembling the shape of a scorpion[3]. The kinematic classes found within this shape consist of

- Class A (the tail) with high v_0, low $r_{0,v}$ and low a_v
- Classes AS and AT (the torso) with low v_0, intermediate a_v and $r_{0,v}$
- Classes S and T (the claws) with low v_0 and stretching out in regions of either high $r_{0,v}$ (and low a_v) for the T class or high a_v (and low $r_{0,v}$) for the S class.

Classes AS and AT are not as distinct as the other three, and there is a possibility that they may end up being the same class for a larger sample of galaxies.

The shape of the 'scorpion' diagram indicates a relationship between maximum velocity and turnover radius and slope of the outer rotation curve. There does not seem to be any high velocity galaxies with particularly high values of turnover radius and slope. Also, there does not seem to exist any low velocity galaxies with short turnover radius and slope. This could be an indication that the turnover radius and slope values are a direct physical consequence of the maximum velocity of the rotation curve.

Guided by correlations found in the literature between rotation curve behaviour and a number of galaxy characteristics, we searched for correlations that could be applied to the kinematic classes found in this chapter.

Using 79 galaxies, we found indications of correlations in particular between the maximum rotational velocity parameter and absolute B magnitude, morphology and size of optical disk, which is in agreement with literature. We also found that the star formation rate increases with rotational velocity (Figure 6.17). The kinematic A class was thus found to include a higher number of galaxies with high SFR, but these were mainly galaxies of later type morphology. There were inconclusive indications of trends with the HI

[3]Note that this nomenclature (scorpion, claws) will not be utilised in future papers.

mass and mass ratio (gas mass over dynamical mass), such that Class A galaxies may have a larger amount of HI mass, but a lower mass ratio. There does not seem to be any correlation between the kinematic class and presence of bar.

It is hard to discern conclusive correlations with the other two parameters, turnover radius ($r_{0,v}$) and outer slope (a_v), other than how they are already correlated with velocity (i.e. high velocity Class A galaxies also have short turnover and low slope value, and therefore the attributes found for these galaxies also apply to the A class range of values for turnover radius and slope). In the ranges outside of the A class, in particular for the S and T classes, the number of galaxies is low and any pronounced trends in that range are hard to discern.

For ten galaxies, of which seven are in Class A, disk scale length and parameters pertaining to the mass of the halo (measured via mass modelling in Chapter 5) were investigated as well. Although the number of galaxies is low in the sample, they suggest that the dynamical M/L (M_{dyn}/L_i) decreases as the rotational velocity increasses (right panel of Figure 6.20). One galaxy, NGC 2841, is an interesting exception to this. .

These findings often agree with those found in the literature (see e.g. Table 6.1). For example, they support findings that there is a correlation between the morphological (Hubble) type and velocity, which was not as clear in early investigations using only optical rotation curves.

Apart from the rotational velocity which has a low uncertainty ($\sim$3%), there are significant uncertainties in the other kinematic parameters. Thus it is important to further investigate this exploratory kinematic classification scheme by using a large sample of galaxies, with homogenously derived rotation curves. Additionally, a larger number of galaxies is needed to better delineate correlations between classes and halo characteristics.

Our investigation also indicated that a rotation curve model which more accurately chatacterises the inner region of the RC, would improve our ability to assess correlations.

Another intriguing result is that of the candidates for declining rotation curves found in Chapter 5: NGC 2841, NGC 3521 and NGC 5055. It was found that none of these galaxies conform to the attributes given in literature to accompany galaxies with declining rotation curves (listed in § 6.1 and Table 6.1). For example, all three galaxies are flocculent (patchy spiral arms that are difficult to trace), in contrast to the results of Elmegreen & Elmegreen (1990) who connected declining RCs to grand design spiral arm galaxies. Additionally, according to our sample, they have intermediate disk scale lengths of 4.4, 4.5 and 4.0 kpc respectively, and again, are to our knowledge non-interacting. If they are indeed understood to have declining RCs, these findings illustrate a conundrum which should be further investigated.

We note that this preliminary classification scheme, if confirmed using a larger, homogenous dataset, has the potential to be useful for delineating properties for galaxies, when only their kinematic characteristics are known. For large data sets from upcoming surveys (e.g. Wallaby, MONGHOOSE, see Chapter 7), the classification scheme can be used to indicate the existence of other properties in galaxies. In cases where the emission is faint or of low quality, it might still be possible to assess characteristics of these galaxies, by noting which class they are in. Additionally, many galaxies which are similar and exist in one particular class, could be studied to assess the origins of spatial and velocity anomalies. This could distinguish between velocity anomalies generated by, for example, cosmological inflows and outflows due to star formation processes. Additionally, the classification scheme may be regenereated to include dark matter parameters or other parameters when defining the classes in the clustering process (see § 7.3).

Chapter 7

Summary and conclusions

7.1 Summary

As mentioned in the introductory chapter, this thesis is a study of the kinematics of nearby spiral galaxies. In particular, it is an exploration on how to characterize their choreographies and find the common personal characteristics that influence the way they rotate. One of the main questions of this thesis was whether a classification scheme based on the kinematics could be devised. Building on that question, an attempt was made to answer the question whether such a classification scheme relates to galaxy properties such as optical brightness or amount of dark matter. For this assessment we used neutral hydrogen data (HI) complemented by near infrared data (NIR), we explored a new way of modelling HI cubes, and we used mass modelling to characterise the dark matter (DM) halo component of the galaxies. We used a hierarchical clustering method on parameterized rotation curves to find similarities in rotation curve behaviour, and based a classification scheme on these results.

Below, each chapter of the thesis is summarised. We list the conclusions at the end of the chapter with a brief discussion on the results and an outlook on future work.

Chapter 2 – Data: observations and processing

Galaxy interactions can considerably change the behaviour of a galaxy, but we were interested in finding the *intrinsic* properties of the kinematic behaviour in galaxies. Thus we have made an effort to find data for spiral galaxies which are isolated and non-interacting and of morphological type Sa-Sd. In order to trace the kinematic behaviour out to large galactocentric radii, we used an inhomogenous collection of three HI data cubes provided by J. Irwin, four provided by the WHISP team, and publically available data from the THINGS survey. The data range in synthesized beam resolution from 6″ to 58″, and the sensitivity is between 0.2 and 1.8 mJy/beam (rms noise). We complemented these data with near infrared (NIR) data from the SDSS survey to measure luminosity profiles of the stellar component.

Chapter 3 – Methods: mass models

In Chapter 3 we describe how we derived mass models by calculating the contribution to the HI rotation curve from the different constituents of a galaxy (gas, stellar bulge and stellar disk); the halo component is the difference between the sum of the (squared) constituents and the HI rotation curve (squared) following Equation 3.1. Rotation curves were derived by two different methods: the tilted ring method in the software GIPSY, and (in the following chapter) the HI modelling software GalAPAGOS. The HI data were also used to derive the gas mass contribution. The luminosity profile was measured from SDSS i-band data. These profiles were decomposed into the disk and bulge components, in order to find the contribution to the total rotation curve from these. The halo component was modelled as an isothermal sphere in the mass modelling process since it produces a good fit and permits homogenous comparisons.

Chapter 4 – Methods and analysis: HI modelling

Chapter 4 presents the testing of a new software package for modelling HI cubes, called GalAPAGOS. GalAPAGOS, based on a genetic algorithm, uses the full 3D cube (as opposed to the 2D velocity field) and a set of parameterised modelling equations. It uses a set of ∼23 parameters to find a family of solutions that describe the observed input galaxy. More than 140 artificial galaxies demonstrate that GalAPAGOS accurately retrieves the parameters of the input data under a number of different conditions, such as variations of galaxy inclination, surface density distribution, rotational behaviour and warps. Subsequent tests using observed data in a range of inclinations show that judicious binning of the data is necessary to generate reasonable run times. We found that GalAPAGOS reliably determines the kinematic information for galaxies of inclinations 40 ° and above.

Chapter 5 – Results: rotation curves and mass models

Part I

The models derived using GalAPAGOS and in particular the rotation curves, were evaluated and compared to the tilted ring method. The results for 15 galaxies, ranging in inclination from 41 °–76 ° were individually examined.

The results for geometrical parameters (inclination, position angle, etc) are excellent, and we find that the models give reasonable results for the physical parameters. The system temperature parameter is however unreliable, possibly due to problems with high temperatures in the radiative transfer function.

For some galaxies with short turnover radius, the GalAPAGOS solutions tend to favour a too-short turnover radius. This is due to a resolution problem, caused by the binning of the data in order to improve run times. We find that the inner region (from centre to turnover radius) needs to be spanned by at least 5 pixels. Additionally, low resolution

data such as from single dish observations need to be spanned by more than 4 beams in order for GalAPAGOS to find any constraints in the solutions.

We note that the GalAPAGOS rotation curve modelling equation could also be improved by accounting for changes in the slope as a function of radius in the region beyond the turnover radius.

Part II

In the subsequent mass modelling and analysis, we included 10 of the galaxies with measured rotation curves. Although only pairs of "best fit" models are shown (one figure for the GIPSY RC and one for the GalAPAGOS RC), we also investigated a maximum disk model, a minimum disk model and a model for which the M/L for the disk was predicted by a Salpeter initial mass function as a function of morphological type. The resulting values from all these models were used to delineate the uncertainty ranges in the derived characteristics.

We found that the mass model is sensitive to how well the inner region, especially the bulge, is constrained. Additionally, the isothermal model halo parameters (core radius and density) are very sensitive to small changes in M/L for stellar components. The uncertainties thus become unpractically large for these parameters. Halo mass (at the outer radius) and mass ratios were calculated for further analysis in Chapter 6

Three candidates of declining rotation curves were found which require further investigation.

Chapter 6 – Analysis: development of a classification scheme

This chapter uses the simple global parametrization for the rotation curves employed by GalAPAGOS on a larger sample of galaxies. The aim was to find similarities among galaxies based on the kinematic parameters and devise a classification scheme.

We used 79 rotation curves, of which the majority were culled from the literature. A

hierarchical classification algorithm was applied to the kinematic parameters to determine clusters of similar galaxies. Combining the results of the algorithm with visual inspection, 5 classes were found: Class A is characterised predominantly by high rotational velocity; AS and AT have intermediate velocities and their secondary characteristics are based on slope and turnover radius, respectively. The S and T classes are dominated by slope and turnover radius, as well as low rotation velocity. This is a preliminary scheme; for example, taking the uncertainties into account, there is a chance that classes AS and AT might be combined into one class.

We searched for correlations between the kinematic classes and other galaxy characteristics. We found correlations between, in particular, higher maximum rotational velocity and the following galaxy properties: higher brightness, earlier type morphology, larger size of the disk and higher star formation rate. We also found indications of trends between lower velocity with a higher ratio of the HI mass over the dynamical mass.

We investigated possible trends between the velocity and a) the ratio of halo mass over baryonic mass, b) the dynamical mass-to-luminosity ratio as well as c) disk scale length for the 10 mass modelled galaxies. All but three of these galaxies are Class A galaxies, and the low number of the sample makes it hard to discern any correlations. For higher values of a) and b), there are possible indications of a trend with lower velocities, but there is no discernable trend with the disk scale length. These properties need to be investigated with a larger sample of galaxies that includes representatives from each kinematic class.

In summary, 10 galaxies were useful for creating mass models in order to assess the DM component. This was done by using a) NIR data to measure luminosity profiles which were divided up into the bulge and disk components to assess their contribution

to the mass model, and b) HI data to measure the mass contribution from the HI gas in emission, as well as the rotation curve of the total dynamical mass. Combining all components provides a model for the DM halo. A new approach (GalAPAGOS) to semi-automatically determine the rotation curve was used, which compares well with the traditional approach (tilted ring method) and is more successful for inclinations above 70°. Hierarchical clustering was used on the rotation curve parameters for 79 galaxies to devide a preliminary kinematic classification scheme. Correlations were confirmed between observational characteristics such as magnitude, morphology and star formation rate and kinematic properties, in particular the maximum rotational velocity. Properties from the 10 mass modelled galaxies, such as the ratio of DM over baryonic matter, were compared to the classification scheme.

7.2 Conclusions and discussion

The following main conclusions can be drawn from the work conducted in this thesis:

- The new software GalAPAGOS[1] generates valid solutions to modelling equations if the HI data for unperturbed spiral galaxies have sufficient resolution (i.e. at least 5 pixels spanning the region from the centre to the turnover radius). GalAPAGOS has several advantages compared to traditional softwares for rotation curve derivation: It is robust for high inclinations (above 70°) and flexible (the user can define the rotation curve form). It finds the global characteristics of galaxies, while evading local minima. Its ability to work without user input or initial guesses makes it useful for large surveys, for which the datacubes can be pipelined directly into the software. We recommend running GalAPAGOS twice on a data cube in order to

[1]Recall that the name of this software will be changed from GalAPAGOS to another name in future publications, since the name is already in use for another application in published papers.

check for consistency in the results. Current run times for a sufficiently well resolved galaxy is 1-2 weeks on a computer with 8 cores.

- Mass models fitted to GalAPAGOS rotation curves show similar results to those fitted to GIPSY rotation curves. At moderate inclinations where GIPSY rotation curves are considered accurate, the mass models generate a difference of $\sim$20% in disk M/L. Based on the artificial galaxy tests, we believe that GalAPAGOS successfully models high inclination galaxies.

- Halo parameters are, however, very sensitive to the fitting of the inner region (in particular the bulge M/L) to the rotation curve. Therefore, with the current modelling equations, the halo parameters of density and core radius derived using the GalAPAGOS RC are imprecise. Issues with the bulge M/L can be resolved by more informed mass modelling. Improvements can also be made with regards to the GalAPAGOS parameterised form of the rotation curve.

- Rotation curves can be separated into different classes, based on the values of three parameters: maximum rotational velocity, turnover radius and slope of the outer curve. A preliminary kinematic classification scheme is constructed, consisting of five classes; A, AS, AT, S and T (summarised briefly in the previous section). The overall distribution ("scorpion" shape) is robust, but since the sample size is at a lower limit for analysis, the boundaries of the classes might shift using larger samples of galaxies.

- Correlations are found between the kinematic classes and a number of galaxy characteristics. The classes, their characteristics and correlations are listed in Table 7.1.

- Ten galaxies for which halo information had been derived have been investigated for correlations between DM mass and the classification scheme. However, the results

are inconclusive due to the limited sample and need to be further studied.

- Three galaxies, NGC 2841, NGC 3521 and NGC 5055 in the data sample exhibit rotation curves that are candidates for declining rotation curves, with declines from the maximum velocity to the outer radius of ∼20%. The decline occurs for rotation curves derived using both GalAPAGOS and GIPSY methods. Similar to the declining rotation curves found by Noordermeer et al. (2007), the rotation curves derived using the tilted ring method seem to flatten out just before the outer radius, an indication of the presence of large amounts of dark matter despite the declining behaviour. Even though the GalAPAGOS model includes a warp (which all three of these galaxies exhibit) the GalAPAGOS rotation curve still show a strong decline. Additionally, these galaxies do not fall into categories listed in literature to be connected to declining rotation curves such as interacting, grand design spiral arm galaxies and short disk scale length.

Correlation	**A**	**AS**	**AT**	**S**	**T**
v_0	high	intermediate–low		low	low
$r_{0,v}$	short	intermediate	intermediate	intermediate	long
a_v	flat–decline	flat–increase	flat	increase	flat–decline*
M_B	high	intermediate	intermediate	low	low
Morphology	Sbc	Scd	Scd	Sd	Scd
D_{25} [kpc]	30	15	13	13	11
SFR $[M_\odot$/year]	0.7	0.1	0.05	0.001	0.4
HI $[\times 10^9 M_\odot]$	5	3	1	1	1
HI/M_{dyn} (%)	3	6	7	5	6

Table 7.1: A summary of the classes, their characteristics and correlations with other galaxy properties. The results listed here refer to the *average* value in each class. (*) Although the T class ha low slope numbers, the actual velocity decrease from the maximum value at the turnover radius is only a few %, due to the large turnover radius.

From these investigations, we conclude that the rotation curve form used in GalAPAGOS may be too simple for precise mass modelling. Indeed, while GalAPAGOS finds the global characteristics of the curve, smaller fluctuations in the outer region which might be important for finding the flattening of declining rotation curves, for example, are disregarded. Thus, the rotation curve form may benefit from including modulation parameters to better match smaller scale velocity variations and characterise the rotation curve. Finding a more detailed physical parameterisation might be hard – in the early days of GalAPAGOS another version of the equation was tested which incorporated an inner slope parameter, which traded off with the outer slope parameter. A modulated rotation curve form such as the one used for the surface density in GalAPAGOS could be a useful option (J. Fiege, priv. comm.). The current rotation curve parameterisation, which gives the global characteristics, could then be retained, and smaller scale velocity variations would be determined using modulation parameters (similar to the SDM parameters used for the surface density).

The short turnover radius problem (found for fast rotating galaxies), could be solved in some cases by less binning, but at the cost of longer run times. Note, however, that in cases of very highly resolved galaxies, such as THINGS data, a too-high spatial resolution might lead GalAPAGOS to (unsuccessfully) use the warp parameters to try to account for the small scale variations in the data, resulting in non-physical solutions. Because of this problem, we did not run full-resolution data sets on these data. There are potentially two ways to deal with this issue. A simple solution would be to retain a better pixel resolution (less binning), but convolve the data with a larger beam (i.e. decrease the beam resolution). Another approach, discussed with J. Fiege, would be to use a non-uniform resolution grid for the data. That is, using different binnings in different regions of the galaxy would thereby model the inner region more precisely.

In conclusion, we note that GalAPAGOS has the advantage that the modelling equations can be adapted by the user and we found that the GalAPAGOS rotation curves are reasonable for rotation curve analysis. With the adaptations noted above, mass models should be able to provide more appropriate bulge M/L values, making it possible to more accurately determine the halo parameters. The preliminary kinematic classification scheme is a continuum from high rotational velocities (combined with low values of turnover radius and slope), through low rotational velocities, where it branches out towards either high turnover radius or high slope values (ressembling a scorpion shape). Comparing a sub-sample of 42 galaxies to the full sample indicates that this general scheme is robust. A larger sample yet will indicate whether the current sub-classes are statistically meaningful. Such a sample, with complimentary NIR data for mass modelling is needed to determine if dark matter halo parameters could be incorporated into the classification scheme. A few galaxies (NGC 2841, NGC 3521 and NGC 5055) are candidates for declining rotation curves, but do not exhibit qualities normally associated with such a kinematic behaviour.

7.3 Future work

The classification scheme is thus far showing interesting results. However, it is important to note that it is still in its first, exploratory, form. The classification scheme is based on HI rotation curves in the literature, without available data of galaxy properties of interest such as baryonic mass fraction. Additionally, uncertainties for the outer radius are large.

Thus, the classification scheme needs to be tested on a larger, more homogenous, HI data set. Using the furthest radius detectable at a specified column density isophote for the

outer radius would lower the uncertainties considerably. This would improve the scaling of the spatial parameters and thus enable more precise values for the turnover radius and outer slope parameter. Observing HI with Australian Square Kilometre Array Pathfinder (ASKAP, consisting of 36 12m antennas), which is to be commissioned in 2013, would be an interesting option for this. Indeed, the ASKAP HI All-Sky Survey, named WALLABY (PIs: B. Koribalski and L. Staveley-Smith) will, among its numerous data products deliver 3D HI data for ∼1000 spatially well resolved galaxies, similar in quality to the THINGS survey, and of sufficient diameters for such an investigation using GalAPAGOS. We would need a sample of (still non-interacting) galaxies which are represented in all kinematic classes of the classification scheme which this survey should be able to provide.

A brief discussion on the usefulness of this classification scheme is provided in § 6.8. Currently, my thesis supervisor (J. English) is working with simulated data to test the robustness of the classification scheme.

The mass models need be improved, with a better constrained inner region and a higher number of galaxies (see above). Using CO data for the inner region (a project that was started in this thesis with NGC 925) from the NGLS project (PI: C. Wilson) would provide better constraints on M/L ratios for the bulge and inner disk. Additionally, it might be possible to model the inner region using CO data with GalAPAGOS. Consequently the halo parameters in the mass models can be better constrained, making it possible to explore correlations between these (halo density and core radius if using the isothermal sphere halo model) and the kinematic classes.

With a final homogenous HI sample from WALLABY, additional ancillary data for these galaxies (CO, NIR) can be proposed for (JCMT for CO) if it is not already available in other surveys.

An example of additional galaxy property to examine is the bulge/disk scale ratio, which was found by Graham & Prieto (1999) to be independent of morphological type.

With more galaxies with derived scale lengths, a potential correlation with the kinematic classification could be investigated.

As was mentioned in the above discussion, an important project is the one of modifying the parametrised form of the rotation curve used in GalAPAGOS. This could impact correlations with the classification scheme. We should also note that it is possible to expand the number of parameters in the actual hierarchical clustering algorithm to a multi–dimensional parameter space. While it would not be useful to use any unphysical parameters in the classification (such as modulation parameters), if the rotation curve form could be expanded in its physical form, those additional parameters could also be incorporated into the clustering algorithm. As well, now that we have determined potential correlations with observed characteristics (such as star formation rate and velocity), these observables can also be used in the multi-dimensional parameter space to better illuminate correlations with other parameters than the three kinematic ones that were used here.

HI models of galaxies reveal the rotational behaviour of the disk as well as the distribution of gas that fuels star formation. The rotation curve in particular provides fundamental information about the kinematics in the outer parts of galaxies, thus making it possible to probe and constrain the dark matter content. The velocity behaviour of a galaxy might also affect its star formation properties (see § 6.7). Galaxy properties such as DM content and star formation properties impact the evolution of galaxies.

Therefore, the hope is that this work on modelling rotation curves and the kinematic classification scheme can be further developed, providing an important contribution towards illuminating, for example, how the dark matter gravitational potential might affect the evolution of isolated galaxies.

While our sample of 10 galaxies was insufficient to illuminate how the rotational velocity due to the total mass is related to features such as the ratio of dark matter

to baryonic mass, and disk scale length, potential relationships could be revealed using the strategy we developed here on the large homogenous databases generated by the Square Kilometre Array pathfinder telescopes.

Thus, our pioneering use of the GalAPAGOS software is an important step towards its further development and use in upcoming surveys such as WALLABY mentioned above. Indeed, it has already been adopted to be used for the MHONGOOSE survey (PI: E. de Blok) which is to be observed with the MeerKAT array, the South African Square Kilometre Array pathfinder, generating a sample of 300 galaxies.

Bibliography

Alcock, C., Allsman, R. A., Alves, D. R., Axelrod, T. S., Becker, A. C., Bennett, D. P., Cook, K. H., Dalal, N., Drake, A. J., Freeman, K. C., Geha, M., Griest, K., Lehner, M. J., Marshall, S. L., Minniti, D., Nelson, C. A., Peterson, B. A., Popowski, P., Pratt, M. R., Quinn, P. J., Stubbs, C. W., Sutherland, W., Tomaney, A. B., Vandehei, T., & Welch, D. 2000, ApJ, 542, 281

Athanassoula, E., & Bosma, A. 1988, in IAU Symposium, Vol. 130, Large Scale Structures of the Universe, ed. J. Audouze, M.-C. Pelletan, & S. Szalay, 391

Bagetakos, I., Brinks, E., Walter, F., de Blok, W. J. G., Usero, A., Leroy, A. K., Rich, J. W., & Kennicutt, R. C. 2011, AJ, 141, 23

Barnes, E. I., Sellwood, J. A., & Kosowsky, A. 2004, AJ, 128, 2724

Barnes, J. E. 1987, in Nearly Normal Galaxies. From the Planck Time to the Present, ed. S. M. Faber, 154

Begeman, K. G. 1987, PhD thesis, Kapteyn Institute, (1987)

—. 1989, A&A, 223, 47

Bell, E. F., & de Jong, R. S. 2001, ApJ, 550, 212

Bendo, G. J., Wilson, C. D., Warren, B. E., Brinks, E., Butner, H. M., Chanial, P., Clements, D. L., Courteau, S., Irwin, J., Israel, F. P., Knapen, J. H., Leech, J., Matthews, H. E., Mühle, S., Petitpas, G., Serjeant, S., Tan, B. K., Tilanus, R. P. J., Usero, A., Vaccari, M., van der Werf, P., Vlahakis, C., Wiegert, T., & Zhu, M. 2010, MNRAS, 402, 1409

Binney, J., & Merrifield, M. 1998, Galactic astronomy (Princeton University Press)

Binney, J., & Tremaine, S. 2008, Galactic Dynamics: Second Edition, ed. Binney, J. & Tremaine, S. (Princeton University Press)

Blais-Ouellette, S., Amram, P., & Carignan, C. 2001, AJ, 121, 1952

Blumenthal, G. R., Faber, S. M., Flores, R., & Primack, J. R. 1986, ApJ, 301, 27

Boomsma, R. 2007, PhD thesis, Kapteyn Astronomical Institute, University of Groningen

Bosma, A. 1978, PhD thesis, PhD Thesis, Groningen Univ., (1978)

—. 1981a, AJ, 86, 1791

—. 1981b, AJ, 86, 1825

Bosma, A. 1999, in Astronomical Society of the Pacific Conference Series, Vol. 182, Galaxy Dynamics - A Rutgers Symposium, ed. D. R. Merritt, M. Valluri, & J. A. Sellwood, 339

Bottema, R. 1999, A&A, 348, 77

Bottema, R., & Verheijen, M. A. W. 2002, A&A, 388, 793

Briggs, D. S., Schwab, F. R., & Sramek, R. A. 1999, in Astronomical Society of the Pacific Conference Series, Vol. 180, Synthesis Imaging in Radio Astronomy II, ed. G. B. Taylor, C. L. Carilli, & R. A. Perley, 127

Buote, D. A., Jeltema, T. E., Canizares, C. R., & Garmire, G. P. 2002, ApJ, 577, 183

Burstein, D., & Rubin, V. C. 1985, ApJ, 297, 423

Capaccioli, M. 1989, in World of Galaxies (Le Monde des Galaxies), ed. H. G. Corwin Jr. & L. Bottinelli, 208

Carignan, C., Beaulieu, S., & Freeman, K. C. 1990a, AJ, 99, 178

Carignan, C., Charbonneau, P., Boulanger, F., & Viallefond, F. 1990b, A&A, 234, 43

Carignan, C., & Freeman, K. C. 1985, ApJ, 294, 494

Casertano, S. 1983, MNRAS, 203, 735

Casertano, S., & van Gorkom, J. H. 1991, AJ, 101, 1231

Chattopadhyay, T., & Chattopadhyay, A. K. 2006, AJ, 131, 2452

Chaves, T. A., & Irwin, J. A. 2001, ApJ, 557, 646

Chemin, L., Carignan, C., & Foster, T. 2009, ApJ, 705, 1395

Clowe, D., Bradač, M., Gonzalez, A. H., Markevitch, M., Randall, S. W., Jones, C., & Zaritsky, D. 2006, ApJ, 648, L109

Condon, J. J. 1992, ARA&A, 30, 575

Condon, J. J., Cotton, W. D., Greisen, E. W., Yin, Q. F., Perley, R. A., Taylor, G. B., & Broderick, J. J. 1998, AJ, 115, 1693

Conselice, C. J., Gallagher, J. S., Calzetti, D., Homeier, N., & Kinney, A. 2000, AJ, 119, 79

Corradi, R. L. M., & Capaccioli, M. 1990, A&A, 237, 36

Courteau, S. 1997, AJ, 114, 2402

Courteau, S., & Rix, H. 1999, ApJ, 513, 561

de Blok, W. J. G., Walter, F., Brinks, E., Trachternach, C., Oh, S.-H., & Kennicutt, R. C. 2008, AJ, 136, 2648

de Jong, R. S. 1996, A&A, 313, 45

de Vaucouleurs, G. 1948, Annales d'Astrophysique, 11, 247

—. 1959, Handbuch der Physik, 53, 275

de Vaucouleurs, G., de Vaucouleurs, A., & Corwin, Jr., H. G. 1976, Second reference catalogue of bright galaxies. Containing information on 4,364 galaxies with references to papers published between 1964 and 1975., ed. de Vaucouleurs, G., de Vaucouleurs, A., & Corwin, H. G., Jr.

de Vaucouleurs, G., de Vaucouleurs, A., Corwin, Jr., H. G., Buta, R. J., Paturel, G., & Fouque, P. 1991, Third Reference Catalogue of Bright Galaxies, ed. de Vaucouleurs, G., de Vaucouleurs, A., Corwin, H. G., Jr., Buta, R. J., Paturel, G., & Fouque, P.

Dicaire, I., Carignan, C., Amram, P., Marcelin, M., Hlavacek-Larrondo, J., de Denus-Baillargeon, M., Daigle, O., & Hernandez, O. 2008, AJ, 135, 2038

Dickey, J. M., & Lockman, F. J. 1990, ARA&A, 28, 215

Elmegreen, D. M., & Elmegreen, B. G. 1990, ApJ, 364, 412

English, J., Fiege, J., Wiegert, T., Koribalski, B., Kerzendorf, W., & Freeman, K. C. 2010, in Galaxies and their Masks (in prep.), ed. D.L. Braun, K.C. Freeman, & I. Puerari, Springer (New York)

Ewen, H. I., & Purcell, E. M. 1951, Nature, 168, 356

Fiege, J. D., Johnstone, D., Redman, R. O., & Feldman, P. A. 2004, ApJ, 616, 925

Fraternali, F., Oosterloo, T. A., Sancisi, R., & Swaters, R. 2005, in Astronomical Society of the Pacific Conference Series, Vol. 331, Extra-Planar Gas, ed. R. Braun, 239

Freedman, W. L., Madore, B. F., Gibson, B. K., Ferrarese, L., Kelson, D. D., Sakai, S., Mould, J. R., Kennicutt, Jr., R. C., Ford, H. C., Graham, J. A., Huchra, J. P., Hughes, S. M. G., Illingworth, G. D., Macri, L. M., & Stetson, P. B. 2001, ApJ, 553, 47

Freeman, K. C. 1970, ApJ, 160, 811

García-Barreto, J. A., Carrillo, R., & Vera-Villamizar, N. 2003, AJ, 126, 1707

García-Ruiz, I., Sancisi, R., & Kuijken, K. 2002, A&A, 394, 769

Giovanelli, R., Haynes, M. P., Salzer, J. J., Wegner, G., da Costa, L. N., & Freudling, W. 1994, AJ, 107, 2036

Graham, A. W., & Prieto, M. 1999, ApJ, 524, L23

Gunn, J. E., et al. 1998, AJ, 116, 3040

Haynes, M. P., van Zee, L., Hogg, D. E., Roberts, M. S., & Maddalena, R. J. 1998, AJ, 115, 62

Hernández-Toledo, H. M., Vázquez-Mata, J. A., Martínez-Vázquez, L. A., Avila Reese, V., Méndez-Hernández, H., Ortega-Esbrí, S., & Núñez, J. P. M. 2008, AJ, 136, 2115

Hoekstra, H., van Albada, T. S., & Sancisi, R. 2001, MNRAS, 323, 453

Hoffman, G. L., Lu, N. Y., Salpeter, E. E., Farhat, B., Lamphier, C., & Roos, T. 1993, AJ, 106, 39

Holland, J. H. 1975, Adaptation in Natural and Artificial Systems (Ann Arbor, MI, USA: University of Michigan Press)

Honma, M., & Sofue, Y. 1999, in IAU Symposium, Vol. 183, Cosmological Parameters and the Evolution of the Universe, ed. K. Sato, 157

Hubble, E. 1958, The realm of the nebulae, ed. Hubble, E.

Hubble, E. P. 1926, ApJ, 64, 321

—. 1936, Realm of the Nebulae (New Haven: Yale University Press)

Irwin, J. A. 2007, Astrophysics: Decoding the Cosmos (Wiley-VCH Verlag)

Irwin, J. A., & Chaves, T. 2003, ApJ, 585, 268

Irwin, J. A., Saikia, D. J., & English, J. 2000, AJ, 119, 1592

Irwin, J. A., & Seaquist, E. R. 1991, ApJ, 371, 111

Irwin, J. A., Hoffman, G. L., Spekkens, K., Haynes, M. P., Giovanelli, R., Linder, S. M., Catinella, B., Momjian, E., Koribalski, B. S., Davies, J., Brinks, E., de Blok, W. J. G., Putman, M. E., & van Driel, W. 2009, ApJ, 692, 1447

Johnson, S. C. 1967, Psychometrika, 2, 241

Józsa, G. I. G., Kenn, F., Klein, U., & Oosterloo, T. A. 2007, A&A, 468, 731

Kalnajs, A. J. 1983, in IAU Symposium, Vol. 100, Internal Kinematics and Dynamics of Galaxies, ed. E. Athanassoula, 109

Kamphuis, J., & Sancisi, R. 1993, A&A, 273, L31

Kant, I. 1755, Allgemeine Naturgeschichte und Theorie des Himmels (J.F. Peterson, Knigsberg and Leipzig), Part I

Karachentsev, I. D. 2005, AJ, 129, 178

Karachentsev, I. D., Karachentseva, V. E., Huchtmeier, W. K., & Makarov, D. I. 2004, AJ, 127, 2031

Karachentseva, V. E. 1973, Astrofizicheskie Issledovaniia Izvestiya Spetsial'noj Astrofizicheskoj Observatorii, 8, 3

Kennicutt, Jr., R. C. 1998, ApJ, 498, 541

Kennicutt, Jr., R. C., Tamblyn, P., & Congdon, C. E. 1994, ApJ, 435, 22

Kent, S. M. 1987, AJ, 93, 816

King, D., & Irwin, J. A. 1997, New Astronomy, 2, 251

Koribalski, B. S., et al. 2004, AJ, 128, 16

Kregel, M., van der Kruit, P. C., & de Grijs, R. 2002, MNRAS, 334, 646

Lequeux, J. 1983, A&A, 125, 394

Macri, L. M., Stetson, P. B., Bothun, G. D., Freedman, W. L., Garnavich, P. M., Jha, S., Madore, B. F., & Richmond, M. W. 2001, ApJ, 559, 243

Madore, B. F., & Freedman, W. L. 1991, PASP, 103, 933

McKee, C. F., & Ostriker, E. C. 2007, ARA&A, 45, 565

Mihalas, D., & Binney, J. 1981, Galactic astronomy: Structure and kinematics /2nd edition/, ed. Mihalas, D. & Binney, J.

Milgrom, M. 1983, ApJ, 270, 365

Miller, E. D., & Bregman, J. N. 2005, in Astronomical Society of the Pacific Conference Series, Vol. 331, Extra-Planar Gas, ed. R. Braun, 261

Navarro, J. F., Frenk, C. S., & White, S. D. M. 1996, ApJ, 462, 563

Noordermeer, E., van der Hulst, J. M., Sancisi, R., Swaters, R. A., & van Albada, T. S. 2005, A&A, 442, 137

Noordermeer, E., van der Hulst, J. M., Sancisi, R., Swaters, R. S., & van Albada, T. S. 2007, MNRAS, 376, 1513

Ostriker, J. P., & Peebles, P. J. E. 1973, ApJ, 186, 467

Palunas, P., & Williams, T. B. 2000, AJ, 120, 2884

Paturel, G., Petit, C., Prugniel, P., Theureau, G., Rousseau, J., Brouty, M., Dubois, P., & Cambrésy, L. 2003, A&A, 412, 45

Persic, M., & Salucci, P. 1990, MNRAS, 245, 577

Persic, M., Salucci, P., & Stel, F. 1996, MNRAS, 281, 27

Pierce, M. J. 1994, ApJ, 430, 53

Pisano, D. J., Wilcots, E. M., & Elmegreen, B. G. 1998, AJ, 115, 975

Portinari, L., Sommer-Larsen, J., & Tantalo, R. 2003, Ap&SS, 284, 723

Richter, O., & Sancisi, R. 1994, A&A, 290, L9

Rogstad, D. H., Lockhart, I. A., & Wright, M. C. H. 1974, ApJ, 193, 309

Rogstad, D. H., & Shostak, G. S. 1972, ApJ, 176, 315

Rubin, V. C. 1983, Science, 220, 1339

Rubin, V. C., Burstein, D., Ford, Jr., W. K., & Thonnard, N. 1985, ApJ, 289, 81

Rubin, V. C., Thonnard, N., & Ford, Jr., W. K. 1978, ApJ, 225, L107

Rupen, M. P. 1999, in Astronomical Society of the Pacific Conference Series, Vol. 180, Synthesis Imaging in Radio Astronomy II, ed. G. B. Taylor, C. L. Carilli, & R. A. Perley, 229

Sackett, P. D. 1997, ApJ, 483, 103

Saglia, R. P., & Sancisi, R. 1988, A&A, 203, 28

Sandage, A. 1975, Classification and Stellar Content of Galaxies Obtained from Direct Photography (the University of Chicago Press), 1

Sanders, R. H. 1996, ApJ, 473, 117

Sanders, R. H., & Verheijen, M. A. W. 1998, ApJ, 503, 97

Schlegel, D. J., Finkbeiner, D. P., & Davis, M. 1998, ApJ, 500, 525

Schommer, R. A., Bothun, G. D., Williams, T. B., & Mould, J. R. 1993, AJ, 105, 97

Seigar, M. S., James, P. A., Puerari, I., & Block, D. L. 2003, in Revista Mexicana de Astronomia y Astrofisica, vol. 27, Vol. 17, Revista Mexicana de Astronomia y Astrofisica Conference Series, ed. V. Avila-Reese, C. Firmani, C. S. Frenk, & C. Allen, 184

Slipher, V. M. 1913, Lowell Observatory Bulletin, 2, 56

Sofue, Y. 1999, Ap&SS, 269, 593

Sofue, Y., & Rubin, V. 2001, ARA&A, 39, 137

Spano, M., Marcelin, M., Amram, P., Carignan, C., Epinat, B., & Hernandez, O. 2008, MNRAS, 383, 297

Stil, J. M. 1999, PhD thesis, Ph. D Thesis Leiden University (NL), (1999)

Swaters, R. A. 1999, PhD thesis, , Rijksuniversiteit Groningen, (1999)

Swedenborg, B. 1734, Principia rerum naturalium; sive novarum tentaminum phenomena mundi elementaris philosophia explicandi (English translation: Rendell, J.R. & Tansley, I., 1912., Swedenborg Society, London), Part III, Chap. I–II

Taylor, G. B., Carilli, C. L., & Perley, R. A., eds. 1999, Astronomical Society of the Pacific Conference Series, Vol. 180, Synthesis Imaging in Radio Astronomy II

Teuben, P. J. 2002, in Astronomical Society of the Pacific Conference Series, Vol. 275, Disks of Galaxies: Kinematics, Dynamics and Peturbations, ed. E. Athanassoula, A. Bosma, & R. Mujica, 217

Toomre, A., & Toomre, J. 1972, ApJ, 178, 623

Tully, R. B., & Fisher, J. R. 1977, A&A, 54, 661

van Albada, T. S., Bahcall, J. N., Begeman, K., & Sancisi, R. 1985, ApJ, 295, 305

van Albada, T. S., & Sancisi, R. 1986, Royal Society of London Philosophical Transactions Series A, 320, 447

van den Bergh, S. 1960, ApJ, 131, 215

van der Hulst, J. M., Terlouw, J. P., Begeman, K. G., Zwitser, W., & Roelfsema, P. R. 1992, in Astronomical Society of the Pacific Conference Series, Vol. 25, Astronomical Data Analysis Software and Systems I, ed. D. M. Worrall, C. Biemesderfer, & J. Barnes, 131

van der Hulst, J. M., van Albada, T. S., & Sancisi, R. 2001, in Astronomical Society of the Pacific Conference Series, Vol. 240, Gas and Galaxy Evolution, ed. J. E. Hibbard, M. Rupen, & J. H. van Gorkom, 451

van der Hulst, T., & Sancisi, R. 1988, AJ, 95, 1354

van der Kruit, P. C., & Searle, L. 1981, A&A, 95, 105

van der Marel, R. P., & Franx, M. 1993, ApJ, 407, 525

Verheijen, M. A. W. 1997, PhD thesis, PhD thesis, Univ. Groningen, The Netherlands , (1997)

Vogt, N. P., Haynes, M. P., Herter, T., & Giovanelli, R. 2004, AJ, 127, 3273

Walter, F., Brinks, E., de Blok, W. J. G., Bigiel, F., Kennicutt, R. C., Thornley, M. D., & Leroy, A. 2008, AJ, 136, 2563

Warner, P. J., Wright, M. C. H., & Baldwin, J. E. 1973, MNRAS, 163, 163

Warren, B. E., Wilson, C. D., Israel, F. P., Serjeant, S., Bendo, G. J., Brinks, E., Clements, D. L., Irwin, J. A., Knapen, J. H., Leech, J., Matthews, H. E., Mühle, S., Mortimer, A. M. J., Petitpas, G., Sinukoff, E., Spekkens, K., Tan, B. K., Tilanus, R. P. J., Usero, A., van der Werf, P. P., Vlahakis, C., Wiegert, T., & Zhu, M. 2010, ApJ, 714, 571

Whitmore, B. C., Forbes, D. A., & Rubin, V. C. 1988, ApJ, 333, 542

Wilson, C. D., Warren, B. E., Israel, F. P., Serjeant, S., Bendo, G., Brinks, E., Clements, D., Courteau, S., Irwin, J., Knapen, J. H., Leech, J., Matthews, H. E., Mühle, S., Mortier, A. M. J., Petitpas, G., Sinukoff, E., Spekkens, K., Tan, B. K., Tilanus, R. P. J., Usero, A., van der Werf, P., Wiegert, T., & Zhu, M. 2009, ApJ, 693, 1736

Wolf, M. 1914, Vjschr. astr. Ges, 49, 151

Worthey, G. 1994, ApJS, 95, 107

Wright, T. 1750, An Original Theory or New Hypothesis of the Universe (London), 83–84

Wrobel, J. M., & Walker, R. C. 1999, in Astronomical Society of the Pacific Conference Series, Vol. 180, Synthesis Imaging in Radio Astronomy II, ed. G. B. Taylor, C. L. Carilli, & R. A. Perley, 171

York, D. G., et al. 2000, AJ, 120, 1579

Zasov, A. V., & Smirnova, A. A. 2005, Astronomy Letters, 31, 160

Zeilinger, W. W., Vega Beltrán, J. C., Rozas, M., Beckman, J. E., Pizzella, A., Corsini, E. M., & Bertola, F. 2001, Ap&SS, 276, 643

Zwicky, F. 1933, Helvetica Physica Acta, 6, 110

Appendix A

Channel maps of modelled galaxies

The following figures show channel maps of galaxies which have been modelled with GalAPAGOS for the work in this thesis. This includes a galaxy that has not been presented previously in the thesis: NGC 0055 from the HIPASS survey. The lowest χ^2 GalAPAGOS model contours are overlaid on the binned input data cube. Note that not all channels are shown for each galaxy since many have a low velocity resolution. Instead of displaying an unpractically large number of channel maps, we skip channels in steps of 1-7. The contour levels are at 5%, 30%, 60% and 90 % of the peak emission level of the modelled cube. For a few of the galaxies, the grey scale is stretched in order to show faint emission.

Plots of the rotation curve families from the family of optimal solutions acquired from each run are available in § 5.2 of Chapter 5.

Here, the modelled cubes have a pixel resolution matching the binned input data cubes (note however, that they can be set to any desired pixel resolution). The resolution and other information pertinent to each galaxy, are noted in the caption of each figure. Other information, such as beam resolution, is available in Chapter 2.

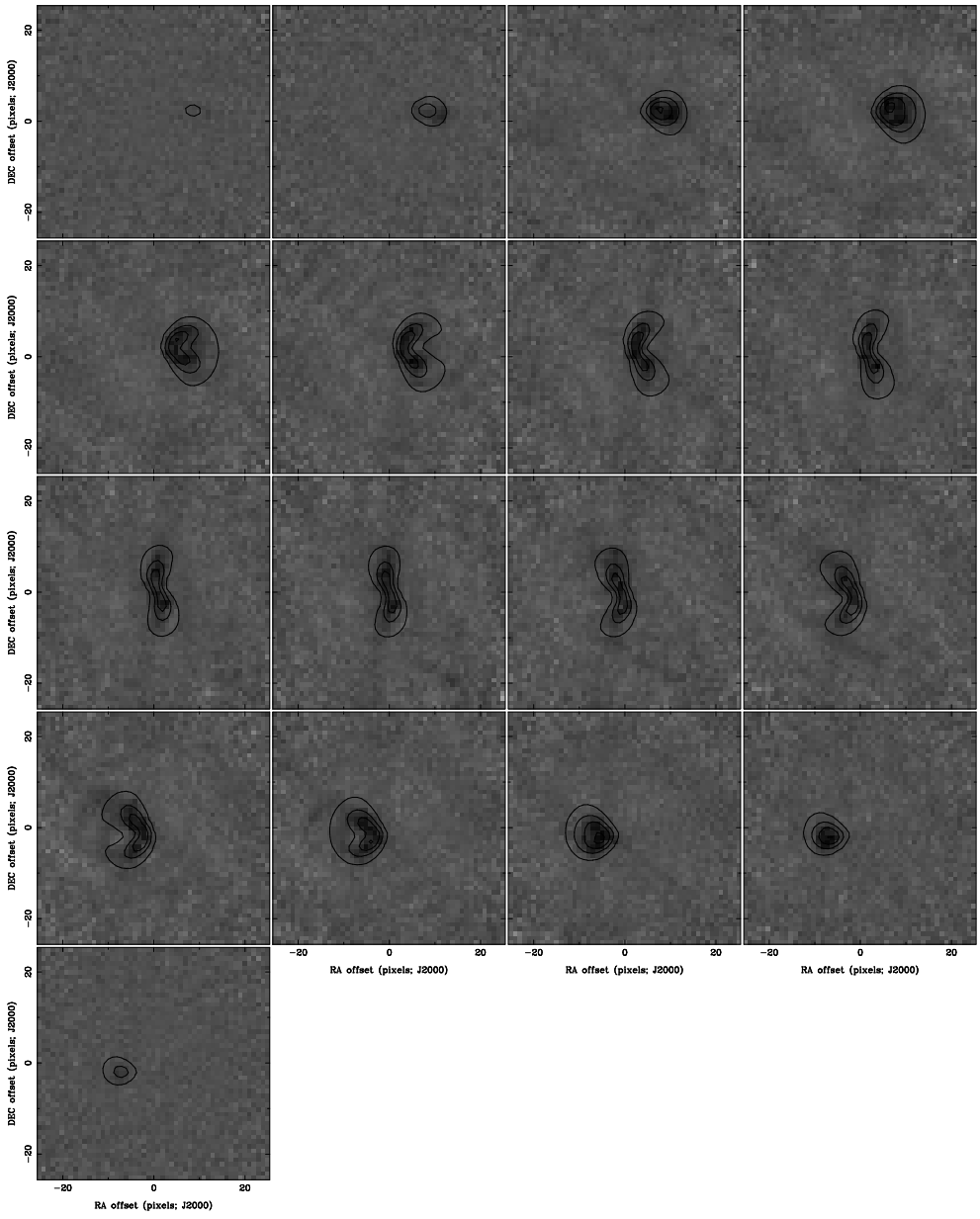

Figure A.1: Channel maps of NGC 925 with input data from THINGS, and the best fit GalAPAGOS overlaid as a contour map. The input data are binned to a pixel resolution of 30″/pixel. The

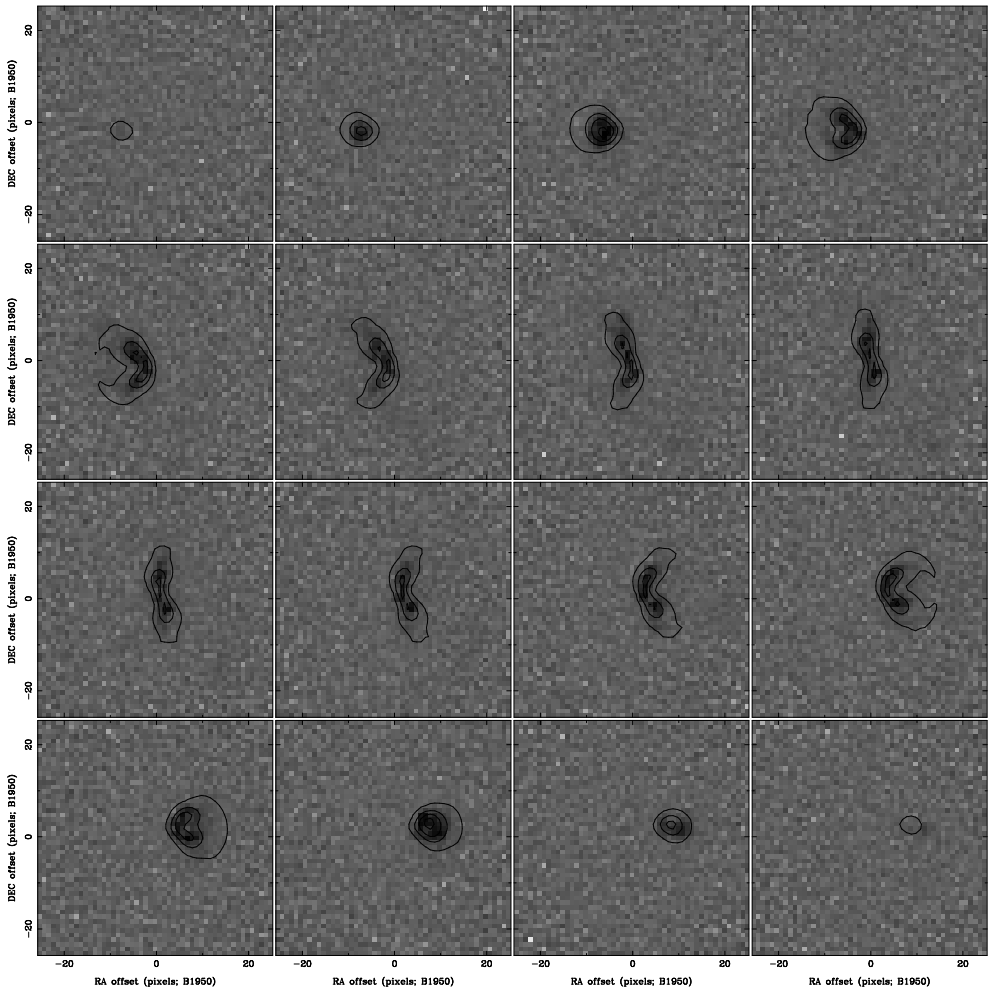

Figure A.2: Channel maps of NGC 925 with input data from WHISP, and the best fit GalAPAGOS model overlaid as a contour map. The input data are binned to a pixel resolution of 30″/pixel.

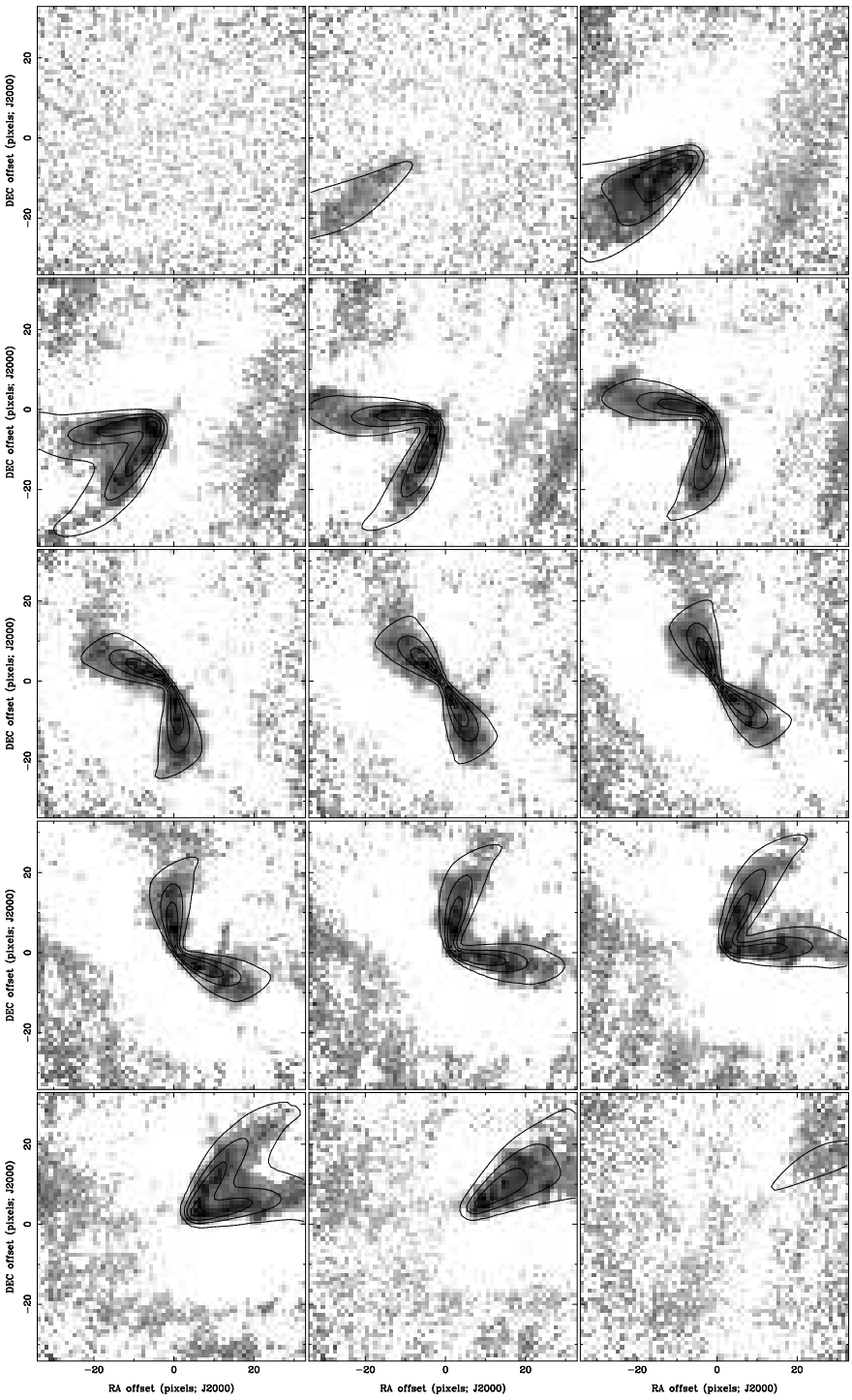

Figure A.3: Channel maps of NGC 2403, with input data from THINGS, and the best fit GalAPAGOS model overlaid as a contour map. The input data are binned to a pixel size of 30″/pixel. The greyscale is stretched to show the faint emission in the outer parts of the galaxy. The channel maps show the full field of view, which is not quite enough to span the large angular size of the galaxy.

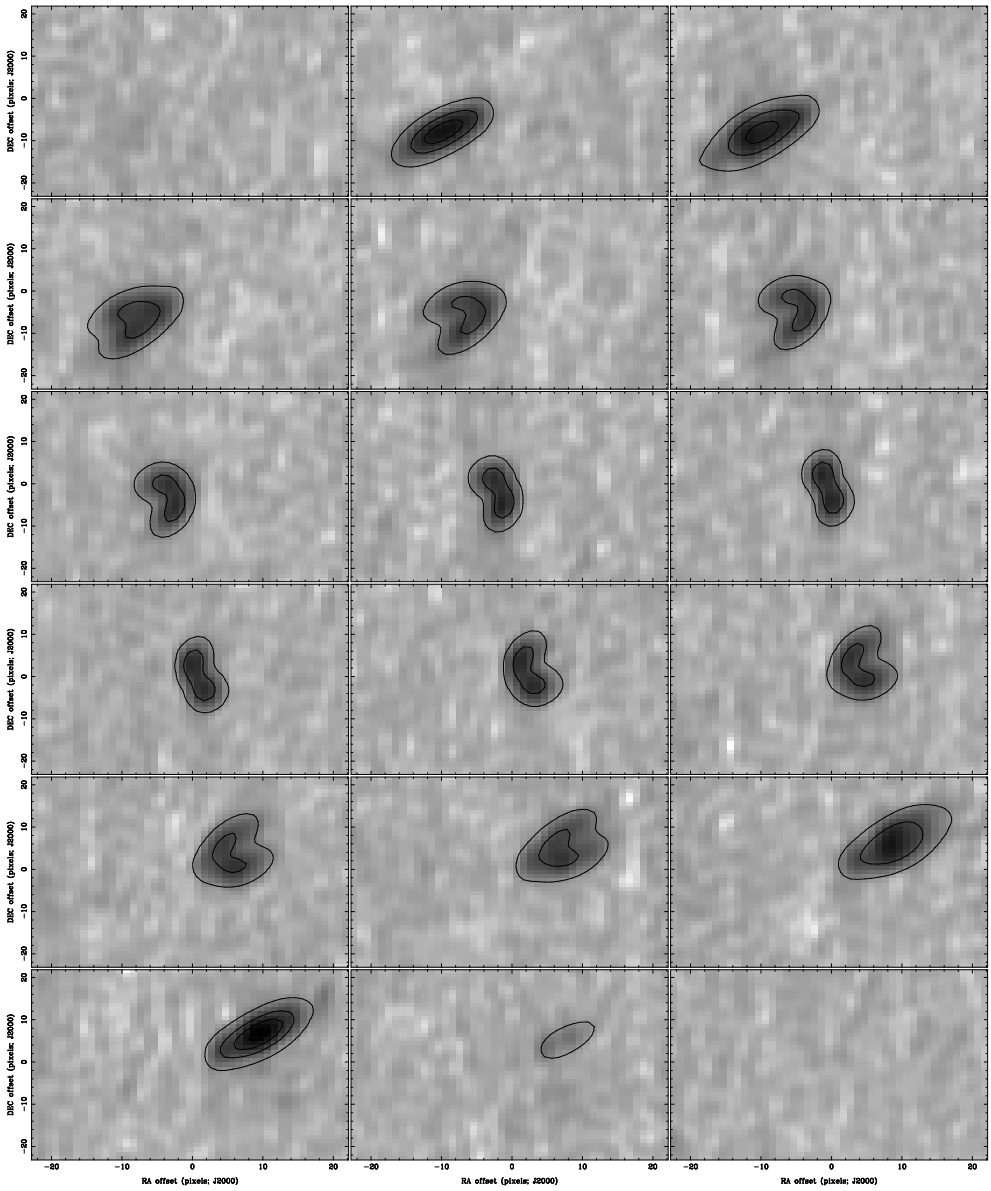

Figure A.4: Channel maps of NGC 2613 with input data provided by J. Irwin and the best fit GalAPAGOS model overlaid as a contour map. The input data are not binned and have resolution of 15″/pixel.

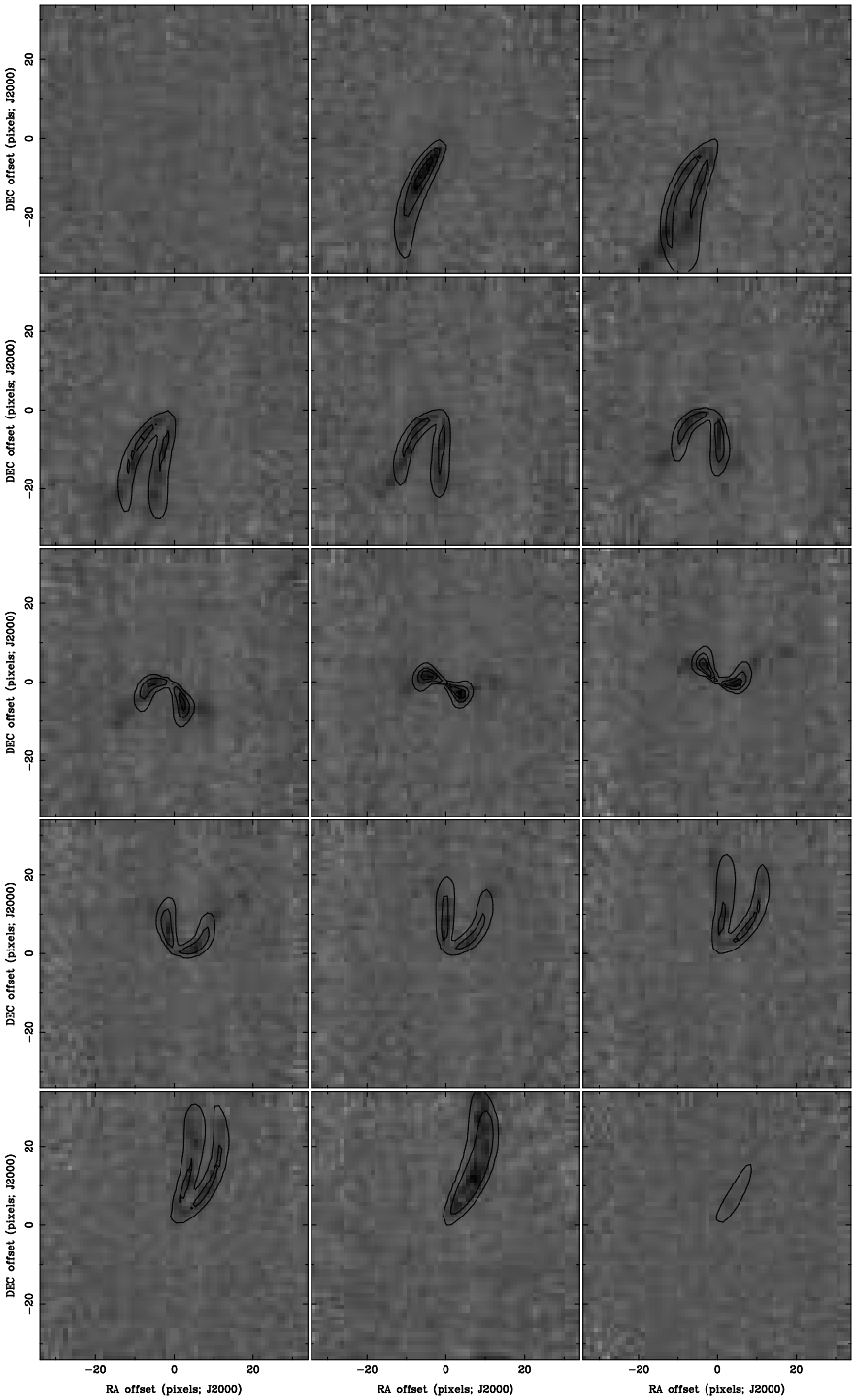

Figure A.5: Channel maps of NGC 2841 with input data from THINGS, and the best fit GalAPAGOS model overlaid as a contour map. The input data are binned to a pixel resolution of 22.″5/pixel.

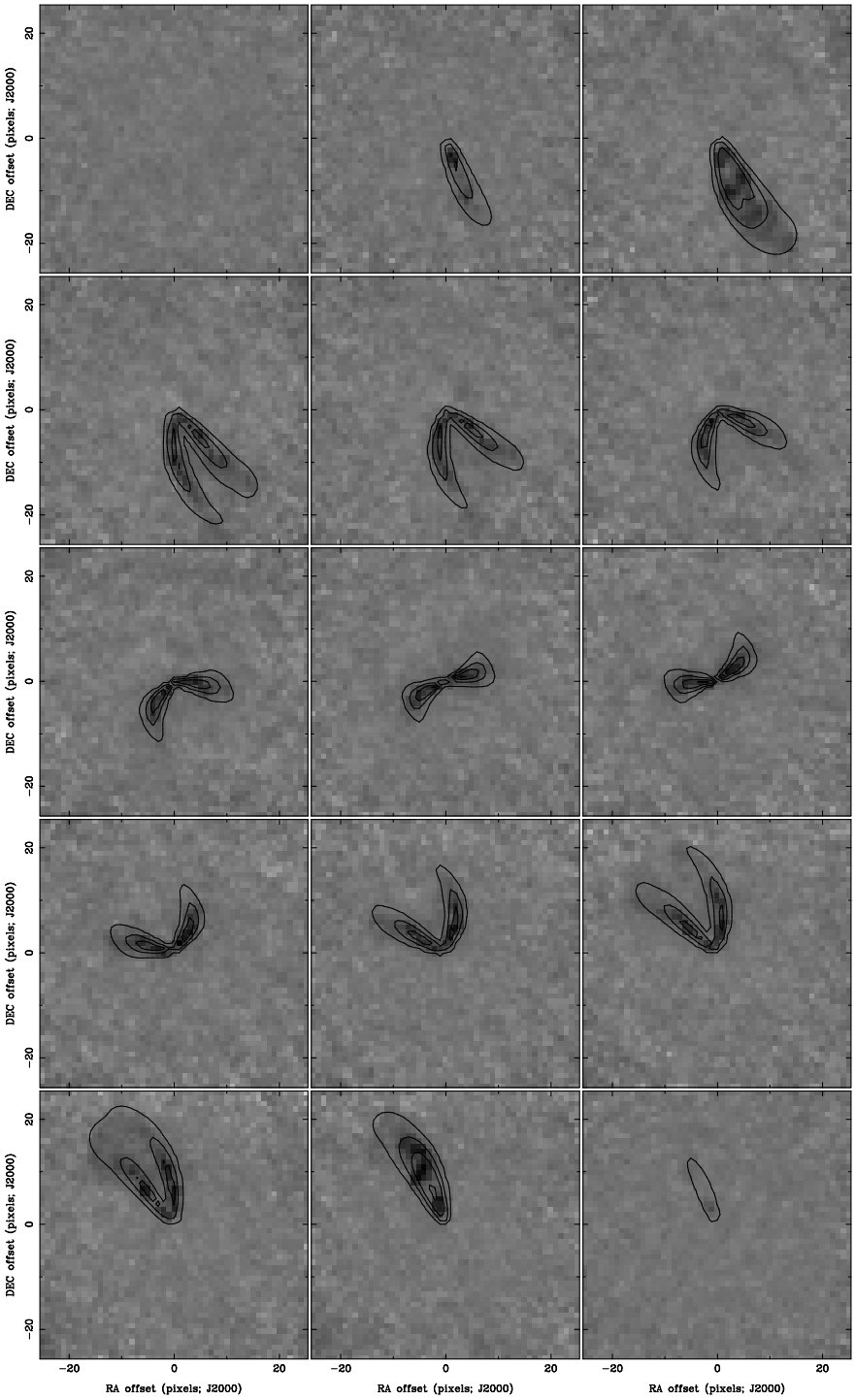

Figure A.6: Channel maps of NGC 2903 with input data from THINGS, and the best fit GalAPAGOS model overlaid as a contour map. The input data are binned to a pixel resolution of 30″/pixel.

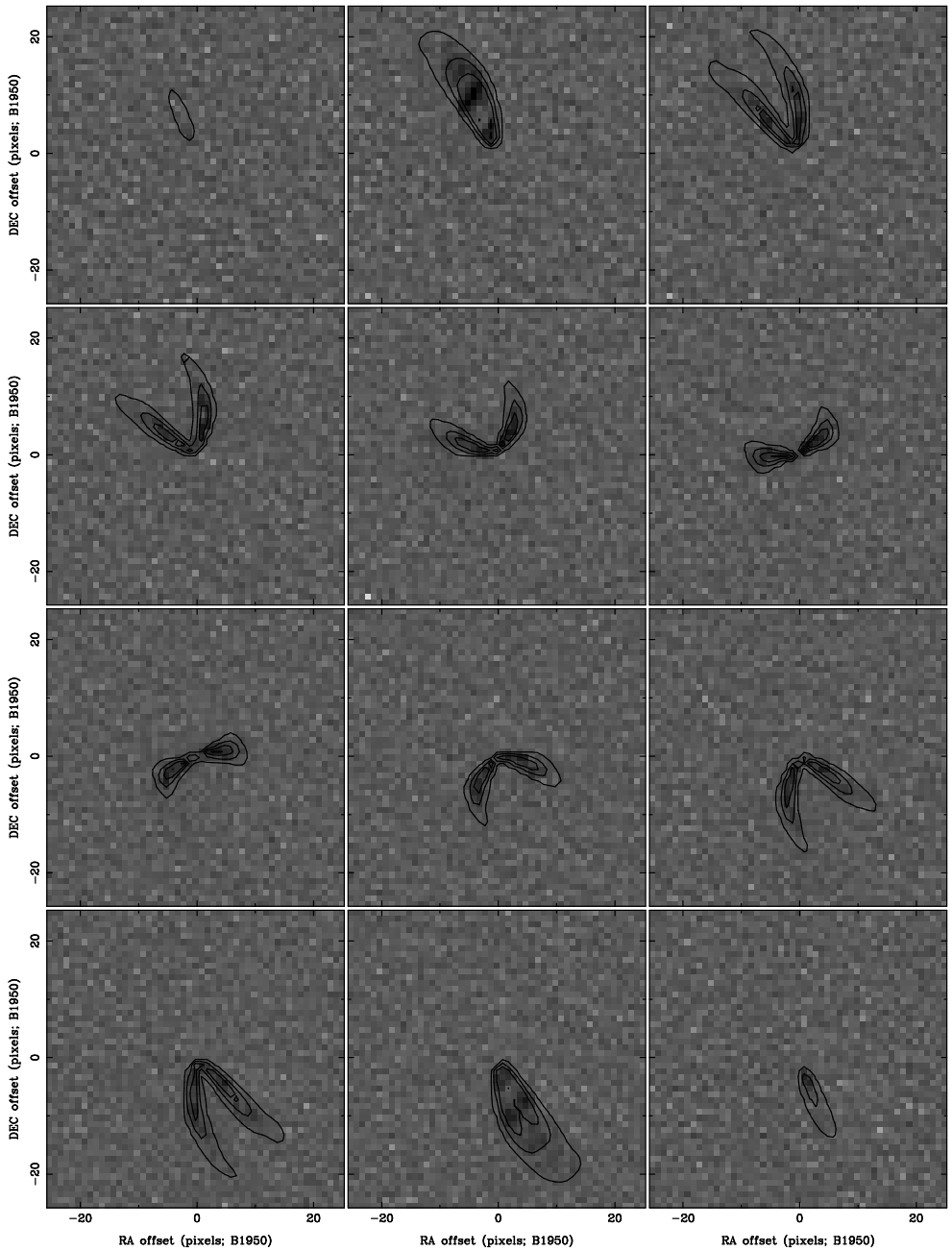

Figure A.7: Channel maps of NGC 2903 with input data from WHISP, and the best fit GalAPAGOS model overlaid as a contour map. The input data are binned to a pixel resolution of 30″/pixel.

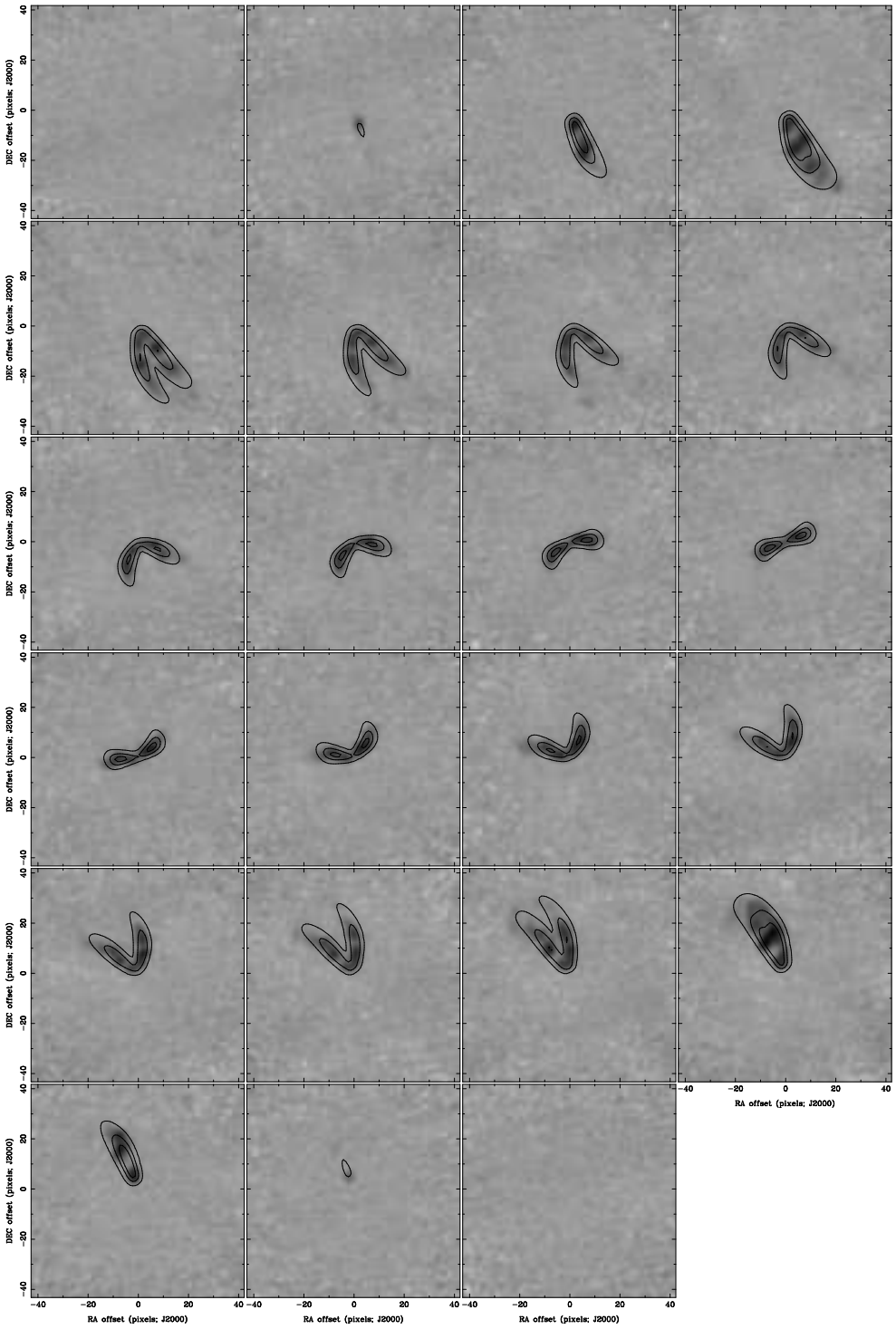

Figure A.8: Channel maps of NGC 2903 with input data provided by J. Irwin, and the best fit GalAPAGOS model overlaid as a contour map. The input data are binned to a pixel resolution of 20″/pixel.

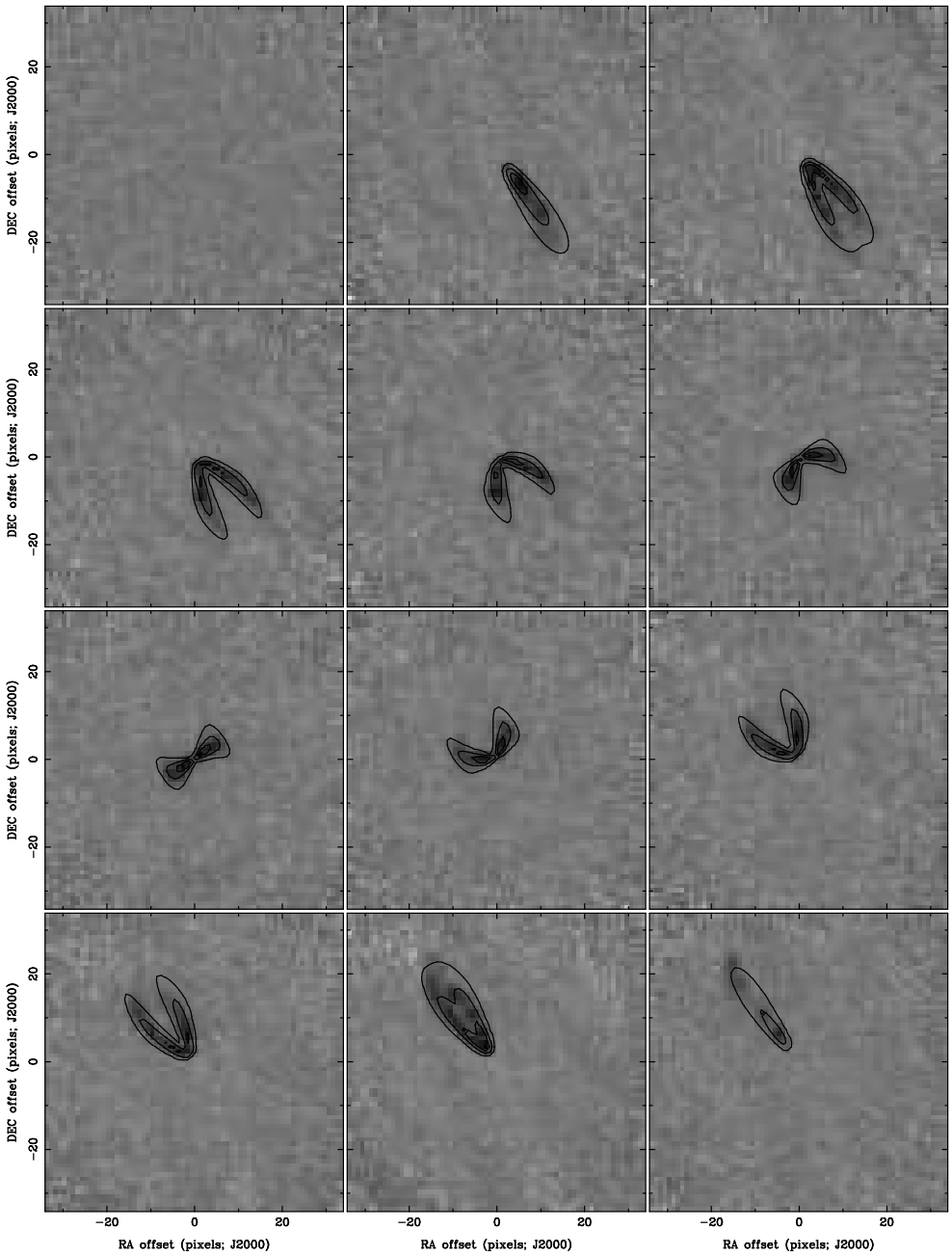

Figure A.9: Channel maps of NGC 3198 with input data from THINGS, and the best fit GalAPAGOS model overlaid as a contour map. The input data are binned to a pixel resolution of 22.″5/pixel.

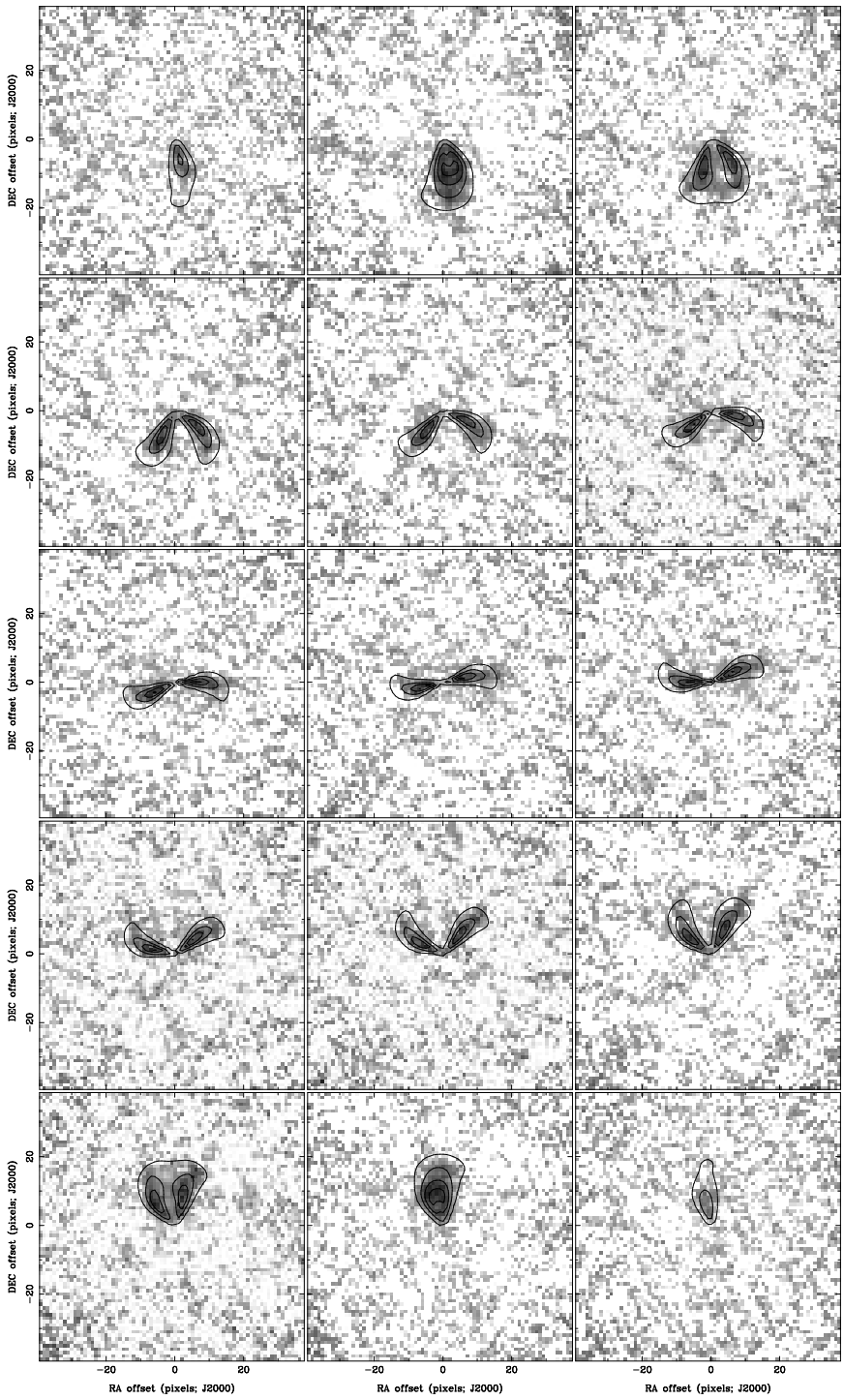

Figure A.10: Channel maps of NGC 3351 with input data from THINGS, and the best fit GalAPAGOS model overlaid as a contour map. The input data are binned to a pixel resolution of 19.″5/pixel. The greyscale is stretched to show the faint emission in the outer parts of the galaxy.

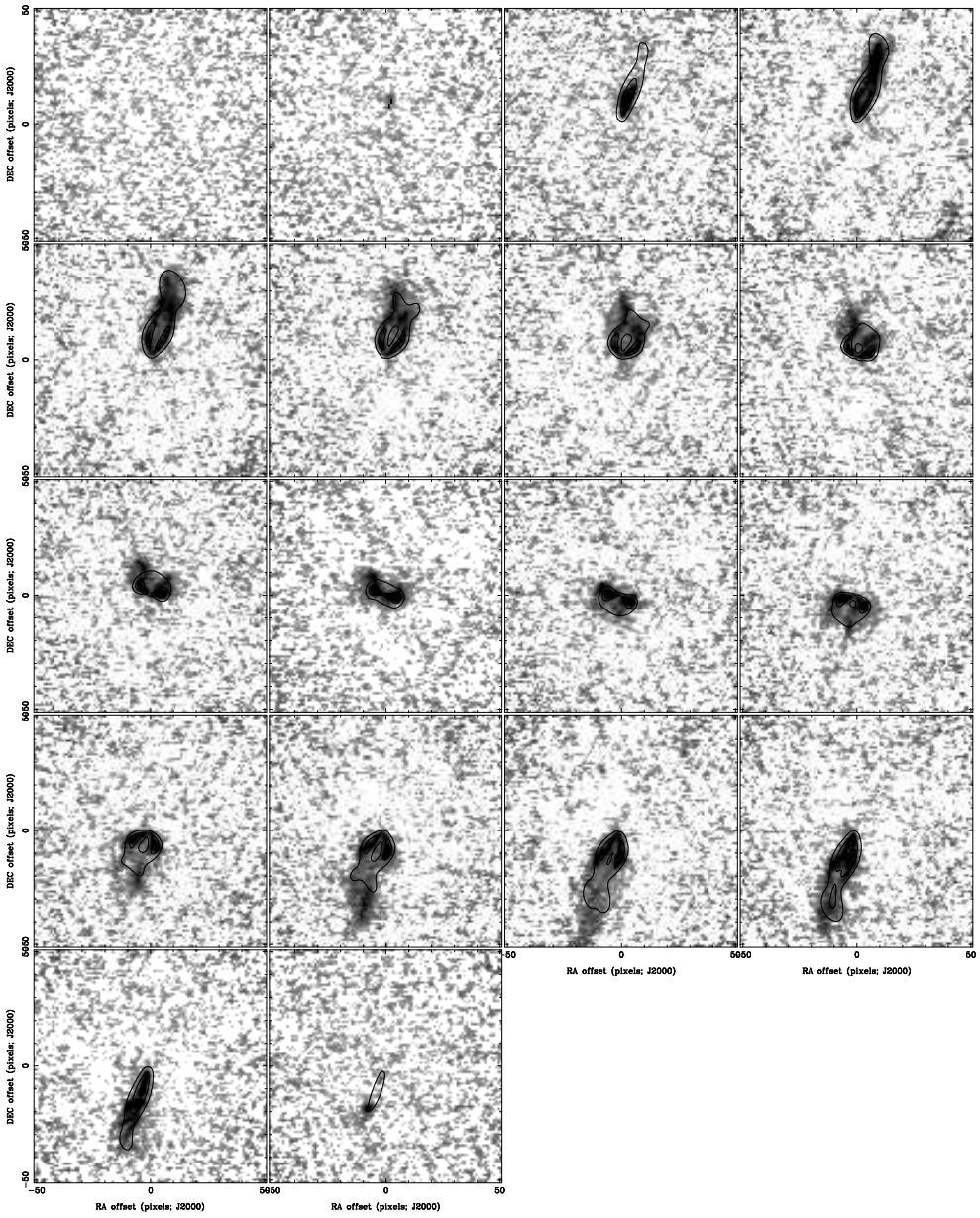

Figure A.11: Channel maps of NGC 3521 with input data from THINGS, and the best fit GalAPAGOS model overlaid as a contour map. The input data are binned to a pixel resolution of 15″/pixel. The greyscale is stretched to show the faint emission in the outer parts of the galaxy.

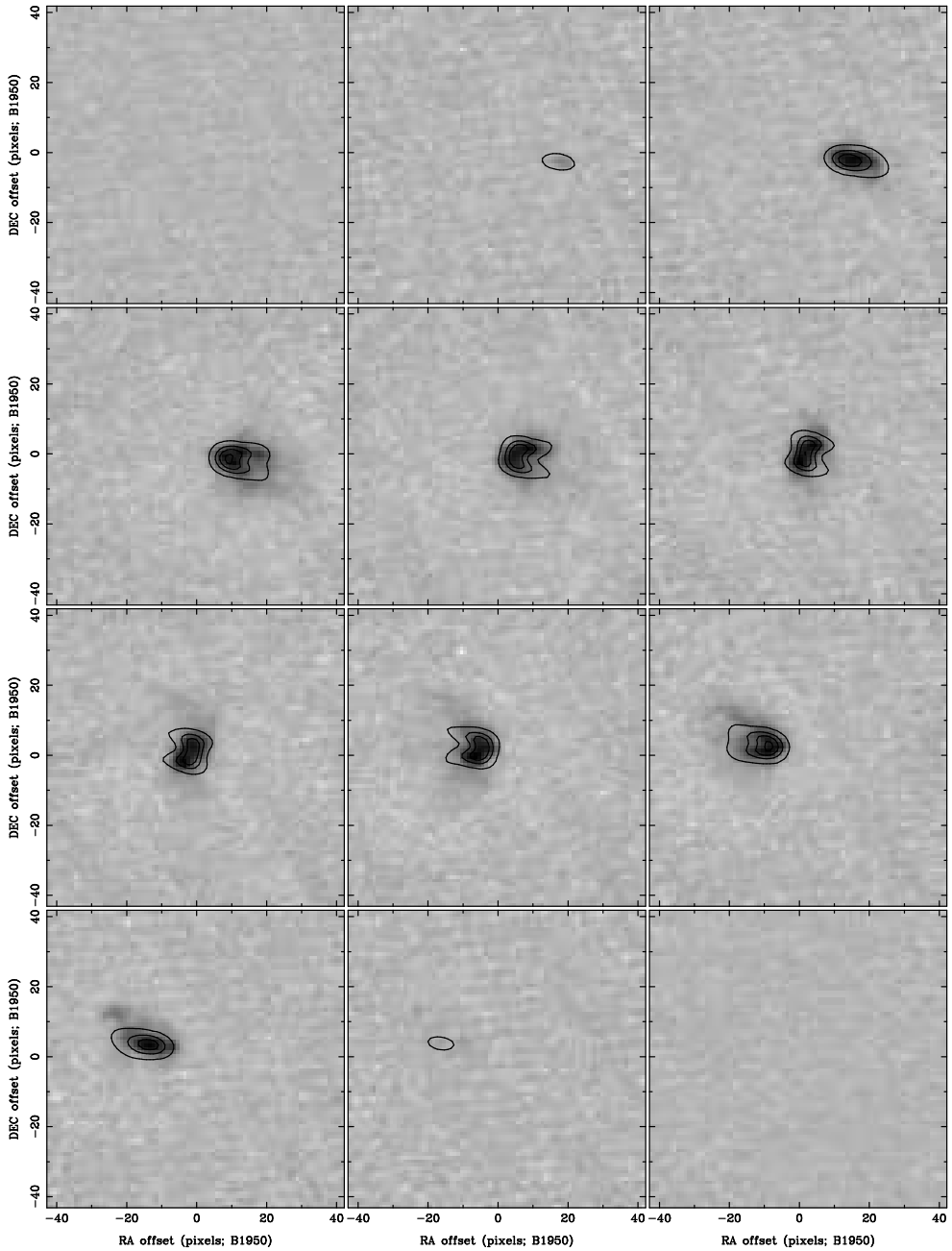

Figure A.12: Channel maps of NGC 3556 with input data provided by J. Irwin, and the best fit GalAPAGOS model overlaid as a contour map. The input data are binned to a pixel resolution of 12″/pixel.

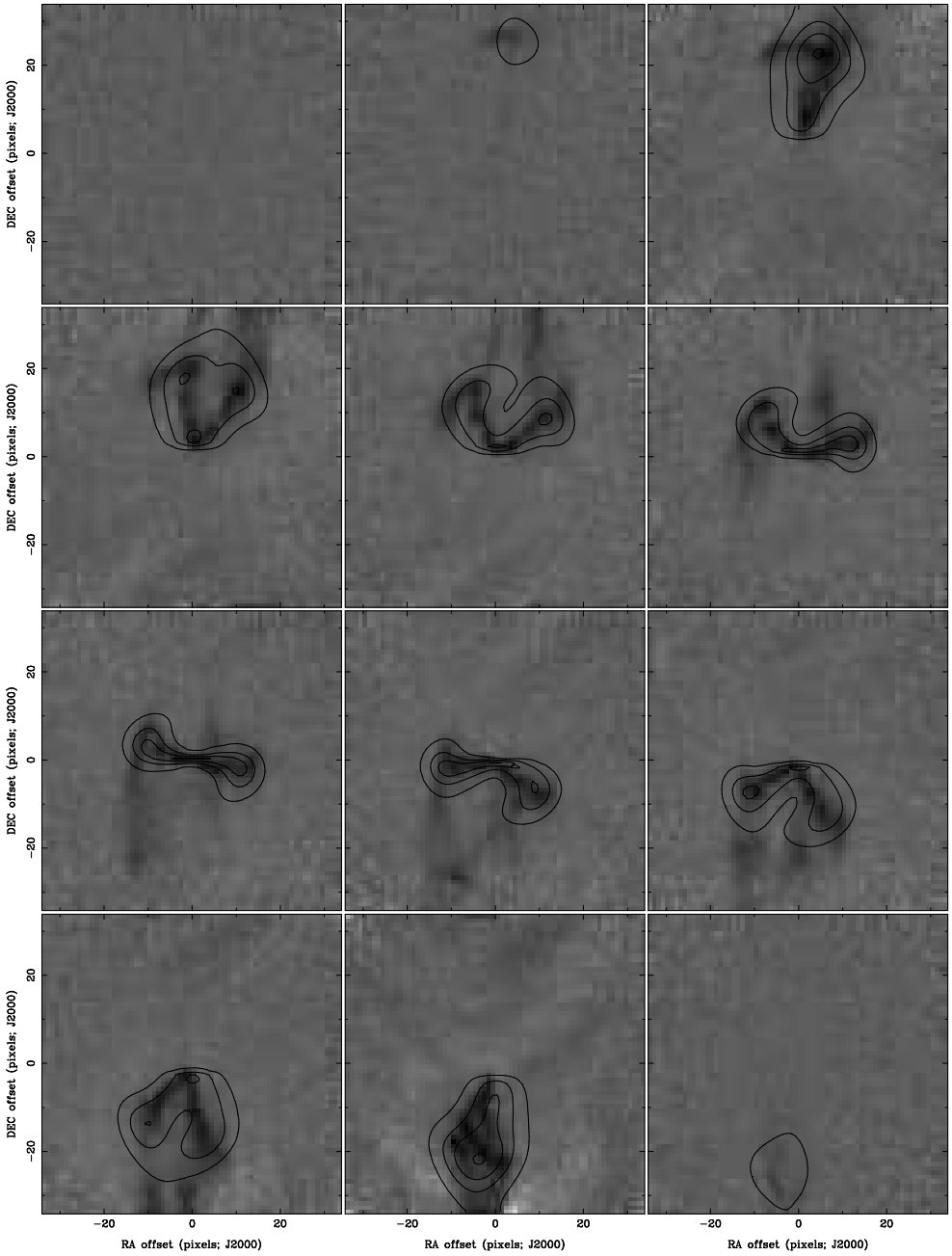

Figure A.13: Channel maps of NGC 3621 with input data from THINGS, and the best fit GalAPAGOS model overlaid as a contour map. The input data are binned to a pixel resolution of 22.″5/pixel.

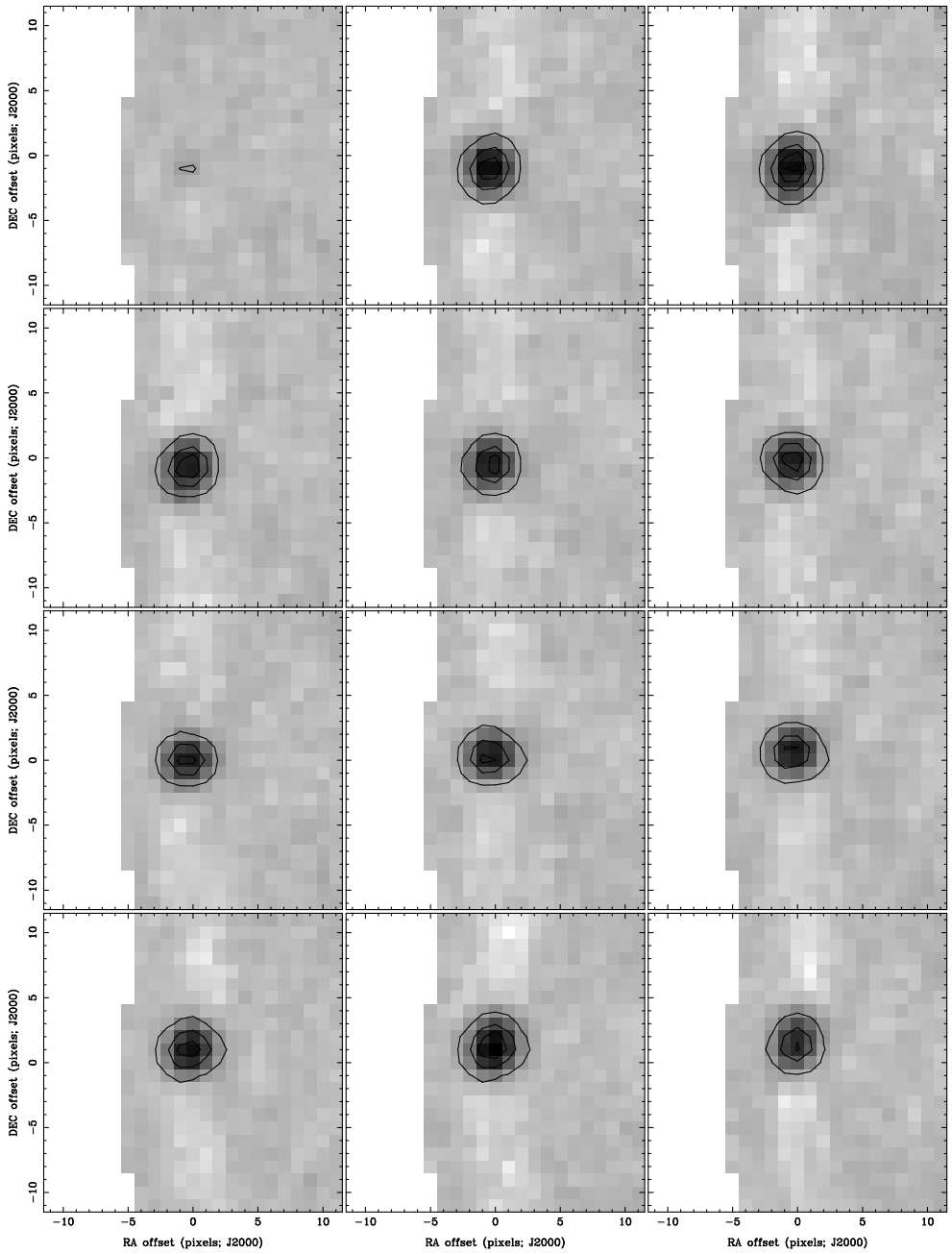

Figure A.14: Channel maps of NGC 3621 with input data from HIPASS, and the best fit GalAPAGOS model overlaid as a contour map. The pixel resolution of these unbinned data is 8′.

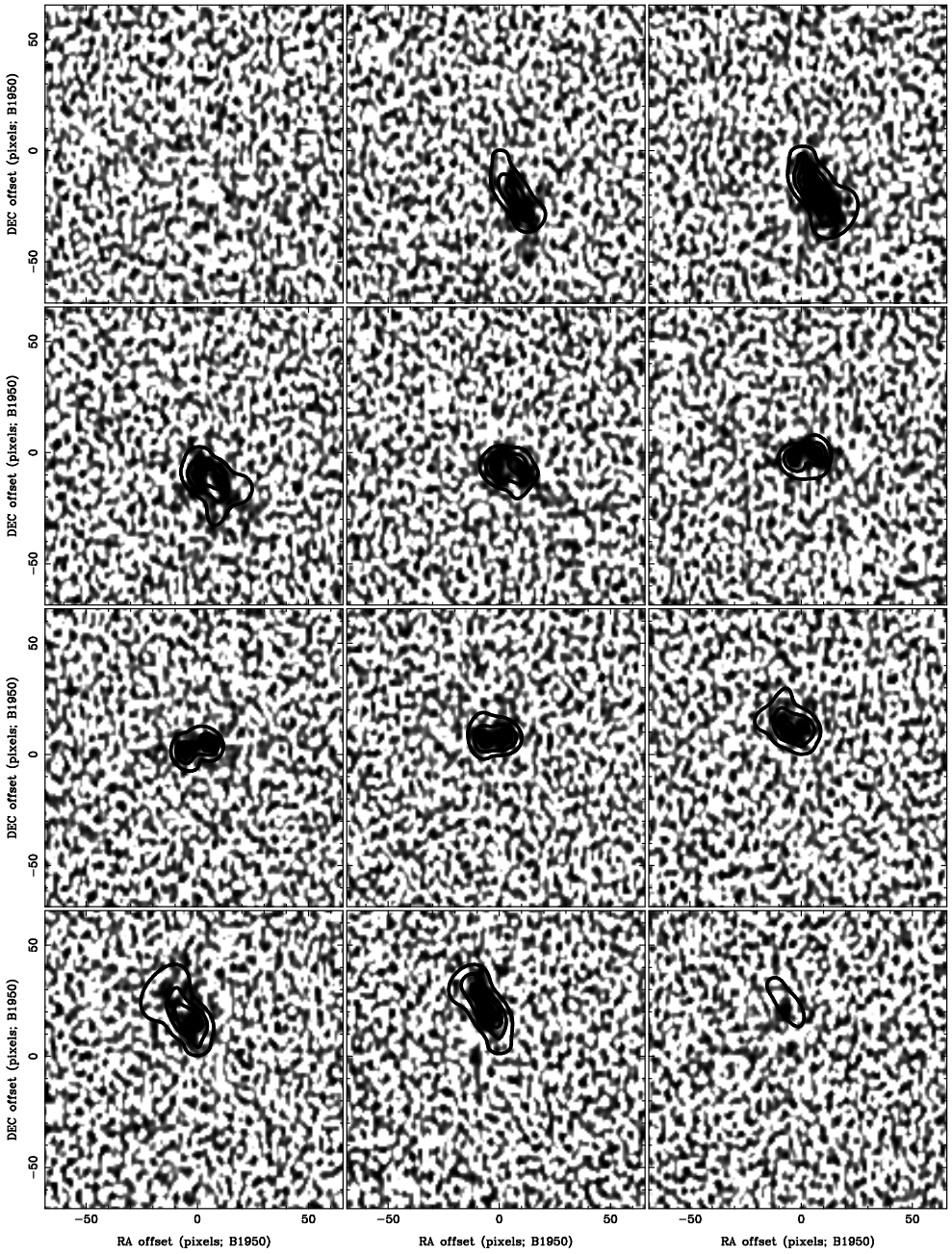

Figure A.15: Channel maps of NGC 4096 with input data from WHISP, and the best fit GalAPAGOS model overlaid as a contour map. The pixel resolution of these unbinned data is 5″. The greyscale is stretched to show the faint emission of the galaxy.

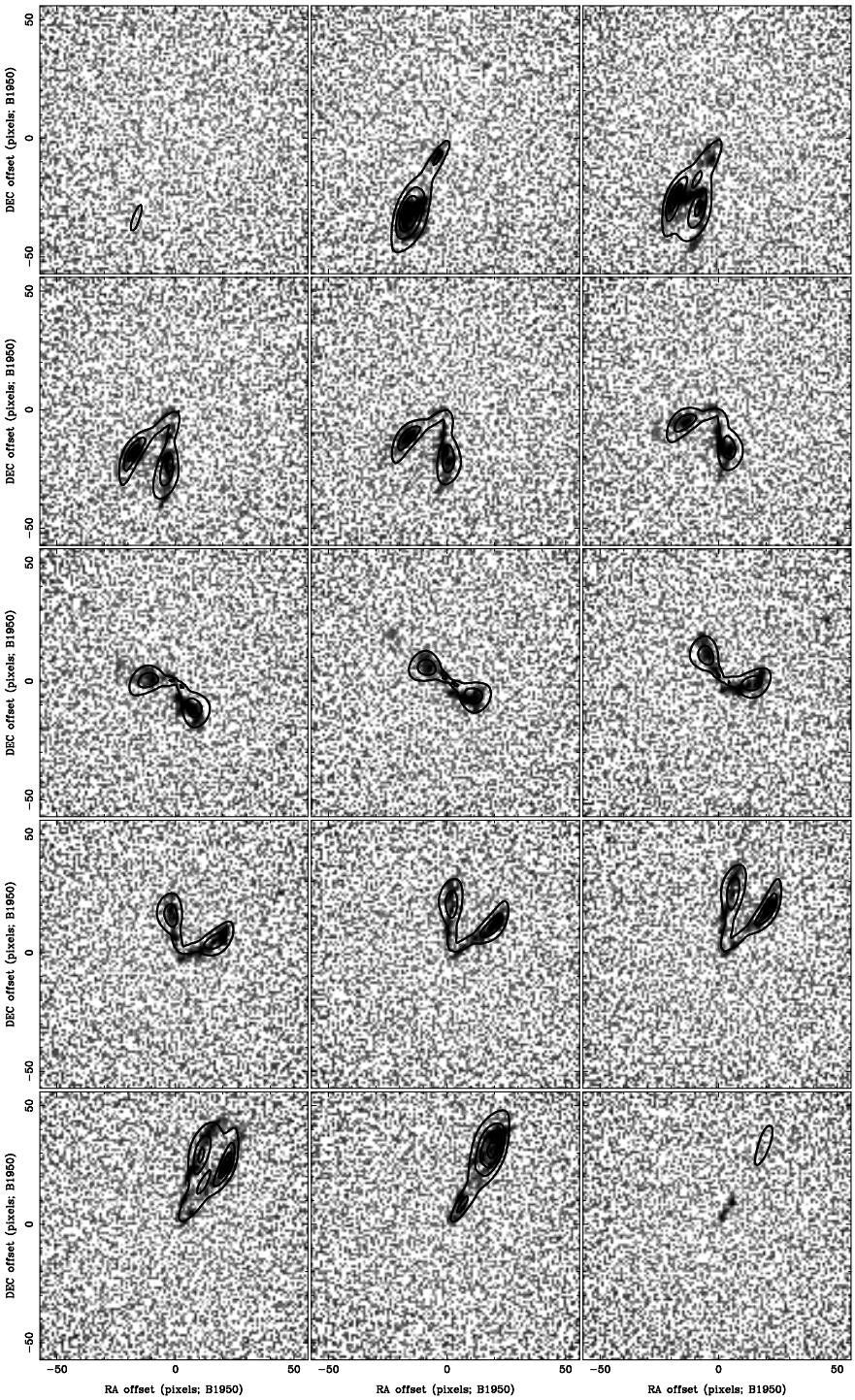

Figure A.16: Channel maps of NGC 4258 with input data from WHISP, and the best fit GalAPAGOS model overlaid as a contour map. The input data are binned to a pixel resolution of 15″. The greyscale is stretched to sho faint emission.

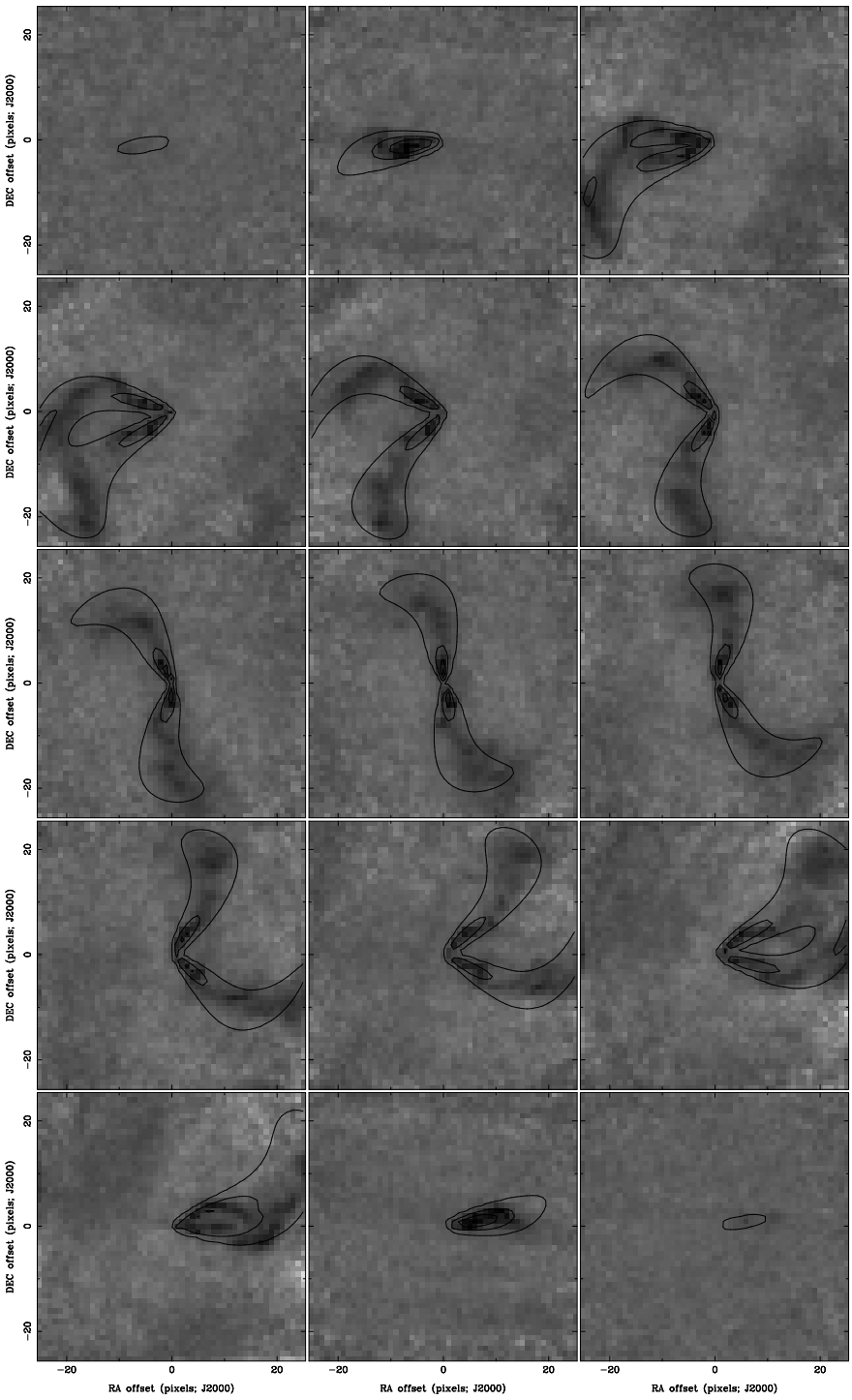

Figure A.17: Channel maps of NGC 5055 with input data from THINGS, and the best fit GalAPAGOS model overlaid as a contour map. The input data are binned to a pixel resolution of 30″/pixel. The channel maps show the full field of view of the data, which is not quite enough to span the large angular size of the galaxy.

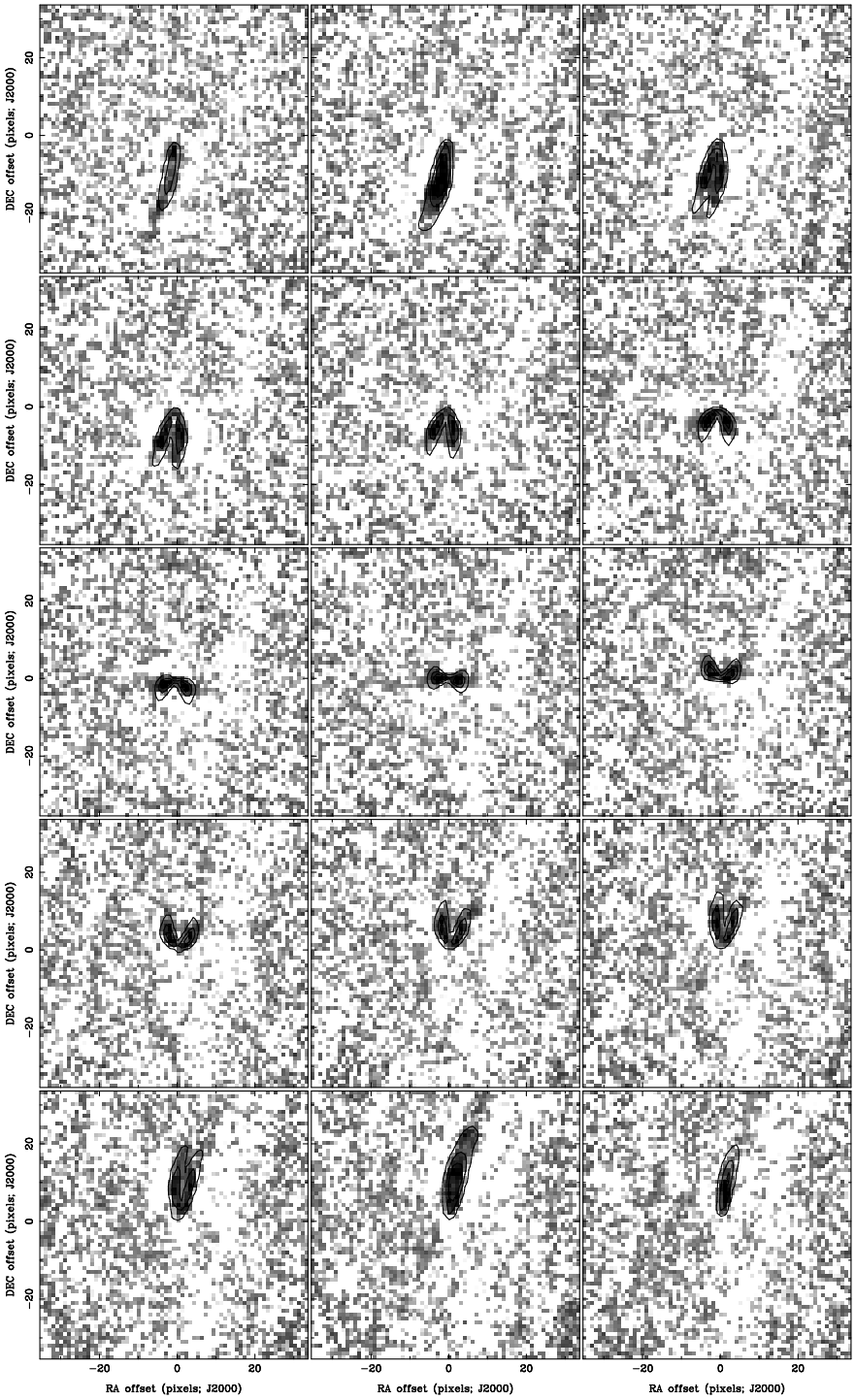

Figure A.18: Channel maps of NGC 7331 with input data from THINGS, and the best fit GalAPAGOS model overlaid as a contour map. The input data are binned to a pixel resolution of 19.″5/pixel. The greyscale is stretched to show faint emission.

Appendix B

List of acronyms

Table B.1: Table of acronyms, their meaning and pages where more information can be found.

Acronym	**Meaning**	**Page**
AGN	Active Galactic Nucleus	226
AIPS	Astronomical Image Processing System	63
ASKAP	Australia Square Kilometre Array Pathfinder	241
CO	Carbon monoxide	21
Dec	Declination	25
DM	Dark Matter	8
DN	Data Number	54
FITS	Flexible Image Transport System	26
FWHM	Full Width Half Maxmimum	78
GA	Genetic algorithm	65
GaLAPAGOS	Galaxy Astrophysical Parameter Acquisition by Genetic Optimization Software	65
GIPSY	The Groningen Image Processing System	44
HI	Neutral hydrogen	21

Continued on next page...

... continued from previous page

Acronym	Meaning	Page
HIPASS BGC	HIPASS Bright Galaxy Catalogue	33
HIPASS	The HI Parkes All Sky Survey	33
HVC	High velocity clouds	4
IMF	Initial Mass Function	59
IPAC	Infrared Processing and Analysis Center	53
IRAF	Image Reduction and Analysis Facility	53
IRSA	NASA/IPAC InfraRed Science Archive	53
JCMT	James Clerk Maxwell Telescope	36
MeerKAT	the Karoo Array Telescope	243
M/L	Mass-to-Luminosity Ratio	40
MONGHOOSE	MeerKAT HI Observations of Nearby Galactic Objects: Observing Southern Emitters	243
NASA	National Aeronautics and Space Administration	53
NED	NASA/IPAC Extragalactic Database	55
NFW	Navarro, Frenk and White halo model	59
NGC	New General Catalogue	29
NGLS	Nearby Galaxies Legacy Survey	36
NIR	Near infrared	29
NRAO	National Radio Astronomy Observatory	25
NVSS	NRAO VLA Sky Survey Catalog	220
PA	Position Angle	46
RA	Right ascension	25
RC	Rotation curve	103
SDM	Surface density modulation	72

Continued on next page...

... continued from previous page

Acronym	Meaning	Page
SDSS	Sloan Digital Sky Survey	34
SFR	Star formation rate	220
SINGS	Spitzer Infrared Nearby Galaxies Survey	36
S/N	Signal-to-noise ratio	79
THINGS	The HI Nearby Galaxy Survey	29
TR	Tilted ring	42
URC	Universal rotation curve	169
VLA	Very Large Array	25
WALLABY	Widefield ASKAP L-band Legacy All-sky Blind surveY (The ASKAP HI All-Sky Survey)	241
WHISP	Westerbork observations of HI in Irregular and SPiral galaxies	31
WIMPs	Weakly Interacting Massive Particles	9
WSRT	Westerbork Synthesis Radio Telescope	25

Table B.1: List of acronyms, their meanings and pages where more information can be found.